Modeling fluid injection effects in dynamic fault rupture using Fast Boundary Element Methods

Laura Bagur

INSTITUT POLYTECHNIQUE DE PARIS

NNT : 2024IPPAE010

Thèse de doctorat

ENSTA

IP PARIS

Modeling fluid injection effects in dynamic fault rupture using Fast Boundary Element Methods

Thèse de doctorat de l'Institut Polytechnique de Paris
préparée à l'École nationale supérieure de techniques avancées

École doctorale n°626 École doctorale de l'Institut Polytechnique de Paris (EDIPP)
Spécialité de doctorat : Mécanique des fluides et des solides, acoustique

Thèse présentée et soutenue à Palaiseau, le 12/07/2024, par

LAURA BAGUR

Composition du Jury :

David Néron Professeur des universités, ENS Paris-Saclay (LMPS)	Président
Vladislav Yastrebov Chargé de Recherche (HDR), Mines Paris - PSL (Centre des Matériaux)	Rapporteur
Brice Lecampion Associate Professor, EPFL (GEL)	Rapporteur
Véronique Lazarus Professeure, ENSTA Paris (IMSIA)	Examinatrice
Mathilde Radiguet Chargée de recherche, Université Grenoble Alpes (ISTERRE)	Examinatrice
Stéphanie Chaillat Directrice de recherche, ENSTA Paris (POEMS)	Directrice de thèse
Ioannis Stefanou Professeur des universités, École Centrale de Nantes (GEM)	Co-directeur de thèse
Jean-François Semblat Professeur, ENSTA Paris (IMSIA)	Co-directeur de thèse
Pierre Romanet Docteur, Université de Rome (La Sapienza) et Université Côte d'Azur (Géoazur)	Invité

Acknowledgements

Tout d'abord, je tiens à remercier les membres de mon jury de thèse pour leur présence et pour m'avoir donné l'opportunité de discuter de mon travail de manière approfondie tout en m'imprégnant de leurs sensibilités par rapport à mon sujet de thèse. Je remercie chaleureusement mes rapporteurs, Vladislav Yastrebov et Brice Lecampion, qui m'ont fait l'honneur de relire avec beaucoup d'attention ce manuscrit et m'ont fait de précieux retours pour me permettre de prendre davantage de recul sur ce travail. Un grand merci à David Néron pour avoir accepté de présider mon jury de thèse, après m'avoir eue comme élève à l'ENS Paris Saclay, et pour son investissement avec Brice Lecampion dans mon comité de suivi de thèse. Je suis également très reconnaissante envers Véronique Lazarus et Mathilde Radiguet, qui a fait le déplacement depuis Grenoble, pour l'intérêt et l'attention qu'elles ont porté à mes travaux.

Durant cette thèse, j'ai eu la chance de travailler sur un sujet pluridisciplinaire entre mathématiques appliquées, mécanique, et géophysique grâce à l'expertise complémentaire et à l'encadrement de mes directeurs de thèse : Stéphanie Chaillat, Jean-François Semblat et Ioannis Stefanou. Je tiens à les remercier pour leur confiance et leur soutien durant ces trois années. A Stéphanie, merci de m'avoir fait découvrir et approfondir les BEMs en cours puis en stage et enfin en thèse. Merci pour ta disponibilité pour échanger sur les aspects numériques, tes encouragements, tes nombreuses relectures du manuscrit et tes précieux conseils pour la préparation de ma soutenance. À Jean-François, merci pour tes conseils, pour nos échanges qui m'ont permis de prendre du recul sur mon travail, de m'avoir permis de collaborer avec toi en enseignement, et pour ton accueil chaleureux à l'unité de mécanique. À Ioannis, merci pour le temps que tu m'as consacrée pour discuter de développements aussi bien théoriques que numériques et pour ton accueil chaleureux à Nantes. Tu m'as poussée à me poser des questions sur chaque hypothèse, à construire des bases solides et rigoureuses pour mon travail.

Pendant ces trois années, j'ai eu la chance de faire beaucoup de rencontres qui ont également façonné mon travail de thèse. Je tiens en particulier à remercier Pierre Romanet, que j'ai connu grâce à mes encadrants, qui m'a énormément appris sur les simulations de glissements sismique et asismique et qui m'a transmis sa passion pour cette thématique. Merci de m'avoir permis de travailler avec toi et de connaître l'équipe dans laquelle tu travailles au laboratoire Géoazur. Grâce à Ioannis, j'ai rencontré les doctorants et post-doctorants investis dans le projet européen CoQuake. Merci à Alexandros pour sa gentillesse et pour cette super semaine passée ensemble à l'EGU à Vienne. Merci à Georgios pour ton aide sur la fin de la rédaction. Et merci à Filippo, Ahmad, Timos, Diego, Abdallah pour leur accueil à Nantes et au sein de l'équipe. C'était un plaisir d'en apprendre plus sur vos travaux

lors des meetings CoQuake. Grâce à Stéphanie, j'ai eu l'opportunité de passer deux semaines à l'Université de Stanford, pendant lesquelles j'ai pu discuter de mon travail avec Eric Dunham, Paul Segall, So Ozawa, Vidar Stierström, Martin Almquist, Gustav Eriksson et Ian Mc Bearty. Je tiens à les remercier pour leur accueil chaleureux et les échanges passionnants que nous avons eus. J'ai également eu la chance de rencontrer Harsha Bhat, Michelle Amalkari, Jinhui Chen, Navid Kheirdast et Carlos Villafuerte à l'ENS ULM. Merci pour votre accueil, votre bienveillance, j'ai beaucoup apprécié de pouvoir discuter avec vous et d'en apprendre plus sur vos recherches.

J'ai eu la chance de passer trois ans entre l'unité de mathématiques appliquées et l'unité de mécanique à l'ENSTA Paris. Je voudrais remercier les membres de chaque équipe pour leur accueil et l'environnement qu'ils offrent aux stagiaires, doctorants et post-doctorants. À Patrick Ciarlet qui m'a encadré en stage, à Sonia Fliss, Eliane Bécache, Pierre Marchand et Sabine Ortiz avec qui j'ai eu plaisir à collaborer en enseignement. Merci en particulier à Corinne de m'avoir permis de travailler dans des conditions idéales tout en m'aidant à aller en conférence en prenant soin à chaque fois de t'en occuper comme si cela avait été pour toi. Un grand merci à tous les doctorants, post-doctorants, stagiaires que j'ai rencontrés et qui font un travail incroyable dans ces laboratoires. Adrian, Quentin, Cédric, Louise, Hugo et Nail, j'ai de la chance de vous avoir eu comme co-bureau, c'était très agréable de travailler à vos côtés. Pierre, Etienne, Amond, Fabien, Thibault, Natalia, Aziz, Rose-Cloé, Matias, Sarah, Morgane, Farah, En, Antonin, Thimotée, Raphaël, Paul, Zoé, merci pour votre bonne humeur à l'UMA, nos conversations au sujet du travail ou pendant les pauses, vous avez été d'un précieux soutien pendant ces trois ans. Un merci spécial à Fabien, mon binôme de covoiturage. Merci à Élodie, Adrien, Vincent, André, Yoann, Antoine, Sébastien, David, pour leur accueil chaleureux à l'UME et pour avoir souvent partagé leur bureau avec moi. Un grand merci à Alice pour ton soutien de chaque instant, j'ai adoré travaillé à tes côtés depuis le M2 et partager des voyages et plein de bons moments avec toi. Sara, j'ai adoré discuter et travailler avec toi depuis la première fois où l'on s'est rencontrées. Merci d'avoir été là pour moi. Élodie, merci pour ton soutien, ta gentillesse, c'était toujours un plaisir de travailler et de passer du temps avec toi à l'UME. Clara, merci pour ta bienveillance et pour ton soutien. J'étais très heureuse de te retrouver en thèse à l'UMA après le temps passé ensemble à l'ENS. Cristian, Aurélien, merci d'avoir partagé votre passion pour la danse avec moi en plus de plein de bons moments à l'UMA. À Orane et Fanshuo, que j'ai eus comme élèves à l'ENSTA et dont la détermination et les encouragements m'ont boostée jusqu'au bout.

Pendant la rédaction de mon manuscrit, j'ai passé une année extrêmement enrichissante en tant qu'ATER à Sorbonne Université sur le site de Jussieu. Je souhaite exprimer toute ma gratitude à toute l'équipe de l'Institut Jean-Le-Rond d'Alembert pour leur accueil. Un merci particulier à Régis Wunenburger, Jean-Camille Chassaing, Régis Marchiano, Juliette Pierre et Tony Valier-Brasier sans l'aide de qui je n'aurai pas pu vivre cette expérience. J'ai eu la chance de collaborer avec Alice Marcotte, Lucas Frerot, Antoine Hajczak, Nicolas Auffray, Sylvie Le Moine, Benoit Tallon, Jose Fullana, François Ollivier, Rémi Cornaggia, Fatiha Bouchelaghem, et Sophie Dartois en enseignement. Je me suis très vite sentie intégrée grâce à vous, merci pour tout. Alice et Lucas, je tenais particulièrement à vous remercier pour votre bienveillance au cours de cette année et pour votre aide et vos précieux conseils lors de la fin de ma thèse et des répétitions de ma soutenance. Un merci spécial à mes élèves qui m'ont suivie

jusqu'à la soutenance et en particulier à Eder, Axelle, Saif, Nicolas, Amath, Simon, Binta, Neil, Lynn, Mounia, Laëtitia et Junior pour leurs encouragements. L'intérêt et l'enthousiasme dont vous avez fait preuve en TD/TP m'ont énormément encouragée pour poursuivre la rédaction de mon manuscrit de thèse et dans la préparation de ma soutenance en parallèle des enseignements que j'ai donné à Sorbonne Université.

Enfin, je souhaite remercier mes amis de l'ENS, ceux avec qui j'ai continué de danser : Lev-Arcady, Marie, Théo, Alex, Jean et ceux que j'ai pu continuer à voir au cours de ces trois ans : François, Floriane, Alexandre, Michèle, Lucas, Clément, Robin, Nadine, Théodore, Amandine et Guillaume qui m'ont soutenu pour poursuivre dans l'enseignement. Un grand merci à François Rondeau d'être venu me chercher en prépa à Marseille pour ne pas abandonner mon rêve de rentrer à l'ENS Cachan. À Caroline, Antoine et Marie du Lycée Thiers d'être venus (en présentiel ou en visio) fêter avec moi l'aboutissement de ce travail. À mon amie Margaux qui est toujours d'un soutien exceptionnel. À Anthony et Julia qui ont continué de prendre de mes nouvelles même quand je n'avais plus de week-end. Un merci particulier à Yahia Chibah qui m'a suivie depuis la prépa, m'a transmis sa passion pour l'enseignement des Sciences de l'Ingénieur et m'a soutenue à chaque étape de mon parcours. Je termine par remercier Flavien pour son soutien sans faille, ses conseils toujours avisés et qui m'a aidée et encouragée sans relâche pour me permettre d'arriver au bout de ce projet. À ma famille, Maud pour les dernières répétitions et tout au long de ma thèse, Hugo, Claude et Brigitte pour votre soutien et en particulier ma maman, mon papa et mon frère Jean-François, d'être toujours à mes côtés et de trouver les mots justes pour m'encourager à chaque étape.

Contents

Front Matter **i**
Acknowledgements . . . i
Contents . . . v
List of Tables . . . ix
List of Figures . . . xi

Introduction **1**
1 Motivations . . . 1
2 Scientific approach . . . 2
3 Overview of the thesis . . . 3

1 Fast methods for earthquake cycles **7**
1 Instability and its mitigation . . . 8
1.1 Observation of seismic cycles: the genesis . . . 8
1.2 Definition of a seismic cycle: a kinematic approach . . . 9
1.3 Linear stability analysis (LSA) with rate-and-state friction . . . 11
1.4 Fluid-injection effects on the condition for steady state slip of the spring-slider analog . . . 16
1.5 Limitations of the reduced order model . . . 17
2 Generic spatio-temporal fault behavior . . . 18
2.1 Fault geometry . . . 18
2.2 Momentum balance and constitutive equations . . . 20
2.3 Interface conditions . . . 22
2.4 Boundary conditions . . . 26
2.5 Initial conditions . . . 27
3 Simulating seismic cycles . . . 27
3.1 Existing methods for spatio-temporal discretization of the problem . . . 28
3.2 Validation vs. verification of the simulations . . . 34
4 Mitigating the seismic risk using fluid injection? . . . 34
4.1 Evidence of fault slip due to fluid injection . . . 34
4.2 Earthquake mitigation strategies using fluid injection . . . 35
4.3 Incorporating hydro-mechanical couplings . . . 37

2 Fast methods for 2D quasi-dynamic planar fault problems 43
1 Problem formulation at the continuous level : key assumptions 44
1.1 Boundary Integral Equations for fault problems 46
1.2 Interface problems for mode II and mode III planar-fault configurations 57
2 Space discretization of the boundary integral equation 59
2.1 Spectral Boundary Element Method for a planar discontinuity 62
2.2 Fast Boundary Element Method based on Hierarchical matrices 63
2.3 Comparison between the two approaches 67
3 Time discretization 67
3.1 Main time stepping methods implemented 67
3.2 A priori theoretical comparison of the different numerical methods . . . 71
4 Convergence assessment 72
4.1 Proposition of a configuration with an analytical aseismic solution . . . 72
4.2 Methodology for the convergence study 75
4.3 Accuracy of one calculation of the shear-stress change τ^{qs} 76
4.4 Convergence in time 82
5 Numerical test on a seismic cycle benchmark 91
6 Summary of the qualities and drawbacks of space and time discretization/integration methods 96

3 Modeling fluid-injection effects in the vicinity of a fault 101
1 Fluid-injection in simplified fault-mechanics problem 102
2 Reduction of the complete poroelastodynamic equations 104
3 Existing simplified models for fluid effects on fault slip 105
4 Scaling poroelastodynamic equations 107
4.1 Scaling 1D poroelastodynamic equations without source 107
4.2 Scaling 1D poroelastodynamic equations with a fluid source 115
4.3 Extension to 2D 117
4.4 Synthesis of the dimensional analysis of the poroelastodynamic equations 119
5 Illustration with a one-dimensional poroelastic problem 122
5.1 Problem formulation 122
5.2 Laplace domain Green's functions for both the complete and the simplified models 124
5.3 Convolution quadrature method 125
5.4 Comparison between the complete poroelastodynamic model and the simplified model at the timescale of a seismic motion 127

Conclusion 143
1 Main contributions to the modeling of fluid injection effects in dynamic fault rupture using Fast Boundary Element Methods 143
2 Main numerical developments 145
3 Directions for future work 146

Appendices 151

A Currently used codes for seismic cycles simulations 153

B Numerical test on fluid-injection induced slow slip Benchmark 157

C Dimensional analysis of poroelastodynamic equations 161
1 Assessing the governing parameters . . . 161
2 Scaling poroelastodynamic equations . . . 162
3 Determining 1D poroelastodynamic fundamental solutions . . . 163

D Extended abstract in French 169
1 Motivations . . . 169
2 Approche scientifique . . . 170
3 Organisation de la thèse . . . 172
4 Principaux résultats et conclusions . . . 172
5 Principaux développements numériques . . . 175

Bibliography 179

List of Tables

1.1 Balance momentum and constitutive equations for anti-plane and in-plane shear cases for a 1D fault lying in the plane $\{\mathbf{e}_1, \mathbf{e}_3\}$. 22
1.2 Ingredients for modeling a seismic cycle. 27

2.1 A priori comparison of the different time integration methods used. 72
2.2 Compute node specifications. 72
2.3 Parameters used for the convergence study. 75
2.4 Space discretization parameters for convergence study with respect to $L_b/\Delta z$. . 77
2.5 Space discretization parameters for convergence study with respect to N_{rep}. . . 78
2.6 Space discretization parameters for convergence study with respect to N_{rep}. . . 79
2.7 Space discretization parameters to compare the performances of the standard BEM, the H-BEM and the S-BEM. 80
2.8 Parameter values used for quasi-dynamic in-plane case. 82
2.9 Space discretization parameters for the convergence tests on the different time-stepping methods using the analytical aseismic solution Equation (2.79). 84
2.10 Relative final L^2-norm error on the slip δ, the slip-rate V, the shear-stress τ and the state variable θ with respect to the tolerance of the Newton-Raphson method $\varepsilon_{\text{Newton}}$ for the predictor-corrector time-stepping method, using the H-BEM. 85
2.11 Space discretization parameters for the comparison study between our results and the results provided by Pierre Romanet (personal communication) on a seismic cycle simulation. 87
2.12 Time discretization parameters for the comparison study between our results and the results provided by Pierre Romanet (personal communication) on a seismic cycle simulation. 88
2.13 Errors on time at which $V > 1$ m/s for each seismic event. 88
2.14 Relative L^2-norm error on each interface unknown, for each seismic event. . . . 89
2.15 Space discretization parameters for the overkill seismic cycle simulation. 89
2.16 Time discretization parameters for the overkill seismic cycle simulation. 89
2.17 Parameter values used for BP1 SEAS benchmark simulation. 95
2.18 Space discretization parameters for the benchmark problem 1 (BP1 SEAS). . . . 95
2.19 Time discretization parameters for the benchmark problem 1 seismic cycle simulation. 96

3.1 Scales introduced for the dimensional analysis of poroelastodynamic equations. 109

3.2 Parameters for the dimensional analysis of poroelastodynamic equations. . . . 114
3.3 Summary of our results for the scaling of poroelastodynamic equations at different timescales: predominant effects (✓), negligible effects (X), corresponding equations. . . . 121

A.1 Details of currently active codes for seismic cycles simulations and configurations considered. . . . 154

B.1 Parameter values used for BP1 SEAS. . . . 158
B.2 Time discretization parameters for the benchmark problem 6 (BP6) seismic cycle simulation. . . . 159
B.3 Space discretization parameters for the benchmark problem 6 (BP6) seismic cycle simulation. . . . 159

List of Figures

1.1 Idealized representation of inter-seismic and co-seismic phases through the analogy between the spring-slider system ((a) and (b)) and a strike-slip fault ((c) and (d)) (Modified from Rolandone (2022)). Figures (a) and (c) represent the stress accumulation phase (inter-seismic phase). Figures (b) and (d) represent the stress-release phase (co-seismic phase). 10

1.2 Response of a fault under slip-weakening friction during an earthquake (a) Slip-rate $V(t)$ (orange curve) and slip $\delta(t)$ (black curve) in terms of time t. (b) Frictional (black curve) and spring (red dashed line) response in terms of slip. The shaded area corresponds to the released elastic energy per unit area, $\bar{E}_R$. (c) The energy budget consists in the radiated energy per unit area, $\bar{E}_R$ in blue, the fracture energy per unit area, $\bar{E}_G$, in red and the frictional dissipation per unit area, $\bar{E}_H$ in green. 15

1.3 Simplified illustration of fluid effects ranging from unstable to stable slip (modified from Tzortzopoulos (2021)). 17

1.4 Planar-fault Γ embedded in a semi-infinite medium Ω. 20

1.5 Evolution of the interface unknowns: (a) the slip δ, (b) the slip-rate V, (c) the shear-stress τ and (d) the state-variable θ on with respect to time over three seismic cycles. 26

1.6 Adapted from Kanamori and Brodsky (2004): Mohr circle diagram. Given principal stress magnitudes σ_1 and σ_3, possible combinations of shear and normal stresses resolved on a plane are given by Equation (1.46) which is plotted as the circle. The failure criterion $\tau = \mu\sigma$ is the dashed line. The failure criterion in the presence of pore fluid is the solid line $\tau = \mu(\sigma - p)$. Failure on a plane at an angle θ_{opt} from the orientation of σ_1 occurs at the $*$. 36

2.1 Problems considered: planar fault embedded in a homogeneous, linear, elastic, isotropic infinite space. For each case, the fault is governed by rate-and-state friction on the fault width W_f and is loaded in mode II or III with a constant creep rate V_{pl} to the infinite depth. 45

2.2 Fault (Γ) of arbitrary shape embedded in an infinite space Ω. Fault faces Γ^+ and Γ^- have opposite normal vectors $\mathbf{n}^+ = -\mathbf{n}^-$. 46

2.3 Figure from Bonnet (1999), introduction of an exclusion neighborhood for a proper formulation of the limiting process. 49

2.4 Two methods to take into account a free surface condition in $x_3 = 0$ (a) by replication of the fault geometry with respect to the free surface, (b) by the method of images, in the case of the 2D case of a planar fault perpendicular to the free surface. 52

2.5 Evolution of the kernel $W(p)$ with its argument. 57

2.6 (a) Space discretization of a 1D planar fault with 16 1D elements. The mesh nodes are located in the center of the elements. (b) Evolution of the amplitude of the coefficients of corresponding Boundary Element matrix. Diagonal coefficient represents close interactions between geometrically close degrees of freedom while off diagonal coefficients of lower amplitude represent far interactions between geometrically far degrees of freedom. 61

2.7 Clustering of the DOFs of a 1D planar fault embedded in an infinite space and loaded in mode II or III. 64

2.8 Hierarchical decomposition of the boundary element matrix for the case of a 1D planar fault embedded in an infinite space and loaded in mode II or III. (a) Building of the binary tree from the complete set of DOFs. Two subsets of nodes X and Y at the third level of the binary tree satisfy the admissibility condition and correspond to an admissible (green) block in the matrix (b), where non-admissible blocks are displayed in red. 65

2.9 Structure of the algorithm for one prediction/correction step to estimate interface unknowns (in red) at the next time step 68

2.10 Structure of the algorithm for one step of the prediction-correction method to estimate interface unknowns (in red) at the next time step 69

2.11 Structure of the algorithm for one step of the explicit RK method to estimate interface unknowns (in red) at the next time step 69

2.12 Structure of the algorithm for one step of the hybrid method to estimate interface unknowns (in red) at the next time step 70

2.13 Structure of the algorithm for seismic cycle simulations 71

2.14 Normalized evolution of initial values of the slip $\delta(z,0)$ and the quasi-static shear-stress change $\tau^{qs}(z,0)$ with respect to space on the rate-and-state fault width $W_f = 5L_{\text{nuc}}$. 74

2.15 Spatial evolution of (a) the slip and (b) the shear-stress change at $t = 4.4$ s, during the first seismic event (simulation of a mode II configuration with a no-opening condition on the fault cf. Figure 2.1). 74

2.16 Relative L^2-norm error on (a) the quasi-static shear-stress change τ^{qs}: $\varepsilon_{\tau^{qs}}$ and on (b) its time derivative $\dot{\tau}^{qs}$: $\varepsilon_{\dot{\tau}^{qs}}$ with respect to $L_b/\Delta z$. 77

2.17 Relative L^2-norm error on (a) the quasi-static shear-stress change τ^{qs} and on (b) its time derivative $\dot{\tau}^{qs}$ with respect to the size of the discretized in terms of number of nucleation length N_{rep}. $L_b/\Delta z \approx 62$. 78

2.18 Relative L^2-norm error on the quasi-static shear-stress change τ^{qs} with respect to ε_{ACA} for different values of η; $L_b/\Delta z \approx 6$. 79

2.19 Observed and estimated (a) CPU time to compute the BEM matrix with respect to the number of DOFs N; (b) CPU time to compute the quasi-static shear-stress change τ^{qs} with respect to the number of DOFs N; (c) memory requirement N_s and (d) compression rate $\tau(\mathscr{H})$ with respect to the number of DOFs N; (e) CPU time to compute τ^{qs} with respect to $\varepsilon_{\tau^{qs}}$. 81

2.20 Evolution of the maximum in depth of (a) the slip δ, (b) the slip-rate V, (c) the shear-stress τ, and (d) the state variable θ with respect to time during one seismic event for different values of $L_b/\Delta z$. 83

2.21 Relative L^2-norm error on (a) the slip δ, (b) the slip-rate V, (c) the shear-stress τ, and (d) the state variable θ with respect to the solver tolerance $\varepsilon_{\text{solver}}$ for the explicit time-stepping method using the H-BEM. 85

2.22 Relative final L^2-norm error on (a) the slip δ, (b) the slip-rate V, (c) the shear-stress τ, and (d) the state variable θ with respect to the solver tolerance $\varepsilon_{\text{solver}}$ for different values of the tolerance for the Newton-Raphson method $\varepsilon_{\text{Newton}}$ for the hybrid time-stepping method using the H-BEM. 86

2.23 Error in time at which $V > 1$ m/s for 1st and 2nd seismic event when solved with prediction-correction method. 90

2.24 Relative L^2-norm error on each interface unknown, for the 1st seismic event, when solved with prediction-correction method. 91

2.25 Relative L^2-norm error on each interface unknown, for the 2nd seismic event, when solved with prediction-correction method. 92

2.26 Error in time at which $V > 1$ m/s for 1st and 2nd seismic event when solved with explicit method. 92

2.27 Relative L^2-norm error on each interface unknown, for the 2nd seismic event, when solved with explicit method. 93

2.28 Error in time at which $V > 1$ m/s for 1st and 2nd seismic event when solved with hybrid method. 93

2.29 Relative L^2-norm error on each interface unknown, for the 2nd seismic event, when solved with hybrid method. 94

2.30 Rate-and-state parameters with respect to depth. 95

2.31 Time evolution of (a) slip δ, (b) slip rate V, (c) shear stress τ, (d) state variable θ, at $z = 12.5$ km, close to nucleation region. 96

2.32 (a) Error on the starting time of each seismic instability, (b) Duration of each interseismic period. 97

3.1 Strike-slip fault configurations in (a) mode III or (b) mode II with a no-opening condition on the fault. Fluid is injected through an impermeable borehole at a given distance D from the fault Γ embedded in a poroelastic half-space Ω. . . . 102

3.2 Geometry and boundary conditions of the poroelastic column. 122

3.3 Validation test of the CQM with $G = \cos(t)\mathscr{H}(t)$, $f(t) = \mathscr{H}(t)$ and $q(t) = \sin(t)$ for different time steps Δt, (a) (left) Superposition of the approximated convolution product $q_{\text{app}}(t)$ of $q(t)$ (with $t = n\Delta t$) obtained with different time steps and compared to the analytical solution $q(t)$, (right) Time evolution of the absolute error $\mathrm{E}_q(t)$ (b) Evolution of the relative L^2-norm error in time on $q(t)$: ε_q^t with respect to Δt. 128
3.4 Comparison of the "Simplified" with the "Full" models with respect to the z-coordinate for undrained boundary conditions applied to both models. . . . 130
3.5 Comparison of the "Simplified" with the "Full" models with respect to time for "undrained" boundary conditions applied to both models. 131
3.6 Comparison of the "Simplified" with the "Full" models with respect to the z-coordinate for a constant perturbation ($\Delta P/P_0^* = 10^{-1}$) on the pressure at the top of the column for the "Full" model. 134
3.7 Evolution of the L^2-norm relative errors in space and time on the solid displacement $\varepsilon_u^{z,t}$ and on the pore pressure $\varepsilon_p^{z,t}$ with respect to the amplitude of the loading perturbation $\Delta P/P_0^*$. 135
3.8 Comparison of the "Simplified" with the "Full" models with respect to the z-coordinate for a sinusoidal perturbation ($\Delta P/P_0^* = 10^{-1}\cos(10^3 t)$) on the pressure at the top of the column. 137
3.9 Comparison of the "Simplified" with the "Full" models with respect to the z-coordinate for a sinusoidal perturbation ($\Delta P/P_0^* = 10^{-1}\cos(t)$) on the pressure at the top of the column. 138
3.10 Comparison of the "Simplified" with the "Full" models with respect to the z-coordinate for a sinusoidal perturbation ($\Delta P/P_0^* = 10^{-1}\cos(10^{-2} t)$) on the pressure at the top of the column. 139
3.11 Evolution of the L^2-norm relative errors in space and time on the solid displacement $\varepsilon_u^{z,t}$ and on the pore pressure $\varepsilon_p^{z,t}$ with respect to the pulsation of the loading perturbation. 140

B.1 2D illustration of benchmark problem 6 (BP6 SEAS) from https://strike.scec.org/cvws/seas/download/SEAS_BP6_Nov18.pdf. 157
B.2 Time evolution of the slip rate at $z = 0$ km, close to the fluid injection point and to the nucleation region of the slow slip event (SSE). 160

Introduction

1 Motivations

On March 11th, 2011, a moment magnitude (M_w) 9.1 undersea megathrust earthquake occurred in the Pacific Ocean, 72 km east of the Oshika Peninsula of the Tōhoku region. The Japan Trench has moved by up to 60 m as a result of the quake, the Earth was shifted on its axis so that the day was shortened by 1.8 microseconds, and the earthquake triggered a tsunami which caused the Fukushima Daiichi nuclear disaster. On February 6th, 2023, a moment magnitude (M_w) 7.8 earthquake struck southern and central Turkey and northern and western Syria. It ruptured approximately 370 km of the East Anatolian Fault producing a maximum slip of 9 m within the Earth's crust. What is interesting is that, the seismic waves detected worldwide, and responsible for severe human and infrastructure damage, represent only a small part of the energy released during a seismic event. In fact, most of the energy is dissipated through friction (Kanamori & Brodsky, 2004; Kanamori & Rivera, 2006). Therefore, the mechanisms behind friction are still investigated to understand the nucleation, evolution and arrest of seismic events. A particular attention is paid to the apparent cyclic friction behavior of faults (Bakun & Lindh, 1985).

Earthquakes are usually known as natural disasters, but they can also be induced by anthropogenic sources. On September 12th, 2016, and on November 15th, 2017, two moment magnitude (M_w) 5.5 earthquakes struck South Korea (Gyeongju and Pohang earthquake respectively) to a major right-lateral fault, the Yangsan fault, and close to an Enhanced Geothermal Systems (EGSs) site. At this EGS site between early 2016 and September 2017, many thousands of cubic meters of water were injected under pressure into wells reaching approximately 4 km of depth, which suggests that the EGS activity induced both earthquakes. On November 12th, 2019, the geothermal energy company Georhin, is likely to have induced a magnitude 3.1 earthquake north of Strasbourg. Environment friendly industrial activities such as deep geothermal energy projects and CO2 sequestration require the injection of large amounts of fluids in the Earth's crust. Current experiences show that earthquakes of moderate to large magnitudes can be induced/triggered, which endangers the viability of such environmentally promising projects.

We are still unable to predict both natural and induced earthquakes. However, based on the established concept that fault slip can be stimulated by fluid injection in the Earth's crust, a new and timely question in the community is to show that the earthquake instability could be mitigated by active control of fluid pressure. Such a study is being conducted in the context of the European Research Council CoQuake's project (Controlling earthQuakes,

www.coquake.eu). It proposes to avoid earthquake instabilities by inducing them at a lower energetic level, hence reducing the seismic risk and its human and economic cost. These points and the fact that both natural and induced earthquakes' nucleation relies on similar physics, justify the development of efficient large-scale numerical tools to simulate the earthquake instability.

In this work, we focus on the development of efficient and accurate simulations of fluid effects in dynamic fault rupture, when the fluid is injected at a given distance from the fault. This objective can be decomposed into two main tasks:

- An in-depth comparative study of existing numerical tools for seismic cycles to determine the most promising approach for an accurate description of the dynamic fault rupture;
- Proposition of simplified models tailored to the study of fluid injection effects in dynamic fault rupture.

The developed numerical tools set the basis to help the community developing more and more realistic simulations (incorporating 3D realistic fault geometries and multi-physics couplings), in order to understand and mitigate earthquakes instabilities.

2 Scientific approach

This work aims at modeling fluid injection effects in dynamic fault rupture, i.e. seismic fault slip. To this end, the first step consists in modeling the seismic instability. A dynamic fault rupture is one of the three main steps of a seismic cycle, which takes into account the slow accumulation of the shear stress at a fault zone until the nucleation of a seismic slip, and its arrest followed by the accommodation of the Earth's crust to a new equilibrium state. Therefore, we first propose to model and simulate a seismic cycle problem to accurately describe the seismic motion from its initiation to its arrest.

An important part of this thesis is devoted to the development of effective, state-of-the-art, numerical tools in order to simulate seismic cycles, before incorporating fluid injection effects on fault slip. We use the Boundary Element Method (BEM), known to be efficient for solving elastodynamic problems in large-scale unbounded domains (Chaillat et al., 2017; Kpadonou et al., 2020), and seismic cycles problems (Ando (2016), Luo et al. (2017), Barbot (2021), and Ozawa et al. (2022) among others). For this class of problems, the BEM presents many advantages compared to the volume methods such as Finite Difference (FD) or Finite Element Method (FEM): reduction of one dimension of the computational domain, very good accuracy and no artificially truncation of the calculation domain thanks to an exact formulation of the radiation condition at infinity. Moreover, the recent development of Fast BEMs, such as Fast Multipole Accelerated BEMs or Hierarchical matrices-based BEMs, lead to competitive simulations with very low computational cost. The method is now mature enough to handle complex geometries and realistic configurations Chaillat et al. (2012), but for single physics. A progressive approach is adopted in this work, considering simplified problems before a more complex large-scale case could be considered with the developed numerical tools. Due to the fact that natural earthquakes and fluid injection induced earthquakes follow similar

physics as far as it concerns their nucleation, a starting point is to first focus on a “dry” case without fluid injection.

This dissertation focus on the verification and comparison of different time integration methods incorporating Fast BEMs, which are commonly used in the seismic cycle community, and to their sensitivity with respect to their parameters. Code verification exercises are still largely discussed as detailed by Erickson et al. (2020a, 2023). For this purpose, the simulation of an aseismic motion is distinguished from a seismic cycle simulation. An analytical solution is proposed to verify the simulation of an aseismic slip, and a procedure to compare seismic cycle results to reference results is detailed.

Another challenging part is to extend the capabilities of the developed numerical tools to incorporate fluid injection effects in fault slip. The present work is mainly focused on fluid injection effects at the specific timescale of a seismic motion, which has not been considered in the literature. We also assume that the fluid is injected in the Earth’s crust at a given distance from the fault. The poroelastodynamic framework is chosen to incorporate hydromechanical couplings. However, a complete poroelastodynamic model would require non-negligible computational costs or approximations. Thus, a reduction of the complete model is required to provide an effective model than would be easier to integrate in the proposed numerical framework, and would accurately take into account the predominant fluid effects at the timescale of a seismic or aseismic motion. A dimensional analysis enables rigorous simplifications of the complete model. A numerical illustration of the results obtained is crucial before running a multi-physic test using Fast BEMs to solve a dynamic fault rupture problem with fluid injection at the timescale of a seismic slip.

3 Overview of the thesis

This dissertation is organized in three chapters.

- Chapter 1 defines the concepts of earthquake instability and seismic cycle used in this work, and provides the motivations for studying fluid effects on frictional fault slip. Special attention is given to the modeling and the simulation of seismic cycle problems without fluid-injection. These are key steps to develop efficient and accurate numerical tools to study, in a second step, fluid-injection effects on dynamic fault rupture. This chapter details the ingredients required to model a generic seismic cycle problem and incorporate fluid effects on fault slip. It gives a broad literature review on the existing numerical methods to solve seismic cycles problems and highlights the challenging verification of such simulations.

- Chapter 2 concentrates on the comparison of seismic cycle simulations for simplified mode II and mode III two-dimensional quasi-dynamic problems for planar faults. This chapter presents the space and time integration methods developed to obtain our numerical results. The numerical tools developed contain three explicit (respectively explicit-implicit) time integration methods and use Fast Boundary Element Methods accelerated using Fast Fourier Transform or Hierarchical matrices. It offers, in a single code, an extensive comparison study between existing methods to solve seismic

cycles problems, as well as a sensitivity study on the parameters of each method. It allows to determine the most appropriate numerical methods to incorporate fluid-injection effects at the timescale of a seismic motion, and to then consider realistic configurations.

- Chapter 3 is dedicated to the modeling of fluid effects on fault slip at the timescale of an earthquake instability in the case where the fluid is injected in the Earth's crust at a given distance of the fault. After highlighting the difficulties inherent to the use of complete poroelastodynamic equations to incorporate hydromechanical couplings, a dimensional analysis of the complete poroelastodynamic equations is conducted to assess formally the predominant fluid effects at the timescale of a seismic or aseismic motion. These developments enable to assess the model we want to use and to discuss the commonly used models in the literature. A numerical illustration of the results of the dimensional analysis using a simplified one-dimensional poroelastodynamic problem is proposed to assess the validity range of the simplified model obtained at the timescale of a seismic slip.

Conclusions and perspectives of this work are finally proposed.

1

Fast methods to simulate sequences of earthquakes and aseismic slips

Contents

1 Instability and its mitigation 8

1.1 Observation of seismic cycles: the genesis 8

1.2 Definition of a seismic cycle: a kinematic approach 9

1.3 Linear stability analysis (LSA) with rate-and-state friction 11

1.4 Fluid-injection effects on the condition for steady state slip of the spring-slider analog 16

1.5 Limitations of the reduced order model 17

2 Generic spatio-temporal fault behavior 18

2.1 Fault geometry 18

2.2 Momentum balance and constitutive equations 20

2.3 Interface conditions 22

2.4 Boundary conditions 26

2.5 Initial conditions 27

3 Simulating seismic cycles 27

3.1 Existing methods for spatio-temporal discretization of the problem . . 28

3.2 Validation vs. verification of the simulations 34

4 Mitigating the seismic risk using fluid injection? 34

4.1 Evidence of fault slip due to fluid injection 34

4.2 Earthquake mitigation strategies using fluid injection 35

4.3 Incorporating hydro-mechanical couplings 37

1 Instability and its mitigation

1.1 Observation of seismic cycles: the genesis

When will the Big One hit? California is preparing for two major earthquakes in the next few years. The West Coast of United States lies on the San Andreas Fault, a fracture zone over 1,000 km long that extend all over to Mexico. This geological boundary between the Pacific Ocean and North American continental plates is conducive to large-scale seismic phenomena. But how did the question of studying faults to understand the possibility of a seismic event to occur ?

Human and material damage caused by natural earthquakes urged the scientists to develop in situ observations of such phenomenons (e.g. geodetic techniques[1], Rolandone (2022)). In particular, geodetic observations of the Parkfield segment of the San Andreas Fault first confirmed a faulting origin of earthquakes (as reviewed by Romanet (2017)). A cyclic pattern emerged from these observations that the fault had ruptured during six earthquakes of magnitude 6 or greater, between 1850 and 1966, with a recurrence time of about 20 year (Bakun & Lindh, 1985). This study lead to conduct an experiment to predict future earthquake on the basis of the periodicity highlighted. Nevertheless, it could not validate the predictions as it had underestimated the complexity of the different deformation phases at stake. So far, we are still not able to predict seismic events but studying seismic cycles can help to estimate areas at risk and to get a better understanding of such devastating phenomenons. However, it appeared from geodetic observations, that the slip dynamics of faults is more complex than simply periodic (discovery of slow slip events for instance, reviewed by Romanet (2017)). The monitoring facilities developed to study earthquakes of natural cause, also exhibit earthquakes due to anthropogenic sources (called induced earthquakes), that represent a non-negligible number of earthquake phenomena.

Nowadays, in situ observation of both natural and anthropogenic earthquakes benefit from many new monitoring survey and networks worldwide: the United States Geological Survey (USGS) https://www.usgs.gov/programs/earthquake-hazards thanks to the Advance National Seismic Survey, in France, the national research infrastructure Epos-France (part of the European Plate Observing System). HiQuake (The Human-Induced Earthquake Database) provides the most complete database of anthropogenic projects to have induced earthquake sequences. A world map of the induced events and their corresponding subsurface engineering technology are available on https://inducedearthquakes.org/.

So far, the understanding of earthquakes still relies on the collaboration between experimentalist of rocks (laboratory experiments), geologists and physicists (geological observations), applied mathematicians and solid and fluid mechanicians (numerical experiments and theoretical models). This active transdisciplinary connections are emphasized by Rolandone (2022), Bizzarri and Bhat (2012), and Ferrand et al. (2023) among others. In this work, we focus on theoretical and numerical aspects of fault mechanics. As a first step, we propose a kinematic model to explain the different phases of the earthquake processes called “the seismic cycle”.

[1] Review of techniques to image earthquake and post-seismic phases by Zacharie Duputel and Frédérique Rolandone in chapters 2 and 3 of Rolandone (2022)

1.2 Definition of a seismic cycle: a kinematic approach

Seismic cycles are characteristic patterns that were revealed by geodetic observations. In this part, we first propose a definition of this concept. Used since 1960 (Fedotov, 1968), the expression "seismic cycles" refers to the recurring alternance between an inter-seismic phase and a co-seismic phase at the vicinity of a fault. By "fault", we mean the region of the rock that is under pronounced localized shear deformation due to the far field tectonic movement. Originally, the definition of a seismic cycle is based on Reid's "elastic rebound theory" (Reid, 1910) whose principles are recalled by Segall (2010):

1. The fracture of the rock, which causes a tectonic earthquake, is the result of elastic strains, greater than the strength of the rock can withstand, produced by the relative displacements of neighboring portions of the earth's crust.

2. These relative displacements are not produced suddenly at the time of the fracture, but attain their maximum amounts gradually during a more or less long period of time.

3. The only mass movements that occur at the time of the earthquake are the sudden elastic rebounds of the sides of the fracture towards position of no elastic strain; and these movements extend to distances of only a few miles from the fracture.

4. The earthquake vibrations originate in the surface of fracture; the surface from which they start has at first a very small area, which may quickly become very large, but at a rate not greater than the velocity of compressional elastic waves in the rock.

5. The energy released at the time of an earthquake was, immediately before the rupture, in the form of energy of elastic strain of the rock. (Reid 1911, p. 436)

A better understanding of the seismic cycle was allowed by the emergence of the plates tectonic theory and advances made in the field of imaging the Earth's interior[2] (Coltice et al., 2017; Rolandone, 2022). The plates tectonic theory emphasized the relatively continuous displacement of the lithospheric plates with respect to one another in the convective system in the interior of the earth as the main loading of the rock system. A review of the concept of seismic cycle is given by Rolandone (2022).

In the present work, we consider the following definition of a seismic cycle as a chain of causal physical phenomena, the only visible part of which is the earthquake. The seismic cycle comprises three phases. These are:

- An inter-seismic phase, which corresponds to the slow accumulation of shear deformation at a fault zone until it exceeds the ability of the frictional forces to prevent slip. This period can last from tens to hundreds of years.

- A co-seismic phase, which consists in the sudden release of the accumulated stress resulting from a rapid displacement at the fault interface. This leads to an earthquake, characterized by seismic wave propagation, a variation in the temperature of the rock, plastic damage in the vicinity of the fault zone etc. This phase can last a few seconds.

[2] Review of links between mantle convection and tectonics to date by Coltice et al. (2017), see chapters 2 and 3 from Rolandone (2022) for a review on imaging techniques for both co-seismic and post-seismic phases

- A post-seismic phase that lasts from minutes to years after an earthquake. It consists in additional movement of the Earth crust as it accommodates a new equilibrium state. This remaining flow can lead to aftershocks at the fault interface or eventually decays back to the steady inter-seismic motion.

To understand the mechanisms behind seismic cycles, let's consider a simplified kinematic model. Figure 1.1 ((a) and (b)) represents a simplified kinematic model, idealizing the seismic cycle as the stick-slip behavior of a reduced order spring-slider model. This model mimics the behavior of a strike-slip fault represented on Figure 1.1 ((c) and (d)). By strike slip fault, we mean a fault on which two Earth crust blocks slide past one another, resulting in a horizontal motion. The strike refers to the fault azimuth, conventionally described with respect to north. The spring-slider comprises a block that represents the mobilized rock mass during an earthquake. The block weight allows for compression at the interface, which stands for the far field loading that is normal to the fault in the strike slip case. The spring, of initial length l_0, represents the elastic behavior of the lithosphere surrounding the fault rock. The tension applied to the spring mimics the relative motion of the lithospheric plates. The fault is modelled as a planar interface between the rigid block and a rigid surface in the case of the spring-slider, while it lies between two elastic blocks in the case of the strike-slip fault.

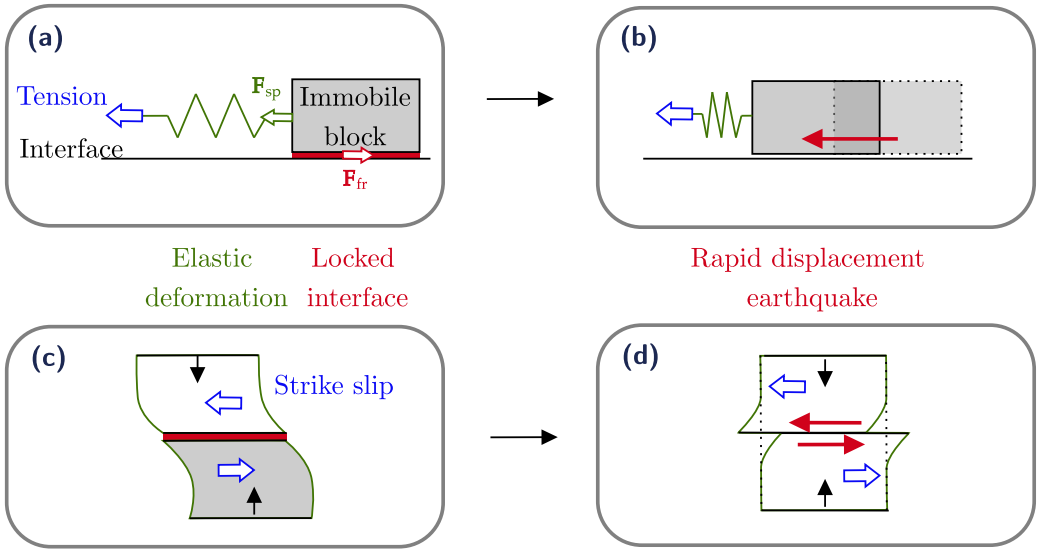

Figure 1.1 • Idealized representation of inter-seismic and co-seismic phases through the analogy between the spring-slider system ((a) and (b)) and a strike-slip fault ((c) and (d)) (Modified from Rolandone (2022)). Figures (a) and (c) represent the stress accumulation phase (inter-seismic phase). Figures (b) and (d) represent the stress-release phase (co-seismic phase).

Figure 1.1 (a) is analogous to the inter-seismic phase. It represents the elongation of the spring in response to the tension imposed. Elastic deformation accumulates and a frictional force $\mathbf{F}_{fr}$, applies at the locked interface (in red) and opposes to the spring force $\mathbf{F}_{sp}$ and to the movement of the block.

Figure 1.1 (c) extends the configuration described for Figure 1.1 (a) to a strike-slip fault.

In Figure 1.1 (b), a sudden displacement of the block occurs, combined with the compression of the spring and the release of the accumulated elastic energy. This corresponds to the co-seismic phase as represented for the strike slip fault on Figure 1.1 (d). A brutal slip occurs at the fault interface combined with the brittle behavior of the part of the lithospheric blocks surrounding the fault and the release of the elastic energy previously accumulated.

1.3 Linear stability analysis (LSA) with rate-and-state friction

To understand the transition from inter-seismic to co-seismic phase, we need to study the stability of the equilibrium state of the system. We use the reduced order spring-slider model in this part, which allows us to re-derive stability results from Lapusta et al. (2000). The conditions under which the equilibrium state of the spring-slider system is unstable and triggers a seismic event can be easily understood by (re-)deriving the linear stability analysis of equilibrium state of the quasi-static velocity-driven spring-slider system, as discussed by Lapusta et al. (2000), Ruina (1983). We consider that the spring-slider moves steadily at rate V^*, which mimics the relative motion of lithospheric plates. Under the quasi-static assumption, the instability criterion depends only on the frictional properties at the interface. In the quasi-static configuration, the balance momentum equation writes as the equilibrium between the friction force and the spring force applied to the mobilized block. Its projection on the horizontal axis, writes

$$0 = -\tau A - \overline{k} A \delta \tag{1.1}$$

where τ is the shear stress, A is the active frictional surface, $\overline{k}$ is the spring stiffness per unit area, and δ is the slip of the mobilized block. (1.1) is completed by an interface condition to have a well-posed problem. Here, the rate-and-state friction law given in equation (1.2) (detailed in Section 2.3) is considered at the interface between the block and the rigid surface. At this stage, we only need to know that the interface frictional behavior described with rate-and-state friction law implies that the shear stress is a function, denoted Ψ, of the slip-rate $V = \mathrm{d}\delta/\mathrm{d}t$ and of an internal state variable θ. The time derivative of θ is also given as a function, denoted φ of V and θ. In the following, we denote by $\dot{\cdot}$ the time derivative $\mathrm{d}\cdot/\mathrm{d}t$.

$$\tau = \Psi(V,\theta), \quad \dot{\theta} = \varphi(V,\theta). \tag{1.2}$$

Injecting the constitutive rate-and-state friction law (1.2) into the balance momentum equation (1.1) and replacing $V(t) = \dot{\delta}(t)$, we obtain the non-linear differential equations on $(\delta(t),\theta(t))$

$$0 = -\Psi(\dot{\delta},\theta) A - \overline{k} A \delta, \quad \dot{\theta} = \varphi(\dot{\delta},\theta). \tag{1.3}$$

The equilibrium state $(\delta^*, V^*, \theta^*)$ is given by

$$\delta^* = -\Psi(V^*,\theta^*)/\overline{k}, \quad \varphi(V^*,\theta^*) = 0 \tag{1.4}$$

where the steady state slip rate V^* corresponds to the imposed loading.

We apply the 1$^{\text{st}}$ Lyapunov method to study the stability of the equilibrium point. The objective is to determine the conditions under which the parameters of the system allow a

perturbation of the equilibrium state to decay or to grow away. To this aim, we linearize the system in the vicinity of the equilibrium state by calculating the Jacobian of the system (1.3).

$$\begin{aligned} 0 &\approx -\left(\Psi(V^*,\theta^*) + \left(\frac{\partial\Psi}{\partial V}\right)_{V=V^*,\theta=\theta^*}\dot{\tilde{\delta}} + \left(\frac{\partial\Psi}{\partial\theta}\right)_{V=V^*,\theta=\theta^*}\tilde{\theta}\right) A - \overline{k}A(\delta^* + \tilde{\delta}), \\ \dot{\tilde{\theta}} &\approx \quad \varphi(V^*,\theta^*) + \left(\frac{\partial\varphi}{\partial V}\right)_{V=V^*,\theta=\theta^*}\dot{\tilde{\delta}} + \left(\frac{\partial\varphi}{\partial\theta}\right)_{V=V^*,\theta=\theta^*}\tilde{\theta} \end{aligned} \tag{1.5}$$

where $(\tilde{\delta},\dot{\tilde{\delta}},\tilde{\theta})$ denotes the perturbation of the equilibrium state described by (δ^*,V^*,θ^*) in (1.4).

To keep more compact notations, we denote:

$$\left(V\frac{\partial\Psi}{\partial V}\right)_{V=V^*,\theta=\theta^*} = A^*, \quad \left(\frac{\partial\Psi}{\partial\theta}\right)_{V=V^*,\theta=\theta^*} = C^*, \quad \left(\frac{\partial\varphi}{\partial V}\right)_{V=V^*,\theta=\theta^*} = -\frac{B^*}{LC^*}, \quad \text{with } L = \left(V/\frac{\partial\varphi}{\partial\theta}\right)_{V=V^*,\theta=\theta^*}$$

Injecting (1.4) in (1.5) and rearranging the equations as an Ordinary Differential Equation system on the perturbation $(\tilde{\delta},\tilde{\theta})$, we obtain

$$\frac{\dot{\tilde{\delta}}}{V^*} = -\frac{\overline{k}}{A^*}\tilde{\delta} - \frac{C^*}{A^*}\tilde{\theta}, \quad \frac{C^*L\dot{\tilde{\theta}}}{B^*V^*} = \frac{\overline{k}}{A^*}\tilde{\delta} - \frac{(B^*-A^*)}{A^*}\frac{C^*}{B^*}\tilde{\theta} \tag{1.6}$$

Linear Stability Analysis is carried out on the dimensionless form of (1.6), namely

$$\frac{\mathrm{d}D}{\mathrm{d}T} = -\frac{\overline{k}L}{A^*}D - \frac{B^*}{A^*}\Theta, \quad \frac{\mathrm{d}\Theta}{\mathrm{d}T} = \frac{\overline{k}L}{A^*}D + \frac{B^*-A^*}{A^*}\Theta \tag{1.7}$$

where:

$$\tilde{\delta} = DL, \quad t = TL/V^*, \quad \tilde{\theta} = \Theta B^*/C^* \tag{1.8}$$

Hence, the Jacobian of the linear system (1.7) is

$$[J] = \begin{bmatrix} -\overline{k}L/A^* & -B^*/A^* \\ \overline{k}L/A^* & (B^*-A^*)/A^* \end{bmatrix}. \tag{1.9}$$

As the obtained system is autonomous (non-explicit dependence in time i.e. $\underline{\dot{X}} = \underline{f}(\underline{X})$ with $\partial\underline{f}/\partial t = \underline{0}$), we use the definition of stability in the sense of Lyapunov. If the real part of all the Jacobian eigenvalues is negative, a perturbation of the equilibrium state decays exponentially, whereas if at least, one eigenvalue has a positive real part, the perturbation grows exponentially. If the largest real part is 0, we obtain a long-time periodic motion.

The characteristic equation of the Jacobian $\det([J]-\lambda[\mathrm{I}]) = 0$ writes

$$\lambda^2 - \mathrm{tr}([J])\,\lambda + \det([J]) = 0. \tag{1.10}$$

In our case, the product of all eigenvalues is strictly positive $\det([J]) > 0$. So both eigenvalues have the same sign. We denote $\Delta = \mathrm{tr}([J])^2 - 4\det([J])$, the discriminant of (1.10). Thus, if the sum of all eigenvalues is negative $\mathrm{tr}([J]) < 0$, both eigenvalues have a negative real part and the perturbation decays exponentially, whereas if $\mathrm{tr}([J]) > 0$ both eigenvalues have a positive real part and the perturbation grows exponentially. This comes from the fact that the square

root of the absolute value of the discriminant is lower than the absolute value of the sum of all eigenvalues $\sqrt{|\Delta|} < |\mathrm{tr}([J])|$. When $(B^* - A^*) < 0$, $\mathrm{tr}([J]) < 0$, whereas when $(B^* - A^*) > 0$, the sign of $\mathrm{tr}([J])$ depends on the sign of $\overline{k} - (B^* - A^*)/L$, which defines a critical stiffness per unit area $\overline{k}_{\mathrm{cr}}$

$$\overline{k}_{\mathrm{cr}} = \frac{B^* - A^*}{L} \tag{1.11}$$

where L is generally interpreted as the characteristic slip length as the frictional resistance drops (transition from static to dynamic friction) when slip occurs.
As a consequence, we can distinguish 3 cases:

- If $\overline{k} > \overline{k}_{\mathrm{cr}}$, $(\delta^*, V^*, \tau^*, \theta^*)$ denotes an asymptotically stable equilibrium and the small perturbations decays back to the initial equilibrium;
- If $\overline{k} < \overline{k}_{\mathrm{cr}}$, $(\delta^*, V^*, \tau^*, \theta^*)$ denotes an unstable equilibrium and unstable slip occurs;
- If $\overline{k} = \overline{k}_{\mathrm{cr}}$, the perturbed equilibrium remains bounded around the equilibrium (stable in the sense of Lyapunov).

To interpret this result in the case of the strike slip fault, we can express the apparent stiffness per unit area of the fault as (Dieterich, 1979):

$$\overline{k} \approx \frac{G}{L_{\mathrm{ac}}} \tag{1.12}$$

where G is the shear modulus of the elastic lithosphere blocks surrounding the fault and L_{ac} is basically the length of the fault that slips over the fault plane. Thus, the instability condition can rewrite

$$L_{\mathrm{ac}} > L_{\mathrm{cr}} \approx \left| \frac{LG}{B^* - A^*} \right|, \tag{1.13}$$

meaning that the length of the zone that slips must be greater than a critical size L_{cr} in order to lead to unstable slip and earthquake nucleation. In practice L_{cr} is called the nucleation length and denoted L_{nuc}.

In the previous calculations, inertial effects and the viscosity of the surrounding rock have been neglected. These effects are key to model a complete seismic cycle. In effect, the quasi-static approximation only allows to model the inter-seismic phase and the initiation of the instability (co-seismic phase) but not the post-seismic phase as it leads to unbounded slip velocities during the frictional instability (Barras et al., 2019). Thus, to simulate a complete seismic cycle in Figure 1.2, we take into account both inertial effects and the viscosity. We consider a mass-spring-damper model (Kelvin-Voigt rheology is assumed). The force balance equation we solve in this case writes

$$m\ddot{\delta} = -\tau A + \overline{k} A(\delta_\infty(t) - \delta) + \eta(V_\infty - \dot{\delta}) \tag{1.14}$$

where m is the mass of the mobilized slider, $\delta_\infty(t) = V_\infty t$ corresponds to the far-field displacement resulting from the far field velocity V_∞ imposed to the system, and η is the damping coefficient in the Kelvin-Voigt rheological model, taking into account the viscous effect of the rock surrounding the fault zone. V_∞ is previously introduced as the steady state slip-rate

V^*. The far-field displacement had been neglected in the quasi-static case. As explained by Stefanou (2019), this is a strong assumption leading to incorrect results regarding stability. The difficulty is that the far field displacement depends explicitly on time and leads to a non-autonomous system when combining the friction law with the equation of motion. Deriving Lyapunov stability condition for a non-autonomous system is not an easy task as a uniformly stable system has to be distinguished from a simply stable system (Hale, 1977; LaSalle, 1960). To overcome this difficulty Stefanou (2019) proposes a double-scale approach. It consists in noticing that the far-field velocity is much slower than the seismic slip-rate, leading to introduce slow and fast time scales in the equations (respectively associated with far-field movement, δ written as εt with $\varepsilon \ll 1$, and with t). From that assumption, each interface variable depends on two time scales, and it allows to expand each term of the equation in power series of ε. Considering the equation obtained at zeroth order of ε, thanks to this perturbation approach, the force balance equation (1.14) would write in the form of a first order

$$\begin{aligned} \dot{V} &= -\tau A/m + \overline{k}A(\delta_\infty - \delta)/m + \eta(V_\infty - \dot{\delta})/m \\ \dot{\delta} &= V \end{aligned} \tag{1.15}$$

where δ_∞ acts as a constant parameter.

> **Remark 1.1.** *Taking into account the far field displacement resulting from the far field velocity imposed to the system in the quasi-static case and applying the double scale approach would give the equilibrium equation at zeroth order of ε*
>
> $$0 = -\tau A - \overline{k}A(\delta_\infty - \delta) \tag{1.16}$$
>
> *As a consequence, it influences on the interface variable values at steady state, but the instability condition derived in equations* (1.11) *and* (1.3) *remains the same.*

Results of the linear stability analysis incorporating inertia and viscosity effects are (re-) derived by Tzortzopoulos (2021). Again, Lyapunov stability analysis is carried out as detailed by Rice and Ruina (1983). It consists in showing that the equilibrium is stable as the spring stiffness goes to infinity and unstable when $k = 0$. Thus, as the stiffness k reduces from ∞ to 0, one passes through a critical value k_{cr}. At this critical stiffness value, the roots of the characteristic polynomial of the Jacobian of the system are in the form $\pm i\beta$. Thus, at this point, the interface unknowns are oscillating (Hopf bifurcation). The expression of k_{cr} is deduced in this case,

$$k_{\text{cr}} = \frac{(B^* - A^*)A - \eta V_\infty}{L}\left(1 + \frac{mV_\infty}{(A^*A + \eta V_\infty)L}\right) \tag{1.17}$$

We can notice that the latter tends to the expression obtained in Equation (1.11) when both inertial force and viscosity are neglected ($m = 0$ and $\eta = 0$).

Solving (1.15), we can simulate an isolated seismic event using the mass-spring-damper system with rate-and-state friction law in order to simulate a complete seismic cycle. Results are shown in Figure 1.2 (inspired from Tzortzopoulos (2021)) in terms of response of the mass-spring-damper system in case $\overline{k} \leqslant \overline{k}_{\text{cr}}$. Figure 1.2 (a) shows the superposition of the slip-rate

$V(t)$ and the slip $\delta(t)$ at the interface during a seismic cycle. Figure 1.2 (b) and (c) allow to assess the response of the fault in terms of dissipated energy. These figures highlight that the energy radiated to the environment through seismic waves represent only a small portion of the energy budget, yet sufficient to cause significant human and material damage. Figure 1.2 (b) represents the frictional response associated with a shear stress drop with respect to the accumulated slip. At point A, the fault is reactivated and the instability nucleates. The system follows the black curve until it reaches a new equilibrium point (point B) of lower energy. The accumulated slip from point A to point B corresponds to the characteristic slip length L which appears in the expression of the critical spring stiffness (1.11). During the instability, the spring is unloaded with a rate $-\overline{k}$ with respect to slip as represented by the red dashed line. The shaded area between the two curves corresponds to the released elastic energy per unit area, $\overline{E}_R$. Figure 1.2 (c) shows two other energy forms that complete the energy budget during a seismic event (Kanamori & Brodsky, 2004). The red shaded area corresponds to the fracture energy per unit area, $\overline{E}_G$, while the green shaded area corresponds to the frictional dissipation per unit area, $\overline{E}_H$. Parameters are taken from tables 1.1 (a) and (c) from Tzortzopoulos (2021). In the context of the stability analysis of a rate-and-state finite fault Viesca (2016b, 2016a)

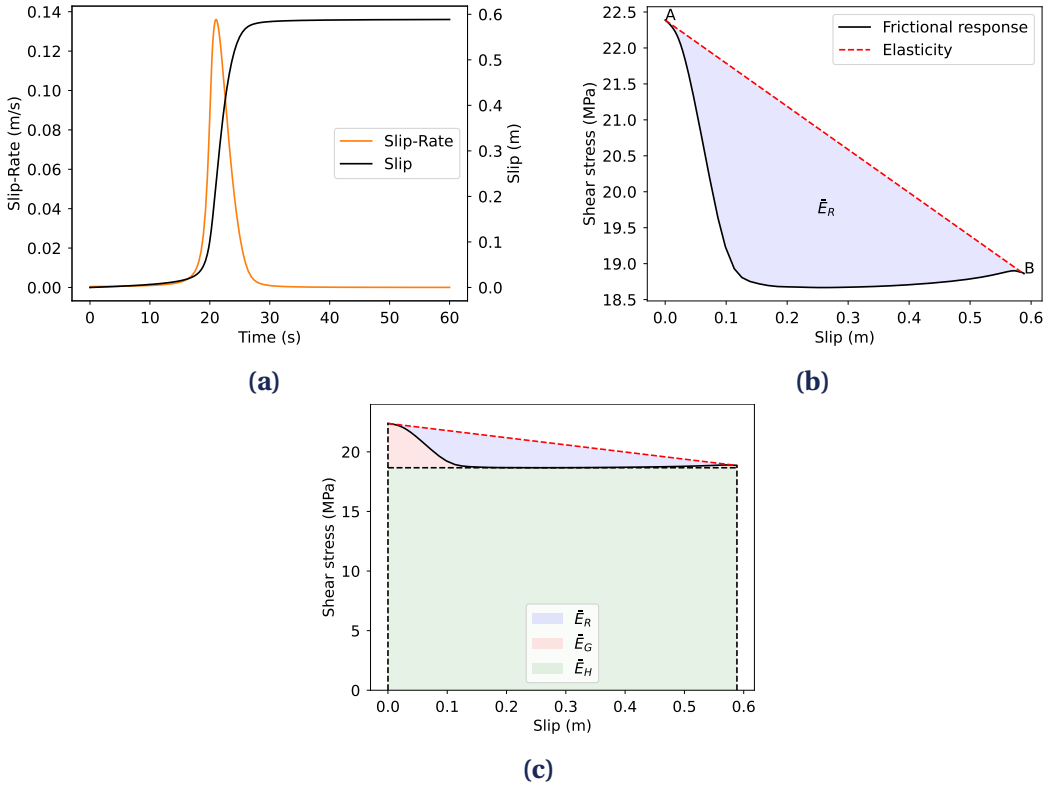

Figure 1.2 • Response of a fault under slip-weakening friction during an earthquake (a) Slip-rate $V(t)$ (orange curve) and slip $\delta(t)$ (black curve) in terms of time t. (b) Frictional (black curve) and spring (red dashed line) response in terms of slip. The shaded area corresponds to the released elastic energy per unit area, $\bar{E}_R$. (c) The energy budget consists in the radiated energy per unit area, $\bar{E}_R$ in blue, the fracture energy per unit area, $\bar{E}_G$, in red and the frictional dissipation per unit area, $\bar{E}_H$ in green.

extended the previous results using non-linear developments. Here, we concentrated on a comprehensive approach of the transition from aseismic to seismic slip.

1.4 Fluid-injection effects on the condition for steady state slip of the spring-slider analog

At this stage, we know how to model a seismic cycle. However, in the present work, we are interested in assessing fluid-injection effects on the response of a single fault submitted to steady far field loading at the timescale of the seismic instability. We come back to our reduced order spring-slider model. A simplified model of fluid injection effects at the fault interface consists in considering a weak coupling effect and fluid-injection at constant pressure with respect to time. Such a fluid model only modifies the effective normal stress applied on the fault. Assuming Coulomb friction, we can write the critical stiffness from Equation (1.17) as follows

$$k_{\mathrm{cr}}^{\mathrm{inj}} = \frac{(b-a)\sigma_n' A - \eta V_\infty}{L}\left(1 + \frac{mV_\infty}{(A^* A + \eta V_\infty)L}\right) \tag{1.18}$$

where a and b are rate-and-state friction parameters presented in subsection 2.3, and σ_n' is the effective normal stress applied at the interface. The fluid pressure change modifies the effective normal stress. Using Terzaghi's principle (Terzaghi, 1923), the effective normal stress applied at the fault interface writes

$$\sigma_n' = \sigma_n - p \tag{1.19}$$

where, σ_n is the total normal stress at the fault interface and p is the fluid pressure, which is assumed to be constant here. As a consequence, for increasing pore pressure, the critical stiffness from 1.18 decreases. A first illustration of fluid effects, based on the spring-slider reduced order model equations, is illustrated in Figure 1.3. It represents the analog of Figure 1.2 (b) without and with fluid injection. We observe that, in the dry case (Figure 1.3 top), under the assumption of a spring-slider reduced order model, the evolution of the shear stress τ with respect to cumulated slip δ follows the softening branch of slope $-\overline{k}$ (red line, spring stiffness per unit surface). If $-\overline{k} > -\overline{k}_{\mathrm{cr}}$, then the steady state slip is unstable and accumulated elastic energy is released. The case $-\overline{k} < -\overline{k}_{\mathrm{cr}}$ leads to stable slip and a new equilibrium state is reached. The condition $-\overline{k} > -\overline{k}_{\mathrm{cr}}$ holds here, and the blue shaded area corresponds to the released elastic energy per unit area $\overline{E}_R$. In the injection case (Figure 1.3 bottom), the friction force decreases as fluid is injected and the critical stiffness per unit area $-\overline{k}_{\mathrm{cr}}^{\mathrm{inj}}$ is smaller than $\overline{k}_{\mathrm{cr}}$. The shear stress τ at equilibrium in the dry case is greater than in the injection case and the shear stress drop is of lower amplitude in the injection case than in the dry case. If $-\overline{k} > -\overline{k}_{\mathrm{cr}}^{\mathrm{inj}}$, unstable slip occurs, but a smaller amount of accumulated elastic energy is released compared to the dry case. The case $-\overline{k} < -\overline{k}_{\mathrm{cr}}^{\mathrm{inj}}$ leads to stable slip towards a new equilibrium state. The condition $-\overline{k} < -\overline{k}_{\mathrm{cr}}^{\mathrm{inj}}$ is satisfied here and a stable slip occurs. However, as explained by Stefanou (2019), if the necessary condition for instability $\overline{k} = \overline{k}_{\mathrm{cr}}$ is reached, but instability conditions are not satisfied, then slow aseismic slip arise.

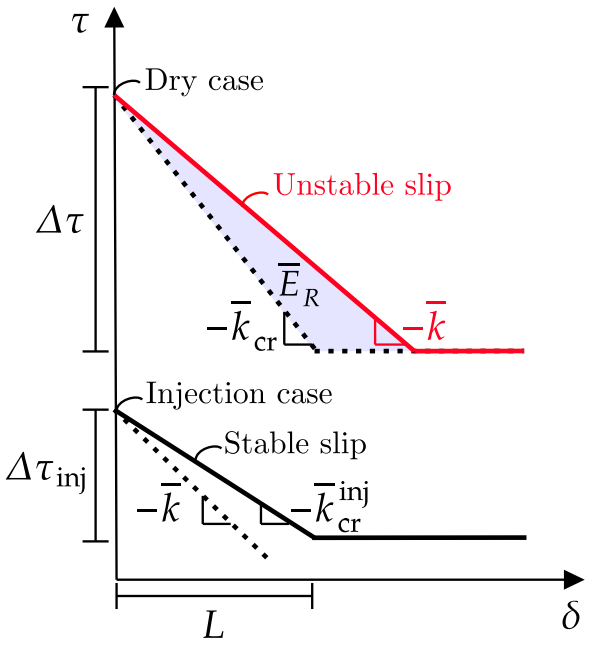

Figure 1.3 • Simplified illustration of fluid effects ranging from unstable to stable slip (modified from Tzortzopoulos (2021)).

1.5 Limitations of the reduced order model

The spring-slider model has been largely used in the literature (Ruina, 1983; Gu et al., 1984; Lapusta et al., 2000). It allowed modeling and simulating seismic cycles as a stick-slip phenomenon Gilbert (1884). Nevertheless, as all simplified models, this reduced-order model has some main limitations.

The first limitation concerns the modeling of the fault and of friction. In both the spring-slider model and the strike-slip fault representation (Figure 1.1), the fault is modeled as a mathematical plane due to its very small thickness compared to other characteristic lengths in the problem (length of the locked interface for instance). Stefanou (2019) highlights that this thickness is linked to the reduction of friction as a function of slip, slip-rate, and other multi-physic variables. Rattez et al. (2018a, 2018b) and Stathas and Stefanou (2023) used Cosserat continuum and considered a perfectly (visco-)elastoplastic Drucker-Prager material to take into account a more realistic model of the fault gouge and have a better understanding of friction. In this work, we want to take into account frictional properties that can vary along the fault.

The second limitation relates to the dimensionality of the problem. Nussbaum and Ruina (1987) and Huang and Turcotte (1990), among others, proposed an extension of single spring-slider case as two spring-sliders coupled by a spring and submitted to the same loading. Also, p-degrees-of-freedom models have been considered by Burridge and Knopoff (1967) and Carlson and Langer (1989). They studied p coupled oscillators, for which the p sliders are in contact with a moving substrate and linked to a fixed support by p springs of identical stiffness. In particular, Huang and Turcotte (1992), for two coupled spring-sliders, and Erickson et al. (2011), for the Burridge-Knopoff model, proved chaotic behavior of these p-degrees-of-freedom (p>2) kinematic models. Studies on the aperiodicity of the seismic cycle by Erickson

et al. (2008) emphasized the limitations of the simplified spring-slider analog and questioned the applicability of these models to actual fault systems. The spatio-temporal complexity raised by the introduction of discrete coupled/assembled spring-slider models could not be observed for a correctly discretized continuous problem of a planar fault under rate-and-state friction (Rice, 1993). A potential candidate to explain the broad range of seismic and aseismic slip phenomenons (slow-slips, earthquakes, pre- / post-seismic phenomenons) could be to represent geometry complexities of fault networks (non-planar faults + overlapping faults for instance as investigated by Romanet (2017), Romanet et al. (2020), Bhat et al. (2023), and Cheng et al. (2023)). This corroborates the point of Rice (1993), that the solution for unstable slip along a chain of coupled spring-slider models in the continuous limit had an uncertain relation to dynamical solution for unstable slip along a fault embedded in a surrounding elastic continuum. In case of discrete models, an instantaneous change in shear stress τ implies an instantaneous change in the acceleration $\ddot{\delta}$, but there is no instantaneous change in slip rate $\dot{\delta}$ as it is the case for continuous models (as detailed in 2 1.1). This motivates the use of continuous medium models in the present work.

> **Remark 1.2.** *The stability results derived in this subsection have been extended to continuous models by Rice and Ruina (1983) (with spatially periodic slip-rate perturbations along their interface) and by Aldam et al. (2017).*

2 Generic spatio-temporal fault behavior

The previous section allowed us to define the concept of seismic cycle, to study the analogy with a reduced order model to explain its main features, and to highlight specificities of discrete versus continuous models. The latter made us aware of the limitations of reduced-order models and of the need for a more realistic model which could incorporate more complexities. Therefore, we are interested in the ingredients to model a seismic cycle problem based on a continuous model. One challenge highlighted here, is the difficulty to model a realistic seismic cycle. Ideally, both the realistic frictional behavior at the fault interface and the influence of other external phenomenons than the relative plate tectonics motion should be acknowledged (as detailed by Rolandone (2022) (section 4.3.2)). We detail the different assumptions for both generic and standard seismic-cycle problems. Our objective is to model an adequate fault mechanics problem to simulate seismic cycles. This section is set into four subsections introducing the geometry, the balance momentum equation and constitutive laws, interface conditions and finally, the boundary conditions.

2.1 Fault geometry

In the most generic case, we consider an infinite space Ω containing a discontinuity Γ (or fault) of arbitrary shape. The two crack faces Γ^+ and Γ^- are geometrically identical such that $\Gamma = \Gamma^+ = \Gamma^-$ and have opposite unit normal vectors $\mathbf{n}^+ = -\mathbf{n}^-$, which points towards the exterior of the medium.

In geophysics (dynamic rupture and seismic cycles communities), planar faults embedded

in a semi-infinite medium have been largely studied (Rice, 1993; Lapusta et al., 2000; Harris et al., 2009; Erickson et al., 2020a). However, many references focus on more realistic models considering non-planar faults and faults with complex geometries as a key component to understand real seismic events. Particularly, Romanet et al. (2020), emphasized on the curvature as a link between geometrical complexities and the origin of slip complexities.

Different kinds of geometry complexities have been considered: faults with a change in strike[1], influence of fault branches, faults with a kink or a bend, and parallel fault segments. Studies of those different configurations are reviewed in the following paragraphs.

Bouchon and Streiff (1997) looked into a two-dimensional dynamic rupture of a fault with a change in strike. They highlighted that the rupture velocity slowed down as well as slip amplitude, when rupture propagates onto a segment unfavorably oriented with respect to the regional stress field.

The influence of fault branches in earthquake rupture dynamic has been considered in various studies. Aochi and Fukuyama (2002), provided a realistic 3D simulation of the 1992 Landers, California earthquake. Kame et al. (2003), studied mode II rupture along a planar main fault intersecting a branching fault. A review on the role of fault branches in earthquake rupture dynamics and a comparison between the case of infinite and finite branches was developed by Bhat et al. (2007). Motivated by the normal fault configuration in the vicinity of Yucca Mountain, Nevada, Templeton et al. (2010), studied branched fault activation. Kame et al. (2003), Bhat et al. (2004), emphasized the role of the fault pre-stress state, branching angle, and the incoming rupture velocity at the branching junction in determining whether the rupture would follow the branch or continue on the main fault or both. Fliss et al. (2005) questions the directivity of rupture and proposes a mechanism of creation of a backward branch related to field observations.

Templeton et al. (2009), analyzed shear crack nucleation and propagation along non-planar kinked and branched fault. Numerous studies considered bent faults such as Aochi et al. (2000), who observed that rupture could decelerate or arrest from some bend angles. Oglesby and Archuleta (2003), simulated repeated earthquake events on a thrust fault with a bend at depth. Duan and Oglesby (2005), also incorporated the effect of a strike-slip fault with a bend during several seismic cycles. He insisted on taking into account a viscoelastic model during inter-seismic process to avoid pathological stress around the bend. Romanet et al. (2020), proposes a small slope approximation to overcome complex geometries effect regarding numerical simulations extents.

Other works concentrate on parallel fault segments (Harris et al., 1991; Harris & Day, 1993; Romanet, 2017; Barbot, 2019, 2021).

In the present work, we concentrate on planar faults embedded in a (semi-)infinite medium as a starting configuration since our main interest is to study fluid-injection effects on fault slip at the timescale of the seismic instability. This kind of configuration is represented in Figure 1.4. We focus on a simplified two-dimensional configuration of a strike-slip fault. In particular, we consider a planar fault, infinitely long along $\mathbf{e}_2$ and $\mathbf{e}_3$ directions. We also consider the case of a semi-infinite (along $\mathbf{e}_3$ direction) planar fault in a semi-infinite space. As a shear motion is imposed on either side of the fault, anti-plane strain or in-plane strain

[1] The strike refers to the fault azimuth, conventionally described with respect to north

configurations are considered. As a starting point, we neglect complex fault geometries, and we consider a single fault.

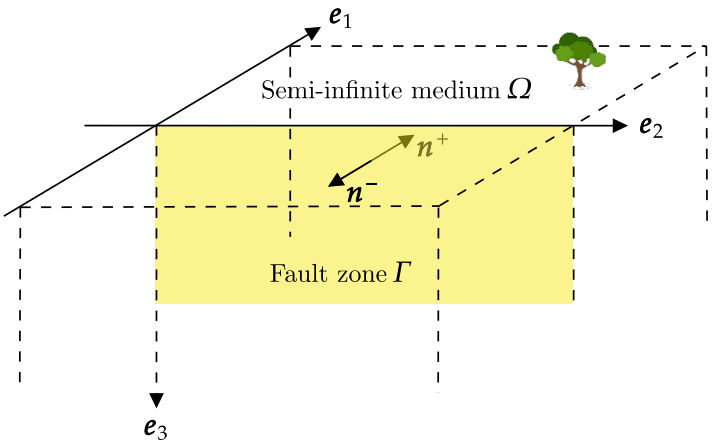

Figure 1.4 • Planar-fault Γ embedded in a semi-infinite medium Ω.

2.2 Momentum balance and constitutive equations

Now that we chose the geometry, we want to derive the equations to model the seismic cycle. Everywhere in Ω, the momentum balance equation has to be satisfied. This equation is completed by a constitutive equation linking stress and strain tensors. This constitutive equation depends on the material properties assumed. On the discontinuity Γ, a constitutive friction law is considered. It is detailed in Section 2.3.

In the literature, elastic off-fault material has been largely assumed (Tse & Rice, 1986; Rice, 1993; Lapusta et al., 2000; Kaneko et al., 2011). Nevertheless, other constitutive properties have also been considered in order to build a more realistic model.

Viscoelasticity has been incorporated to represent the different deformation mechanisms in depth. Kato (2002), considered a vertical strike-slip fault embedded in a semi-infinite medium composed of an elastic layer overlying a viscoelastic half-space. He showed that this model could explain postseismic slip deformation observed at the Earth's surface. He observed an effect for short relaxation times. Johnson and Segall (2004), proposes the study of a strike-slip fault in an elastic lithosphere coupled to a viscoelastic asthenosphere. A fault-containing elastic layer over a viscoelastic half-space was studied by Kato (2002), Lambert and Barbot (2016). Allison and Dunham (2018), reviews seismic cycles studies that examined the role of viscoelasticity on earthquakes. They simulated earthquake cycles with rate-and-state fault friction and off-fault power-law viscoelasticity for the classical problem of a vertical, strike-slip plate boundary fault.

Other works incorporated plasticity to take into account irreversible deformations around the fault zone. Off fault plasticity and viscoelasticity is considered by Ma and Andrews (2010), Dunham et al. (2011a), Dunham et al. (2011b), Kaneko and Fialko (2011) (Drucker-Prager

plasticity criterion), Erickson et al. (2017), Andrews (2005), Xu et al. (2012) (Mohr-Coulomb plasticity criterion).

The case of a fault intersecting a sedimentary basin is studied by Erickson and Dunham (2014), Fialko et al. (2005) who emphasized shallow slip deficit as large earthquake cannot penetrate through sedimentary layers.

Finally, the case of off-fault dissimilar materials is reviewed and explored by Ranjith and Rice (2001) who concentrated on the link between the ill-posedness of such a problem and on the existence of an interfacial Rayleigh wave. Many studies were also conducted on the incorporation of hydro-mechanical couplings and will be developed in section 4.

Cauchy continuum was assumed in all these works while studies conducted by Rattez et al. (2018b), Rattez et al. (2018a) and Stathas and Stefanou (2023) who focused on modeling the fault gouge and understanding friction, used momentum balance equations derived from fault modeling using Cosserat continuum. They consider a perfectly (visco-)elastoplastic Drucker-Prager material.

In this work, as a starting point, we consider a strike slip fault embedded in an elastic medium. We use Cauchy continuum here. We consider a linear, elastic, homogeneous isotropic medium with constitutive properties defined by mass density ρ, shear modulus $\mu = G$ (not to be confused with the friction coefficient often denoted μ), the Poisson ratio ν and the first Lamé coefficient $\lambda = 2G\nu/(1-2\nu)$. The displacement is denoted $\mathbf{u}$ and the Cauchy stress tensor $\boldsymbol{\sigma}$. In this configuration, the balance momentum equation writes as in (1.20)

$$\boldsymbol{\nabla}\cdot\boldsymbol{\sigma} + \rho\mathbf{F} = \rho\ddot{\mathbf{u}} \tag{1.20}$$

where $\rho\mathbf{F}$ corresponds to the body force vector distribution which may have various origins (gravity, thermal effects, fluid effects). Einstein convention is used in the following part. Deformations are described by the strain tensor $\boldsymbol{\varepsilon}$ which writes, for linear elasticity under small strain assumption

$$\varepsilon_{ij} = \frac{1}{2}\left(u_{i,j} + u_{j,i}\right) \tag{1.21}$$

where u_i denotes the i-th component of the displacement and $u_{i,j}$ is the derivative of u_i with respect to x_j. The balance momentum equation (1.20) is here completed by the isotropic constitutive Hooke's law

$$\sigma_{ij} = C_{ijkl}\varepsilon_{kl}, \text{ with } C_{ijkl} = G\left[\frac{2\nu}{1-2\nu}\delta_{ij}\delta_{kl} + \delta_{ik}\delta_{jl} + \delta_{il}\delta_{jk}\right]. \tag{1.22}$$

Equations (1.22) and (1.21) injected into (1.20) lead to the Navier equation of motion

$$\frac{G}{1-2\nu}\boldsymbol{\nabla}\left(\boldsymbol{\nabla}\cdot\mathbf{u}\right) + G\boldsymbol{\nabla}^2\mathbf{u} + \rho\mathbf{F} = \rho\ddot{\mathbf{u}} \tag{1.23}$$

In this thesis, we concentrate on anti-plane and in-plane strain configurations (with a no-opening condition on the fault for the in-plane configuration) which allow us to manipulate scalar equations as a first step. Resulting balance momentum and constitutive equations for particular anti-plane et in-plane strain configurations are gathered in table 1.1. This problem is completed by interface and boundary conditions.

Dislocation	Balance momentum equation	Constitutive Hooke's law
Mode III $\mathbf{u} = u_2(x_1, x_3, t)\mathbf{e}_2$	$\dfrac{\partial \sigma_{12}}{\partial x_1} + \dfrac{\partial \sigma_{23}}{\partial x_3} = \rho \dfrac{\partial^2 u_2}{\partial t^2}$	$\sigma_{12} = G u_{2,1}, \sigma_{23} = G u_{2,3}$
Mode II $\mathbf{u} = u_1(x_1, x_3, t)\mathbf{e}_1 + u_3(x_1, x_3, t)\mathbf{e}_3$	$\begin{cases} \dfrac{\partial \sigma_{11}}{\partial x_1} + \dfrac{\partial \sigma_{13}}{\partial x_3} = \rho \dfrac{\partial^2 u_1}{\partial t^2} \\ \dfrac{\partial \sigma_{13}}{\partial x_1} + \dfrac{\partial \sigma_{33}}{\partial x_3} = \rho \dfrac{\partial^2 u_3}{\partial t^2} \end{cases}$	$\sigma_{11} = (\lambda + 2G)\dfrac{\partial u_1}{\partial x_1} + \lambda \dfrac{\partial u_3}{\partial x_3}$ $\sigma_{13} = G\left(\dfrac{\partial u_1}{\partial x_3} + \dfrac{\partial u_3}{\partial x_1}\right)$ $\sigma_{33} = \lambda \dfrac{\partial u_1}{\partial x_1} + (\lambda + 2G)\dfrac{\partial u_3}{\partial x_3}$

Table 1.1 • Balance momentum and constitutive equations for anti-plane and in-plane shear cases for a 1D fault lying in the plane $\{\mathbf{e}_1, \mathbf{e}_3\}$.

2.3 Interface conditions

Across the discontinuity Γ, we define the displacement jump (slip) $\boldsymbol{\delta}(\mathbf{x}, t)$

$$\boldsymbol{\delta}(\mathbf{x}, t) = \mathbf{u}^+(\mathbf{x}, t) - \mathbf{u}^-(\mathbf{x}, t). \tag{1.24}$$

In the mode III configuration, this leads to

$$\boldsymbol{\delta}(\mathbf{x}, t) = \delta_2(x_3, t)\mathbf{e}_2, \text{ where } \delta_2(x_3, t) = u_2(x_1 = 0^+, x_3, t) - u_2(x_1 = 0^-, x_3, t). \tag{1.25}$$

In the mode II configuration we assume a "no-opening condition" on the fault, namely that

$$\begin{aligned} &u_1(x_1 = 0^+, x_3, t) = u_1(x_1 = 0^-, x_3, t) \\ &\Rightarrow \boldsymbol{\delta}(\mathbf{x}, t) = \delta_3(x_3, t)\mathbf{e}_3, \text{ where } \delta_3(x_3, t) = u_3(x_1 = 0^+, x_3, t) - u_3(x_1 = 0^-, x_3, t). \end{aligned} \tag{1.26}$$

We define the slip velocity vector $\mathbf{V}(\mathbf{x}, \mathbf{t})$ as the time derivative of the displacement discontinuity vector $\boldsymbol{\delta}(\mathbf{x}, t)$.

$$V_j(\mathbf{x}, t) = \frac{\partial \delta_j}{\partial t} \Rightarrow \mathbf{V}(\mathbf{x}, \mathbf{t}) = V_2(x_3, t)\mathbf{e}_2 = \frac{\partial \delta_2}{\partial t} \text{ (mode III)}, \ \mathbf{V}(\mathbf{x}, \mathbf{t}) = V_3(x_3, t)\mathbf{e}_3 = \frac{\partial \delta_3}{\partial t} \text{ (mode II)}. \tag{1.27}$$

Traction at the fault interface $\mathbf{t}^{D^\pm}$ must be given to close the problem. Here, we assume the media, the loading, and the material properties symmetrical on either side of the fault so that the traction components were continuous at the interface:

$$\begin{aligned} &(\boldsymbol{\sigma}\mathbf{n})^+ = -(\boldsymbol{\sigma}\mathbf{n})^- \\ &\Rightarrow \begin{cases} \sigma_{12}(x_1 = 0^+, x_3, t) = \sigma_{12}(x_1 = 0^-, x_3, t), \text{ (mode III)} \\ \sigma_{11}(x_1 = 0^+, x_3, t) = \sigma_{11}(x_1 = 0^-, x_3, t), \\ \text{and } \ \sigma_{13}(x_1 = 0^+, x_3, t) = \sigma_{13}(x_1 = 0^-, x_3, t), \text{ (mode II)} \end{cases} \end{aligned} \tag{1.28}$$

At the fault interface, traction is initially imposed resulting from the far-field loading. We denote $\boldsymbol{\sigma}_0$ the corresponding pre-stress and $\mathbf{t}_0$ the corresponding traction vector. In addition to this pre-stress state, the interactions between the two elastic media on either side of

the fault are specified by an interface law. A change in elastic deformation in the medium on either side of the fault will change the displacement discontinuity at the fault interface, therefore the traction at the interface. On the other hand, the contact traction will influence the elastic deformation of the medium. We separate the normal pre-stress $\boldsymbol{\sigma}_{n_0}$ and the shear pre-stress $\boldsymbol{\tau}_0$. The corresponding stress change is denoted $\Delta\boldsymbol{\sigma}$ (respectively $\Delta\mathbf{t}$ for the traction change at the fault interface). Within the traction change vector at the fault interface, we distinguish the normal stress change $\Delta\boldsymbol{\sigma}_n$ and the shear stress change $\Delta\boldsymbol{\tau}$. On the frictional domain, the shear stress $\boldsymbol{\tau} = \boldsymbol{\tau}_0 + \Delta\boldsymbol{\tau}$ is equal to fault shear resistance $\mathbf{F}$, namely

$$\boldsymbol{\tau}(\mathbf{x}, t) = \mathbf{F}(\boldsymbol{\delta}, \mathbf{V}, \theta, t) \tag{1.29}$$

where the frictional resistance can depend on slip, slip-rate, a state variable, time, etc. We assume Coulomb friction so that the frictional resistance writes as the product of the effective normal stress σ_n by the friction coefficient $f(\boldsymbol{\delta}, \mathbf{V}, \theta, t)$ which can depend on slip, slip-rate, a state variable, time, etc.

$$\boldsymbol{\tau}(\mathbf{x}, t) = \sigma_n \mathbf{f}(\boldsymbol{\delta}, \mathbf{V}, \theta, t) \frac{\mathbf{V}}{\|\mathbf{V}\|}. \tag{1.30}$$

Different friction laws can be considered to define the friction coefficient. Frérot (2020) reviews the arising of friction laws. An important point before considering different friction models is the introduction of the characteristic slip distance D_c, which combined to the slip-rate, corresponds to the weakening time in which the friction decreases from static to dynamic friction. It is associated with a finite energy quantity released at the rupture front. D_c corresponds to the quantity $L = V/(\partial\varphi(V,\theta)/\partial\theta)_{V=V^*,\theta=\theta^*}$ defined in Equation (1.11) in Section 1.2 for the stability analysis of the spring-slider reduced order model. Considering the analogy with the spring-slider, the critical stiffness (under quasi-static assumption) per unit surface of a fault is defined as

$$\begin{aligned} \overline{k}_{\text{fault}} &= \frac{G}{L_{\text{nuc}}} \left(= \overline{k}_{\text{cr}} = \sigma_n \frac{b-a}{D_c} \text{ for the spring-slider} \right), \\ L_{\text{nuc}} &= \frac{G D_c}{\sigma_n (b-a)}. \end{aligned} \tag{1.31}$$

where L_{nuc} is the nucleation length[1] meaning the portion of the fault plane behind the crack tip where the shear stress decreases from its static value to its dynamic value and the instability can occur. Other expressions of the nucleation length were given by Dieterich (1992) and Rubin and Ampuero (2005).

In Rolandone (2022)[2], a chronological state of the art of friction laws from the arising of the idea of a frictional control of faults thanks to the works of Brace and Byerlee (1966) to the description of the friction law currently used in the seismic cycles' community is given. In the field of fault mechanics, the most common friction models that can lead to earthquake-like instabilities are:

- slip-weakening friction law (SW)

[1] Also called the cohesive (or slip-weakening) zone length in the literature, which is ambiguous (cf. Section 1.2) as it refers to damage and fracture mechanics and not to contact mechanics that is considered here.

[2] in chapter 4 from Rolandone (2022), by Marion Thomas and Harsha Bhat

- rate-weakening friction law (SRW)
- rate-and-state friction laws (RSF)

Slip-weakening friction (SW)

The SW law was first introduced to study the occurrence of singularities at the rupture tip for faults loaded in tension. Introduced by Ida (1972) and Andrews (1976) in 2D and Day (1982) in 3D in mode II. The corresponding friction coefficient writes:

$$\mu(\delta) = \begin{cases} (\mu_s - \mu_d)(1 - \delta/D_c) + \mu_d, \text{ if } \delta < D_c \\ \mu_d \text{ if } \delta > D_c \end{cases} \tag{1.32}$$

where $\mu_d < \mu_s$ and D_c is a critical slip value. Slip is equal to zero until the shear stress reaches the elastic limit τ_s. Once τ_s is reached, the friction resistance decreases to reach the value τ_d, whereas the slip increases until its critical value D_c. If the slip is greater than D_c, the shear stress is equal to τ_d. This law is appropriate to model one dynamic rupture but not a complete seismic cycle as it does not take into account the healing process of the fault. Also, it does not explain when rupture stops. Another expression is given by Scholz (2002)

$$\mu(\delta) = (\mu_s - \mu_d)\exp(-\delta/D_c) + \mu_d \tag{1.33}$$

Slip-rate-weakening friction (SRW)

Slip-rate-weakening friction is an empirical friction law proposed by Burridge and Knopoff (1967). It allows to model the healing process in addition to the dynamic rupture. Once slip has reached the critical value D_c, friction becomes a function of the slip rate V.

$$\tau(V) = (\tau_f^s - \tau_f^d)(V_0/(V_0 + V)) + \tau_f^d \tag{1.34}$$

When the slip rate is much smaller than the characteristic slip rate V_0, the friction resistance is equal to the product of the static friction coefficient by effective normal stress. Whereas, when the slip rate is greater than V_0, $\tau = \mu_d \sigma_{\text{eff}}$, a different form of the slip rate weakening law is given by Huang and Turcotte (1992):

$$\mu(V) = \mu_s/(1 + V/V_0) \tag{1.35}$$

Where V_0 is a characteristic slip rate describing the friction coefficient drop due to slip rate weakening.

Rate-and-state friction (RSF)

Rate-and-state friction laws consist in empirical laws that quantify the shear response of a fault submitted to a jump in slip-rate. Experimentally, the effect on the friction coefficient of a jump in velocity is first a direct effect with sudden increase followed by a relaxation phase towards a new steady state value of the friction coefficient. Dieterich (1979), Ruina (1983) and Rice and Ruina (1983) were the first to introduce this law. Dieterich linked the

decrease in the friction coefficient with velocity as an effect of decrease in the average contact time. This allows to gather the static and the dynamic friction law as only one friction coefficient, depending on the slip rate. Chris Marone (Marone, 1998) proposed a modern version of the rate-and-state dependent friction law and gave an exhaustive review of laboratory observations. The friction coefficient given by Marone writes:

$$\mu(V,\theta) = \mu_0 + a\log(V/V_0) + b\log(\theta V_0/D_c) \tag{1.36}$$

where a and b are state variables linked to the direct effect and to the relaxation phase respectively. θ corresponds to a state variable often interpreted as the average contact time of asperities. It is completed by a state law:

- aging law: $\dot{\theta} = 1 - V\theta/D_c$,
- slip evolution law: $\dot{\theta} = -V\theta/D_c \log(V\theta/D_c)$,
- other state laws (Perrin et al. (1995) for instance).

The correct form of the state law is still an open question. The aging law does not give a symmetrical response depending upon the positive or negative velocity jump imposed. The slip evolution law does not take into account the logarithmic evolution of the static friction coefficient in time, which is in favor of the use of the aging law.

As an illustration of a seismic cycle simulation using rate-and-state friction with aging law, Figure 1.5 represents the evolution of interface unknowns: the slip δ, the slip-rate V, the shear stress τ and the state variable θ with respect to time during three seismic cycles over two hundred years. We used the spring-mass-damper model from Section 1.2 for this simulation. After a transient regime, we can observe a periodic alternance of co-seismic and inter-seismic phases. The period between two seismic events lasts about 80 years.

An important point concerning laboratory derived friction laws such as the rate-and-state friction law is that it can lead to an ill-posed problem Pipping (2019). A regularization procedure can tackle this mathematical issue. In the present work, we use one of the regularized expression of the friction coefficient proposed by Pipping (2019).

$$\mu(V,\Psi) = a\,\mathrm{sinh}\left(\frac{V}{2V_\Psi}\right), \text{ where } V_\Psi = V_0 \exp\left(-\frac{\mu_0+\Psi}{a}\right), \text{ and } \Psi = b\ln\left(\frac{\theta}{\theta_0}\right) \tag{1.37}$$

Tzortzopoulos (2021) showed that the different friction laws mentioned here are Lipschitz continuous, which allows for existence and uniqueness of the solution for elastodynamic problems with such friction laws. Van den Ende et al. (2018) compared the rate-and-state friction law with microphysical models. Stathas and Stefanou (2023) studied fault friction under thermo-hydro-mechanical couplings during large coseismic slip and justified rate-and-state friction law numerically. Nevertheless, we have to be aware that the previous modeling only describe an approximation of the complexity of the fault gouge and of the friction and wear phenomenons at stake at the frictional surface (Myers & Aydin, 2004).

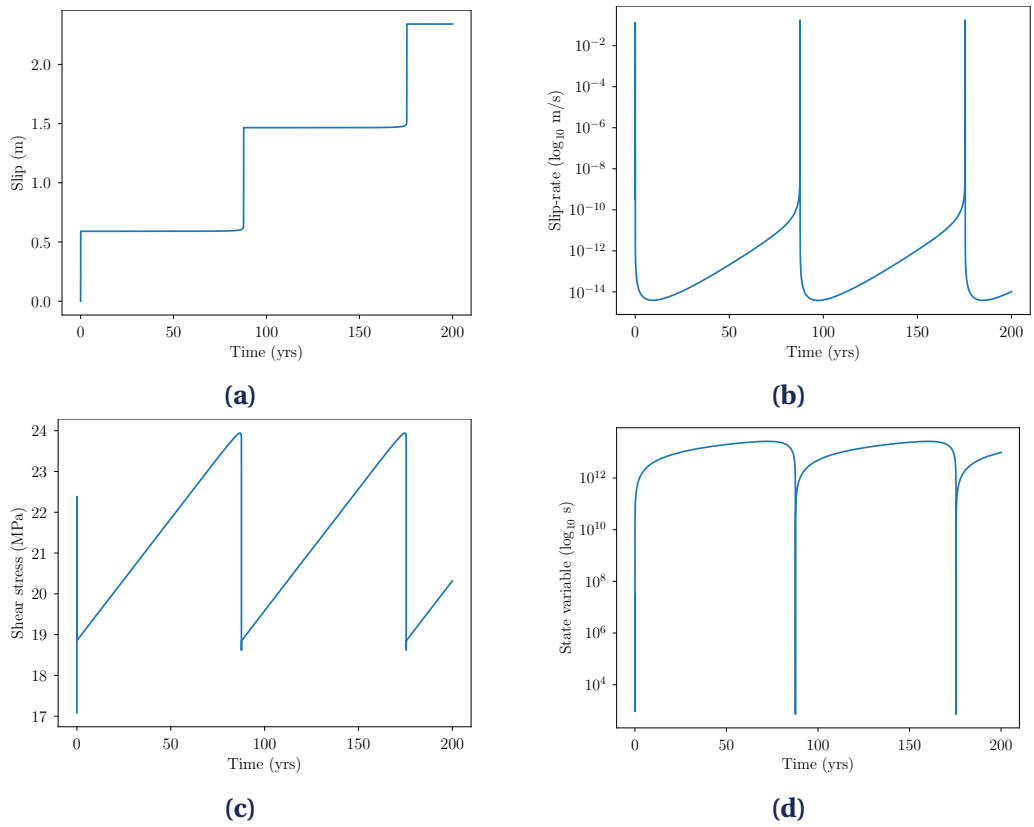

Figure 1.5 • Evolution of the interface unknowns: (a) the slip δ, (b) the slip-rate V, (c) the shear-stress τ and (d) the state-variable θ on with respect to time over three seismic cycles.

2.4 Boundary conditions

When dealing with an unbounded domain, boundary conditions at infinity have to be prescribed. In particular, mechanical fields (displacement and stress changes due to displacement discontinuity) are expected to decay at infinity. Only outgoing waves are allowed. The energy flux at infinity is outgoing, no energy may be radiated into the source region from infinity. Nevertheless, as we consider a time-domain problem, the solutions (which propagate at a finite rate) reach infinity at $t \to \infty$. Hence, the boundary conditions depend on the size of the domain we choose for the problem. If we artificially truncate the domain $(x_1, x_2, x_3) \in]-\infty, \infty[\,]-\infty, \infty[\,]-\infty, \infty[$:

- we either have to ensure that the domain is large enough so that the solution does not reach the boundary at the maximum time instant considered,
- or we impose absorbing boundary conditions so that the solution does not reflect on the boundary and radiate into the dislocation region,
- or we impose far enough of the seismogenic zone that the mechanical fields correspond to the far-field plate tectonics relative motion imposed as a rigid body translation.

A more realistic configuration than a fault embedded in an infinite medium may be to consider a fault embedded in a half-space. In this case, a free surface condition must be taken

into account. The traction components at the free surface are equal to zero

$$\boldsymbol{\sigma}\mathbf{n} = \mathbf{0}, \quad \text{on } \partial\Omega \tag{1.38}$$

In the present work, we consider a fault that is large enough compared to the nucleation length, and we impose a slip-rate loading far enough from the seismogenic zone. We use the case of a fault embedded in an infinite medium to validate the numerical tools we developed, and we present benchmark results in case of a fault embedded in a semi-infinite medium with a free-surface condition in Chapter 2

2.5 Initial conditions

Initial conditions on the different (volume and interface) unknowns are required to solve the problem. Thus, $\mathbf{u}(\mathbf{x},0)$, $\mathbf{V}(\mathbf{x},0)$, $\boldsymbol{\theta}(\mathbf{x},0)$ must be given. These initial conditions have to be consistent with the friction law chosen. In any case, initial conditions must perturb the steady state, so that instability could occur. A perturbation of the slip-rate or of the shear stress change can be chosen to nucleate the first rupture right after the initialization (Ampuero et al., 2002). For the validation of the numerical tools we developed, we give initial values of the interface unknowns (slip $\boldsymbol{\delta}(\mathbf{x},0)$, slip-rate $\mathbf{V}(\mathbf{x},0)$ and state-variable $\boldsymbol{\theta}(\mathbf{x},0)$), eventually with a perturbation in slip-rate to validate results during a co-seismic phase and a seismic cycle.

Table 1.2 summarizes the ingredients for modeling a seismic cycle. The columns in the table refer to the choice of geometry, material properties, interface conditions and boundary conditions respectively. The level of difficulty of each modeling choice increases from left to right. The ingredients considered in this work are highlighted in red.

Ingredients	Increasing complexity			
Geometry	Planar fault	Parallel faults Overlapping faults	Faults with a kink / branch(es) / bend(s)	Fault of realistic geometry
Continuum and material properties	Cauchy continuum Homogeneous, elastic, isotropic medium	Cauchy continuum incorporating viscoelasticity / plasticity of the medium / Porous medium	Cauchy continuum incorporating heterogeneity of the medium	Cosserat continuum to model the fault gouge
Interface conditions	Coulomb friction	Slip-Weakening (SW) friction	Slip-Rate-Weakening (SRW) friction	Rate-and-State friction (RSF)
Boundary conditions	Conditions at infinity	Conditions at infinity + free-surface condition		

Table 1.2 • Ingredients for modeling a seismic cycle.

The fault dynamics can be determined by solving equations resulting from the combination of the elastodynamic equations (Equation (1.23)) with friction law (Equation (1.28)+(1.37) here), as well as boundary conditions (Equation (1.38) + conditions at infinity or artificial truncation of the domain) and initial conditions.

3 Simulating seismic cycles

After having detailed the ingredients to model a seismic cycle, we now look into the numerical simulation of this problem and the associated computational challenges. The specificity of

this problem is the broad range of time and spatial scales involved. On the one hand, time scales span from inter-seismic periods which may last tens to hundreds years to dynamic co-seismic rupture phase in the order of seconds. Taking into account the full dynamic of a fault rupture requires a high computational cost for the time integration. On the other hand, the space discretization should be fine enough to resolve the controlling lengths highlighted by the linear stability analysis (nucleation length). A fault measured in tens to hundreds of kilometers may be discretized. Moreover, the fault is assumed to be embedded in an unbounded domain.

3.1 Existing methods for spatio-temporal discretization of the problem

Efficient numerical methods are required to solve the problem detailed in Section 2. Their objective is to compute the evolution of the displacement discontinuity and of the stress-state at the frictional interface. We separate space discretization methods and time discretization methods used to solve seismic-cycles problems in this part.

Space discretization

We can distinguish three main categories of methods used for the space discretization

- volume methods:
  - finite differences;
  - finite elements;
  - spectral elements;
  - discontinuous Galerkin.
- surface methods:
  - Spectral Boundary Element Methods;
  - Fast Boundary Element Methods based on Fast-multipole methods, or based on Hierarchical matrices.
- hybrid (Finite-Element/Boundary-Element) methods.

Volume methods. The most used methods to solve partial differential equations (PDEs) are volume methods. The common point between these methods is that (i) a volume mesh of the medium on either side of the fault is required when using volume methods, (ii) an artificial truncation of the domain containing the fault is required[3], and (iii) the discretization of the equations to solve leads to sparse matrices.

In case of volume methods, the equations satisfied are discretized in space on the mesh. Summation-by-part have been largely used to approximate differential operators in case of finite difference methods (Erickson and Dunham (2014), Erickson et al. (2020b), Almquist

[3]Some relevant techniques using infinite elements or absorbing boundary conditions like perfectly matched layers (PML) (Liu et al., 2020) or similar can be used to take into account radiation conditions at infinity.

and Dunham (2021), and Kozdon et al. (2021) among others) and penalty terms are used to weakly enforce the boundary conditions. Both techniques allow to stabilize the solving. A discretization of the weak formulation of the volume problem is performed in case of the Finite Element Method as well as for Spectral Elements and Discontinuous Galerkin methods.

The volume methods used for seismic cycles simulations are geometrically flexible as they allow considering complex fault geometries. The advantage of Discontinuous Galerkin method over other volume methods is that the values defined on the face of each cell are double-valued, so that it would naturally include the displacement discontinuity at the fault while split nodes at the fault or Lagrange multipliers are considered in case of Finite Differences or Finite Elements. Also, the Discontinuous Galerkin Method can be easily parallelized.

For seismic cycles, finite difference method allowed to simulate the kinematics of a planar fault under rate-and-state friction law embedded in a 2D elastic medium (Erickson & Dunham, 2014; Erickson et al., 2017; Allison & Dunham, 2018; Erickson et al., 2020b; Kozdon et al., 2021). 3D cases were also considered (Pranger, 2020; Almquist & Dunham, 2021). Viscoelastic (Allison & Dunham, 2018), thermoelastic (Erickson & Dunham, 2014), plastic (Erickson et al., 2017) material properties were taken into account. Liu et al. (2020) simulated 2D and 3D problems with a planar fault under rate-and-state friction embedded in a linear elastic medium using the Finite Element Method. Roch (2023) used a finite element code name Akantu (Richart & Molinari, 2015) to provide a numerical modeling of a frictional rupture on a planar interface. Discontinuous Galerkin methods have been used for the same configurations (Abhyankar et al., 2018; Uphoff et al., 2022). Similar cases were considered only in 2D with Spectral Element Methods (Kaneko et al., 2011; Thakur et al., 2020). We refer the interested reader for more details on volume methods to the previous cited works.

The main challenge of these methods is the artificial truncation of the domain. Some works have been proposed in the seismic cycle community. In case of finite difference methods, Erickson and Dunham (2014) used symmetries of the problem. This allowed considering only one side of the domain containing the fault. Hence, the discretized domain is limited by a boundary parallel to the fault and at a distance L of it, the fault, a free-surface and is truncated at depth. The boundary that is parallel to the fault is loaded remotely with a displacement boundary corresponding to the far-field plate motion. The volume domain is truncated at depth far enough from the depth at which a seismic event can nucleate. At such depths, the velocity is likely to approach a constant value independent of depth, resulting in a displacement independent of depth too. Which leads the authors to impose a traction-free boundary condition at depth too. This technique requires that the domain is large enough in depth compared to the seismogenic zone, and is commonly used in the case of finite-difference methods (Erickson & Dunham, 2014; Erickson et al., 2017; Allison & Dunham, 2018; Erickson et al., 2020b).

In case of volume methods, the large enough domain required to artificially truncate the domain in the right way raises another difficulty. The larger the seismogenic zone, the more prohibitive the number of mesh nodes. This difficulty is illustrated by Liu et al. (2020), who presents the particular case of a 3D strike slip fault with a bend using finite difference methods. He combined, one for the co-seismic phase (EQdyna) and the inter-seismic phase (EQquasi) respectively. The volume domain is truncated far enough of the fault so as not to

have an influence on the fault slip in case of EQdyna because the stress change induced by spontaneous propagating rupture is simulated. In the case of EQquasi, the fault can extend to the model boundaries because the stress accumulation induced by long-term tectonic loading is simulated. Tectonic loading is applied at the boundaries that are parallel to the fault in EQquasi while Perfectly Matched Layers have been implemented in EQdyna. Example for a size fault of 60 km in length and 30 km in depth, space discretization for EQquasi yields a million hexahedral elements and tens of millions of elements for EQdyna.

Another difficulty apart from the meshing of the volume, is to take into account the discontinuity. Erickson and Dunham (2014) consider a Dirichlet Boundary condition at the fault interface. Other techniques to take into account the fault can be considered. The first two techniques have been detailed by Luis A. Dalguer (Bizzarri & Bhat, 2012) and tested by Andrews, 1999:

- Traction at Split-Node (TSN) scheme also used in Finite Elements (Liu et al., 2020) and Spectral Elements. In this method, the fault discontinuity is explicitly incorporated at velocity and/or displacement nodes. Interactions happen between the halves of the "split nodes" exclusively through the traction (frictional resistance and normal traction) acting between them, and they are in turn controlled by jump conditions and a friction law. This approach allows the separation of equations on each side of fault interface. Roch (2023) used such a node-to-node approach to model the discontinuity numerically.

- Inelastic-zone scheme (Stress Glut (SG)) relies on an approximation of the fault rupture conditions through inelastic increments of the stress components. This method is very easy to implement in Finite Differences codes (a pedagogical script example is given by Bizzarri and Bhat (2012)).

- Cohesive elements (Ortiz & Pandolfi, 1999) allow to model the propagation of a crack, but also stick slip phenomena (Ringoot et al., 2021).

- Phase field approach (Francfort & Marigo, 1998) allows to model complex fault geometries as it is mesh-independent.

Boundary Element Methods. In this work, we use Boundary Element Methods (BEM). This surface methods rely on the Boundary Integral Equation Methods, which consist in reformulating the PDEs satisfied in the volume in an integral equation verified on the domain boundary. This reformulation step of the PDE as a Boundary Integral Equation (BIE) is based on the existence of the fundamental solution of the PDE, which corresponds to the unit force response of the system. The fundamental solution is known analytically for homogeneous material parameters (Bonnet, 1999). In case of more complex material parameters, fundamental solutions may be determined semi-analytically or numerically. Unlike volume methods, the discretization of the BIE leads to a dense matrix. Fast methods can tackle this difficulty by determining a data-sparse approximation of the boundary element matrix. Such methods reduce the CPU-time dedicated both to the computation of the BEM matrix and to

the solving of the Integral Equation from $O(N^2)$ to $O(N\log(N))$, where N is the number of mesh nodes from the discretization of the fault. We can distinguish three categories of fast methods:

- Fast Multipole Methods, introduced by Greengard and Rokhlin (1987). These methods have been used for elastodynamic problems too (Chaillat et al., 2008; Grasso et al., 2012; Chaillat & Bonnet, 2013);

- Methods based on Hierarchical matrices, introduced by Hackbusch (1999) and Hackbusch (2015). These methods have been used for elastodynamic problems (Chaillat et al., 2017).

In the specific context of seismic cycle and dynamic fault rupture simulations, the Fast Fourier Transform accelerated boundary element methods (called Spectral-BEM) is largely considered to simulate the frictional sliding at planar discontinuities (Geubelle & Rice, 1995; Lapusta et al., 2000; Lapusta & Liu, 2009; Barbot, 2019). Important numerical developments using this method have been done in the dynamic rupture / seismic cycle community (Luo et al. (2017) and Roch et al. (2022a) among others).

Many works have considered Boundary Elements Methods for seismic cycles problems. The main advantage is that only the fault geometry has to be meshed, reducing the dimensionality of the problem by one and outperforming volume methods in that sense. 2D/3D planar-fault configurations (Lapusta et al., 2000; Lapusta & Liu, 2009; Barbot, 2019), 2D/3D non-planar fault cases (Romanet, 2017; Romanet et al., 2020; Ozawa et al., 2022; Cheng et al., 2023), and overlapping / parallel faults configurations (Romanet, 2017; Barbot, 2021) have been considered using Boundary Element Methods. Romanet (2017) applied Fast Multipole Methods and Fast BEMs based on Hierarchical matrices to non-planar faults cases. Fast BEMs based on Hierarchical matrices were also applied to non-planar faults seismic cycles problems by (Ohtani et al., 2011; Ozawa et al., 2022).

In this work, we consider both Spectral Boundary Element Method (S-BEM) and Fast Boundary Element Method based on Hierarchical matrices (H-BEM) for mode II and III planar fault configurations. As a starting point, we apply S-BEM to a simplified planar fault problem as it is the more efficient technique in this case. In the particular case of a planar fault in mode II or III, the BIE writes as a Hilbert transform and simplifies in the Fourier domain in space (Geubelle & Rice, 1995). Then we apply H-BEM to the same configurations in order to develop efficient and robust numerical tools to incorporate hydromechanical couplings in our simulations.

Hybrid (Finite-Element/Boundary Element) methods. Hybrid methods can be proposed to combine the versatility of volume methods with the advantages of boundary element methods (Hajarolasvadi & Elbanna, 2017; Abdelmeguid et al., 2019; Roch, 2023). We refer the interested reader for more details on hybrid methods for seismic cycles and dynamic rupture simulations to the previous cited works.

Time discretization

Now, we consider the time discretization of the problem. Time discretization methods for seismic cycles must be able to handle a broad range of timescales, from inter-seismic periods (in the order of tens to hundreds of years) to coseismic phases (in the order of seconds). Adaptive time-stepping algorithm are key to solve seismic cycles problems. They can be separated into three categories.

Explicit methods. Fourth/fifth-order adaptive time-stepping Runge-Kutta methods are the most used schemes (Liu & Rice, 2007; Luo et al., 2017; Barbot, 2019, 2021; Ozawa et al., 2022; Uphoff et al., 2022) and Bulirsch-Stoer method (Romanet, 2017; Luo et al., 2017) are often used. Explicit methods require the reformulation of the equations as a system of Ordinary Differential Equations, which is impossible if inertial effects are considered. Hence, these methods can only deal with quasi-dynamic cases, where inertial effects are approximated at the fault interface only by a radiation damping term $-G/(2c_s)\mathbf{V}(\mathbf{x}, t)$.

Implicit methods. Linear multistep method such as Adams-Moulton or Backwards Difference Formulae are sometimes used (Pranger, 2020). Implicit methods also incorporate a non-linear solving stage which requires linearization to be solved. The corresponding Jacobian matrix has to be assembled and inverted in this case, which is highly demanding numerically.

Hybrid explicit/implicit methods. Prediction-correction methods combined with forward Euler (Lapusta et al., 2000; Lapusta & Liu, 2009; Hajarolasvadi & Elbanna, 2017; Abdelmeguid et al., 2019), second/third-order (Kaneko et al., 2011; Allison & Dunham, 2018; Thakur et al., 2020) or fourth/fifth-order (Erickson & Dunham, 2014; Erickson et al., 2017; Romanet & Ozawa, 2021) accurate adaptive Runge-Kutta time-stepping algorithms among others. Hybrid explicit/implicit methods can be used for both quasi-dynamic and fully-dynamic simulations, but they incorporate a non-linear solving stage (often Newton-Raphson algorithm) of the friction law to determine the slip-rate at the interface. This step can lead to a local minimum of the friction law and thus implies cumulative error on interface unknowns at each time step.

A more exhaustive review of the currently used numerical methods in space and time for seismic cycles simulations is given in Table A.1 of Appendix A. In this work, we have implemented three solving methods: a fourth/fifth-order adaptive time-stepping method inspired by Ozawa et al. (2022), and two hybrid explicit/implicit predictor-corrector schemes, respectively combined with a Forward Euler method (inspired by Lapusta et al. (2000)) or with a fourth/fifth-order adaptive time-stepping method (inspired by Romanet and Ozawa (2021)).

Link between spatial and time discretization: stability condition

Considering dynamic rupture of seismic cycle simulation on a pre-existing fault, spatial and time discretization are interdependent in the sense that the occurrence of fault equilibrium instability and numerical instability are linked. Using the linearized system (1.6)

verified by the perturbation of the equilibrium, we can deduce a numerical stability condition. Discretizing (1.6) with a forward Euler scheme for the sake of simplicity, we obtain

$$\begin{bmatrix} (D^{(n+1)} - D^{(n)})/\Delta T \\ (\Theta^{(n+1)} - \Theta^{(n)})/\Delta T \end{bmatrix} = [J] \begin{bmatrix} D^{(n)} \\ \Theta^{(n)} \end{bmatrix} \tag{1.39}$$

or

$$\begin{bmatrix} D^{(n+1)} \\ \Theta^{(n+1)} \end{bmatrix} = [Q] \begin{bmatrix} D^{(n)} \\ \Theta^{(n)} \end{bmatrix}, \text{ with } [Q] = \begin{bmatrix} 1 - \overline{k}L\Delta T/A^* & -B^*\Delta T/A^* \\ kL\Delta T/A^* & 1 + (B^* - A^*\Delta T/A^*) \end{bmatrix} \tag{1.40}$$

where $D^{(n)}$ and $\Theta^{(n)}$ are the non-dimensional slip and state-variable at the fault interface at *nth* time step $t^{(n)} = n\Delta T$, assuming a constant non-dimensional time step $\Delta T = V^*\Delta t/L$. We determine the eigenvalues of $[Q]$ and compare their values to unity to determine whether the perturbation decays or not. The eigenvalues of the matrix $[Q]$ are given by

$$\lambda_{1,2} = \frac{\mathrm{tr}\,([Q])}{2} \pm \sqrt{\frac{\mathrm{tr}\,([Q])^2}{4} - \det([Q])} = 1 + \left(\frac{1}{2}\mathrm{tr}\,([J]) \pm \sqrt{\frac{1}{4}\mathrm{tr}\,([J])^2 - \frac{\overline{k}L}{A^*}} \right) \tag{1.41}$$

where $[J]$ is the Jacobian matrix defined in (1.9). When discretizing a fault embedded in a (semi-)infinite medium, we can define the stiffness per unit surface $\overline{k}$ as the stiffness of one element from the space discretization of the fault, such that $\overline{k} = G/h$, where h is the space step. The expression of the sum of the eigenvalues of the Jacobian matrix $[J]$ is given by

$$\mathrm{tr}\,([J]) = -\frac{L}{A^*}\left(\overline{k} - \frac{B^* - A^*}{L} \right) = -\frac{L}{A^*}\left(\overline{k} - \overline{k}_{\mathrm{cr}} \right)$$

Now we can compare the eigenvalues $\lambda_{1,2}$ of the matrix $[Q]$ to unity. There are two cases:

- If $\mathrm{tr}\,([J]) > 0$, it corresponds either to the situation with steady-state velocity weakening ($B^* - A^* > 0$) or to the situation where the space discretization is too coarse (implies $\overline{k} < \overline{k}_{\mathrm{cr}}$). In this case, the eigenvalues have their absolute values larger than unity, and the perturbation grows regardless of the chosen time step ΔT. Thus, the only way to pass through the instability is to take into account inertial effects (or at least an approximation) to release the elastic energy accumulated.

- If $\mathrm{tr}\,([J]) < 0$, it corresponds either to the situation with steady-state velocity strengthening ($B^* - A^* < 0$) or steady-state velocity weakening with sufficiently small space step. In this case the eigenvalues can have their absolute values lower than unity and the perturbation can decay if the non-dimensional time step $\Delta T = V^*\Delta t/L$ is sufficiently small.

This leads to the following conditions on the time step which can be written with respect to $\overline{k}$ and $\overline{k}_{\mathrm{cr}}$.

Defining $\chi = \frac{1}{4}\mathrm{tr}\,([J])^2 - \frac{\overline{k}L}{A^*} = \frac{1}{4}\frac{B^* - A^*}{A^*}\left(\frac{\overline{k}}{\overline{k}_{\mathrm{cr}}} - 1 \right)^2 - \frac{\overline{k}}{\overline{k}_{\mathrm{cr}}}$, we have

$$\begin{aligned} &\text{If } \chi > 0,\ \Delta t < \frac{L}{V^*}\frac{A^*}{(B^* - A^*)(\overline{k}/\overline{k}_{\mathrm{cr}} - 1)} = \frac{L}{V^*}\xi_{\chi>0}, \\ &\text{If } \chi < 0,\ \Delta t < \frac{L}{V^*}\left(1 - \frac{\overline{k}}{\overline{k}_{\mathrm{cr}}} \right) = \frac{L}{V^*}\xi_{\chi<0}. \end{aligned} \tag{1.42}$$

Transposing the definition of $\overline{k} = G/h$ to $\overline{k}_{\text{cr}}$ allows to define a critical space step

$$h^* = \frac{GL}{\max[B^* - A^*]} \tag{1.43}$$

where the maximum is sought over all allowable values of $B^* - A^*$ and which quantifies the "sufficiently dense" space discretization criterion. h^* corresponds to the nucleation length L_{nuc}. In practice, to capture seismic slip as well as aseismic slip, the time step is finally chosen as

$$\Delta t = \min[\xi L/V]\,. \tag{1.44}$$

This point is very important as we do not want to confuse real instabilities with numerical artifacts, and we want to perform stable calculations.

3.2 Validation vs. verification of the simulations

Another challenge consists in the validation of the simulations as to our best knowledge, there is no existing analytical solution of seismic cycles problems as highlighted by Day et al. (2005) and Harris et al. (2009). As a response to this difficulty, there has been a recent initiative in the Earthquake cycle community to compare existing codes and provide code verification exercises (Harris et al., 2009; Erickson et al., 2020a) for simulating dynamic earthquake rupture and Sequences of Earthquakes and Aseismic Slip (SEAS). This project is funded by the SCEC (Erickson et al., 2020a) and is based on the preliminary work for the simulation of single earthquake ruptures detailed in Harris et al. (2009), Barall and Harris (2014) and Harris et al. (2018). This initiative has been extended to seismic cycles simulations for which seven Benchmarks are currently proposed. They consider a 1D or 2D planar fault in a 2D or 3D homogeneous, linear elastic half-space or infinite space eventually with along-fault fluid diffusion. For 2D problems, anti-plane shear motion of plane-strain motion is considered. Also, inertial effects are either partially neglected (Quasi-Dynamic model) or taken into account (Fully-Dynamic model). A rate-and-state friction law with either aging or slip law is used to model contact at the fault interface. These numerical tests allow to evaluate the numerical models proposed for the solving as well as evaluating some rupture phenomenon.

4 Mitigating the seismic risk using fluid injection?

Now that the seismic cycle community is active, we can go further in the modeling. A new and timely question in the community is to show that the earthquake instability could be avoided by active control of the fluid pressure. The challenge is here to understand the effects of an increase in fluid pressure on the frictional behavior of the fault, and to determine whether the equilibrium of the fault system under pore-pressure could go from unstable to stable.

4.1 Evidence of fault slip due to fluid injection

The presence of pore fluid in the earth crust plays an important role in fault mechanics and frictional ruptures. Nur and Booker (1972) and Booker (1974) suggested that pore

fluid flow induced by large earthquakes could contribute to aftershock activity. Sáez Uribe (2023) reviews studies on possible natural sources of fluid-driven frictional ruptures. They correspond to natural phenomena usually attributed to the migration of fluids in faults zones. Fluid-driven frictional ruptures can also have anthropogenic causes. The notion of fluid-injection induced earthquakes first emerged with the drill of a deep well at the Rocky Mountain Arsenal northeast of Denver, Colorado in 1961 to dispose contaminated waste water. Ellsworth (2013) reviews the understanding of the causes and mechanics of earthquakes caused by human activity and the possibility to mitigate their risk. In the present work, we are interested in earthquakes mitigation strategies which could ensure the security of subsurface engineering activities.

Several studies (reviewed by Stefanou (2019)) established the concept that pore pressure increase due to fluid injection can trigger fault slip. We can understand this affirmation by using the principal stress system as done by Kanamori and Brodsky (2004). Let us consider the case of a mode III strike-slip fault (infinitely long along $\mathbf{e}_2$ direction) for which anti-plane motion is assumed $\mathbf{u}(\mathbf{x}, t) = u_2(x_1, x_3, t)\mathbf{e}_2$ as an example. The stress state on either side of the fault is given as the sum of a normal pre-stress state (given by σ_0) and of the stress change due to anti-plane elastic displacement.

$$\boldsymbol{\sigma} = \begin{pmatrix} \sigma_0 & Gu_{2,1} & 0 \\ Gu_{2,1} & \sigma_0 & Gu_{2,3} \\ 0 & Gu_{2,3} & \sigma_0 \end{pmatrix} \tag{1.45}$$

Which leads to the following principal stress components $\sigma_1 = \sigma_0 + G\sqrt{u_{2,3}^2 + u_{2,1}^2}$ and $\sigma_3 = \sigma_0 - G\sqrt{u_{2,3}^2 + u_{2,1}^2}$. The corresponding expressions for the shear stress and normal stress on a fault plane at an angle θ to σ_1 are given by

$$\begin{aligned} \tau &= \frac{\sigma_1 - \sigma_3}{2}\sin(2\theta) = G\sqrt{u_{2,3}^2 + u_{2,1}^2}\sin(2\theta) \\ \sigma &= -\frac{\sigma_1 - \sigma_3}{2}\cos(2\theta) + \frac{\sigma_1 + \sigma_3}{2} = -G\sqrt{u_{2,3}^2 + u_{2,1}^2}\cos(2\theta) + \sigma_0 \end{aligned} \tag{1.46}$$

We can represent the two stresses given in (1.46) on a Mohr-circle diagram as represented by Figure 1.6. The normal stress is on the x-axis and the shear stress is on the y-axis. The values (σ, τ) are on a circle of center σ_0 and of radius $\tau_{max} = |\sigma_1 - \sigma_3|/2$. The angle $\angle OO'Q$ in the diagram is 2θ. On the same diagram, we can plot Amonton-Coulomb friction law $\tau = \mu\sigma$. In the presence of interstitial fluid, the effective normal stress on the fault plane changes and the friction law writes $\tau = \mu(\sigma - p)$, where p is the fluid pressure. For a large enough value of the pressure p the Mohr circle intersects the friction law line, which leads to failure at the fault plane. This simplified study allows us to understand the influence of fluid pressure on fault slip.

4.2 Earthquake mitigation strategies using fluid injection

Anthropogenic activities can trigger earthquakes. Understanding the mechanisms behind fluid induced fault slip is not only key to develop induced-earthquake mitigation strategies

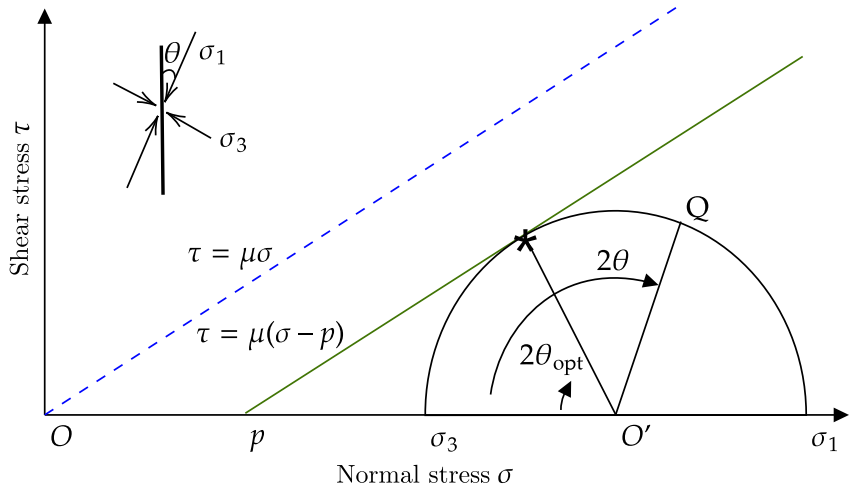

Figure 1.6 • Adapted from Kanamori and Brodsky (2004): Mohr circle diagram. Given principal stress magnitudes σ_1 and σ_3, possible combinations of shear and normal stresses resolved on a plane are given by Equation (1.46) which is plotted as the circle. The failure criterion $\tau = \mu\sigma$ is the dashed line. The failure criterion in the presence of pore fluid is the solid line $\tau = \mu(\sigma - p)$. Failure on a plane at an angle θ_{opt} from the orientation of σ_1 occurs at the $*$.

but also to determine if such studies could one day mitigate earthquakes of natural causes. The 1976 Rangeley experiment (Raleigh et al., 1976) suggested the possibility of earthquake mitigation strategies by controlling the pressure of the fluid injected in the Earth crust. As explained by Raleigh et al. (1976), they monitored pore fluid pressure by injecting and recovering water from wells drilled near the active seismic zone. Laboratory measurements were performed to determine frictional properties of reservoir rocks and in-situ stress measurement was conducted to deduce the value of fluid pressure required to trigger an earthquake. The idea that pore pressure variations could contribute to the stabilization of shear rupture zones against rapid propagation was mentioned by Rice (1973) and Palmer et al. (1997). Recently, Stefanou (2019) explored the possibility of stabilizing a reduced-order spring-slider model (in the spirit of the one presented in Section 1.2) by active control of the pressure of the fluid injected at the interface between the slider and the rigid surface. An experimental work, using absorbent porous paper to represent the fault, has recently been proposed by Tzortzopoulos (2021). His study is based on the idea that large earthquakes could be mitigated by inducing earthquakes of lower intensity (slow slip events). He proposed a control approach regarding the fluid pressure which allowed preventing laboratory earthquakes and drive the fault system aseismically to an equilibrium point of lower energy. Laboratory experiments combined with in-situ tests conducted by Guglielmi et al. (2015b) and Cappa et al. (2019) showed that the increase in fluid pressure induces a change in the friction behavior that promotes stable fault creep during fluid injection. These works give path to further numerical/experimental/in-situ experiments to investigate strategies to ensure the security of the subsurface engineering activities that require to inject large amounts of fluid in the earth's crust, running the risk to (re-)activate fault slip.

In this work, we are interested in choosing an adequate model to incorporate fluid effects

in the fault mechanics problem introduced in Section 2. Particularly, our objective is to investigate fluid-effects on a single fault for a fluid source at a chosen distance from the fault unlike the case of a fluid source located at the fault interface as it is mainly considered in the literature (Dunham and Rice (2008), Sáez Uribe (2023) among others).

4.3 Incorporating hydro-mechanical couplings

This question of modeling fluid-effects on fault-slip requires to change the model proposed in Section 2 to incorporate hydromechanical couplings. The difficulty is to determine an adequate model which could take into account the predominant fluid effects as well as it could be easily implemented in the numerical tools developed to simulate seismic cycles. The approach consists in modeling a porous medium to take into account the coupling between solid-deformation and variations in fluid-pressure. Rice and Cleary (1976) applies the Biot linearized theory of fluid infiltrated porous material (Biot, 1941; Biot, 1956b, 1956a) to incorporate the coupling between a rupturing solid and a variation of its pore-fluid pressure. This linearization is valid under the following assumptions Blanc (2013):

- the wavelength of the fluid perturbation is large in comparison with the characteristic radius of the pores;
- the amplitude of the perturbations in the solid and in the fluid are small: strain - displacement relations are chosen to be linear $\varepsilon^s_{ij} = \frac{1}{2}(u^s_{i,j} + u^s_{j,i})$, $\varepsilon^f_{kk} = u^f_{k,k}$;
- the single fluid phase is continuous;
- the solid matrix is purely elastic;
- the thermo-mechanical effects are neglected.

Particularly, the first assumption gives the validity range for linear balance momentum equation to characterize the homogeneous porous medium. In this case, it is assumed that the relative motion of fluid in the pores is of Poiseuille type. This is valid below a specific frequency, denoted f_c which depends on the depends on the kinematic viscosity of the fluid and on the size of the pores. In the low-frequency range the viscous boundary layer that develops in the fluid is large in comparison with the diameter of the pores, and the viscous efforts are proportional to the relative velocity of the motion between the fluid and solid components, which allows the linearization of the balance momentum equations. Carcione (2007) formally derive the equations in the low-frequency range as well as in the high-frequency range. Here, as in numerous geotechnics applications, we consider a poroelastodynamic problem in the low-frequency range instead of a fluid-structure interaction problem.

In Biot's poroelastodynamic equations (see for example Schanz (2009)), the balance momentum equation results in two equations with the unknowns solid displacement $\mathbf{u}^s$ and fluid displacement $\mathbf{u}^f$, and their dual $\boldsymbol{\sigma}^s$ and $\boldsymbol{\sigma}^f$. Thus, in the case of a linear, isotropic poroelastic medium, the balance momentum equation (1.20) for a (dry) fault mechanics

problem becomes

$$\begin{aligned}\sigma^s_{ij,j} + (1-\Phi) f^s_i &= (1-\Phi)\rho_s \ddot{u}^s_i - \rho_a\left(\ddot{u}^f_i - \ddot{u}^s_i\right) - \frac{\Phi^2}{k/\eta}\left(\dot{u}^f_i - \dot{u}^s_i\right)\\ \sigma^f_{,i} + \Phi f^f_i &= \Phi\rho_f \ddot{u}^f_i + \rho_a\left(\ddot{u}^f_i - \ddot{u}^s_i\right) + \frac{\Phi^2}{k/\eta}\left(\dot{u}^f_i - \dot{u}^s_i\right)\end{aligned} \tag{1.47}$$

where f^s_i (respectively f^f_i) correspond to body forces in the solid skeleton (respectively in the fluid), ρ_s is the solid density, ρ_f is the fluid density, ρ_a is the apparent mass density which depends on the tortuosity, $\Phi = V^f/V$ is the porosity which corresponds to the ratio between the volume of the interconnected pores contained in a sample of the bulk volume V, k is the fluid compressibility and η is the dynamic viscosity.

The partial balances given in (1.47) are completed by two constitutive laws. The first one is a modified version of the Hooke's law (1.22), and relates the total stress $\sigma_{ij} = \sigma^s_{ij} + \sigma^f \delta_{D_{ij}}$ with Biot's effective stress coefficient α, the solid displacement u^s_i and the pore pressure p

$$\sigma_{ij} = 2G\varepsilon^s_{ij} + \lambda\varepsilon^s_{ij}\delta_{D_{ij}} - \alpha\delta_{D_{ij}}p = \sigma^{\text{effective}}_{ij} - \alpha\delta_{D_{ij}}p \tag{1.48}$$

where $\alpha = 1 - K/K^s$, with K (respectively K^s) being the bulk modulus of the porous medium $K = \lambda + 2G/3$ (respectively to the solid skeleton), and p is positive in compression while σ_{ij} is positive in tension.

The second constitutive relation corresponds to the mass balance (continuity equation), which gives the variation in fluid volume per unit reference volume ζ

$$\begin{aligned}&\dot{\zeta} + q_{i,i} = 0,\\ &\text{where } \zeta = \alpha\varepsilon^s_{kk} + \frac{\Phi^2}{R}p,\ R = \frac{\Phi^2 K^f K^s}{K^f(K^s - K) + \Phi K^s(K^s - K^f)},\\ &\text{and } q_i = \Phi(\dot{u}^f_i - \dot{u}^s_i) = \dot{w}_i\end{aligned} \tag{1.49}$$

where R is a coupling modulus between the fluid and the solid phases, q_i is the specific flux, and w_i is the relative fluid-solid displacement.

> **Remark 1.3.** *In Cheng (2016), the modulus denoted M in (time-domain and frequency-domain) poroelastodynamic equations (9.92) to (9.103) of chapter 9 corresponds to R/Φ^2 in this dissertation, where we use notations from Schanz (2009).*

Considering the definition of the total stress, the bulk body force per unit volume $F_i = (1-\Phi) f^s_i + \Phi f^f_i$, the definition of the flux q_i and $\sigma^f = -\Phi p$, the partial balances from Equation (1.47) can rewrite as

$$\begin{aligned}\sigma_{ij,j} + F_i &= \rho_s(1-\Phi)\ddot{u}^s_i + \Phi\rho_f \ddot{u}^f_i\\ q_i = \dot{w}_i &= -\frac{k}{\eta}\left(p_{,i} + \frac{\rho_a}{\Phi}\left(\ddot{u}^f_i - \ddot{u}^s_i\right) + \rho_s \ddot{u}^f_i - f^f_i\right)\end{aligned} \tag{1.50}$$

where the second equation stands for the dynamic version of Darcy's law.

> **Remark 1.4.** *Usually, Darcy's law is presented in the form $q_i = -k/\eta p_{,i}$ disregarding body forces and in the case of a quasi-static fluid flow through interconnected pores (Detournay & Cheng, 1993). We consider the fully dynamic version of the equations here.*

An equivalent (and more adequate for our problem) formulation of the previous equations is a combination of the partial balances and of the constitutive equations in which the set of unknowns is the solid displacement u_i^s and the fluid pressure p. As detailed by Schanz (2009), this solid displacement - pore fluid pressure formulation can only be achieved in the Laplace domain. In fact, the relation between the relative fluid-solid displacement $w_i = u_i^f - u_i^s$ and the pore fluid pressure is nonlinear in the time domain, but becomes linear in the Laplace domain such that

$$\hat{w}_i = -\underbrace{\frac{k/\eta\rho_f\Phi^2 s^2}{\Phi^2 s + s^2 k/\eta(\rho_a + \Phi\rho_f)}}_{\beta(s)} \frac{1}{s^2\rho_f}\left(\hat{p}_{,i} + s^2\rho_f\hat{u}_i^s - \hat{f}_i^f\right) \tag{1.51}$$

where $\mathscr{L}\{f(t)\} = \hat{f}(s)$ denotes the Laplace transform with the complex variable s.

We obtain (in the Laplace domain) a modified version of Navier equations (1.23) incorporating pore-fluid effects

$$\begin{aligned} &G\hat{u}_{i,jj}^s + (\lambda+G)\hat{u}_{j,ij}^s - (\alpha-\beta(s))\hat{p}_{,i} - s^2(\rho-\beta(s)\rho_f)\hat{u}_i^s = \beta(s)\hat{f}_i^f - \hat{F}_i \\ &\frac{\beta(s)}{s\rho_f}\hat{p}_{,ii} - \frac{\Phi^2 s}{R}\hat{p} - (\alpha-\beta(s))s\hat{u}_{i,i}^s = \frac{\beta(s)}{s\rho_f}\hat{f}_{i,i}^f \end{aligned} \tag{1.52}$$

In addition to the momentum balance equations, the change in the pore-fluid pressure has to be considered at the fault interface. Traction at the pre-existing discontinuity is governed by Terzaghi's effective stress. The effective traction vector $\mathbf{t}'$ is defined as

$$t_i'(\mathbf{x},t) = t_i(\mathbf{x},t) - \delta_{i1}p(\mathbf{x},t) \tag{1.53}$$

where $\mathbf{t}$ denotes the total traction vector, δ_{ij} is the Kronecker delta, and '1′ corresponds to the component that is normal to the fault at $\mathbf{x}$ is '2′ and '3′ are assumed to represent the two tangential (shear) components, orthogonal with each other.

If we use complete poroelastodynamic equations and reformulate the volume problem as a BIE on the fault only, we obtain two boundary integral equations (Chen, 1994b, 1994a). They are written as convolutions in time and space, linking the shear stress with the displacement discontinuity and the pore-fluid pressure with the displacement discontinuity. The determination of these boundary integral equations relies on fundamental solutions of the poroelastodynamic equations in response to a unit force applied to the solid phase and on the fundamental solutions of poroelastodynamic equations in response to a unit source applied to the fluid phase. Senjuntichai and Rajapakse (1994), Zheng et al. (2013) derived fundamental solutions for poroelastodynamic equations considering time-harmonic solutions, whereas Manolis and Beskos (1989), Manolis and Beskos (1990), Chen (1994b), Chen (1994a) derived fundamental solutions in the Laplace domain. Theoretically, both methods are convenient, but numerically, they would require to evaluate an inverse Fourier

transform, or an inverse Laplace transform in time with varying time steps due to the time integration methods inspired by seismic cycles simulations we implemented. We want to avoid such a difficulty for a first case incorporating hydro-mechanical couplings.

Simplified poroelastodynamic equations (one way-coupling equations taking into account the effect of pore-fluid variations on the solid deformation only) have mainly been used in the literature to study slow-slip events triggered by fluid injection. Segall and Rice (1995), Bhattacharya and Viesca (2019), Dublanchet (2019), Larochelle et al. (2021), Sáez et al. (2022) assume that the pore fluid pressure satisfies a diffusion equation. Segall and Lu (2015) investigates the effect on injection-induced seismicity of a full poroelastic coupling in quasi-static. Heimisson et al. (2019), Heimisson et al. (2021), Heimisson et al. (2022) consider the effect of slip changes the pore pressure. Notably, he studied the case of a plane-strain-loaded planar fault embedded in a linear isotropic poroelastic half-space submitted to a fluid injection point source on the fault. The solution of simplified poroelastodynamic equations in the Fourier domain in space and in the Laplace domain in time based on the method from Morrissey and Geubelle (1997) combined with the use of Biot potentials as explained in Detournay and Cheng (1993), allows to obtain the boundary integral equations in time and space in the particular case of a plane-strain-loaded planar fault.

2

Numerical methods to simulate fast and slow slips in 2D configurations with planar faults

Contents

1 Problem formulation at the continuous level : key assumptions 44

1.1 Boundary Integral Equations for fault problems 46

1.2 Interface problems for mode II and mode III planar-fault configurations 57

2 Space discretization of the boundary integral equation 59

2.1 Spectral Boundary Element Method for a planar discontinuity 62

2.2 Fast Boundary Element Method based on Hierarchical matrices 63

2.3 Comparison between the two approaches 67

3 Time discretization 67

3.1 Main time stepping methods implemented 67

3.2 A priori theoretical comparison of the different numerical methods . . 71

4 Convergence assessment 72

4.1 Proposition of a configuration with an analytical aseismic solution . . 72

4.2 Methodology for the convergence study 75

4.3 Accuracy of one calculation of the shear-stress change τ^{qs} 76

4.4 Convergence in time 82

5 Numerical test on a seismic cycle benchmark 91

6 Summary of the qualities and drawbacks of space and time discretization/integration methods 96

In this chapter, we develop a boundary-element based solver for frictional slip along a pre-existing planar discontinuity embedded in a two-dimensional linear elastic (half-)space. Mode II and mode III configurations can be considered. A regularized rate-and-state friction law is imposed at the fault interface. The fault dynamics is determined by solving the equations resulting from the combination of the elastodynamic equations with the constitutive friction law, plus boundary conditions, conditions at infinity and initial conditions. From a modeling viewpoint, it is worth mentioning that in this work, we consider that inter-seismic, co-seismic and post-seismic phases occur on pre-existing discontinuities. We do not consider the creation of new fracture that would be described by additional damage and fracture propagation. We define the transition from inter-seismic to co-seismic phases as an unstable equilibrium state characterized by a loss of adhesion and the propagation of a brutal slip over the fault interface. The latter is a friction problem. In the literature, the vocabulary used may be ambiguous as it refers to "fault rupture" when a seismic event occurs. Particularly, Andrews (1976) established that well-established fact that the frictional slip is a form of fracture. This concept is also very well explained by Fineberg and Bouchbinder (2015), Cambonie et al. (2018), and Roch et al. (2022b). Different numerical methods which use boundary element methods (BEMs) to solve fault slip problems exist. The choices regarding the geometry, the continuum and material properties, interface and boundary conditions are summarized in Chapter 1, Section 1.2. We consider two space discretization techniques using either a spectral boundary element method or a collocation boundary element method. For the latter, a data-sparse approximation of the resulting dense boundary element matrix is computed through a hierarchical low-rank approximation technique. We implemented three different methods for time integration. The first one is based on a hybrid explicit-implicit prediction-correction method inspired by Lapusta et al. (2000). The second time-stepping method is based on an explicit fourth/fifth order adaptive time step Runge-Kutta method inspired by Ozawa et al. (2022). And the third one is a hybrid prediction-correction / adaptive time step Runge-Kutta method inspired by Romanet and Ozawa (2021). These methods are not new, but the objectives of this chapter are:

- to assess the capabilities of the different solving methods implemented
- to assess the sensitivity of the different numerical methods implemented to their parameters
- to determine the most performing numerical tools among the methods proposed before complexifying our problem incorporating hydro-mechanical couplings.

1 Problem formulation at the continuous level : key assumptions

The details of the problem statement in both generic and simplified configurations have been derived in Section 2 from Chapter 1. Here we focus on a more specific description of the simplified mode II and mode III configurations that can be handled with a boundary-element based solver. These planar-fault configurations allow to compare different solving

methods in space and time in order to determine the performing numerical tools to solve seismic cycle problems which would be adapted to more complex problems incorporating hydromechanical couplings.

Consider a Cartesian reference system $[\mathbf{0},\mathbf{x},\mathbf{y},\mathbf{z}]$ and its corresponding coordinate system $[\mathbf{0},x,y,z]$. Let Ω be an infinite (respectively semi-infinite) homogeneous, linear, elastic, isotropic medium containing a planar discontinuity Γ at $x=0$, in the $(\mathbf{y},\mathbf{z})$ plane. The geometry of the fault is assumed to be invariant along $\mathbf{y}$ and $\mathbf{z}$ directions. In cases where we consider a planar fault in a semi-infinite space, the fault geometry is invariant along the $\mathbf{y}$ direction only and the fault is assumed to be perpendicular to the free surface $\partial\Omega$. As frictional properties are assumed to vary only at depth, we can consider a two-dimensional problem, where the fault is an infinitely long line along the $\mathbf{z}$ direction embedded in a two-dimensional space $(\mathbf{x},\mathbf{y})$. Figure 2.1 represents two typical planar faults problems, with a mode II (left) or mode III (right) loading imposed, considered in this chapter.

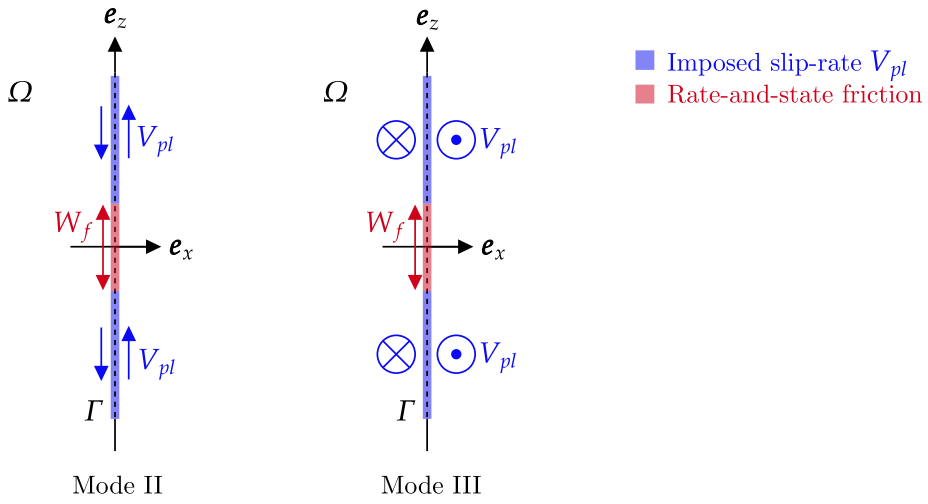

Figure 2.1 • Problems considered: planar fault embedded in a homogeneous, linear, elastic, isotropic infinite space. For each case, the fault is governed by rate-and-state friction on the fault width W_f and is loaded in mode II or III with a constant creep rate V_{pl} to the infinite depth.

We impose shear motion on either side of the fault such that anti-plane motion or in-plane motion with a no-opening condition (no displacement discontinuity at the fault interface in the normal displacement component). We define the only non-vanishing displacement discontinuity component for mode II or III across the fault as

$$\delta(z,t) = u(x=0^+,z,t) - u(x=0^-,z,t), \text{ on } \Gamma \tag{2.1}$$

where $u(x=0^+,z,t)$ and $u(x=0^-,z,t)$ are the displacement components along the $\mathbf{y}$ direction for mode III (respectively $\mathbf{z}$ direction for mode II) at the upper Γ^+ and lower Γ^- faces, and t is the time. The balance momentum equation satisfied in the mode II case and in the mode III case are given in Table 1.1.

Now we want to reformulate the balance momentum equation satisfied in Ω as an integral equation on the fault interface Γ using Boundary Integral Equations. We first detail the

method for the generic case of a fault of arbitrary shape embedded in an infinite elastic medium before deriving the corresponding equations for the simplified mode II and mode III planar-fault configurations.

1.1 Boundary Integral Equations for fault problems

In this part, we detail how to model the fault mechanics problem with Boundary Integral Equations (BIE). We illustrate this approach with the case of an infinite linear elastic isotropic space Ω containing a discontinuity Γ (or fault) of arbitrary shape (detailed by Bonnet (1999)). The two crack faces Γ^+ and Γ^- are geometrically identical such that $\Gamma = \Gamma^+ = \Gamma^-$ and have opposite unit normal vectors $\mathbf{n}^+ = -\mathbf{n}^-$, which point towards the exterior of the medium. The fault faces are loaded by tractions $\mathbf{t}^{D\pm}$. These imposed traction components are assumed to result from a given load applied far enough from the fault.
We use the Boundary Integral Equation Method (BIEM).

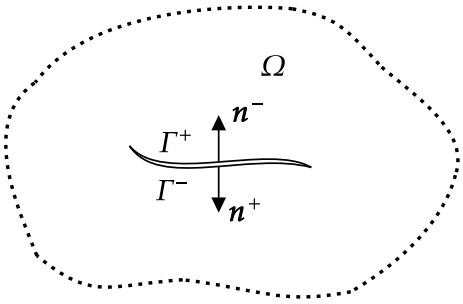

Figure 2.2 • Fault (Γ) of arbitrary shape embedded in an infinite space Ω. Fault faces Γ^+ and Γ^- have opposite normal vectors $\mathbf{n}^+ = -\mathbf{n}^-$.

We need first to derive the displacement integral representation for the fault mechanics problem as detailed by Bonnet (1999), Aki and Richards (2002), and Udías et al. (2014).

Displacement integral representation. For the sake of simplicity, we neglect inertial effects in first approximation. For any elastic state $(\mathbf{u}, \boldsymbol{\sigma})$ satisfying (1.20),(1.21),(1.22), and any virtual displacement field $\mathbf{u}'$ continuously differentiable over Ω, the virtual work principle writes

$$\int_\Omega \boldsymbol{\sigma} : \boldsymbol{\varepsilon}(\mathbf{u}')\, dV - \int_\Gamma (\boldsymbol{\sigma}\mathbf{n}) \cdot \mathbf{u}'\, dS - \int_\Omega \rho \mathbf{F} \cdot \mathbf{u}'\, dV = 0. \tag{2.2}$$

We take two elastic states (one for the unknown and another for the virtual displacement) $(\mathbf{u}^1, \boldsymbol{\sigma}^1, \mathbf{F}^1)$ and $(\mathbf{u}^2, \boldsymbol{\sigma}^2, \mathbf{F}^2)$, apply (2.2) to each and take the difference using the symmetry of the elastic constitutive law

$$\boldsymbol{\sigma}^1 : \boldsymbol{\varepsilon}(\mathbf{u}^2) = \boldsymbol{\sigma}^2 : \boldsymbol{\varepsilon}(\mathbf{u}^1), \tag{2.3}$$

we obtain the Maxwell-Betti reciprocity relation

$$\int_\Gamma \left[(\boldsymbol{\sigma}^1 \mathbf{n}) \cdot \mathbf{u}^2 - (\boldsymbol{\sigma}^2 \mathbf{n}) \cdot \mathbf{u}^1 \right] dS = \int_\Omega \left[\rho \mathbf{F}^2 \cdot \mathbf{u}^1 - \rho \mathbf{F}^1 \cdot \mathbf{u}^2 \right] dV. \tag{2.4}$$

Boundary integral representations use a fundamental solution. The elastostatic fundamental solution $(\mathbf{U}^k, \boldsymbol{\Sigma}^k, \mathbf{F}^k)$ is associated to a point force of unit magnitude, which is applied at a given fixed point $\mathbf{x} \in \mathbb{R}^3$ along the k-direction, and satisfies

$$\begin{aligned} \rho \mathbf{F}^k(\mathbf{y}) &= \delta_{\mathrm{D}}(\mathbf{y}-\mathbf{x})\mathbf{e}_k \\ \Sigma^k_{ij,j}(\mathbf{x},\mathbf{y}) + \delta_{\mathrm{D}}(\mathbf{y}-\mathbf{x})\delta_{ik} &= \mathbf{0} \end{aligned} \tag{2.5}$$

where δ_{D} is the Dirac distribution, $\mathbf{y}$ is the field point, $\mathbf{x}$ is the source point, k is the direction of the load, $U^k_i(\mathbf{x},\mathbf{y})$ and $\Sigma^k_{ij}(\mathbf{x},\mathbf{y})$ are respectively components of the fundamental displacement vector $\mathbf{U}^k(\mathbf{x},\mathbf{y})$ and of the fundamental stress tensor $\boldsymbol{\Sigma}^k(\mathbf{x},\mathbf{y})$. $\boldsymbol{\Sigma}^k$ is at equilibrium with $\mathbf{F}^k$ and is related to $\mathbf{U}^k$ through the Hooke's law.

$$\Sigma^k_{ij}(\mathbf{x},\mathbf{y}) = C_{ijab} U^k_{a,b}(\mathbf{x},\mathbf{y}) \tag{2.6}$$

$\mathbf{T}^k$ is the traction vector of the fundamental solution for elastostatics.

$$T^k_i(\mathbf{x},\mathbf{y}) = \Sigma^k_{ij}(\mathbf{x},\mathbf{y}) n_j(\mathbf{y}) \tag{2.7}$$

Then, we apply the Maxwell-Betti theorem to the unknown state $(\mathbf{u}, \boldsymbol{\sigma}, \mathbf{0})$ (we neglect body forces) and to the fundamental solution for linear elastostatics $(\mathbf{U}^k, \boldsymbol{\Sigma}^k, \mathbf{F}^k)$ in the sense of distributions. We obtain the integral representation formula for the unknown displacement

$$u_k(\mathbf{x}) = \int_\Gamma \left\{ t_i(\mathbf{y}) U^k_i(\mathbf{x},\mathbf{y}) - u_i(\mathbf{y}) T^k_i(\mathbf{x},\mathbf{y}) \right\} dS_y, \ \forall \mathbf{x} \notin \Gamma. \tag{2.8}$$

We develop (2.8) on the crack faces

$$\begin{aligned} u_k(\mathbf{x}) = &\int_{\Gamma^+} \left\{ t^+_i(\mathbf{y}) U^k_i(\mathbf{x},\mathbf{y}) - u^+_i(\mathbf{y}) \left(\Sigma^k_{ij}(\mathbf{x},\mathbf{y}) n_j(\mathbf{y}) \right)^+ \right\} dS_y \\ &+ \int_{\Gamma^-} \left\{ t^-_i(\mathbf{y}) U^k_i(\mathbf{x},\mathbf{y}) - u^-_i(\mathbf{y}) \left(\Sigma^k_{ij}(\mathbf{x},\mathbf{y}) n_j(\mathbf{y}) \right)^- \right\} dS_y \\ \underset{\mathbf{n}=\mathbf{n}^-=-\mathbf{n}^+}{=} &\int_\Gamma \{ \underbrace{(u^+_i(\mathbf{y}) - u^-_i(\mathbf{y}))}_{\boldsymbol{\delta}(\mathbf{y})} T^k_i(\mathbf{x},\mathbf{y}) + \underbrace{(t^+_i(\mathbf{y}) + t^-_i(\mathbf{y}))}_{\boldsymbol{\Psi}(\mathbf{y})} U^k_i(\mathbf{x},\mathbf{y}) \} dS_y \ \forall \mathbf{x} \notin \Gamma. \end{aligned} \tag{2.9}$$

We introduce $\boldsymbol{\delta} = \mathbf{u}^+ - \mathbf{u}^-$, the displacement discontinuity across Γ, and $\boldsymbol{\Psi} = \mathbf{t}^+ + \mathbf{t}^-$, the traction discontinuity across Γ and $\left(\Sigma^k_{ij}(\mathbf{x},\mathbf{y}) n_j(\mathbf{y}) \right)^\pm = \Sigma^k_{ij}(\mathbf{x},\mathbf{y}) n^\pm_j(\mathbf{y})$. The displacement representation formula for the case of an infinite medium containing a fault finally writes

$$u_k(\mathbf{x}) = \int_\Gamma \left\{ \delta_i(\mathbf{y}) T^k_i(\mathbf{x},\mathbf{y}) + \Psi_i(\mathbf{y}) U^k_i(\mathbf{x},\mathbf{y}) \right\} dS_y, \ \forall \mathbf{x} \in \Omega \backslash \Gamma. \tag{2.10}$$

The first term is in the form of a double layer potential $\mathscr{D}\delta_i(\mathbf{x})$, whereas the second term is a single layer potential $\mathscr{S}\Psi_i(\mathbf{x})$, where we have used the notations

$$\begin{aligned} \mathscr{D}\delta_i(\mathbf{x}) &= \int_\Gamma \delta_i(\mathbf{y}) T^k_i(\mathbf{x},\mathbf{y}) dS_y, \ \forall \mathbf{x} \notin \Gamma, \\ \mathscr{S}\Psi_i(\mathbf{x}) &= \int_\Gamma \Psi_i(\mathbf{y}) U^k_i(\mathbf{x},\mathbf{y}) dS_y, \ \forall \mathbf{x} \notin \Gamma. \end{aligned} \tag{2.11}$$

Using Trace theorems on Γ^+ (respectively Γ^-), using the convention $\mathbf{n} = \mathbf{n}^-$ for the unit normal vector, we have

$$\begin{aligned}(\mathscr{D}\delta_i)^{\pm}(\mathbf{x}) &= \pm\frac{1}{2}\delta_i(\mathbf{x}) + D\delta_i(\mathbf{x}) \text{ discontinuity of the double-layer potential } \forall \mathbf{x}\in\Gamma \\ (\mathscr{S}\Psi_i)^{\pm}(\mathbf{x}) &= S\Psi_i(\mathbf{x}) \text{ continuity of the single-layer potential } \forall \mathbf{x}\in\Gamma\end{aligned} \tag{2.12}$$

where

$$\begin{aligned}D\delta_i(\mathbf{x}) &= \int_\Gamma \delta_i(\mathbf{y}) T_i^k(\mathbf{x},\mathbf{y}) dS_y, \ \forall \mathbf{x}\in\Gamma, \\ S\Psi_i(\mathbf{x}) &= \int_\Gamma \Psi_i(\mathbf{y}) U_i^k(\mathbf{x},\mathbf{y}) dS_y, \ \forall \mathbf{x}\in\Gamma.\end{aligned} \tag{2.13}$$

$D\delta_i(\mathbf{x})$ is a singular integral and is defined in the sense of Cauchy Principal Value (CPV) as in 3D, it behaves like $|\mathbf{y}-\mathbf{x}|^{-2}$ and takes singular values when $\mathbf{x}=\mathbf{y}$. Applying the Trace theorem (2.12) on side $\Gamma^{\pm}$ to (2.10), the singular integral $D\delta_i(\mathbf{x})$ appears. Thus, a regularized version of the displacement BIE is required on the fault Γ. We use a rigid body identity (Bonnet, 1999) to regularize

$$\frac{1}{2}\left(u_k^+ + u_k^-\right) = \delta_i(\mathbf{x}) K_i^k(\mathbf{x},\Gamma) + \int_\Gamma \left\{(\delta_i(\mathbf{y}) - \delta_i(\mathbf{x})) T_i^k(\mathbf{x},\mathbf{y}) + \Psi_i(\mathbf{y}) U_i^k(\mathbf{x},\mathbf{y})\right\} dS_y, \ \forall \mathbf{x}\in\Gamma \tag{2.14}$$

where $K_i^k(\mathbf{x},\Gamma) = \int_\Gamma T_i^k(\mathbf{x},\mathbf{y}) dS_y$ allows to regularize the BIE.

Now, let $\mathbf{u}_0$ be a uniform displacement field in the volume Ω, continuous across the fault Γ, yielding to a uniform traction $\mathbf{t^0}$ applied on the crack faces $\Gamma^{\pm}$. Since (2.14) does not change when the loading applied to the crack faces is $\mathbf{t}^{\pm}+\mathbf{t}^0$ instead of $\mathbf{t}^{\pm}$, and introducing $\Delta\mathbf{u} = \mathbf{u}-\mathbf{u}_0$, (2.14) writes

$$\frac{1}{2}\left(\Delta u_k^+ + \Delta u_k^-\right) = \delta_i(\mathbf{x}) K_i^k(\mathbf{x},\Gamma) + \int_\Gamma (\delta_i(\mathbf{y}) - \delta_i(\mathbf{x})) T_i^k(\mathbf{x},\mathbf{y}) dS_y, \ \forall \mathbf{x}\in\Gamma \tag{2.15}$$

(2.15) degenerates in the form $\mathscr{L}\Delta u = 0$ where $\mathscr{L}$ is a linear operator, and we have assumed a symmetrically loaded crack such that $\mathbf{\Psi} = 0$. Such a homogeneous equation has an infinite number of solutions and cannot be exploited to solve the problem of an infinite linear, elastic, isotropic medium containing a crack. Fault mechanic problems are similar to screens problems. In both situations, Bonnet (1999) emphasizes the inapplicability of the displacement (respectively temperature for screens problems) Boundary Integral Equation.

> **Remark 2.1.** *In the particular case of a planar crack in an anisotropic infinite 2D medium or finite plate, displacement and traction fundamental solution are given analytically by Snyder and Cruse (1975). In this case, the displacement boundary integral equation can be used.*

Traction Boundary Integral Equation. One way to avoid this is to use a BIE based on representations for stresses as proposed by Bonnet (1999) (chapter 13). By differentiating (2.9) with respect to $\mathbf{x}$, we can deduce the representation formula for the displacement gradient:

$$u_{k,l}(\mathbf{x}) = \int_\Gamma \left\{t_a(\mathbf{y}) U^k_{a,\bar{l}}(\mathbf{x},\mathbf{y}) - u_a(\mathbf{y}) n_b(\mathbf{y}) \Sigma^k_{ab,\bar{l}}(\mathbf{x},\mathbf{y})\right\} dS_y, \ \forall \mathbf{x}\notin\Gamma, \tag{2.16}$$

where $f_{,\bar{l}}(\mathbf{x},\mathbf{y})$ denotes the partial derivative of f with respect to the l-coordinate of its first argument, the source point $\mathbf{x}$. Kelvin fundamental solution for isotropic infinite elastic medium has the following symmetry properties for all $\mathbf{x},\mathbf{y}$ in the volume Ω

$$U^k_{i,\bar{l}}(\mathbf{x},\mathbf{y}) = -U^k_{i,l}(\mathbf{x},\mathbf{y}) \quad \Sigma^k_{ij,\bar{l}}(\mathbf{x},\mathbf{y}) = -\Sigma^k_{ij,l}(\mathbf{x},\mathbf{y}) \tag{2.17}$$

Using (2.17) in (2.16) plus an integration by part step yields

$$u_{k,l}(\mathbf{x}) = \int_\Gamma \left\{ D_{lb} u_a(\mathbf{y}) \Sigma^k_{ab}(\mathbf{x},\mathbf{y}) - t_a(\mathbf{y}) U^k_{a,l}(\mathbf{x},\mathbf{y}) \right\} dS_y, \ \forall \mathbf{x} \notin \Gamma \tag{2.18}$$

where we have introduced the differential operator $D_{lb}() = n_l()_{,b} - n_b()_{,l}$.

> **Remark 2.2.** (2.16) *is hypersingular as* $\Sigma^k_{ab,\bar{l}}(\mathbf{x},\mathbf{y})$ *is singular like* $|\mathbf{y}-\mathbf{x}|^{-3}$. (2.18) *is only singular as it involves only kernels behaving like* $|\mathbf{y}-\mathbf{x}|^{-2}$. *Therefore, we choose to explain the method to derive the traction BIE to solve the problem of an infinite medium containing a fault using* (2.18) *that is less singular.*

Regularized formulation. Even if (2.18) is less singular, it still requires to be regularized to be expressed as a weakly singular integral. Regularization using integration by part has been detailed by Tada and Yamashita (1996, 1997) for 2D anti-plane and in-plane strain configurations that are considered in this work. After the regularization step, a limiting process is used to go from the representation formula to the corresponding boundary integral equation.

A proper formulation of the limiting process then consists in introducing an exclusion neighborhood $v_\varepsilon(\mathbf{x})$ removed from Ω (as represented on Figure 2.3) such that

$$\Omega_e(\mathbf{x}) = \Omega - v_\varepsilon(\mathbf{x}), \quad \Gamma_\varepsilon = (\Gamma - e_\varepsilon) + s_\varepsilon, \quad s_\varepsilon = \Omega \cap \partial v_\varepsilon, \quad e_\varepsilon = \Gamma \cap v_\varepsilon \tag{2.19}$$

Thus, the integral representation formula for the displacement gradient is defined as the

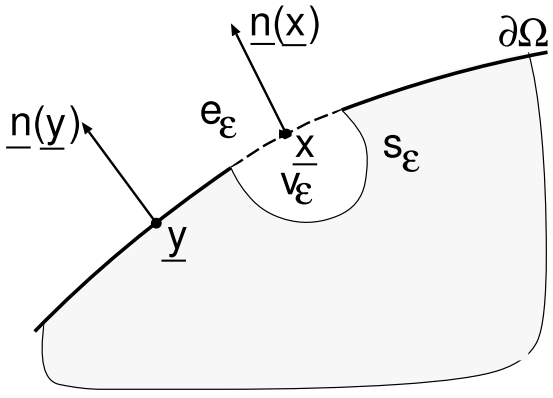

Figure 2.3 • Figure from Bonnet (1999), introduction of an exclusion neighborhood for a proper formulation of the limiting process.

limiting form for $\varepsilon \to 0$ of (2.18) with $\mathbf{x} \notin \Omega_\varepsilon$, i.e.,

$$0 = \int_{(\Gamma - e_\varepsilon)+s_\varepsilon} \left\{ D_{lb} u_a(\mathbf{y}) \Sigma^k_{ab}(\mathbf{x},\mathbf{y}) - t_a(\mathbf{y}) U^k_{a,l}(\mathbf{x},\mathbf{y}) \right\} dS_y, \ \forall \mathbf{x} \notin \Omega_e. \tag{2.20}$$

In order to regularize (2.20), a particular elastostatic state u^* is introduced, of the form

$$u_a^*(\mathbf{y}) = u_a^0 + a_{ac}(y_c - x_c), \quad t_i(\mathbf{y}) = C_{ijab} n_j(\mathbf{y}) a_{ab}. \tag{2.21}$$

It corresponds to the superposition of a rigid body translation and a uniform strain, with u_i^0, a_{ij} being arbitrary constants. The constants in $\mathbf{u}^*$ are chosen equal to the unknown displacement and displacement gradient at the source point $\mathbf{x}$, $\{\mathbf{u}^0, \mathbf{a}\} = \{\mathbf{u}(\mathbf{x}), \boldsymbol{\nabla}\mathbf{u}(\mathbf{x})\}$. Applying (2.20) to the chosen elastostatic state $\mathbf{u}^*$, doing the difference with (2.20) and assuming that u_i has $\mathscr{C}^{1,\alpha}$ smoothness, we can conclude in the limit $\varepsilon \to 0$. After applying Hooke's law, the following weakly singular (i.e. convergent) integral representation formula for the stress is obtained

$$\begin{aligned}\frac{1}{2}\sigma_{ij}(\mathbf{x}) = {} & C_{ijkl}\int_\Gamma \left[D_{lb}u_a(\mathbf{y}) - D_{lb}u_a(\mathbf{x})\right]\Sigma_{ab}^k(\mathbf{x},\mathbf{y})dS_y \\ & - \int_\Gamma \left[t_a(\mathbf{y}) - t_a(\mathbf{x})\right]\Sigma_{ij}^a(\mathbf{x},\mathbf{y})dS_y + D_{lb}u_a(\mathbf{x})C_{ijkl}A_{ab}^k(\mathbf{x},\Gamma) - t_a(\mathbf{x})A_{ij}^a(\mathbf{x},\Gamma)\end{aligned}, \ \forall \mathbf{x} \notin \Gamma \tag{2.22}$$

where $A_{ij}^k(\mathbf{x},\Gamma) = \int_\Gamma \Sigma_{ij}^k(\mathbf{x},\mathbf{y})dS_y$. It can be reformulated in terms of weakly singular integrals by an integration by part. (2.22) does not allow to take into account the coupling between the displacement and stress field quantities $(\mathbf{u},\sigma)$ on each fault face. In our case, we model the fault as a discontinuity under a friction constitutive law, which is different from considering the fault faces as boundaries with Neumann boundary conditions. To take into account the coupling induced by the friction interface condition, we use the displacement discontinuity approach detailed by Bonnet (1999) (section 13.3). We introduce two volumes Ω^+ and Ω^- by introducing the surface $\tilde{\Gamma}$, such that $\Gamma \cup \tilde{\Gamma}$ enclosed Ω^- and that $\Omega^+ = \mathbb{R}^3 - \Omega^-$. The closed smooth surface $\Gamma \cup \tilde{\Gamma}$ is of exterior unit normal $\mathbf{n}$. Writing (2.22) for a point $\mathbf{x}$ located on the fault surface and relative to each subdomain $\Omega^\pm$ and adding the resulting identities gives

$$\begin{aligned}\frac{1}{2}\left[\sigma_{ij}^+ + \sigma_{ij}^-\right](\mathbf{x}) = {} & -C_{ijkl}\int_{\Gamma\cup\tilde{\Gamma}} \left[D_{lb}\delta_a(\mathbf{y}) - D_{lb}\delta_a(\mathbf{x})\right]\Sigma_{ab}^k(\mathbf{x},\mathbf{y})dS_y \\ & - \int_{\Gamma\cup\tilde{\Gamma}} \left[\Psi_k(\mathbf{y}) - \Psi_k(\mathbf{x})\right]\Sigma_{ij}^k(\mathbf{x},\mathbf{y})dS_y - C_{ijkl}A_{ab}^k(\mathbf{x},\Gamma\cup\tilde{\Gamma})D_{lb}\delta_a(\mathbf{x}) - \Psi_k(\mathbf{x})A_{ij}^k(\mathbf{x},\Gamma\cup\tilde{\Gamma})\end{aligned}, \ \forall \mathbf{x} \in \Gamma \tag{2.23}$$

where $\delta_i = u_i^+ - u_i^-$ is the displacement discontinuity across $\Gamma\cup\tilde{\Gamma}$, $\Psi_i = t_i^+ + t_i^-$ is the traction discontinuity across $\Gamma\cup\tilde{\Gamma}$, and D_{lb} refers to the normal $\mathbf{n} = \mathbf{n}^-$. Knowing that the displacement field and the traction components are continuous across $\tilde{\Gamma}$, that $A_{ab}^k(\mathbf{x},\Gamma\cup\tilde{\Gamma}) = A_{ab}^k(\mathbf{x},\Gamma) + A_{ab}^k(\mathbf{x},\tilde{\Gamma})$ and that the global equilibrium is satisfied on $\tilde{\Gamma}$ we obtain

$$\begin{aligned}\frac{1}{2}\left[\sigma_{ij}^+ + \sigma_{ij}^-\right](\mathbf{x}) = {} & -C_{ijkl}\int_\Gamma \left[D_{lb}\delta_a(\mathbf{y}) - D_{lb}\delta_a(\mathbf{x})\right]\Sigma_{ab}^k(\mathbf{x},\mathbf{y})dS_y \\ & - \int_\Gamma \left[\Psi_k(\mathbf{y}) - \Psi_k(\mathbf{x})\right]\Sigma_{ij}^k(\mathbf{x},\mathbf{y})dS_y - C_{ijkl}A_{ab}^k(\mathbf{x},\Gamma)D_{lb}\delta_a(\mathbf{x}) - \Psi_k(\mathbf{x})A_{ij}^k(\mathbf{x},\Gamma)\end{aligned}, \ \forall \mathbf{x} \in \Gamma \tag{2.24}$$

To obtain the traction BIE, we take the product of (2.24) by the unit normal vector $\mathbf{n} = \mathbf{n}^-$. Denoting $\mathbf{t}^D = \mathbf{t}^{D-}$, we get

$$\frac{1}{2}\left[\sigma_{ij}^+ + \sigma_{ij}^-\right](\mathbf{x})n_j(\mathbf{x}) = t_i^D(\mathbf{x}) - \frac{1}{2}\Psi_i(\mathbf{x}), \ \forall \mathbf{x} \in \Gamma. \tag{2.25}$$

It leads to the traction BIE

$$\begin{aligned} t_i^D(\mathbf{x}) = &-n_j(\mathbf{x})C_{ijkl}A_{ab}^k(\mathbf{x},\Gamma)D_{lb}\delta_a(\mathbf{x}) - \Psi_k(\mathbf{x})\left(A_{ij}^k(\mathbf{x},\Gamma) - \frac{1}{2}\delta_{\mathrm{D}_{ik}}\right) \\ &- n_j(\mathbf{x})C_{ijkl}\int_\Gamma \left[D_{lb}\delta_a(\mathbf{y}) - D_{lb}\delta_a(\mathbf{x})\right]\Sigma_{ab}^k(\mathbf{x},\mathbf{y})dS_y - n_j(\mathbf{x})\int_\Gamma \left[\Psi_k(\mathbf{y}) - \Psi_k(\mathbf{x})\right]\Sigma_{ij}^k(\mathbf{x},\mathbf{y})dS_y \end{aligned} \quad , \forall \mathbf{x} \in \Gamma \tag{2.26}$$

Simplifications in 2D cases. From (2.26), we can derive the traction BIE in the case of a planar crack, subjected to symmetrical loading, in an infinite medium for the mode II-III situation. In this case, the fault surface lies in the $(\mathbf{e}_2, \mathbf{e}_3)$ plane. For any two points $\mathbf{x}, \mathbf{y}$ of Γ, one has

$$\begin{aligned} &\mathbf{n}(\mathbf{x}) = \mathbf{n}(\mathbf{y}) = \mathbf{e}_1, \quad r_{,1} = r_{,n} = \frac{y_1 - x_1}{|\mathbf{y}-\mathbf{x}|} = 0, \quad D_{lb}f = \delta_{\mathrm{D}_{l1}}f_{,b} - \delta_{\mathrm{D}_{b1}}f_{,l}, \\ &\mathbf{\Psi} = \mathbf{t}^{D+} + \mathbf{t}^{D-} = \mathbf{0}, \\ &C_{\beta 1k1} = G\delta_{\mathrm{D}_{\beta k}}, \quad C_{\beta 1k\alpha} = G\delta_{\mathrm{D}_{\beta\alpha}}\delta_{\mathrm{D}_{1k}}, \quad \beta,\alpha = 2,3. \end{aligned} \tag{2.27}$$

It follows that the generic regularized traction BIE (2.26) for a crack of arbitrary shape in an elastic, linear, isotropic, infinite medium writes

$$\begin{aligned} t_\beta^D(\mathbf{x}) = &-G\int_\Gamma \left[\delta_{a,\alpha}(\mathbf{y}) - \delta_{a,\alpha}(\mathbf{x})\right]\Sigma_{a\alpha}^\beta(\mathbf{x},\mathbf{y})dS_y - G\delta_{a,\alpha}(\mathbf{x})A_{a\alpha}^\beta(\mathbf{x},\Gamma) \\ &+G\int_\Gamma \left[\delta_{a,\alpha}(\mathbf{y}) - \delta_{a,\alpha}(\mathbf{x})\right]\Sigma_{a1}^1(\mathbf{x},\mathbf{y})dS_y + G\delta_{a,\beta}(\mathbf{x})A_{a1}^1(\mathbf{x},\Gamma) \end{aligned} \quad , \forall \mathbf{x} \in \Gamma. \tag{2.28}$$

Particularly, let us detail the simplified two-dimensional case with an infinite fault along the $\mathbf{e}_2$ direction. In mode III configuration, the balance momentum equation writes as a two-dimensional Laplace equation (see Table 1.1) in quasi-static. The corresponding fundamental solution writes

$$U_2^2(\mathbf{x},\mathbf{y}) = \frac{-\log(r)}{2\pi G}, \quad r = |\mathbf{y}-\mathbf{x}|. \tag{2.29}$$

In this configuration, it is assumed that on either side of the fault:

- The media are symmetrical;
- The material properties are symmetrical;
- The boundary (loading) conditions are symmetrical.

In the case of a symmetrical loading applied on the crack faces, the traction components are continuous across Γ, such that $\mathbf{\Psi} = \mathbf{0} \Leftrightarrow \sigma_{12}(0^+, x_3, t) = \sigma_{12}(0^-, x_3, t)$. Using the analog of the symmetry properties (2.17) for the displacement gradient Green function (2.29), the momentum balance equation and regularizing the BIE with an integration by part, (2.28) writes

$$\boxed{t_2^D(x_3) = \sigma_{12}(x_3) = \frac{G}{2\pi}\int_\Gamma \frac{\partial\delta_2/\partial y_3}{x_3 - y_3}dS_y, \quad \forall \mathbf{x} \in \Gamma.} \tag{2.30}$$

The integral in (2.30) is weakly singular and is given in the sense of Cauchy principal values (CPV). In mode II configuration, using similar developments (as detailed by Tada and Yamashita (1997), Romanet (2017) for non-planar faults), one can obtain the following traction BIE

$$\boxed{t_3^D(x_3) = \frac{G}{2\pi(1-\nu)} \int_\Gamma \frac{\partial \delta_3 / \partial y_3}{x_3 - y_3} dS_y, \quad \forall \mathbf{x} \in \Gamma.} \tag{2.31}$$

The same kind of integral equation can be obtained for the normal traction component in mode II when the non-opening condition is not considered for non-planar faults for instance (effective normal stress applied at the fault front). In this case, a limiting criterion should be added numerically to constrain the evolution of this traction component which keeps accumulating without being released (in quasi-static at least) (Romanet, 2017).

For the mode III (respectively mode II with no-opening condition) planar-fault case, we use Equation (2.30) (respectively (2.31)) in the following developments of this chapter. We denote $t_2^D(x_3)$ (respectively $t_3^D(x_3)$) as $\tau^{qs}(x_3)$, the only non-vanishing shear-stress component resulting from quasi-static slip $\delta_2(x_3)$ (respectively $\delta_3(x_3)$) denoted $\delta(x_3)$.

Free surface condition for BIE. The methods to consider a free surface condition in the case of faults embedded in half-spaces depend on whether we deal with a scalar problem or a vector problem. The free surface condition writes

$$\boldsymbol{\sigma}\mathbf{n} = \mathbf{0}, \quad \text{on } \partial\Omega. \tag{2.32}$$

Figure 2.4 represents two methods to take into account a free surface conditions in the case where a 1D planar fault, embedded in a 2D medium, and perpendicular to the free surface is considered. In the case of a planar fault perpendicular to the free surface, we can take into

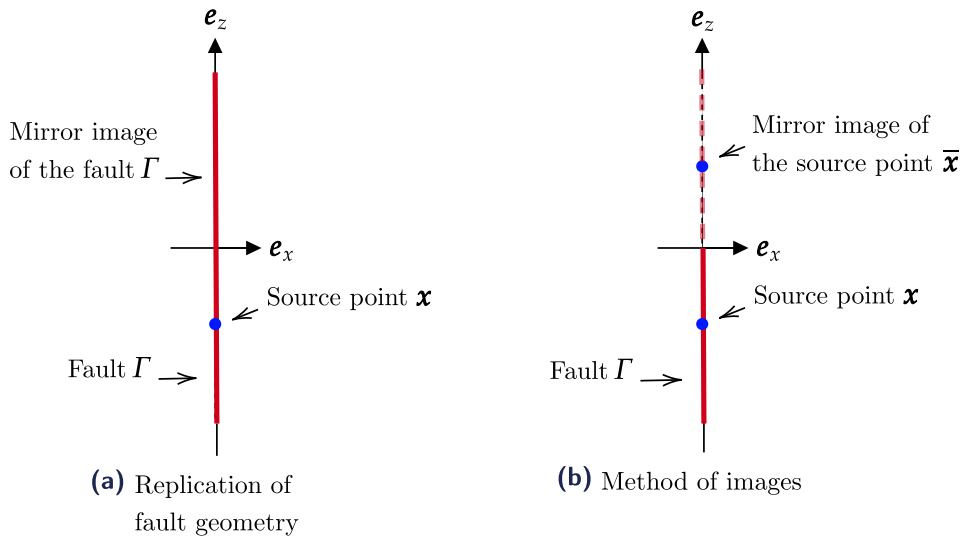

Figure 2.4 • Two methods to take into account a free surface condition in $x_3 = 0$ (a) by replication of the fault geometry with respect to the free surface, (b) by the method of images, in the case of the 2D case of a planar fault perpendicular to the free surface.

account the free-surface condition by adding to the initial fault geometry its mirror image with respect to the free surface (Figure 2.4 (a)). For the particular anti-plane case or in-plane strain case with a no-opening condition on the fault ($\delta_1(x_3) = 0$, which corresponds to pure Mode II), considering the free surface condition reduces to the following scalar condition

$$\frac{\partial \delta_2}{\partial x_3}|_{x_3=0} = 0, \quad \text{(Mode III)}, \quad \frac{\partial \delta_3}{\partial x_3}|_{x_3=0} = 0, \quad \text{(Mode II)}. \tag{2.33}$$

This method duplicates the size of the discretized domain but does not change the expression of the Green's function.

A second method is the method of images (Bonnet (1999)) as illustrated in Figure 2.4 (b). It consists in a superposition method, which combines the free surface fundamental solutions for sources at $\mathbf{x} = (x_1, x_2, x_3)$ and at its mirror image with respect to the free surface $\bar{\mathbf{x}} = (x_1, x_2, -x_3)$. For our specific Mode III scalar problem for instance, the resulting fundamental solution for the elastic half-space is

$$U_2^2(\mathbf{x}, \mathbf{y}) = -\frac{\log(r)}{2\pi G} - \frac{\log(\bar{r})}{2\pi G}, \quad r = |\mathbf{y} - \mathbf{x}|, \quad \mathbf{r} = |\mathbf{y} - \bar{\mathbf{x}}|. \tag{2.34}$$

The method of images can be only used in the case of scalar problems. This second method differs from the first one as the discretized domain does not change, while the Green's function changes. This method does not extend to vector problem (general elastostatics or elastodynamics) as the symmetry with respect to the boundary is no longer satisfied in such cases but for this configuration, a more complex Green function can be defined Bonnet (1999).

Extension to elastodynamics. Taking into account inertial effects is more difficult. For elastodynamic problems, different fundamental solutions are used. In addition, a convolution product in time is added in the traction BIE. Bonnet (1999) gives the regularized time-domain traction BIE for a fault of arbitrary shape embedded in an infinite medium and subjected to symmetrical loading on the crack faces such that $\mathbf{\Psi} = \mathbf{0}$. The relation between the loading $t_i^D(\mathbf{x}, t)$ and the displacement discontinuity history $\delta_i(\mathbf{y}, \tau)$, $(0 \leqslant \tau \leqslant t)$ is

$$\begin{aligned} t_i^D(\mathbf{x}, t) = & - C_{ijkl} n_j(\mathbf{x}) D_{lb} \delta_a(\mathbf{x}, t) A_{ab}^k(\mathbf{x}, \Gamma) \\ & - C_{ijkl} n_j(\mathbf{x}) \left[\left\{ \int_\Gamma \int_0^t \Sigma_{ab}^k(\mathbf{x}, \mathbf{y}, t - t') D_{lb} \delta(\mathbf{y}, t') dt' \right\} - D_{lb} \delta_a(\mathbf{x}, t) \Sigma_{ab}^k(\mathbf{x}, \mathbf{y}) \right] dSy \\ & - C_{ijkl} n_j(\mathbf{x}) \rho \int_\Gamma \int_0^t U_a^k(\mathbf{x}, \mathbf{y}, t - t') \delta_a(\mathbf{y}, t') n_l(\mathbf{y}) dS_y \end{aligned} \tag{2.35}$$

where both the elastodynamic fundamental solution $(U_a^k(\mathbf{x}, \mathbf{y}, t), \Sigma_{ab}^k(\mathbf{x}, \mathbf{y}, t))$ and the elastostatic fundamental solutions $(U_a^k(\mathbf{x}, \mathbf{y}), \Sigma_{ab}^k(\mathbf{x}, \mathbf{y}))$ are introduced for regularization purpose, since they have the same singularity (see Bonnet (1999) page 176). The particular traction BIE for a two-dimensional in-plane strain configuration of a non-planar fault embedded in a two-dimensional linear elastic medium is given by Romanet and Ozawa (2021) based on the Green's function given by Tada and Yamashita (1997). Cochard and Madariaga (1994) give a regularized fully-dynamic BIE in mode III between the traction $t_2^D(x_3, t)$ (which is

scalar corresponding to the only non-vanishing traction component in mode III) and the displacement discontinuity $\delta(x,t)$ (also a scalar in mode III)

$$t_2^D(x_3,t) = -\frac{G}{2c_s}\frac{\partial \delta}{\partial t} - \frac{G}{2\pi}\int_\Gamma \int_0^{t_m} \frac{\sqrt{(t-t')^2 - (x_3-\xi)^2/c_s^2}}{(t-t')(x_3-\xi)} \frac{\partial \delta}{\partial \xi}(\xi,t')\mathrm{d}t'\mathrm{d}\xi \tag{2.36}$$

where $t_m = \max(0, t - \|x_3 - \xi\|/c_s)$.

A "quasi-dynamic" approximation of the inertial effects is often privileged to reduce the computational cost as it prevents to compute the convolution in time in addition to the convolution in space. However, the inertial effects cannot be totally neglected otherwise, the corresponding simulation could not pass the seismic event Rice (1993). The approximation consists in a "viscous" term considered at the interface whereas quasi-static equations are solved in the surrounding volume. This approximation is majorly used in mode III for which the remaining kernel is showed to decrease rapidly with its argument (see Lapusta and Liu (2009) and Romanet and Ozawa (2021)). In such cases (mode III), the shear-stress t_2^D change due to slip δ_2 writes

$$\boxed{t_2^D(x_3,t) = -\frac{G}{2c_s}\frac{\partial \delta_2}{\partial t} - \frac{G}{2\pi}\int_\Gamma \frac{\partial \delta_2/\partial \xi}{x_3-\xi}\mathrm{d}\xi, \quad \forall \mathbf{x} \in \Gamma.} \tag{2.37}$$

In the mode II case, the "quasi-dynamic" approximation of the non-vanishing shear-stress component $t_3^D(x_3,t)$ writes (Geubelle & Rice, 1995)

$$\boxed{t_3^D(x_3,t) = -\frac{G}{2c_s}\frac{\partial \delta_3}{\partial t} - \frac{G}{2\pi(1-\nu)}\int_\Gamma \frac{\partial \delta_3/\partial \xi}{x_3-\xi}\mathrm{d}\xi, \quad \forall \mathbf{x} \in \Gamma.} \tag{2.38}$$

The latter integro-differential expressions contain weakly singular integrals, which are given in the sense of Cauchy principal values (CPV). The term $-G/(2c_s)\partial\delta/\partial t$ in Equations (2.37) and (2.38) corresponds to the so-called radiation damping. The radiation damping term is defined as the instantaneous stress drop at a given point $x_3\mathbf{e}_3$ along the fault Γ due to a local change in slip-rate.

For the mode III (respectively mode II with no-opening condition) planar-fault case, we use Equation (2.37) (respectively (2.38)) in the following developments of this chapter. We denote $t_2^D(x_3,t)$ (respectively $t_3^D(x_3,t)$) as $\tau(x_3,t)$, the only non-vanishing shear-stress component resulting from slip $\delta_2(x_3,t)$ (respectively $\delta_3(x_3,t)$) denoted $\delta(x_3,t)$.

Alternative approach in the particular case of planar faults embedded in an elastic medium

In the particular case of planar faults in infinite spaces, a spectral reformulation of the previous traction BIEs is possible and very efficient. The approach consists in solving the momentum balance equation in the Fourier domain in space and in the Laplace domain in time. The calculations have been performed by Geubelle and Rice (1995) and Morrissey and Geubelle (1997). We (re-)derive the calculations in the particular case of a Mode III dynamic fault slip problem.

Following the anti-plane shear assumptions detailed in Table 1.1, the only non-vanishing displacement component u_2 is independent of the y-coordinate and satisfies the scalar wave equation

$$G\left(\frac{\partial^2 u_2}{\partial x_1^2}+\frac{\partial^2 u_2}{\partial x_3^2}\right)=\rho\frac{\partial^2 u_2}{\partial t^2} \iff c_s^2\left(\frac{\partial^2 u_2}{\partial x_1^2}+\frac{\partial^2 u_2}{\partial x_3^2}\right)=\frac{\partial^2 u_2}{\partial t^2} \tag{2.39}$$

where $G\frac{\partial u_2}{\partial x_1}$ is continuous at $x_1 = 0$ and corresponds to the only non-vanishing traction component. Focusing our attention on one spectral component of u_2 we can write

$$u_2(x_1, x_3, t) = \Omega(x_1, t; k)e^{ikx_3}, \tag{2.40}$$

where k is the wavenumber along $\mathbf{e}_3$ direction. Then, we take the Laplace transform with respect to time of (2.39) yielding to

$$\frac{\partial^2 \hat{\Omega}(x_1, s; k)}{\partial x_1^2} = k\alpha_s \hat{\Omega}(x_1, s; k), \tag{2.41}$$

where $\alpha_s = \sqrt{1+\frac{s^2}{k^2 c_s^2}}$ and s is the Laplace variable. A bounded solution of Equation (2.41) for the upper plane ($x_1 > 0$) must have the form (as $\hat{\Omega} \longrightarrow 0$ as $|x| \longrightarrow \infty$)

$$\hat{\Omega}(x_1, s; k) = \hat{\Omega}_0(s; k)e^{-|k|\alpha_s x_1}. \tag{2.42}$$

It leads to:

$$\hat{u}_2(x_1, x_3, s) = e^{ikx_3}\hat{\Omega}_0(s; k)e^{-|k|\alpha_s x_1}. \tag{2.43}$$

Now, we define the displacement Fourier coefficient $U_2(t; k)$ linked to the displacement at the fault interface

$$u_2(x_1 = 0^+, z, t) = U_2(t; k)e^{ikx_3}, \tag{2.44}$$

and the traction coefficient $T_2(t; k)$ as

$$\sigma_{12}(x_1 = 0^+, x_3, t) = T_2(t; k)e^{ikx_3}. \tag{2.45}$$

Combining (2.43) with Hooke's law, we can relate the traction and displacement Fourier coefficients by

$$\hat{T}_2(s; k) = -G|k|\alpha_s \hat{U}_2(s; k). \tag{2.46}$$

Due to the symmetry of the media, the material properties and the loading on either side of the fault, the displacement solution is antisymmetric with respect to the fracture plane in the mode III configuration. Hence, we may rewrite (2.46) in terms of the displacement discontinuity $\delta_2(x_3, t)$ and its Fourier coefficient $D_2(t; k)$ defined as

$$\delta_2(x_3, t) = u_2(x_1 = 0^+, x_3, t) - u_2(x_1 = 0^-, x_3, t) = 2u_2(x_1 = 0^+, x_3, t) = D_2(t; k)e^{ikx_1} \tag{2.47}$$

to obtain

$$\hat{T}_2(s; k) = -\frac{G}{2}|k|\alpha_s \hat{D}_2(s; k). \tag{2.48}$$

Before we arrive at the final space-time relation, we modify (2.48) by extracting $G/(2c_s)p\hat{D}_2(p; k)$ corresponding to the instantaneous response

$$\hat{T}_2(s; k) = \frac{G}{2c_s}s\hat{D}_2(s; k) - \frac{G|k|}{2}\left\{\alpha_s - \frac{s}{|k|c_s}\right\}\hat{D}_2(s; k). \tag{2.49}$$

Next, we perform an inverse Laplace transform back to the time domain

$$T_2(t;k) = -\frac{G}{2c_s}\dot{D}_2(t;k) + F(t;k) \tag{2.50}$$

where the dot denotes differentiation with respect to time. $T_2(t;k)$ in (2.50) corresponds to the Fourier transform with respect to space of $t_2^D(x_3,t)$ in (2.36), where the radiation damping term has been isolated to exhibit the kernel thereafter.

We write $\hat{W}(s) = \left\{\alpha_s - \frac{s}{|k|c_s}\right\}$. Since $p\hat{W}(s)$ is bounded as $s \to +\infty$, there is a bounded function $W(t)$ whose transform is $\hat{W}(s)$, and the convolution theorem allows us to write

$$F(t;k) = -\frac{G}{2}|k|\int_0^t M(|k|c_s t')D((t-t');k)|k|c_s dt'. \tag{2.51}$$

To find $W(t)$ we extend $\hat{W}(s)$ to the complex plane with branch cut on the imaginary axis between $s = -i|k|c_s$ and $s = i|k|c_s$, and then use the Bromwich inversion formula to write

$$M(|k|c_s t) = \frac{1}{2i\pi}\oint_\Gamma \left(\sqrt{1+\frac{s^2}{k^2c_s^2}} - \frac{s}{|k|c_s}\right)e^{st}ds$$

where the contour Γ can be distorted to circle once around, and shrink onto, the branch cut. Thus letting $s = i|k|c_s \sin\Psi$, with Ψ varying from 0 to 2π, it follows

$$\begin{aligned} M(|k|c_s t) &= \frac{|k|c_s}{2\pi}\int_0^{2\pi}(\cos\Psi - i\sin\Psi)\exp(i|k|c_s t\sin\Psi)\cos\Psi d\Psi \\ &= \frac{|k|c_s}{2}\left[\frac{1}{\pi}\int_0^\pi \cos(|k|c_s t\sin\Psi)d\Psi + \frac{1}{\pi}\int_0^\pi \cos(|k|c_s t\sin\Psi - 2\Psi)d\Psi\right]. \end{aligned} \tag{2.52}$$

The two terms within the brackets are the integral representations of the Bessel functions J_0 and J_2, respectively, such that

$$M(|k|c_s t) = \frac{|k|c_s}{2}\left[J_0(|k|c_s t) + J_2(|k|c_s t)\right] = \frac{J_1(|k|c_s t)}{t}. \tag{2.53}$$

Thus $F(t;k)$, when evaluated with this convolution kernel $W(t)$, gives the functional $f(x_3,t)$, in response to slip history $\delta_2(x_3,t) = D_2(t;k)e^{ikx_3}$, as $f(x_3,t) = F(t;k)e^{ikx_3}$.

$$F(t;k) = -\frac{G}{2}|k|D_2(t';k) + \frac{G}{2}|k|\int_0^t W(|k|c_s t')\dot{D}_2((t-t');k)|k|c_s dt' \tag{2.54}$$

where $W(t) = \int_t^\infty J_1(\theta)/\theta\ d\theta = 1 - tJ_0(t) + J_1(t) - (\pi/2)t(J_1(t)H_0(t) - J_0(t)H_1(t))$, with $H_0(t)$ and $H_1(t)$ being Struve functions of order 0 and 1 respectively (Romanet & Ozawa, 2021). $W(t)$ decreases rapidly when t increases as shown in Figure 2.5. In practice, this is very advantageous as it allows to truncate the convolution in time (reducing its computational cost) without significant loss in its accuracy. Hence, the calculation of $F(t;k)$ allows to obtain the traction $f(x_3,t)$ in response to the slip history given by $\delta_2(x_3,t) = D_2(t;k)e^{ikx_3}$, such that $f(x_3,t) = F(t;k)e^{ikx_3}$. The first term $-\frac{G}{2}|k|D_2(t';k)$ of $F(t;k)$ in (2.54) corresponds to the Fourier transform with respect to space of the quasi-static shear-stress $t_2^D(x_3)$ (τ^{qs}) in (2.30).

Similar results for Mode II and Mode I configurations are given by Geubelle and Rice (1995).

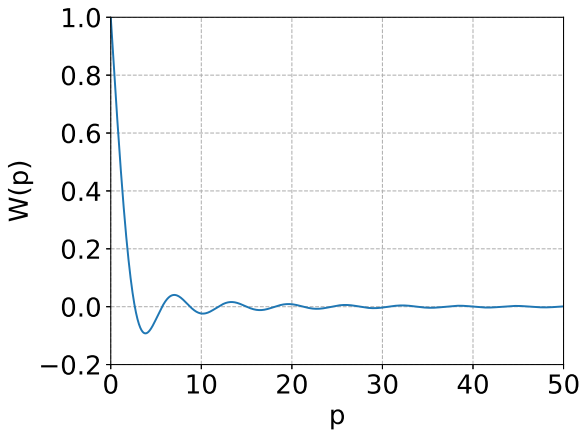

Figure 2.5 • Evolution of the kernel $W(p)$ with its argument.

> **Remark 2.3.** *This approach relies on a strong assumption that the fault geometry repeats periodically at depth, which is not the case with the approach using the BIEM. We show in Section 4.3 from Chapter 2, that this has significant consequences in the numerical solving of fault slip problems.*

This approach has been applied to several coupled planar faults by Barbot (2019). It has also been extended to the case of a non-planar fault of moderate curvature by Romanet and Ozawa (2021).

In the following developments, we now concentrate on mode II and mode III planar fault configurations with symmetrical loading imposed on fault faces.

1.2 Interface problems for mode II and mode III planar-fault configurations

Solving a seismic cycle problem consists in solving the combination of the balance momentum equation with interface conditions, and completed by boundary and initial conditions. We know that we can use the BIEM to reformulate the combination of balance momentum equations, Hooke's law, and boundary conditions as an integral equation on the fault interface Γ.

As a consequence, the BIE relating the only non-vanishing shear-traction component denoted τ at the fault interface to the displacement discontinuity δ as

$$\tau(z,t) = \tau^0(z) + \frac{G}{2\pi\epsilon}\int_\Gamma \frac{\partial\delta/\partial\xi}{z-\xi}d\xi - \frac{G}{2c_s}\frac{\partial\delta}{\partial t} := \tau^0(z) + \tau^{qs}(z,t) - \frac{G}{2c_s}\frac{\partial\delta}{\partial t},\ \forall z\in\Gamma \tag{2.55}$$

where the pre-stress τ^0 corresponds to the steady-state shear-stress due, for instance, to the far-field tectonic loading.

$\tau^{qs}(z,t)$ corresponds to the quasi-static shear-stress change from Equation (2.30) due to the change in the displacement discontinuity at the interface. $\epsilon = 1$ (mode III) or $(1-\nu)$ (mode II). The two-dimensional elastostatic Green function (2.29) for the free-space is considered here as inertial effects are taken into account only at the fault interface. The BIE

defining τ^{qs} has been regularized by integration by part such that the term in the integral is only weakly singular. The BIE is defined in the sense of Cauchy Principal Values. The time evolution of the unknowns comes from the interface conditions.

$G/(2c_s)\partial\delta/\partial t$ is the radiation damping term as in Equation (2.37), proportional to the slip-rate $V = \partial\delta/\partial t$, which approximates inertial effects. This term is negligibly small for aseismic slips and only becomes relevant when slip undergoes a frictional instability. Lapusta et al. (2000) in 2D and Lapusta and Liu (2009) in 3D investigated the comparison between quasi-dynamic and fully-dynamic problems. This study showed that the quasi-dynamic approach resulted in smaller slip per event, smaller slip velocity values and smaller rupture speeds leading to have long-term influences over earthquake cycles especially in 3D. A possibility to improve the comparison is to decrease the radiation damping term in order to increase the slip-velocity values reached during seismic phases. In this work, we do not consider a decreasing factor for the radiation damping term.

Now, we have to relate the obtained integro-differential equation (2.55) to the interface condition. Symmetrical loading imposed on crack faces (see Figure 2.1) imply continuity of the traction components at the interface. We assume that the discontinuity Γ obeys Coulomb friction and consider a regularized rate-and-state friction law to model contact at the fault interface, i.e.

$$\begin{aligned} &\tau(z,t) = \sigma_n \mu(V(z,t),\theta(z,t)), \\ &\text{with} \quad \mu(V(z,t),\theta(z,t)) = a(z)\sinh^{-1}\left[\frac{V(z,t)}{V_0}\exp\left(\frac{\mu_0}{a(z)} + \frac{b(z)\ln(\theta(z,t)/\theta_0)}{a(z)}\right)\right] \\ &\qquad\qquad \frac{\mathrm{d}\theta}{\mathrm{d}t} = 1 - \frac{V(z,t)\theta(z,t)}{D_c} \end{aligned} \tag{2.56}$$

where σ_n is the effective normal stress applied at the fault interface, assumed to be constant. σ_n is equal to a pre-stress value due, for instance, to the far-field tectonic loading. V is the slip-rate. θ is the state variable governed by the so-called aging law. a and b are rate-and-state parameters which can vary in depth. V_0 and μ_0 are respectively a reference slip-rate value and a reference friction coefficient value, and $\theta_0 = D_c/V_0$, where D_c is the characteristic slip distance. Rate-and-state friction is considered on a fault width W_f and outside this rate-and-state zone, the fault creeps at a constant rate given by the interface condition

$$V(z,t) = V_{pl}, \begin{cases} z \notin [-W_f/2, W_f/2] \text{ (for an infinite space)} \\ \text{or } z \geqslant W_f \text{ (for a semi-infinite space)} \end{cases} \tag{2.57}$$

where V_{pl} is the plate rate and mimics the far-field tectonic loading. Along the fault width, the rate-weakening values of the rate-and-state parameters are considered for seismic instability to occur. The choice of these parameters is important from a numerical viewpoint. Notably, Barbot (2019) used the BIEM to simulate seismic cycles in quasi-dynamic on semi-infinite and finite faults loaded in anti-plane (mode III) or in-plane strain (mode II). He performed a non dimensionalization of the governing equations, which revealed non-dimensional parameters that control separate aspects of the fault dynamic. The numerical performances can be affected by the choice of the physical parameters, which also influences the choice of the space step and the evolution of the time step.

Finally, initial conditions for the interface unknowns $\delta(z,t), V(z,t), \theta(z,t)$ are required. We consider that slip δ is initially zero everywhere in the domain and that its initial time derivative value, slip-rate V, is initially constant equal to the plate-rate V_{pl}, corresponding to its steady-state value:

$$\delta(z,0) = 0, \quad V(z,0) = V_{pl}. \tag{2.58}$$

As a consequence, the steady state value of the state variable is $\theta_{ss} = D_c/V_{pl}$. Hence, we define the pre-stress τ^0 as the steady state stress, namely

$$\tau^0 = \sigma_n \mu(V_{pl}, \theta_{ss}) + \frac{G}{2c_s} V_{pl}. \tag{2.59}$$

To be consistent with slip-rate and pre-stress everywhere, the initial state variable can vary at depth and is not necessarily at steady states:

$$\theta(z,0) = \frac{D_c}{V_0} \exp\left\{ \frac{a(z)}{b(z)} \ln\left[\frac{2V_0}{V_{pl}} \sinh\left(\frac{\tau^0 - G/(2c_s)V_{pl}}{a(z)\sigma_n} \right) \right] \right\}. \tag{2.60}$$

$\theta(z,0)$ stands for the perturbation of the equilibrium that leads to seismic cycles due to the material and friction properties chosen (as explained in Section 1.2 in Chapter 1)

Equation (2.55), along with interface conditions (2.56) and (2.57), eventually a free surface condition, and initial conditions (2.58) and (2.60) are solved in space over the time period $0 \leqslant t \leqslant t_{\text{final}}$, where t_{final} is a specified simulation time.

The benchmark proposed here neither takes into account geometric complexities of real faults, nor fault networks, nor complexities of the geological layers. Nevertheless, it is worth mentioning that these simplified configurations enable to focus on the validation of the results produced and on the comparison of the different numerical methods implemented. The anti-plane and in-plane strains problems presented here for a planar fault in quasi-dynamic are similar to benchmark problems BP1/2 and BP3 (in case the fault is embedded in a semi-infinite space and is perpendicular to the free surface) from SEAS project (Erickson et al. (2020a)), whose descriptions are given in Erickson and Jiang (2018) and Erickson et al. (2021) respectively.

In the case of a planar fault perpendicular to the free surface, we add to the initial problem the mirror image of the fault on the other side of the free surface, so that the displacement discontinuity would satisfy $\partial\delta/\partial z|_{z=0} = 0$, which allows to take into account the free surface condition as explained in Section 1.1.

2 Space discretization of the boundary integral equation

Now that the continuous model has been presented, we move to the space discretization. The integro-differential equation (2.55) satisfied at the interface Γ, combined with the rate-and-state constitutive friction law (2.56) are the only equations that need to be discretized in space. Maier et al. (1993) and Bonnet (1999) (chapter 13) among others, considered BEM for contact and crack problems. Maerten (2010) reviews space discretization methods using BEM for earthquakes triggering and fault interactions problems from the introduction of the displacement discontinuity methods (DDM) in 2D by Crouch and Starfield (1983). Bonnet

(1999) extended the DDM to 3D crack problems in infinite space and proposed a so-called multi-region approach in case of bounded-domain problems.

Here, we discretize the pre-existing discontinuity Γ using 1D boundary elements (for 2D domains). We assume piece wise constant slip over each element as done by Rice (1993), Cochard and Madariaga (1994), Romanet (2017), Romanet and Ozawa (2021) among others, and we take as evaluation points the centers of the elements, meaning that the slip $\delta(z,t)$ writes in the discrete form

$$\begin{aligned}\delta(z,t) &\approx \sum_{j=1}^{N} \delta(z_j,t)\left(\mathscr{H}(z-(z_j-\Delta z/2))-\mathscr{H}(z-(z_j+\Delta z/2))\right)\\ &= \begin{cases} \delta(z_j,t) \text{ if } z\in[z_j-\Delta z/2, z_j+\Delta z/2] \triangleq [\xi_j,\xi_{j+1}] \\ 0 \text{ otherwise}\end{cases}\end{aligned} \tag{2.61}$$

where Δz is the space step and $\{\xi_j\}_{j=1,\dots,N+1}$ correspond to the extremities of the 1D elements, and $\mathscr{H}$ is the Heaviside function.

For the sake of a more compact notation, we denote

$$K(z,\xi) = G/(2\pi\epsilon)1/(z-\xi). \tag{2.62}$$

Notably, incorporating the discrete representation (2.61) of the displacement discontinuity δ in the expression of the quasi-static stress change τ^{qs} from (2.55) yields

$$\begin{aligned}\tau^{qs}(z,t) &= \int_\Gamma K(z,\xi)\frac{\partial\delta}{\partial\xi}(\xi,t)d\xi\\ &\approx \int_\Gamma K(z,\xi)\frac{\partial}{\partial\xi}\left(\sum_{j=1}^{N}\delta(z_j,t)\left(\mathscr{H}(z-\xi_j)-\mathscr{H}(z-\xi_{j+1})\right)\right)\\ &= \sum_{j=1}^{N}\delta(z_j,t)\left(\langle K(z,\xi)\delta_D(\xi-\xi_j)\rangle - \langle K(z,\xi)\delta_D(\xi-\xi_{j+1})\rangle\right)\\ &= \sum_{j=1}^{N}\delta(z_j,t)\left(K(z,\xi_j)-K(z,\xi_{j+1})\right)\\ \Rightarrow \tau^{qs}(z_i,t) &\approx \sum_{j=1}^{N}\delta(z_j,t)\left(K(z_i,\xi_j)-K(z_i,\xi_{j+1})\right),\ i=1\dots N\end{aligned} \tag{2.63}$$

It is worth noticing that the latter equality is no more singular thanks to the piece-wise constant slip considered. We avoid the singularity of the kernel as z_j and ξ_j are never the same. They are at least separated by half a space step. Figure 2.6a represents the space discretization of a 1D planar fault with 16 1D elements as an illustration, so that we could easily distinguish the center of the elements and their extremities.

The standard Boundary Element matrix contains the coefficients K_{ij}.

$$K_{ij} = \left\{K(z_i,\xi_j)-K(z_i,\xi_{j+1})\right\}_{i,j=1,\dots,N}. \tag{2.64}$$

It is fully-populated and the matrix vector product required to evaluate the shear-stress field at the collocation points and at each time-step leads to a computational complexity of

$\mathcal{O}(N^2)$, where N is the number of collocation points. It leads to prohibitive computational costs for large problem sizes. The Boundary Element matrix can be viewed as an image of the "interactions" between the degrees of freedom (DOFs). The "interaction" of a DOF with itself is much more significant (due to the singular behavior of the kernel) than the "interaction" between two DOFs that are located far from each other in the geometry. This idea is to factorize "far" interactions to speed up the evaluation of the BEM matrix and the iterative solution.

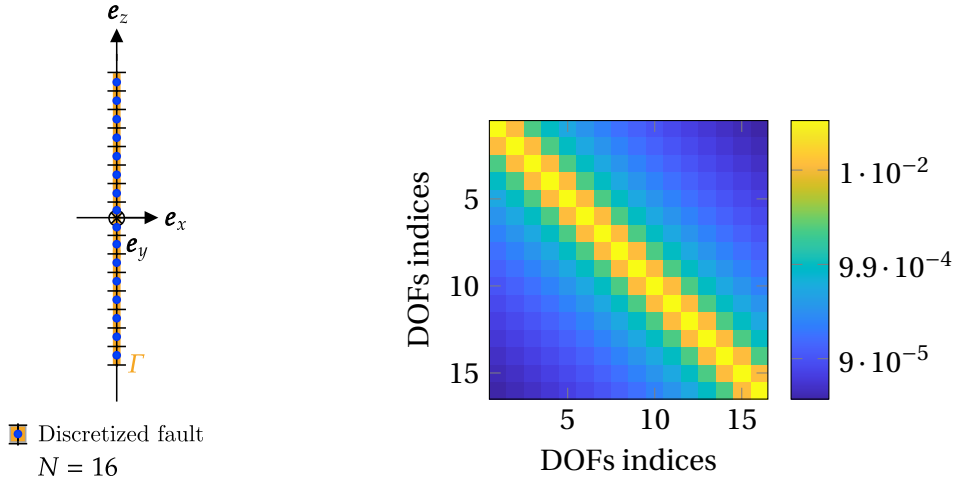

(a)

(b) Amplitude of the BEM matrix coefficients.

Figure 2.6 • (a) Space discretization of a 1D planar fault with 16 1D elements. The mesh nodes are located in the center of the elements. (b) Evolution of the amplitude of the coefficients of corresponding Boundary Element matrix. Diagonal coefficient represents close interactions between geometrically close degrees of freedom while off diagonal coefficients of lower amplitude represent far interactions between geometrically far degrees of freedom.

In case of a planar discontinuity, two accelerated Boundary Element Methods techniques can reduce the computational costs.

- A Spectral Boundary Element Method (S-BEM) based on the use of the Fast Fourier Transform to accelerate the evaluation of the shear-stress field at the collocation points of the fault interface, but limited to simple geometries;
- A Fast Boundary Element Method based on Hierarchical matrices (H-BEM) to provide a data sparse approximation of the standard Boundary Element Matrix to accelerate both its implementation and the matrix vector product with the displacement discontinuity vector.

Another Fast Boundary Element method, the Fast Multipole Method (FMM) (Greengard & Rokhlin, 1987; Ying et al., 2004), based on Taylor series expansion of the Green function to separate close and far contributions, has been used by Romanet (2017). It requires to know the fundamental solution analytically which is the case for elastic, linear, homogeneous, isotropic configurations. $\mathcal{H}$-matrices can be viewed as the algebraic analogue of FMM. Thus, it is not necessary to study FMM in addition to $\mathcal{H}$-matrices here.

2.1 Spectral Boundary Element Method for a planar discontinuity

In the particular case of a planar fault, the quasi-static shear-stress component τ^{qs} of (2.55) writes as a convolution product (also as a Hilbert transform). It simplifies as we take the Fourier transform of τ^{qs} with respect to space.

$$\mathscr{F}\left(\tau^{qs}(z,t)\right) := T^{qs}(t;k) = \mathscr{F}\left(\frac{1}{z}\right)\mathscr{F}\left(\frac{\partial\delta}{\partial z}(z,t)\right) \tag{2.65}$$

where $\mathscr{F}(\cdot)$ is the Fourier transform operator in space and T^{qs} is the Fourier transform in space of the quasi-static shear-stress change τ^{qs}. The Fourier transform of $1/z$ is known analytically

$$\mathscr{F}\left(\frac{1}{z}\right) = -i\pi\frac{k}{|k|} \tag{2.66}$$

where k is the Fourier wavenumber. The spatial partial derivative of the displacement discontinuity writes in the Fourier domain

$$\mathscr{F}\left(\frac{\partial\delta}{\partial z}(z,t)\right) = ik\mathscr{F}\left(\delta(z,t)\right) := ikD(t;k) \tag{2.67}$$

where D is the Fourier transform with respect to space of the slip δ. We finally get:

$$T^{qs}(t;k) = \frac{G}{2}|k|D(t;k). \tag{2.68}$$

Spectral Boundary Element Methods (S-BEM) have been largely used to solve seismic cycles problems for planar faults configurations in 2D (Lapusta et al., 2000; Hillers et al., 2006; Segall, 2010; Erickson et al., 2020a), in 3D (Lapusta & Liu, 2009; Luo et al., 2017; Barbot, 2019). The simplified Boundary Integral Equation has been derived for mode I, II and III configurations Geubelle and Rice (1995), Perrin et al. (1995), Morrissey and Geubelle (1997) by solving the balance momentum equation in the Fourier domain in space and in the Laplace domain in time. The S-BEM for seismic cycle problems has been extended to multiple parallel faults by Barbot (2021) and to non-planar faults of moderated curvature by Romanet and Ozawa (2021), thanks to a "small-slope" approximation.

In practice, the implementation of the S-BEM relies on the use of Fast Fourier Transform (FFT) often based on the Cooley-Tukey algorithm (Cooley (1987) based on a method initially proposed by Gauss). The complexity of the Cooley-Tukey algorithm is in the order of $\mathcal{O}(N\log_2(N))$, where N is the number of degrees of freedom (DOFs). This method is particularly efficient in the case of planar-fault problems where it can be used.

The major drawbacks of this method rely on two strong assumptions:

- The fault has to be planar
- the fault has to be infinite with periodic replication of its frictional behavior.

Numerically, the latter assumption requires the discretized domain containing the fault to be chosen large enough, so that the values of the interface unknowns would not be influenced

by periodic replications. Cochard and Rice (1997) and Noda (2021) proposed a technique to use the S-BEM without artificial periodic boundary conditions of the fault. Also, a uniform space-step has to be chosen in this case.

In the present work, we implemented the S-BEM using the Fast Fourier Transform from the module NumPy in Python. It uses the Cooley-Tukey algorithm.

2.2 Fast Boundary Element Method based on Hierarchical matrices

An alternative approach to overcome the limitations brought by the dense matrix obtained from the discretization of the BIE is based on the concept of hierarchical matrices ($\mathscr{H}$-matrices) (Hackbusch, 1999; Grasedyck & Hackbusch, 2003; Grasedyck, 2005; Bebendorf, 2008; Hackbusch, 2015; Chaillat et al., 2017; Hodapp et al., 2019). $\mathscr{H}$-matrices have been introduced by Hackbusch (1999) to compute a data-sparse representation of some special dense matrices (e.g. matrices resulting from the discretization of non-local operators). This accelerated method also has the advantage to be an algebraic method such that it does not require tedious problem-dependent developments, and it can handle complex Green's functions. This method outperforms the limitations of the S-BEM as it can handle complex fault geometries, and it does not assume that the domain replicates periodically. $\mathscr{H}$-matrices have been used in contact mechanics to study macroscopic quantities (such as thermal, electrical conductivity, sealing properties, ... etc.) whose magnitude is controlled by the true contact area (Beguin & Yastrebov, 2023). Maerten (2010) applies $\mathscr{H}$-matrices to a 3D angular dislocation problem based on the analytical solution given by Comninou and Dundurs (1975). In the case of seismic cycles problems, $\mathscr{H}$-matrices allow speeding up the matrix-vector product required to compute the shear-stress τ (Bradley, 2014). They have been used for 2D Romanet (2017) and 3D non-planar faults problems (Ohtani et al., 2011; Bradley, 2014; Ozawa et al., 2022).

The principle of $\mathscr{H}$-matrices is

- to partition the initial dense matrix into sub-blocks using the fact that the rows and columns of the matrix correspond to successive degrees of freedom (DOFs),
- to approximate the initial dense matrix into a data-sparse one by performing a low-rank approximation of the sub-blocks that correspond to interactions between DOFs that are located far enough from each other

Thereafter, we detail the different steps of the method (in the same order as Chaillat et al. (2017) and Bagur et al. (2022)) through an application on the simplified case of a 1D planar fault in an infinite space.

Clustering of the unknowns. The first step before the partitioning of the BEM matrix is the clustering of the unknowns. It allows to make the correspondence between the sub-blocks of the matrix and the interaction between clusters of DOFs. A cluster is defined as a set of indices corresponding to DOFs that are "close" to each other. At this stage, we perform recursive subdivisions until a stopping criterion corresponding to the minimum number of

points in one cluster is achieved. Each subdivision consists in partitioning a "parent" subset into two disjoints "sons" subsets. This procedure can be represented by a binary tree in which the 0th-level ("root" cell) corresponds to the complete set of indices of the DOFs and the last level ("leaf" cell) is not subjected to further subdivisions. Figure 2.7 gives an illustration of the building of the previous binary tree in the simplified case of a one-dimensional planar fault Γ. We consider a small problem as an illustration for the sake of simplicity.

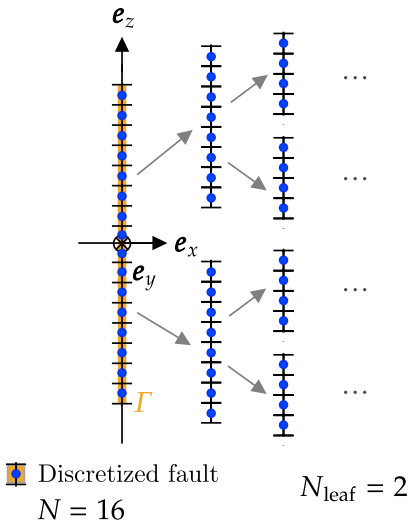

Figure 2.7 • Clustering of the DOFs of a 1D planar fault embedded in an infinite space and loaded in mode II or III.

Partitioning of the matrix. We now perform a partitioning of the matrix, which consists in deducing a hierarchical structure within the matrix based on the comparison of the subsets within a given level of the binary tree. The comparison between the subset of DOFs within a given level of the previously built binary tree allows to characterize a corresponding sub-block of the initial matrix and is based on a geometric criterion which is called "admissibility condition". Let us remark that a subdivision of a "parent" cell in two "son" cells in the binary tree yields to four combinations for subset comparisons leading to the subdivision of an initial sub-block into four sub-blocks in the matrix. The admissibility condition allows to determine whether the block considered is a priori low-rank or not.

Before recalling the expression of the admissibility, we introduce some vocabulary. Let X and Y be two subsets of DOFs which are compared:

- The diameter of X, $\operatorname{diam} X$, (respectively Y, $\operatorname{diam} Y$) is defined as the maximal distance between two distinct nodes from the subset.

- The distance between the clusters X and Y, $\operatorname{dist}(X, Y)$, is defined as the distance between the closer points from both subsets.

The admissibility condition can be derived from theoretical considerations for asymptotically smooth kernels (Hackbusch, 2015), which is the case of the space derivative of the 2D elastostatic Green function for the free space. X and Y are said to be η-admissible ($\eta > 0$) if

$$\min(\operatorname{diam} X, \operatorname{diam} Y) < \eta \operatorname{dist}(X, Y) \tag{2.69}$$

In practice we use $\eta = 3$ (Lizé, 2014). Testing the admissibility condition (2.69) for each sub-block of the dense matrix leads to distinguish admissible and non-admissible blocks. If a block does not satisfy the admissibility condition but corresponds to subsets of DOFs that can be subdivided according to the binary tree, then we test the admissibility of the "sons" subsets until the leaf level of the binary is reached or until an admissible block is found. If a block does not satisfy the admissibility condition and the corresponding subsets are at the leaf-level of the binary tree, then the block is said to be non-admissible (i.e. full rank). If a block verifies the admissibility condition, then we do not go further in the subdivisions of the binary tree and the block is said to be admissible (i.e. a priori low rank). It is worth mentioning that in the matrix, in the case of the 1D planar fault considered, we need finer blocks close to the diagonal (which corresponds to the interaction of a subset of mesh modes on itself) and coarser far away (interaction between far enough subset of DOFs). Figure 2.8a represents two subsets at a given level of the binary and the corresponding sub-block in the matrix. The hierarchical decomposition of the matrix is represented with colors. Green blocks correspond to admissible blocks while red block (finer ones) correspond to non-admissible blocks.

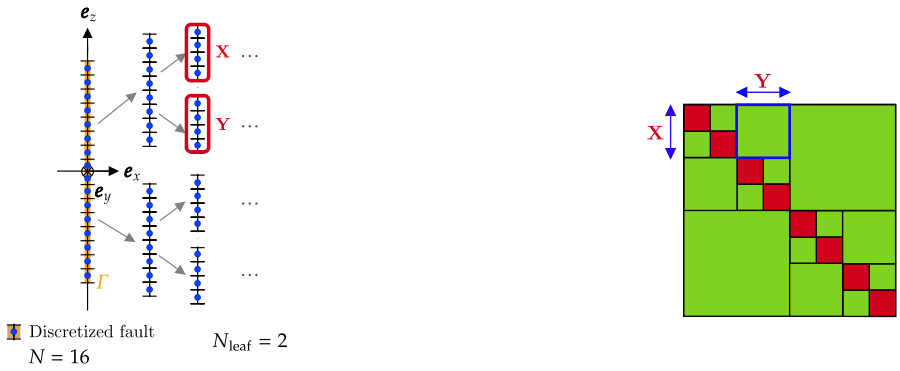

(a) **(b)**

Figure 2.8 • Hierarchical decomposition of the boundary element matrix for the case of a 1D planar fault embedded in an infinite space and loaded in mode II or III. (a) Building of the binary tree from the complete set of DOFs. Two subsets of nodes X and Y at the third level of the binary tree satisfy the admissibility condition and correspond to an admissible (green) block in the matrix (b), where non-admissible blocks are displayed in red.

Low rank approximation of admissible sub-blocks. The last step consists in performing a low rank approximation of the a priori low rank blocks (admissible blocks). This step allows saving

storage for the calculation of the boundary element matrix. A matrix $\mathbf{M} \in \mathbb{R}^{m,n}$ of numerical rank r can be approximated by the product of two matrices $\mathbf{A} \in \mathbb{R}^{m,r}$ and $\mathbf{B} \in \mathbb{R}^{n,r}$, such that $\mathbf{M} = \mathbf{A}\mathbf{B}^T$. Then the storage is reduced from $\mathcal{O}(mn)$ to $\mathcal{O}(r(m+n))$. This factorization also accelerates the matrix-vector product $\mathbf{M}\mathbf{x} = \mathbf{y}$ by decomposing it into two steps

- Step 1 $\mathbf{w} \leftarrow \mathbf{B}^T\mathbf{x}$
- Step 2 $\mathbf{y} \leftarrow \mathbf{A}\mathbf{w}$

which reduces the number of operations from $\mathcal{O}(mn)$ to $\mathcal{O}(r(m+n))$.

It is important to note that in practice, when using Fast BEM based on Hierarchical matrices, the complete dense matrix is never computed. Notably, the clustering of the unknowns and the partitioning of the matrix are exclusively dependent on the geometry and are independent of the Green's function. Different low-rank approximation algorithms exist:

- The most accurate according to Eckart-Young theorem is the Singular value decomposition (SVD). However, computing this decomposition is expensive $\mathcal{O}(r\,mn)$ (for truncated SVD for $m \geqslant n$, where r is the rank of the approximation and n, m are the dimensions of the matrix). Moreover, SVD also requires to assemble the initial dense matrix $\mathcal{O}(mn)$, a step that is prohibitive in our case.

- An alternative to the SVD is the Adaptive Cross Approximation (ACA), that we use here. This method is based on the point that every matrix of rank r is the sum of r matrices of rank 1. Thus, the corresponding algorithm improves at each iteration the accuracy of the approximation by adding rank-1 matrices similarly to a Gauss-pivot algorithm. At iteration k, the matrix $\mathbf{M} \in \mathbb{C}^{m\times n}$ is split into a rank-k approximation $\mathbf{M}_k = \sum_{l=1}^{k} \mathbf{u}_l\mathbf{v}_l^T = \mathbf{U}_k\mathbf{V}_k^T$, where $\mathbf{U}_k \in \mathbb{C}^{m\times k}$ and $\mathbf{V}_k \in \mathbb{C}^{n\times k}$ and a residual $\mathbf{R}_k = \mathbf{M} - \mathbf{M}_k$. The stopping criterion for this algorithm can write $\|\mathbf{M} - \mathbf{M}_k\|_F \leqslant \varepsilon_{\text{ACA}}\mathbf{M}$, where $\varepsilon_{\text{ACA}} > 0$ is a given tolerance and $\|\cdot\|_F$ is the Frobenius norm. Two versions of this method exist:

  - The Fully pivoted ACA which is expensive because it requires $\mathcal{O}(r\,mn)$ iterations to generate an approximation of rank r as well as the assembly of the complete matrix as an input.
  - The Partially pivoted ACA avoids the assembly of the complete matrix. Only one row or one column is assembled at each iteration. This changes the stopping criterion as the algorithm stops when the addition to a new rank-1 approximation does not improve the accuracy of the approximation $\mathbf{M}_k$ anymore: $\|\mathbf{u}_k\|_F\|\mathbf{v}_k\|_F \leqslant \varepsilon_{\text{ACA}}\|\mathbf{M}_k\|_F$. The corresponding complexity is $\mathcal{O}(r^2(m+n))$ instead of $\mathcal{O}(r\,mn)$.

In this work, we use the partially pivoted ACA (see Chaillat et al. (2017) for details).

> **Remark 2.4.** *In quasi-dynamic cases, if the geometry does not change in time, the data-sparse representation matrix is computed only once at the initialization (also true if the standard BEM are used), reducing drastically the computational time.*

2.3 Comparison between the two approaches

Two advantages of the H-BEM over the S-BEM can be mentioned. First, the H-BEM allows to take into account non uniformly discretized and non-planar fault geometries Bradley (2014). In addition, boundary condition can be handled more efficiently with the H-BEM (also true with the standard BEM) than with the S-BEM. Hence, in the simplified case of a 1D planar fault embedded in an infinite medium in mode II or III, the quasi static shear-stress change expressed at the mesh nodes in the center each 1D element can be re-written as follows

$$\begin{aligned}\tau^{qs}(z_i,t) &= \sum_{j=1}^{N} \delta(z_j,t)\left(K(z_i,\xi_j) - K(z_i,\xi_{j+1})\right) \\ &= \left(\delta(z_1,t)K(z_i,\xi_1) - \delta(z_N,t)K(z_i,\xi_{N+1})\right) + \sum_{j=2}^{N} K(z_i,\xi_j)\left(\delta(z_j,t) - \delta(z_{j-1},t)\right)\end{aligned} \tag{2.70}$$

As a consequence, if the displacement discontinuity δ is uniform on the fault width W_f, and the geometry, the materials properties and the loading are symmetrical with respect to the center of the fault, then only the fault width W_f has to be meshed. At the extremity of the mesh, two extremity nodes which take into account the loading must be included. The outer zone does not contribute to the integral and the corresponding quasi static shear-stress change τ^{qs} for a DOF in the outer zone is equal to zero. This is advantageous compared to the S-BEM which requires to truncate the domain far enough from the seismogenic zone, so that the periodic replications of the domain (assumed due to the use of FFT) would not influence the unknowns values at the fault interface.

3 Time discretization

Now, we can focus on the time discretization. Various methods exist as detailed in Section 3 in Chapter 1 and in A.A.1. We focus on the three adaptive time step methods implemented in this work that are among the most used methods in the earthquake cycle community. The first time stepping method is based on a hybrid explicit-implicit prediction-correction method inspired by Lapusta et al. (2000). The second time-stepping method is based on an explicit fourth/fifth order adaptive time step Runge-Kutta method inspired by Ozawa et al. (2022). And the third one is a hybrid prediction-correction / adaptive time step Runge-Kutta method inspired by Romanet and Ozawa (2021).

3.1 Main time stepping methods implemented

For all these methods, the discretized values of slip $\delta_i(t)$, slip-rate $V_i(t)$, state variable $\theta_i(t)$, shear-stress $\tau_i(t)$, quasi-static shear-stress $\tau_i^{qs}(t)$, state rate $\dot{\theta}_i(t)$ and quasi-static shear-stress rate $\dot{\tau}_i^{qs}(t)$ are computed at the centers of the elements at each time t.

(A) Predictor-corrector scheme (Lapusta et al., 2000). It starts with a prediction step

1. Initial prediction for slip and state variable at time $t+\Delta t$ using an explicit Euler scheme:

$$\delta_i^*(t+\Delta t) = \delta_i(t) + \Delta t V_i(t), \quad \theta_i^*(t+\Delta t) = \theta_i(t) + \Delta t \dot{\theta}_i(t). \tag{2.71}$$

2. Evaluation of the corresponding prediction of shear transfer $\tau_i^{qs}(t+\Delta t)$ using a Fast Fourier Transform and the computation of the Fourier coefficients of $\delta_i^*(t+\Delta t)$ or using Fast BEMs with $\mathscr{H}$-matrices.

3. Non-linear solution of the friction law for $V_i^*(t+\Delta t)$.

4. Evaluation of the corresponding state rate $\theta_i^*(t+\Delta t)$ from the evolution law on the state variable.

The second part is a correction step.

1. Final prediction for slip and state variable at time $t+\Delta t$ using an explicit Euler scheme:

$$\begin{aligned}\delta_i^{**}(t+\Delta t) &= \delta_i(t) + \Delta t/2\left(V_i(t) + V_i^*(t+\Delta t)\right),\\ \theta_i^{**}(t+\Delta t) &= \theta_i(t) + \Delta t/2\left(\dot\theta_i(t) + \dot\theta_i^*(t+\Delta t)\right).\end{aligned} \tag{2.72}$$

2. Evaluation of the corresponding prediction of shear transfer $\tau_i^{qs}(t+\Delta t)$ using a Fast Fourier Transform and the computation of the Fourier coefficients of $\delta_i^{**}(t+\Delta t)$ or using Fast BEMs with $\mathscr{H}$-matrices.

3. Non-linear solution of the friction law for $V_i^{**}(t+\Delta t)$.

4. Evaluation of the corresponding state rate $\theta_i^{**}(t+\Delta t)$ from the evolution law on the state variable.

5. Return $\delta_i^{**}(t+\Delta t)$, $V_i^{**}(t+\Delta t)$, $\theta_i^{**}(t+\Delta t)$, $\dot\theta_i^{**}(t+\Delta t)$

6. Evaluation of the evolution time step Δt which satisfies the criteria given in Lapusta et al. (2000) to ensure stability of the method and return to 1.

Figure 2.9 gives the structure of one prediction/correction step. Figure 2.10 represents

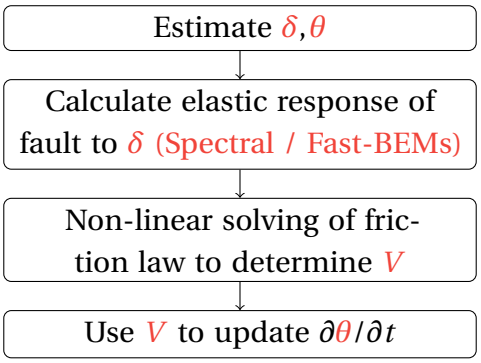

Figure 2.9 • Structure of the algorithm for one prediction/correction step to estimate interface unknowns (in red) at the next time step

one step of the prediction-correction method.

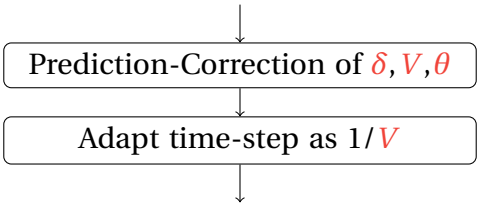

Figure 2.10 • Structure of the algorithm for one step of the prediction-correction method to estimate interface unknowns (in red) at the next time step

(B) Explicit method Ozawa et al. (2022). An alternative approach consists in first reformulating the contact problem as an ODE system. The unknowns of the ODE system considered are the shear-stress and the state-variable. One time-step relies on a fourth- fifth-order adaptive time-step Runge-Kutta method. One time-step of the algorithm is decomposed into three steps:

1. Evaluation of the quantities $\tau_i(t+\Delta t)$ and $\theta_i(t+\Delta t)$ with a fourth- fifth-order adaptive time-step Runge-Kutta method (Press & Teukolsky, 1992).
2. Evaluation of the field $V_i(t+\Delta t)$ using the friction law and the values of τ and θ at $t+\Delta t$.
3. Evaluation of the quasi-static shear-stress rate $\dot{\tau}_i^{qs}(t+\Delta t)$.

Figure 2.11 gives the structure of one step of the explicit RK method.

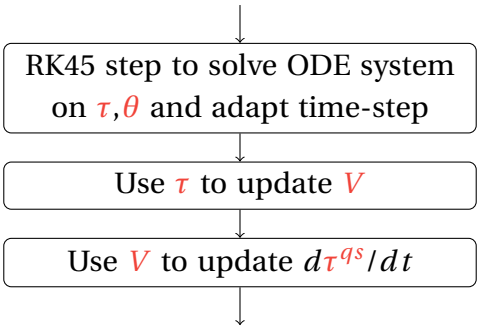

Figure 2.11 • Structure of the algorithm for one step of the explicit RK method to estimate interface unknowns (in red) at the next time step

(C) Hybrid scheme (Romanet & Ozawa, 2021). The third alternative consists in one prediction-correction stage on the full current time-step in parallel to two successive prediction-correction steps on half of the time-step.

1. Evaluation of $\delta_i(t+\Delta t)$, $V_i(t+\Delta t)$, $\theta_i(t+\Delta t)$ with a prediction-correction stage on the full current time-step. The results are denoted $\delta_{i_{\text{full}}}(t+\Delta t)$, $V_{i_{\text{full}}}(t+\Delta t)$, $\theta_{i_{\text{full}}}(t+\Delta t)$.
2. Evaluation of $\delta_i(t+\Delta t)$, $V_i(t+\Delta t)$, $\theta_i(t+\Delta t)$ with two successive prediction-correction stage on half of the current time step. The results are respectively denoted $\delta_{i_{\text{half}_1}}(t+\Delta t)$, $V_{i_{\text{half}_1}}(t+\Delta t)$, $\theta_{i_{\text{half}_1}}(t+\Delta t)$ and $\delta_{i_{\text{half}_2}}(t+\Delta t)$, $V_{i_{\text{half}_2}}(t+\Delta t)$, $\theta_{i_{\text{half}_2}}(t+\Delta t)$.

3. Evaluation of the error on slip and state variable at $t+\Delta t$ between the results of the prediction-correction on the full time step and the results after two successive prediction-correction stages on half time step

$$\varepsilon_\delta = \max_{i=1\ldots N_{ele}} \left| \frac{\delta_{i_{\text{full}}} - \delta_{i_{\text{half}_2}}}{\delta_{i_{\text{half}_2}}} \right|, \; \varepsilon_\theta = \max_{i=1\ldots N_{ele}} \left| \frac{\theta_{i_{\text{full}}} - \theta_{i_{\text{half}_2}}}{\theta_{i_{\text{half}_2}}} \right|, \; \varepsilon = \max\{\varepsilon_\delta, \varepsilon_\theta\}, \tag{2.73}$$

where $\delta_{i_{\text{full}}}, \delta_{i_{\text{half}_2}}, \theta_{i_{\text{full}}}, \theta_{i_{\text{half}_2}}$ are evaluated at $t+\Delta t$.

4. Adapt the time-step $\Delta t = 0.9 \left(\frac{\varepsilon_{\text{solver}}}{\varepsilon} \right)^{\frac{1}{3}} \Delta t$. $\varepsilon_{\text{solver}}$ corresponds to the solver tolerance.

5. Return $\delta_{i_{\text{half}_2}}(t+\Delta t)$, $V_{i_{\text{half}_2}}(t+\Delta t)$, $\theta_{i_{\text{half}_2}}(t+\Delta t)$, $\dot{\theta}_{i_{\text{half}_2}}(t+\Delta t)$

The comparison between the results obtained with both prediction-correction procedures allow to adapt the time step in the spirit of adaptive time-step Runge-Kutta method.

Figure 2.12 gives one step of the hybrid method. Where, the prediction-correction step is

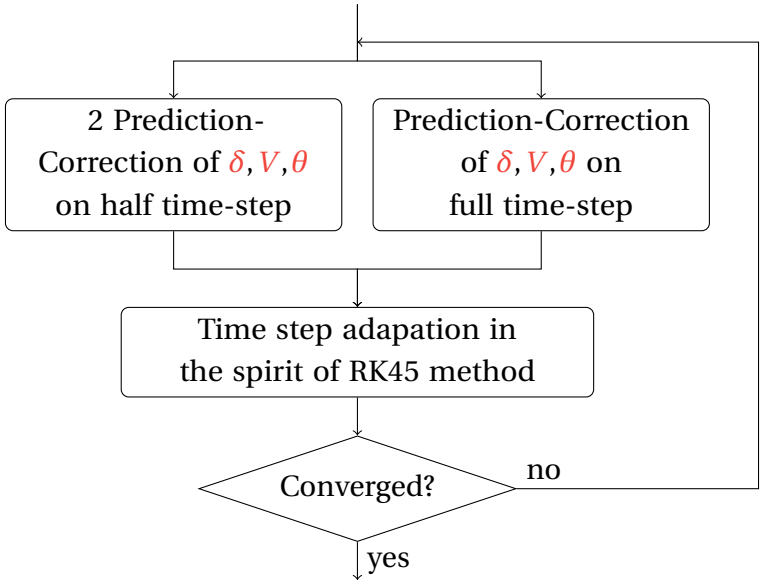

Figure 2.12 • Structure of the algorithm for one step of the hybrid method to estimate interface unknowns (in red) at the next time step

detailed in Figure 2.9.

Structure of the algorithm. Figure 2.13 gives an explanatory scheme that illustrates the structure of the algorithm for seismic cycle simulations. It highlights the choice of both time-stepping and space methods within the algorithm. The inputs correspond to:

- physical parameters (shear modulus, shear wave velocity, Poisson coefficient),
- rate-and-state parameters (cf. Table 2.17 for instance),
- creep rate out of rate and state zone V_{pl},

- space discretization and time discretization parameters (space method chosen, $\mathscr{H}$-matrix parameters, length of the rate-and-state zone, number of elements in the rate-and-state zone, size of the discretized domain, free surface option, final simulation time, eventually minimum time step)
- time stepping method parameters (time stepping method chosen, $\varepsilon_{\text{solver}}$, $\varepsilon_{\text{Newton}}$, $\text{maxiter}_{\text{Newton}}$)
- initial values of interface unknowns,
- export parameters

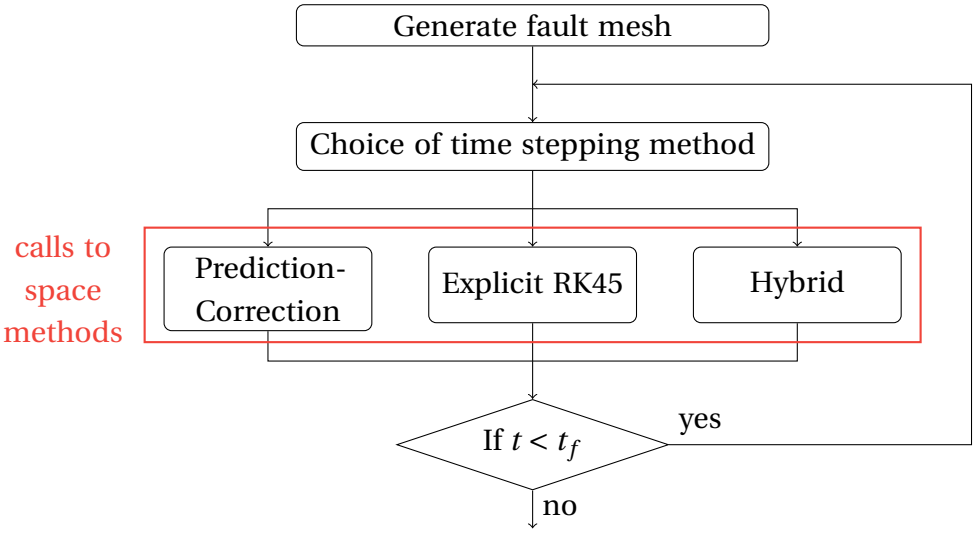

Figure 2.13 • Structure of the algorithm for seismic cycle simulations

The convergence of these numerical methods has not been investigated theoretically.

3.2 A priori theoretical comparison of the different numerical methods

The calculation of the shear-stress change from (2.55) is the most expensive step at each iteration. It is important to notice that, as we use time integration methods based on explicit time discretization schemes, we do not solve the boundary integral equation relating the shear stress change to the slip. We only need to calculate a convolution product in space, under the quasi-dynamic approximation (respectively in space and time for the fully-dynamic case) between the slip and the fundamental solution of the balance momentum equation to obtain the corresponding shear stress change at each iteration. In practice this operation is accelerated using the Fast-Fourier-Transform (S-BEM), which leads to compute a simple product at each iteration, or using Hierarchical matrices based BEM (H-BEM), which leads to compute a matrix-vector product at each iteration, in the code. To compare the different algorithms, we give the theoretical complexity of the calculation of the shear-stress change. If the S-BEM or the H-BEM are used, the estimated complexity is in the order of $\mathscr{O}(N\log(N))$ where N is the number of DOFs on the discretized fault. In addition, a comparison of the different time stepping methods used is required. Table 2.1 presents an a priori comparison of

Advance-in-time methods	Predictor-corrector scheme Lapusta et al. (2000)	Explicit method Ozawa et al. (2022)	Hybrid method Romanet and Ozawa (2021)
Number of times τ^{qs} is calculated in one time-step	2	$6 \times N_{\text{iter}}$	$6 \times N_{\text{iter}}$
Order of approximation of interface unknowns	2	5	2
Choice of the time step	Heuristic	Convergence based	Convergence based
Dynamic cases	✗	✗	✓

Table 2.1 • A priori comparison of the different time integration methods used.

the different advance-in-time methods used. We implemented each of these time integration methods mentioned in Table 2.1 with both the S-BEM and the H-BEM. Calculating the shear-stress using the H-BEM at each time-step allows to take into account more complex geometries and more complete physics in the model. The convergence of the implemented solvers has not been investigated theoretically, but we have studied their convergence as well as their sensitivity to the parameter that scale both space and time discretization in practice. Such convergence and sensitivity studies are not detailed in the literature. They are key to bridge the gap of a relevant comparison of existing numerical methods and propose a joint code to simulate seismic cycles.

4 Convergence assessment

We ran the calculations on a compute node from Unité de Mathématiques Appliquées (UMA) at ENSTA Paris for all the results obtained in this chapter. The specifications of the compute node used are given in Table 2.2.

CPU Reference	Core / CPU	Memory (GB)
Intel(R) Xeon(R) Gold 6244 3.60GHz	32	377

Table 2.2 • Compute node specifications.

4.1 Proposition of a configuration with an analytical aseismic solution

So far, the comparison and validation of seismic cycle simulations is still a challenging point (Harris et al., 2009; Day et al., 2005; Erickson et al., 2020a, 2023). In order to compare and validate numerically the different methods implemented, we need a reference solution. In this part, we propose a particular initialization of a seismic cycle problem that provides an analytical aseismic solution. The initialization of the problem differs from the one detailed in Section 1. The analytical aseismic solution proposed here is derived from an analytical solution for the boundary integral equation relating the quasi-static shear-stress change τ^{qs} and the slip δ (2.55) proposed by Segall (2010). To our best knowledge, this extension of this analytical value of τ^{qs} into an analytical aseismic solution has not been studied.

We consider the simplified quasi-dynamic mode II configuration (equivalent to mode III configuration in the simplified case of a planar fault) represented on Figure 2.1. The configuration considered consists in a planar fault embedded in a homogeneous, linear, elastic, isotropic infinite space. In-plane motion is assumed on either side of the fault. The quasi-dynamic approximation is considered. A regularized rate-and-state friction given by Equation (2.56) is considered on width W_f. Outside of width W_f, a constant creep rate V_{pl} is imposed.

Let us recall that the nucleation length is defined by (Rubin & Ampuero, 2005)

$$L_{\text{nuc}} = \begin{cases} 2 \times 1.3774 \times L_b, \ 0 \leqslant a/b \leqslant 0.3781 \\ \dfrac{2L_b}{\pi(1-a/b)^2}, \ a/b \to 1 \end{cases} \text{, where } L_b = \frac{GD_c}{\sigma_n b}. \tag{2.74}$$

Here the rate-and-state parameters a and b are chosen, so that a velocity strengthening state were considered, meaning that a perturbation of the steady state would die away as shown in Section 1.2 in Chapter 1. In practice, the fault width W_f is chosen large enough compared to L_{nuc}, so that it were large enough compared to the distance along fault on which unstable slip occurs.

Figure 2.14 represents the normalized initial values of the slip δ and the quasi-static shear-stress change τ^{qs}. The initial slip distribution writes

$$\delta(z,0) = \begin{cases} (1-(z/A)^2)^{3/2} \ \text{ if } |z| \leqslant A, \\ 0 \text{ if } |z| > A, \end{cases} \tag{2.75}$$

where A is the width along $\mathbf{z}$ direction on which the slip is non-zero. Here we choose A equal to the nucleation length $A = L_{\text{nuc}}$.

We recall the expression of the quasi-static shear-stress change τ^{qs}

$$\tau^{qs}(z,t) = \frac{G}{2\pi\epsilon} \int_\Gamma \frac{1}{z-\xi} \frac{\partial \delta}{\partial \xi}(\xi,t) d\xi. \tag{2.76}$$

Segall (2010) (see section 4.4 in his book) showed that using integral relations on Chebyshev polynomials, the corresponding initial quasi-static shear-stress change writes

$$\tau^{qs}(z,0) = -\frac{3G}{4A\epsilon} \begin{cases} 1-2(z/A)^2 \ \text{ if } |z| \leqslant A, \\ 1-2(z/A)^2 + 2|z/A|\sqrt{(z/A)^2-1} \text{ if } |z| > A. \end{cases} \tag{2.77}$$

The expression when $|z| > A$ is given by Romanet (2017). This example allows for a non-singular stress distribution everywhere on the fault. The analytical solutions proposed for δ and τ^{qs} have the advantage to be representative of the evolution of the slip and the quasi-static shear-stress change during a seismic event as shown on Figure 2.15.

The initial slip rate V and state-variable θ are chosen at their steady state values

$$V(z,0) = V_{pl}, \quad \theta(z,0) = \frac{D_c}{V_{pl}}. \tag{2.78}$$

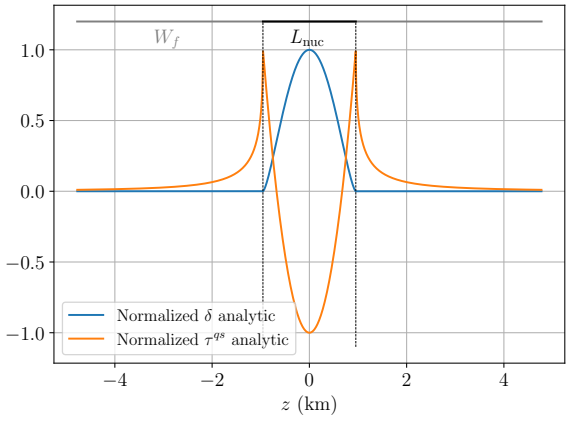

Figure 2.14 • Normalized evolution of initial values of the slip $\delta(z,0)$ and the quasi-static shear-stress change $\tau^{qs}(z,0)$ with respect to space on the rate-and-state fault width $W_f = 5L_{\text{nuc}}$.

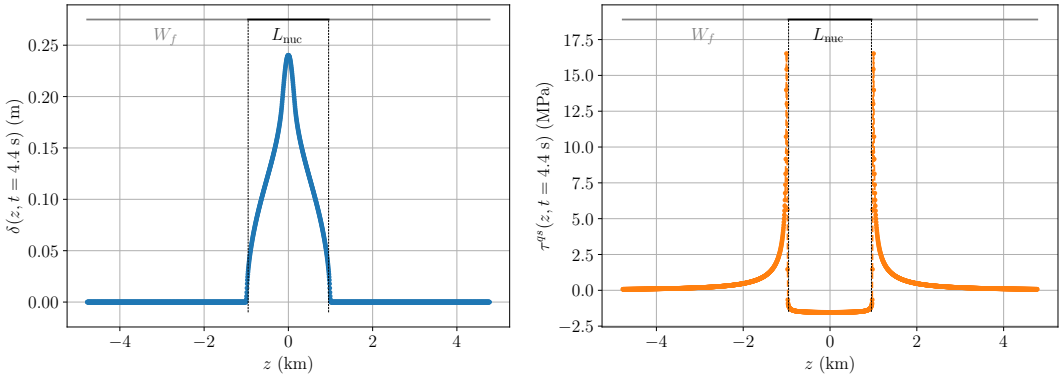

(a) **(b)**

Figure 2.15 • Spatial evolution of (a) the slip and (b) the shear-stress change at $t = 4.4$ s, during the first seismic event (simulation of a mode II configuration with a no-opening condition on the fault cf. Figure 2.1).

The corresponding analytic solution is given by

$$\begin{aligned} &\delta(z,t) = \delta(z,0) + V_{pl}\,t, \quad V(z,t) = V(z,0), \\ &\tau(z,t) = \tau^0 + \tau^{qs}(z,0) - \frac{G}{2c_s}V(z,0), \quad \theta(z,t) = \theta(z,0), \end{aligned} \tag{2.79}$$

where, τ^0 is constant due to constant values chosen for rate-and-state parameters a and b, and is defined consistently with the rate-and-state friction law as

$$\tau^0 = \sigma_n a \sinh^{-1}\left[\frac{V(z,0)}{2V_0}\exp\left(\frac{f_0 + b\ln(V_0/V(z,0))}{a}\right)\right] + \frac{G}{2c_s}V(z,0) - \tau^{qs}(z,0). \tag{2.80}$$

τ^0 takes into account the initial quasi-static shear stress value $\tau^{qs}(z,0)$ in order to ensure that the system remains in its steady state at each iteration.

The objectives are to assess the convergence of the developed numerical methods and to study the sensitivity of each method to its simulation parameters, in order to ensure the accurate and efficient use of these numerical tools. We distinguish sensitivity studies with

Parameter	Definition	Value, Unit
G	Shear modulus	$\simeq 30$ GPa
c_s	Shear wave velocity	3000 m/s
ν	Poisson coefficient	0.25
σ_n	Effective normal stress	100 MPa
a	Rate-and-state parameter	0.01
b	Rate-and-state parameter	0.009
D_c	Characteristic slip distance	1 mm
V_{pl}	Imposed slip-rate	10^{-9} m/s
V_0	Reference slip-rate	10^{-6} m/s
f_0	Reference friction coefficient	0.6
L_{nuc}	Nucleation length	1910 m
W_f	Rate-and-state fault width	$5L_{\text{nuc}}$

Table 2.3 • Parameters used for the convergence study.

respect to parameters that scale the space and time discretizations as proposed in the section below.

4.2 Methodology for the convergence study

We showed in Section 3.1 in Chapter 1 that the convergence of the results of a seismic cycle simulation relied on both space and time discretizations. Therefore, a sensitivity study with respect to the parameters of the different implemented numerical methods is key to choose parameter values that allow relevant interpretations of the seismic cycle simulations performed. It is crucial to choose refined enough parameters in order to simulate seismic cycles for which the seismic instability observed is not due to numerical artifacts, and the nucleation of the instabilities is well resolved for actual events. It is also important to balance this aspect with memory and computational costs. A complete sensitivity of the numerical methods implemented is difficult as they depend on numerous parameters. Focusing on the most relevant interactions between these parameters, we propose a strategy for the sensitivity study. Section 4.3 concentrates on one calculation of the quasi-static shear stress change τ^{qs} to study its accuracy with respect to the parameters that scale the space discretization and to the parameters inherent to the H-BEM. The numerical solution is compared to the analytical solution (2.77). Section 4.4 studies the sensitivity of the calculation of the interface unknowns δ, V, τ, θ, with respect to parameters that scale the time discretization for the different implemented time-stepping methods, using H-BEM. The simulations of an aseismic phase and of seismic cycles are distinguished in this part. The aseismic results are compared to the analytical solution (2.79), whereas the seismic cycle results are first compared to

reference results provided by Pierre Romanet (personal communication), then to refined results obtained with standard BEMs.

4.3 Accuracy of one calculation of the shear-stress change τ^{qs}

As a first step, we consider the accuracy of calculation of the quasi-static shear-stress change τ^{qs}. We concentrate on one calculation of τ^{qs} (in the quasi-dynamic approximation) as the calculation of the shear-stress change is the only stage of the algorithm that relies directly on the space discretization. Other steps are performed independently on each DOF. The calculation of τ^{qs} consists in the discretization of the BIE (2.76). It allows to compare the standard BEM to the H-BEM and the S-BEM. This sensitivity study is performed with respect to parameters which scale the space discretization of the fault Γ, i.e.:

- The number of mesh nodes that resolve the characteristic length L_b, the corresponding quantity $L_b/\Delta z$ is directly linked to the space step Δz.
- The ratio between the size of the discretized domain and the fault width W_f, denoted N_{rep} such that the length of the interface that is discretized writes $N_{\text{rep}} \times W_f$.

Our reference solution here is the analytical value of τ^{qs} (2.77) resulting from the slip distribution (2.75).

Convergence assessment with respect to $L_b/\Delta z$. We first vary the number of elements that resolve the characteristic length L_b: $L_b/\Delta z$. An adequate discretization of L_b ensures that the nucleation length is well resolved. In the case of seismic cycle simulations, it means that we can resolve correctly the occurrence of unstable slip on the fault. Numerical solutions for τ^{qs} obtained with the standard BEM, the H-BEM or the S-BEM are compared to the analytical solution (2.77) using a relative L^2-norm error defined as

$$\varepsilon_{\tau^{qs}} = \frac{\|\tau^{qs}_{\text{app}} - \tau^{qs}_{\text{ex}}\|_{L^2}}{\|\tau^{qs}_{\text{ex}}\|_{L^2}}, \tag{2.81}$$

where τ^{qs}_{app} is the quasi-static shear-stress change computed numerically, and τ^{qs}_{ex} is the analytical value of the quasi-static shear-stress change (2.77) evaluated at the centers of the 1D mesh elements. The L^2-norm is defined as $\|\mathbf{f}\|_{L^2} = \sqrt{\Delta z \sum_{i=1}^{N} f_i^2}$ since we assume the interface field quantities are constant per element, with N the number of DOFs, and Δz is the space step. We also consider the calculation of the time derivative of τ^{qs}, denoted $\partial\tau^{qs}/\partial t = \dot{\tau}^{qs}$ such that, recalling the definition of the slip-rate $\dot{\delta} = V$,

$$\dot{\tau}^{qs} = \frac{G}{2\pi\epsilon}\int_{\Gamma} \frac{1}{z-\xi}\frac{\partial V}{\partial \xi}(\xi, t)\, d\xi = 0, \quad \text{since } \frac{\partial V}{\partial \xi} = 0. \tag{2.82}$$

Given the evolution of slip in (2.79), and as it results from a uniform in space slip-rate distribution, the time derivative of the quasi-static shear-stress change should be zero. It confirms our interpretation of Equation (2.70). The Fourier transform with respect to space of $\dot{\tau}^{qs}$ writes

$$\dot{T}^{qs}(t; k) = \frac{G}{2}|k|\dot{D}(t; k) = \frac{G}{2}|k|\delta_D(k) = 0, \tag{2.83}$$

where $\dot{T}^{qs}(t;k)$ and $\dot{D}(t;k)$ are respectively the Fourier transform with respect to space of the time derivative of the quasi-static shear-stress change τ^{qs} and of the slip-rate V. We define the L^2-norm error on $\dot{\tau}^{qs}$

$$\varepsilon_{\dot{\tau}^{qs}} = \|\dot{\tau}^{qs}_{\text{app}} - \dot{\tau}^{qs}_{\text{ex}}\|_{L^2}, \tag{2.84}$$

Note that since $\dot{\tau}^{qs}_{\text{ex}}$ is equal to zero, we consider an absolute error for that case.

Figure 2.16 shows the evolution of the relative L^2-norm errors on the quasi-static shear-stress change τ^{qs} (a) and on its time derivative $\dot{\tau}^{qs}$ (b). Parameters used to compute these results are given in Table 2.4. As visible in Figure 2.16a, we obtain the same convergence

Parameters	N_{rep}	N_{leaf}	η	ε_{ACA}
BEM	1	/	/	/
H-BEM	1	100	3	10^{-5}
S-BEM	51	/	/	/

Table 2.4 • Space discretization parameters for convergence study with respect to $L_b/\Delta z$.

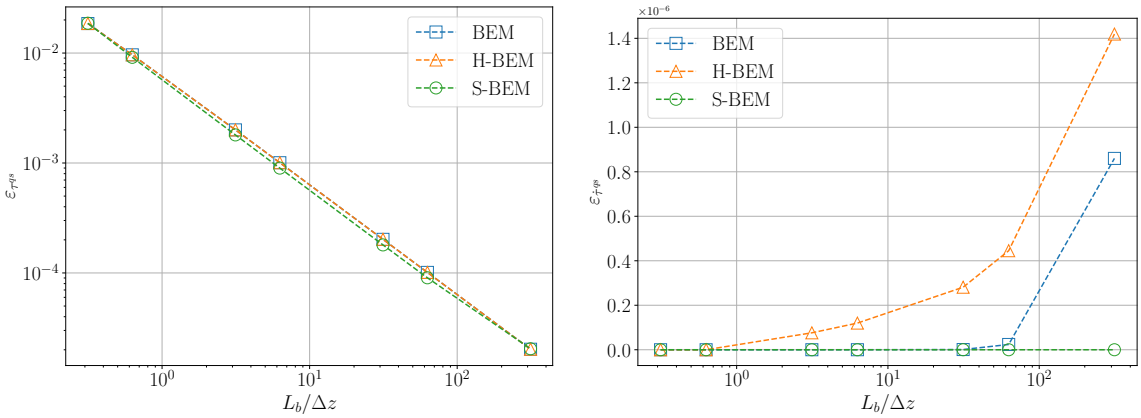

(a) **(b)**

Figure 2.16 • Relative L^2-norm error on (a) the quasi-static shear-stress change τ^{qs}: $\varepsilon_{\tau^{qs}}$ and on (b) its time derivative $\dot{\tau}^{qs}$: $\varepsilon_{\dot{\tau}^{qs}}$ with respect to $L_b/\Delta z$.

rate with the three methods (standard BEM, H-BEM and S-BEM). In Figure 2.16b, we obtain $\dot{\tau}^{qs} = 0$ using the S-BEM. The non-zero error values obtained with the standard BEM are the result of the accumulation of numerical errors, whereas the error values obtained using the H-BEM are, in addition, influenced by the data-sparse approximation of the boundary element matrix. Moreover, the tolerance for the low-rank approximation is fixed to 10^{-5}, and we obtain absolute error values $\varepsilon_{\dot{\tau}^{qs}}$ in the order of 10^{-6} with the H-BEM which makes sense. In practice, we consider $L_b/\Delta z \approx 6$ for the following seismic cycle simulations, which leads to an error of about 10^{-3} on τ^{qs} and about 10^{-7} on $\dot{\tau}^{qs}$ for the H-BEM.

Convergence assessment with respect to N_{rep}. Nevertheless, as explained in Section 2.1, convergence of the S-BEM depends on the size of the discretized domain. It has to be chosen

large enough, so that the interface field quantity values would not be influenced by the periodic replications of the fault behavior inherent to the use of Fast Fourier Transform in the case of the S-BEM. On the contrary, the size of the discretized domain should neither influence the calculation of τ^{qs} nor $\dot{\tau}^{qs}$ when using the standard BEM or the H-BEM, nor the calculation of $\dot{\tau}^{qs}$ when using the S-BEM. Figure 2.17 shows the evolution of the relative L^2-norm error on (a) the quasi-static shear-stress change τ^{qs}, and on (b) its time derivative $\dot{\tau}^{qs}$, with respect to the size of the number of replications of the fault width N_{rep}. Parameters used to compute these results are given in Table 2.5.

Parameters	$L_b/\Delta z$	N_{leaf}	η	ε_{ACA}
BEM	≈ 62	/	/	/
H-BEM	≈ 62	100	3	10^{-5}
S-BEM	≈ 62	/	/	/

Table 2.5 • Space discretization parameters for convergence study with respect to N_{rep}.

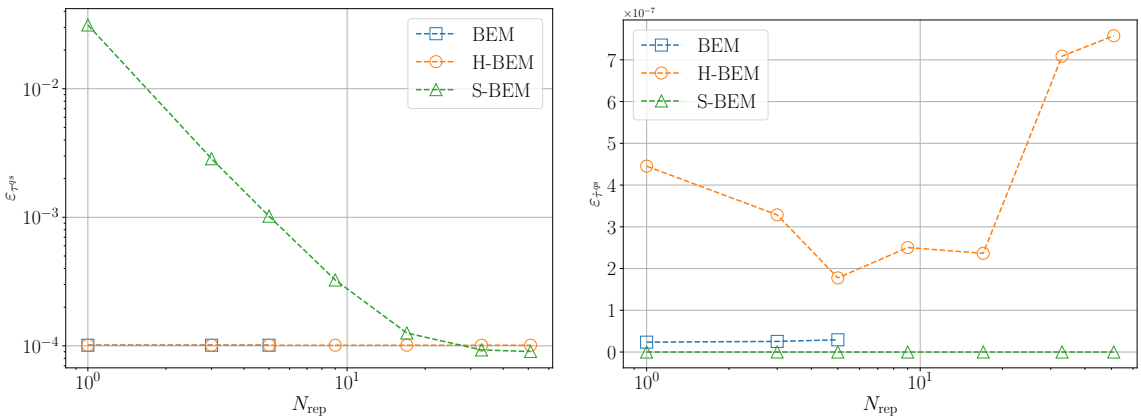

(a) **(b)**

Figure 2.17 • Relative L^2-norm error on (a) the quasi-static shear-stress change τ^{qs} and on (b) its time derivative $\dot{\tau}^{qs}$ with respect to the size of the discretized in terms of number of nucleation length N_{rep}. $L_b/\Delta z \approx 62$.

In Figure 2.17a, we can observe that the convergence is reached for the S-BEM (in the case $L_b/\Delta z \approx 62$), when the size of the domain is in the order of $33W_f$. As expected, a change in the size of the discretized domain does not influence the error values obtained with the standard BEM nor the H-BEM. These tests highlight that large problem sizes become prohibitive when using standard-BEM. In effect, we can notice that only 3 error values over 7 are displayed for the standard BEM. This is due to the fact that for other points, the allocated memory required to build the boundary element matrix using the standard BEMs is prohibitive ($N_{\text{rep}} = 5$ corresponds to a boundary element matrix of size $(N \times N)$ with $N = 10^5$ DOFs). Again, the non-zero error value of the time derivative of the quasi-static shear-stress change $\dot{\tau}^{qs}$ obtained with the standard BEM results from the accumulation of numerical errors, whereas the error values obtained using the H-BEM are, in addition, influenced by the data-sparse approximation of the boundary element matrix.

Convergence assessment with respect to H-BEM parameters. At that point, it is important to study the influence of the parameters introduced by the use of the H-BEM: N_{leaf}, η and ε_{ACA}. We recall that N_{leaf} is the stopping criterion for the clustering of the unknowns, η is the admissibility coefficient that allows to determine a priori low-rank blocks in the boundary element matrix, and ε_{ACA} is the tolerance for the low-rank approximation of admissible blocks. Figure 2.18 represents the evolution of $\varepsilon_{\tau^{qs}}$ with respect to ε_{ACA} for different values of η and when $N_{\text{leaf}} = 200$ (a) or $N_{\text{leaf}} = 5$ (b). Parameter values used for these results are in Table 2.6.

Parameters	$L_b/\Delta z$	N_{rep}
BEM	≈ 6	1
H-BEM	≈ 6	1

Table 2.6 • Space discretization parameters for convergence study with respect to N_{rep}.

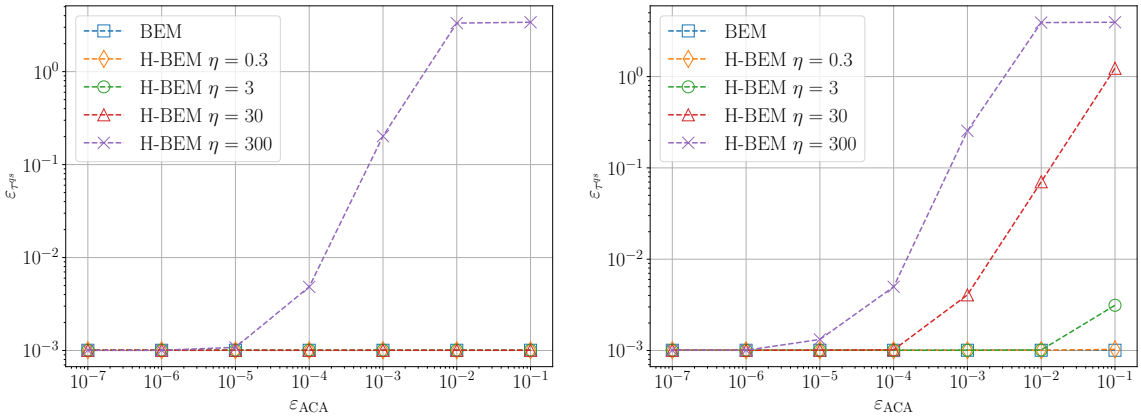

(a) $N_{\text{leaf}} = 200$.

(b) $N_{\text{leaf}} = 5$.

Figure 2.18 • Relative L^2-norm error on the quasi-static shear-stress change τ^{qs} with respect to ε_{ACA} for different values of η; $L_b/\Delta z \approx 6$.

Comparing both figures, we can interpret that the smaller the value of N_{leaf}, the larger the number of admissible blocks for a given value of the admissibility coefficient η. The limiting value for N_{leaf} is $N_{\text{leaf}} = N$, and corresponds to the total number of DOFs. In this case, the H-BEM is equivalent to the standard BEM. As visible in Figure 2.18b, the larger the value of the admissibility coefficient η, the larger the number of a priori low-rank blocks exhibited by the admissibility condition (2.69). Large values of η imply that we consider as admissible full-rank blocks. As a consequence, for large values of η and large values of the tolerance ε_{ACA}, the data-sparse approximation of the BEM matrix and of τ^{qs} is way less accurate with the H-BEM than with the standard BEM. If the value of η is small enough, such that none of the blocks would be admissible, then the H-BEM would again be equivalent to the standard BEM. Finally, the lower the value of the tolerance ε_{ACA} for the low-rank approximation of admissible blocks, the closer to the dense boundary element matrix its data-sparse approximation. The

values $N_{\text{leaf}} = 100$, $\eta = 3$ and $\varepsilon_{\text{ACA}} = 10^{-5}$ chosen for the following simulations allow the H-BEM to reach accurate enough approximations of the quasi-static shear-stress τ^{qs} compared to the standard BEM.

Finally, we compare the performances of the standard BEM, the H-BEM and the S-BEM. Parameters have also been chosen so that the same numbers of DOFs were considered for each method, they are given in Table 2.7. Figure 2.19a shows observed and estimated CPU time to compute BEM matrix with respect to the number of degrees of freedom (DOFs) N for the standard BEM and the H-BEM. It confirms that the CPU time to compute the BEM matrix is in the order of $\mathcal{O}(N^2)$ for the standard BEM and $\mathcal{O}(N\log(N))$ for the H-BEM. Figure 2.19b shows observed and estimated CPU time to compute the quasi-static shear-stress change τ^{qs} with respect to the number of DOFs N. It confirms that the CPU time to compute τ^{qs} is in the order of $\mathcal{O}(N^2)$ for the standard BEM and $\mathcal{O}(N\log(N))$ for the H-BEM and the S-BEM. Here, the computational time is larger for the H-BEM than for the S-BEM as the S-BEM is performed using an optimized Python library, and the other methods are only using in-house non optimized developments. Figure 2.19c and Figure 2.19d respectively represent the storage requirement N_s and the compression rate $\tau(\mathcal{H})$ with respect to the number of DOFs N. N_s is in the order of $\mathcal{O}(N^2)$ for the standard BEM and in the order of $\mathcal{O}(N\log(N))$ for the H-BEM. The compression rate $\tau(\mathcal{H})$ is in the order of $\mathcal{O}(1)$ for the standard BEM as the dense matrix is fully computed, and in the order of $\mathcal{O}(N^{-1}\log(N))$ for the H-BEM. In Figure 2.19, we can notice that only four points over seven are represented for the standard BEM. This is due to the prohibitive memory cost required from $N > 10^5$ DOFs, which shows the advantage of the H-BEM over the standard BEM for large problems. In Figure 2.19e, we show that each simulation carried out with the standard BEM, the H-BEM and the S-BEM to compute τ^{qs} has been performed so that it lead to the same relative L^2-norm error $\varepsilon_{\tau^{qs}}$.

Parameters	$L_b/\Delta z$	N_{rep}	N_{leaf}	η	ε_{ACA}
BEM	$\in \{0.3, 0.6, 3, 6, 15, 31, 62\}$	33	/	/	/
H-BEM	$\in \{0.3, 0.6, 3, 6, 15, 31, 62\}$	33	100	3	10^{-5}
S-BEM	$\in \{0.3, 0.6, 3, 6, 15, 31, 62\}$	33	/	/	/

Table 2.7 • Space discretization parameters to compare the performances of the standard BEM, the H-BEM and the S-BEM.

Conclusions on the convergence assessments in space and link with convergence assessments in time. In this part, we carried out sensitivity tests on the calculation of the quasi-static shear-stress change and its time derivative with respect to parameters that scales the space discretization of the problem. We showed that for a fixed space step Δz (respectively fixed number of elements that resolve the characteristic length L_b: $L_b/\Delta z$), we could choose converged values of the parameters N_{rep} for the S-BEM and N_{leaf}, η and ε_{ACA} for the H-BEM.

Before studying the sensitivity of the different implemented adaptive time-stepping methods with respect to their simulation parameters in the following part, we want to choose an adequate value of $L_b/\Delta z$ so that the solving in time were numerically stable. An appropriate

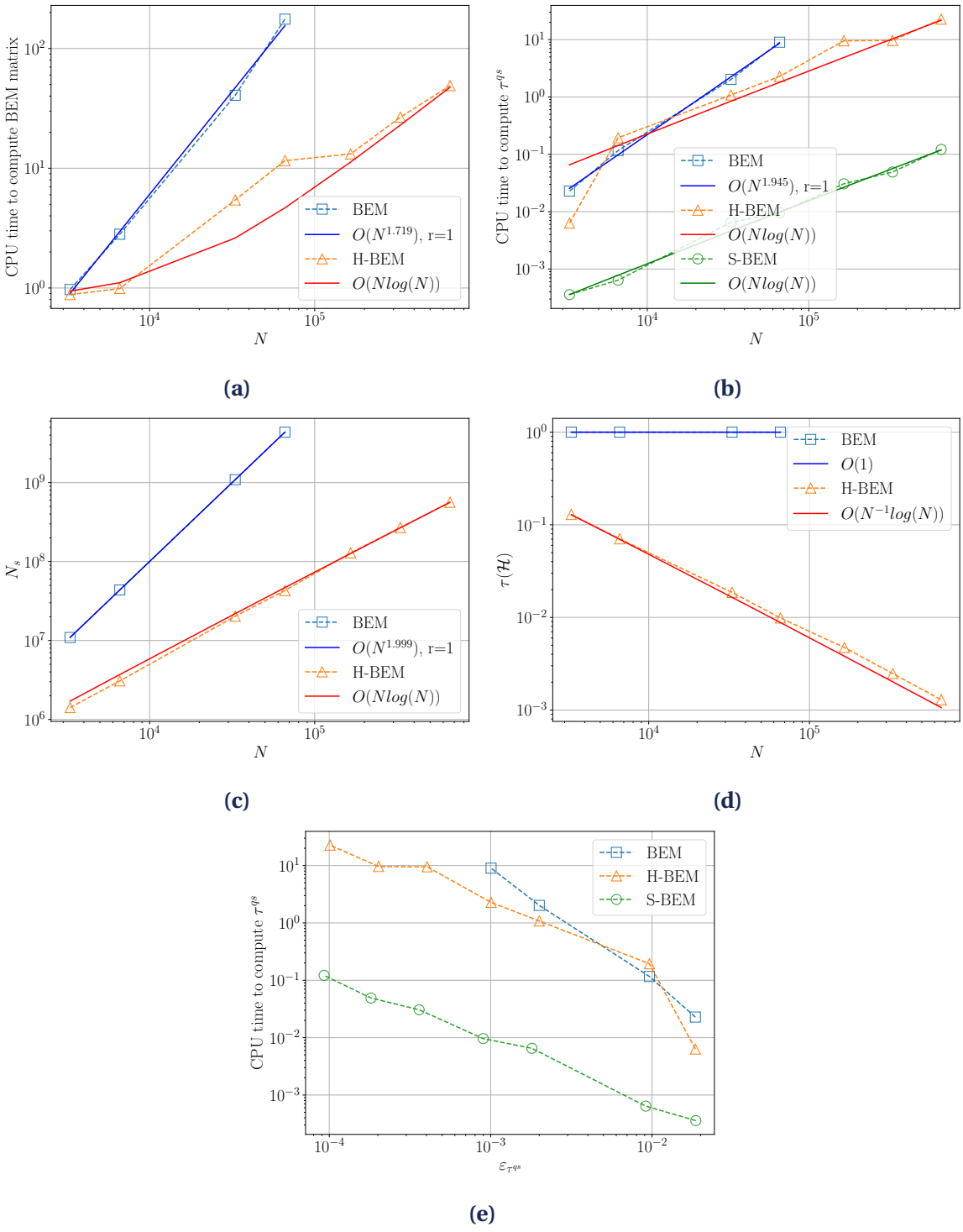

Figure 2.19 • Observed and estimated (a) CPU time to compute the BEM matrix with respect to the number of DOFs N; (b) CPU time to compute the quasi-static shear-stress change τ^{qs} with respect to the number of DOFs N; (c) memory requirement N_s and (d) compression rate $\tau(\mathcal{H})$ with respect to the number of DOFs N; (e) CPU time to compute τ^{qs} with respect to $\varepsilon_{\tau^{qs}}$.

choice of $L_b/\Delta z$ is important as the error in space can cumulate in time. To this aim, we perform a seismic cycle simulation, using the hybrid prediction-correction - RK45 method inspired by Romanet and Ozawa (2021), initialized so that a seismic event occurred right after the initialization for different values of the number of elements that resolve L_b. We consider a planar fault embedded in a linear, isotropic, elastic, infinite medium (see Figure 2.1). In-plane strains and a no-opening condition on the fault are assumed. The fault is under rate-and-state friction along the fault width W_f and rate-weakening values of the rate-and-state parameters are considered so that unstable slip could occur. The quasi-dynamic approximation is considered. The initial values of the interface unknowns are:

$$\begin{aligned}
&\delta(z,0) = 0,\\
&V(z,0) = \begin{cases} 10^{-3}\left(\exp(-z^2/L_{\text{nuc}}) - \exp(-L_{\text{nuc}}/4)\right) + V_{pl}, & \text{if } z \in [-L_{\text{nuc}}/2, L_{\text{nuc}}/2],\\ V_{pl} \text{ otherwise,} \end{cases}\\
&\tau(z,0) = \tau^0 - G/(2c_s)V(z,0),\\
&\theta(z,0) = D_c/V_{pl}.
\end{aligned} \tag{2.85}$$

Figure 2.20 shows the evolution of the maximum in depth of the four interface unknowns: (a) the slip δ, (b) the slip-rate V, (c) the shear-stress τ and (d) the state-variable θ with respect to time for different values of $L_b/\Delta z$. We can observe that for $L_b/\Delta z \geqslant 6$, the time evolution converges towards the most refined solution. Ozawa et al. (2022) had estimated at least $L_b/\Delta z \geqslant 3$. Parameters used for these simulations are given in Table 2.8.

Parameter	Definition	Value, Unit
μ	Shear modulus	$\simeq 30$ GPa
c_s	Shear wave velocity	3000 m/s
σ_n	Effective normal stress at the fault interface	100 MPa
$a(z)$	Rate and state parameter	0.009
$b(z)$	Rate and state parameter	0.01
$D_c(z)$	Characteristic slip distance	1 mm
V_{pl}	Imposed slip rate out of rate-and-state zone	10^{-9} m/s
V_0	Reference slip rate	10^{-9} m/s
f_0	Reference friction coefficient	0.6
W_f	Width of the rate-and-state zone	$5L_{\text{nuc}}$ km

Table 2.8 • Parameter values used for quasi-dynamic in-plane case.

4.4 Convergence in time

Now that we chose converged parameter values for the space discretization, the second step consists in studying the influence of the parameters that scales the time discretization. We first focus on the simulation of an aseismic phase. We compare the results obtained with each adaptive time-stepping method to the analytical aseismic solution Equation (2.79).

The parameters considered are:

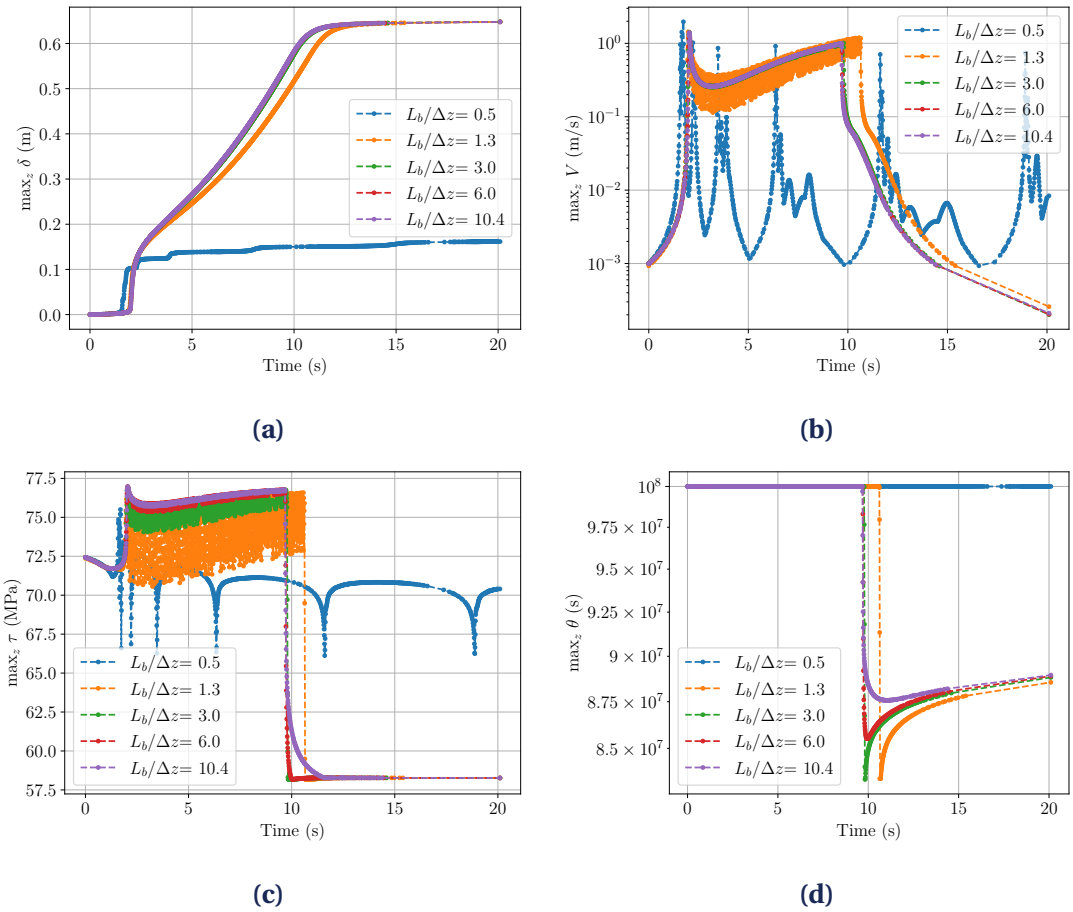

Figure 2.20 • Evolution of the maximum in depth of (a) the slip δ, (b) the slip-rate V, (c) the shear-stress τ, and (d) the state variable θ with respect to time during one seismic event for different values of $L_b/\Delta z$.

- the solver tolerance $\varepsilon_{\text{solver}}$ is a parameter of the explicit method inspired from Ozawa et al. (2022) and of the hybrid method inspired from Romanet and Ozawa (2021), it does not have the same meaning for each method (cf. Section 3.1);
- the Newton-Raphson algorithm tolerance $\varepsilon_{\text{Newton}}$ and the maximum number of iterations of Newton-Raphson algorithm $\text{maxiter}_{\text{Newton}}$ are parameters of the predictor-corrector method inspired from Lapusta et al. (2000) and of the hybrid method inspired from Romanet and Ozawa (2021);
- the coefficient β_{min}, which multiplies the initial time step for the three methods implemented and which influences the minimum time-step value for the predictor-corrector method inspired from Lapusta et al. (2000).

Convergence tests using the analytical aseismic solution Equation (2.79)

We start by showing the convergence tests carried out using the analytical aseismic solution Equation (2.79). The problem is initialized with the analytical solution taken at $t = 0$. The final simulation time is $t_{\text{final}} = 10$ yrs. For each time-stepping method, we define the relative

L^2-norm error in space on each interface unknown at the final time step as

$$\begin{aligned}
\varepsilon_{\delta}^{t_{\text{final}}} &= \frac{\|\delta_{\text{app}}(\cdot, t_{\text{final}}) - \delta_{\text{ex}}(\cdot, t_{\text{final}})\|_{L^2}}{\|\delta_{\text{ex}}(\cdot, t_{\text{final}})\|_{L^2}}, \; \varepsilon_{V}^{t_{\text{final}}} = \frac{\|V_{\text{app}}(\cdot, t_{\text{final}}) - V_{\text{ex}}(\cdot, t_{\text{final}})\|_{L^2}}{\|V_{\text{ex}}(\cdot, t_{\text{final}})\|_{L^2}}, \\
\varepsilon_{\tau}^{t_{\text{final}}} &= \frac{\|\tau_{\text{app}}(\cdot, t_{\text{final}}) - \tau_{\text{ex}}(\cdot, t_{\text{final}})\|_{L^2}}{\|\tau_{\text{ex}}(\cdot, t_{\text{final}})\|_{L^2}}, \; \varepsilon_{\theta}^{t_{\text{final}}} = \frac{\|\theta_{\text{app}}(\cdot, t_{\text{final}}) - \theta_{\text{ex}}(\cdot, t_{\text{final}})\|_{L^2}}{\|\theta_{\text{ex}}(\cdot, t_{\text{final}})\|_{L^2}},
\end{aligned} \tag{2.86}$$

where $\delta_{\text{app}}(\cdot, t_{\text{final}})$, $V_{\text{app}}(\cdot, t_{\text{final}})$, $\tau_{\text{app}}(\cdot, t_{\text{final}})$, and $\theta_{\text{app}}(\cdot, t_{\text{final}})$ correspond to the slip δ, the slip-rate V, the shear-stress τ and the state-variable θ, computed numerically at the final time step, and $\delta_{\text{ex}}(\cdot, t_{\text{final}})$, $V_{\text{ex}}(\cdot, t_{\text{final}})$, $\tau_{\text{ex}}(\cdot, t_{\text{final}})$, and $\theta_{\text{ex}}(\cdot, t_{\text{final}})$ are their analytical values at the final time step. The L^2-norm is defined in the same way as for Equation (2.81). This error quantifies the accumulated error during an aseismic phase.

In order to present more compact results, we concentrate on results obtained for the H-BEM as it is the most promising method for more complex problems (i.e. accounting for multi-physics couplings and geometrical complexities). We fixed the parameters for the space discretization in this study (see Table 2.9).

Parameters	$L_b/\Delta z$	N_{rep}	N_{leaf}	η	ε_{ACA}
H-BEM	6	1	100	3	10^{-5}

Table 2.9 • Space discretization parameters for the convergence tests on the different time-stepping methods using the analytical aseismic solution Equation (2.79).

Predictor-corrector time-stepping method. Table 2.10 gives the values of the relative final L^2-norm error on the slip δ, the slip-rate V, the shear-stress τ and the state variable θ with respect to the tolerance of the Newton-Raphson method $\varepsilon_{\text{Newton}}$ for the predictor-corrector time-stepping method, using the H-BEM. We do not observe a clear convergence with respect to $\varepsilon_{\text{Newton}}$. The error values are in the same order of magnitude, meaning that the method seems to be quite robust regarding the parameter $\varepsilon_{\text{Newton}}$ for this kind of steady state cases. Also, the errors reached are larger than those obtained with explicit and hybrid methods below. This can be linked to the fact that slip-rate values found as an output of the Newton-Raphson algorithm were local minima of the nonlinear friction law that achieved the tolerance of the Newton-Raphson method, which also limits the convergence of the prediction-correction method.

The parameter β_{min} which multiplies the initial time-step and limits the minimum time-step at each iteration does not have any influence here as the minimum time-step is never reached during the aseismic phase. We chose $\beta_{\text{min}} = 0.12$ for each time-stepping method. Also, the maximum number of iterations of the Newton-Raphson algorithm $\text{maxiter}_{\text{Newton}}$ is chosen equal to 40 (for both prediction-correction and hybrid methods), so that it would not influence the convergence of the simulation. In practice, 3 to 4 iterations of the Newton-Raphson algorithm are sufficient at each time-step.

Explicit time-stepping method. Figure 2.21 shows the evolution of the relative final L^2-norm error on (a) the slip δ, (b) the slip-rate V, (c) the shear-stress τ, and (d) the state variable θ

$\varepsilon_{\text{Newton}}$	10^{-1}	10^{-2}	10^{-4}	10^{-6}	10^{-8}
$\varepsilon_{\delta}^{t_{\text{final}}}$	$3.843{\cdot}10^{-4}$	$3.541{\cdot}10^{-4}$	$3.817{\cdot}10^{-4}$	$3.817{\cdot}10^{-4}$	$3.817{\cdot}10^{-4}$
$\varepsilon_{V}^{t_{\text{final}}}$	$1.397{\cdot}10^{-2}$	$1.756{\cdot}10^{-2}$	$1.730{\cdot}10^{-2}$	$1.731{\cdot}10^{-2}$	$1.731{\cdot}10^{-2}$
$\varepsilon_{\tau}^{t_{\text{final}}}$	$4.268{\cdot}10^{-4}$	$3.356{\cdot}10^{-4}$	$3.312{\cdot}10^{-4}$	$3.312{\cdot}10^{-4}$	$3.312{\cdot}10^{-4}$
$\varepsilon_{\theta}^{t_{\text{final}}}$	$1.053{\cdot}10^{-3}$	$1.007{\cdot}10^{-3}$	$9.957{\cdot}10^{-4}$	$9.958{\cdot}10^{-4}$	$9.958{\cdot}10^{-4}$

Table 2.10 • Relative final L^2-norm error on the slip δ, the slip-rate V, the shear-stress τ and the state variable θ with respect to the tolerance of the Newton-Raphson method $\varepsilon_{\text{Newton}}$ for the predictor-corrector time-stepping method, using the H-BEM.

with respect to the solver tolerance $\varepsilon_{\text{solver}}$ for the explicit time-stepping method using the H-BEM. For each interface unknown considered, we observe a nice convergence with respect to $\varepsilon_{\text{solver}}$.

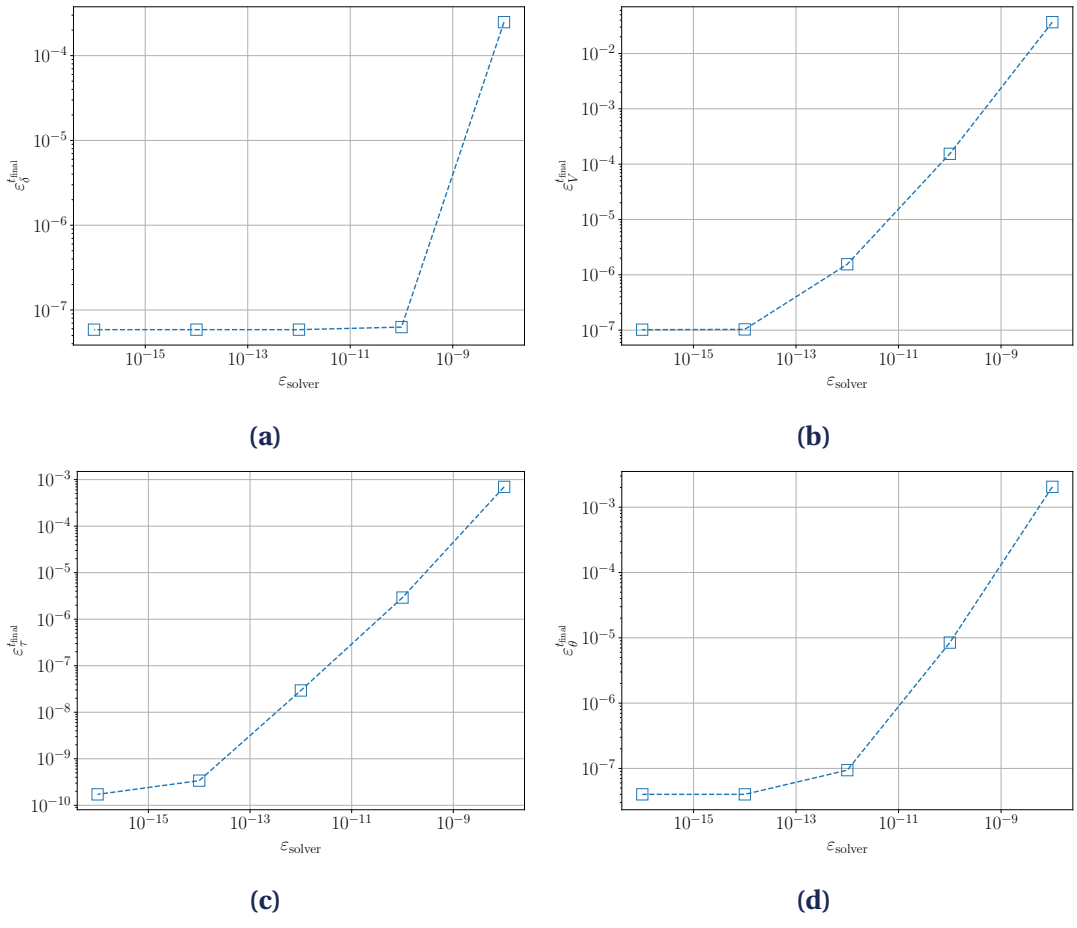

Figure 2.21 • Relative L^2-norm error on (a) the slip δ, (b) the slip-rate V, (c) the shear-stress τ, and (d) the state variable θ with respect to the solver tolerance $\varepsilon_{\text{solver}}$ for the explicit time-stepping method using the H-BEM.

Hybrid time-stepping method. Figure 2.22 shows the evolution of the relative final L^2-norm error on (a) the slip δ, (b) the slip-rate V, (c) the shear-stress τ, and (d) the state variable θ

with respect to the solver tolerance $\varepsilon_{\text{solver}}$ for different values of the tolerance for the Newton-Raphson method $\varepsilon_{\text{Newton}}$ for the hybrid time-stepping method using the H-BEM. For each interface unknown considered, we observe a clear convergence with respect to $\varepsilon_{\text{solver}}$ when $\varepsilon_{\text{Newton}} \geqslant 10^{-4}$. We notice a non-negligible coupling between the effect of $\varepsilon_{\text{solver}}$ and $\varepsilon_{\text{Newton}}$ for the convergence. In particular, if $\varepsilon_{\text{Newton}} > \varepsilon_{\text{solver}}$, it limits the convergence rate towards the analytical solution. The latter interpretation highlights that the error on the slip-rate obtained by the nonlinear solving of the friction law using Newton-Raphson method limits the convergence of the other interface unknowns (the slip δ and the state-variable θ notably) which are calculated thanks to the slip-rate V. Therefore, we must choose $\varepsilon_{\text{solver}} \leqslant \varepsilon_{\text{Newton}}$.

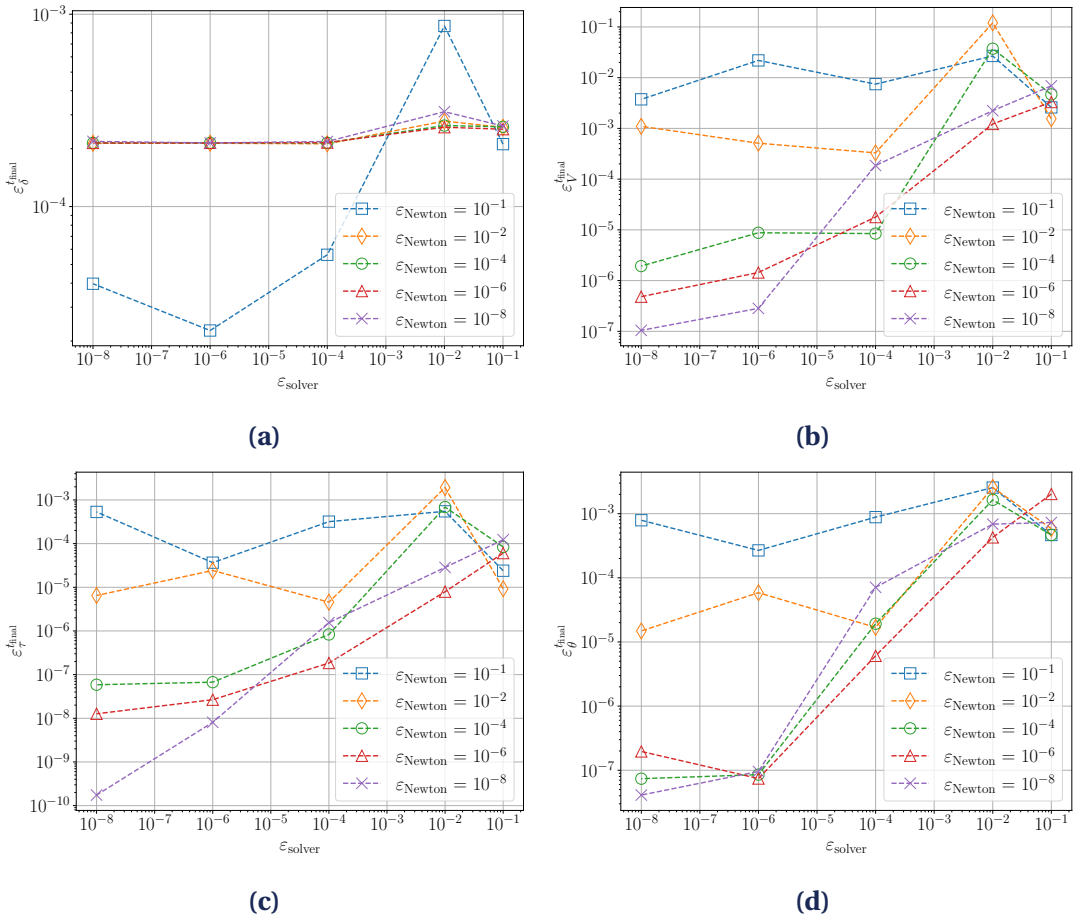

Figure 2.22 • Relative final L^2-norm error on (a) the slip δ, (b) the slip-rate V, (c) the shear-stress τ, and (d) the state variable θ with respect to the solver tolerance $\varepsilon_{\text{solver}}$ for different values of the tolerance for the Newton-Raphson method $\varepsilon_{\text{Newton}}$ for the hybrid time-stepping method using the H-BEM.

In this part, we showed the sensitivity of the different time-stepping methods with respect to parameters that scales the time discretization in the case of an aseismic slip simulation only. However, these results are not sufficient to study the sensitivity of the time-stepping methods implemented with respect to their parameters. The analytical solution considered does not account for rapid variations in the interface unknowns magnitude linked to the occurrence of a seismic event. Thus, in the second part, we want to carry out sensitivity tests on a more realistic seismic cycle simulation.

Comparison of seismic cycle simulations with results provided by Pierre Romanet (personal communication)

As seismic cycle problems do not admit analytical solution, we first propose a comparison between results provided by Pierre Romanet for the in-plane strain configuration of a planar fault under rate-and-state friction embedded in a linear, elastic, isotropic infinite medium as represented in Figure 2.1 and our results. We use the three time-stepping methods implemented. The problem is initialized so that a seismic event would be triggered at initialization (see Equation (2.85)). One difficulty is that seismic cycle simulations are very sensitive to a tiny change in initial condition. Here, as our implementation of the space discretization of the fault is different from Romanet's, which leads to a small change in the initialization of the slip-rate (the only interface unknown that is not uniform in space at initialization). The error is

$$\varepsilon_V^{t=0} = \frac{\| V_{\text{app}}(z,0) - V_{\text{Romanet}}(z,0) \|}{\| V_{\text{Romanet}}(z,0) \|} \approx 3.19 \cdot 10^{-5}. \tag{2.87}$$

Due to this small discrepancy, the adaptive time-stepping method incorporating S-BEM used by Romanet and our different time-stepping methods do not calculate the unknowns at the same time-steps. This can also lead to a shift in time from one result compared to the other, which makes the comparison of the time evolutions of the interface unknowns almost impossible. Hence, we choose the following criterions for the comparison:

- the time at which the slip-rate V first exceeds 1 m/s for each seismic event
- the spatial evolution of the interface unknowns at the time at which the slip-rate V first exceeds 1 m/s for each seismic event (we neglect the small difference in the space discretization between Romanet's results and ours).

Another difficulty of this study, is that the different adaptive time-step methods implemented do not depend on the same parameters.

Tables 2.11 and 2.12 give the simulation parameters used for this comparison study. The results provided by Pierre Romanet were obtained using the S-BEM and the hybrid time-stepping method. Thus, we fixed the same parameters for the S-BEM and the hybrid time-stepping method, and we fixed parameters to obtain similar results for the standard BEM, the H-BEM and for the prediction-correction and the explicit time-stepping methods. The final simulation time is $t_{\text{final}} = 34$ yrs, which allows to observe 3 seismic events. The time period of each inter-seismic phase is in the order of 16,9 yrs.

Parameters	$L_b/\Delta z$	N_{rep}	N_{leaf}	η	ε_{ACA}
standard BEM	6	1	/	/	/
H-BEM	6	1	100	3	10^{-5}
S-BEM	6	9	/	/	/

Table 2.11 • Space discretization parameters for the comparison study between our results and the results provided by Pierre Romanet (personal communication) on a seismic cycle simulation.

Parameters	$\beta_{\min}$	$\varepsilon_{\text{Newton}}$	$\text{maxiter}_{\text{Newton}}$	$\varepsilon_{\text{solver}}$
Prediction-correction	0.12	10^{-8}	40	/
Explicit method	0.12	/	/	10^{-16}
Hybrid method	0.12	10^{-8}	40	10^{-6}

Table 2.12 • Time discretization parameters for the comparison study between our results and the results provided by Pierre Romanet (personal communication) on a seismic cycle simulation.

Table 2.13 gives the absolute and relative errors, denoted $E_{t_{V>1\text{ m/s}}}$ and $\varepsilon_{t_{V>1\text{ m/s}}}$ respectively, on the time at which the slip-rate V first exceeds 1m/s compared to Romanet's results for each seismic event. The absolute error is given in seconds for the first seismic event, and in years for the second and the third seismic event. The absolute errors increase with respect to time but remain acceptable relatively to Romanet's results.

Seismic event index		1		2		3	
Time stepping method	Spatial method	$E_{t_{V>1\text{ m/s}}}$ (s)	$\varepsilon_{t_{V>1\text{ m/s}}}$	$E_{t_{V>1\text{ m/s}}}$ (yrs)	$\varepsilon_{t_{V>1\text{ m/s}}}$	$E_{t_{V>1\text{ m/s}}}$ (yrs)	$\varepsilon_{t_{V>1\text{ m/s}}}$
Prediction-correction	BEM	$1.82\cdot10^{-3}$	$9.04\cdot10^{-4}$	$3.54\cdot10^{-1}$	$2.08\cdot10^{-2}$	$7.07\cdot10^{-1}$	$2.08\cdot10^{-2}$
	H-BEM	$1.82\cdot10^{-3}$	$9.04\cdot10^{-4}$	$3.54\cdot10^{-1}$	$2.08\cdot10^{-2}$	$7.08\cdot10^{-1}$	$2.08\cdot10^{-2}$
	S-BEM	$1.83\cdot10^{-4}$	$9.10\cdot10^{-5}$	$3.43\cdot10^{-1}$	$2.02\cdot10^{-2}$	$6.11\cdot10^{-1}$	$1.80\cdot10^{-2}$
Explicit	BEM	$2.77\cdot10^{-3}$	$1.38\cdot10^{-3}$	$3.24\cdot10^{-1}$	$1.91\cdot10^{-2}$	$6.48\cdot10^{-1}$	$1.91\cdot10^{-2}$
	H-BEM	$2.76\cdot10^{-3}$	$1.37\cdot10^{-3}$	$3.24\cdot10^{-1}$	$1.91\cdot10^{-2}$	$6.47\cdot10^{-1}$	$1.91\cdot10^{-2}$
	S-BEM	$9.25\cdot10^{-4}$	$4.60\cdot10^{-4}$	$2.60\cdot10^{-1}$	$1.53\cdot10^{-2}$	$5.20\cdot10^{-1}$	$1.53\cdot10^{-2}$
Hybrid	BEM	$3.28\cdot10^{-3}$	$1.63\cdot10^{-3}$	$3.31\cdot10^{-1}$	$1.95\cdot10^{-2}$	$6.61\cdot10^{-1}$	$1.95\cdot10^{-2}$
	H-BEM	$3.28\cdot10^{-3}$	$1.63\cdot10^{-3}$	$3.31\cdot10^{-1}$	$1.95\cdot10^{-2}$	$6.61\cdot10^{-1}$	$1.95\cdot10^{-2}$
	S-BEM	$1.44\cdot10^{-3}$	$7.18\cdot10^{-4}$	$2.67\cdot10^{-1}$	$1.57\cdot10^{-2}$	$5.33\cdot10^{-1}$	$1.57\cdot10^{-2}$

Table 2.13 • Errors on time at which $V > 1$ m/s for each seismic event.

Table 2.14 gives the relative L^2-norm errors on the interface unknowns (the slip rate V, the quasi-static shear stress change τ^{qs} and the state variable θ) at time at which the slip-rate V first exceeds 1 m/s for each seismic event. Our values of the slip-rate V, the quasi-static shear stress change τ^{qs}, and the state-variable θ obtained with each time-stepping method implemented using the standard BEM, the H-BEM or the S-BEM, are compared to Romanet's values. The corresponding relative errors are denoted $\varepsilon_V^{t_{V>1\text{ m/s}}}$, $\varepsilon_{\tau^{qs}}^{t_{V>1\text{ m/s}}}$ and $\varepsilon_\theta^{t_{V>1\text{ m/s}}}$ respectively. Error values achieved on each interface unknown with each method show good agreement between our results and Romanet's, except for the prediction-correction method with S-BEM. It may be related to the fact that the time step value is limited by a minimum value at each iteration, which limits the convergence in this case. This can also be linked to the fact that slip-rate values found as an output of the Newton-Raphson algorithm is a local minimum of the nonlinear friction law that achieve the tolerance of the Newton-Raphson method, which also limits the convergence of the prediction-correction method. We also draw attention on the fact that adding a rate-strengthening zone at the extremities of the fault width could help for more numerically stable results.

The different error values obtained with the different spatial and time-stepping methods implemented emphasize that the reproducibility of seismic cycle simulations is challenging,

Seismic event index		1			2			3		
Time stepping method	Spatial method	$\varepsilon_V^{t_{V>1\text{ m/s}}}$	$\varepsilon_{\tau^{qs}}^{t_{V>1\text{ m/s}}}$	$\varepsilon_\theta^{t_{V>1\text{ m/s}}}$	$\varepsilon_V^{t_{V>1\text{ m/s}}}$	$\varepsilon_{\tau^{qs}}^{t_{V>1\text{ m/s}}}$	$\varepsilon_\theta^{t_{V>1\text{ m/s}}}$	$\varepsilon_V^{t_{V>1\text{ m/s}}}$	$\varepsilon_{\tau^{qs}}^{t_{V>1\text{ m/s}}}$	$\varepsilon_\theta^{t_{V>1\text{ m/s}}}$
	BEM	$1.12{\cdot}10^{-2}$	$1.04{\cdot}10^{-2}$	$9.37{\cdot}10^{-4}$	$5.19{\cdot}10^{-2}$	$7.06{\cdot}10^{-2}$	$8.89{\cdot}10^{-2}$	$5.14{\cdot}10^{-2}$	$7.36{\cdot}10^{-2}$	$8.86{\cdot}10^{-2}$
Prediction-correction	H-BEM	$1.12{\cdot}10^{-2}$	$1.04{\cdot}10^{-2}$	$9.37{\cdot}10^{-4}$	$1.19{\cdot}10^{-1}$	$2.15{\cdot}10^{-1}$	$8.89{\cdot}10^{-2}$	$9.36{\cdot}10^{-2}$	$1.54{\cdot}10^{-1}$	$8.88{\cdot}10^{-2}$
	S-BEM	$1.28{\cdot}10^{-3}$	$1.13{\cdot}10^{-3}$	$7.00{\cdot}10^{-5}$	1.77	1.86	1.21	1.58	1.65	$9.62{\cdot}10^{-1}$
	BEM	$1.28{\cdot}10^{-2}$	$1.23{\cdot}10^{-2}$	$1.10{\cdot}10^{-3}$	$2.81{\cdot}10^{-2}$	$4.89{\cdot}10^{-2}$	$2.81{\cdot}10^{-2}$	$2.81{\cdot}10^{-2}$	$4.92{\cdot}10^{-2}$	$2.80{\cdot}10^{-2}$
Explicit	H-BEM	$1.28{\cdot}10^{-2}$	$1.23{\cdot}10^{-2}$	$1.09{\cdot}10^{-3}$	$6.45{\cdot}10^{-2}$	$1.15{\cdot}10^{-1}$	$2.80{\cdot}10^{-2}$	$6.73{\cdot}10^{-2}$	$1.20{\cdot}10^{-1}$	$2.84{\cdot}10^{-2}$
	S-BEM	$9.28{\cdot}10^{-3}$	$8.69{\cdot}10^{-3}$	$6.02{\cdot}10^{-4}$	$2.60{\cdot}10^{-2}$	$4.73{\cdot}10^{-2}$	$2.68{\cdot}10^{-2}$	$2.64{\cdot}10^{-2}$	$4.75{\cdot}10^{-2}$	$2.68{\cdot}10^{-2}$
	BEM	$1.15{\cdot}10^{-2}$	$1.07{\cdot}10^{-2}$	$9.61{\cdot}10^{-4}$	$2.33{\cdot}10^{-2}$	$4.19{\cdot}10^{-2}$	$1.81{\cdot}10^{-2}$	$2.38{\cdot}10^{-2}$	$4.13{\cdot}10^{-2}$	$1.80{\cdot}10^{-2}$
Hybrid	H-BEM	$1.15{\cdot}10^{-2}$	$1.06{\cdot}10^{-2}$	$9.56{\cdot}10^{-4}$	$6.47{\cdot}10^{-2}$	$1.17{\cdot}10^{-1}$	$1.81{\cdot}10^{-2}$	$6.84{\cdot}10^{-2}$	$1.22{\cdot}10^{-1}$	$1.80{\cdot}10^{-2}$
	S-BEM	$7.72{\cdot}10^{-3}$	$6.99{\cdot}10^{-3}$	$4.54{\cdot}10^{-4}$	$1.90{\cdot}10^{-2}$	$3.69{\cdot}10^{-2}$	$1.51{\cdot}10^{-2}$	$2.08{\cdot}10^{-2}$	$3.51{\cdot}10^{-2}$	$1.51{\cdot}10^{-2}$

Table 2.14 • Relative L^2-norm error on each interface unknown, for each seismic event.

which reinforces our interest in this sensitivity study.

Convergence tests with respect to the time discretization parameters for seismic cycle simulations

After a first comparison with simulation results provided by Pierre Romanet, we "build" a reference solution. We propose an overkill solution by simulating the in-plane problem previously considered for the comparison study, with the hybrid time-stepping method inspired by Romanet and Ozawa (2021), and very refined values of the parameters $\varepsilon_{\text{solver}}$ and $\varepsilon_{\text{Newton}}$ that scales the time discretization. Among the methods implemented, the hybrid method is the most adequate method to incorporate fully-dynamic effects and to perform accurate simulations. We use the standard-BEM for the overkill simulation. We show the convergence of our results towards the reference refined solution. The parameters used to simulate the overkill case are given in Tables 2.15 and 2.16.

Parameters	$L_b/\Delta z$	N_{rep}	N_{leaf}	η	ε_{ACA}
standard BEM	6	1	/	/	/

Table 2.15 • Space discretization parameters for the overkill seismic cycle simulation.

Parameters	β_{min}	$\varepsilon_{\text{Newton}}$	$\text{maxiter}_{\text{Newton}}$	$\varepsilon_{\text{solver}}$
Hybrid method	0.12	10^{-12}	40	10^{-10}

Table 2.16 • Time discretization parameters for the overkill seismic cycle simulation.

Figure 2.23 represents the relative error in time at which the slip-rate V first exceeds 1 m/s for the first and the second seismic events with respect to the tolerance $\varepsilon_{\text{Newton}}$ for different values of the coefficient β_{min} for the prediction-correction method. We observe a clear convergence of the time values, and the results seem to be robust with respect to the value of β_{min}.

Figure 2.24 represents the relative L^2-norm error on the different interface unknowns at time at which the slip-rate V first exceeds 1 m/s for the first seismic event with respect to the tolerance $\varepsilon_{\text{Newton}}$ for different values of the coefficient β_{min} for the prediction-correction

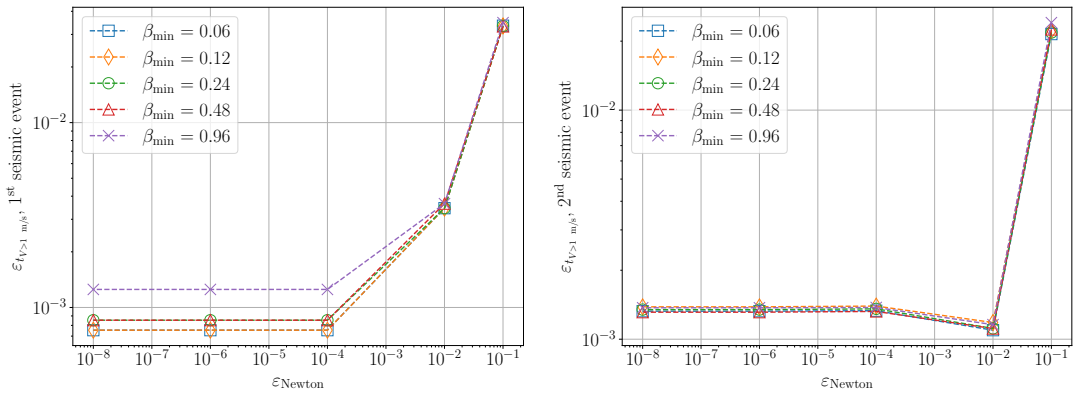

(a) **(b)**

Figure 2.23 • Error in time at which $V > 1$ m/s for 1st and 2nd seismic event when solved with prediction-correction method.

time-stepping method, using H-BEM. We observe a clear convergence of the interface unknown values towards the refined reference, and we observe a non-negligible influence of the coefficient $\beta_{\min}$. The larger the value of $\beta_{\min}$, the worst the convergence. $\beta_{\min} = 0.12$ seems to be a good compromise, whereas the results diverge for $\beta_{\min} = 0.96$ in the sense that the spatial evolution of the interface unknowns at the time at which V first exceeds 1 m/s is completely different from the reference solution. Nevertheless, Lapusta et al. (2000) recommend not to decrease too much the value of $\beta_{\min}$ to ensure convergence. They advise to change the space step instead.

Figure 2.25 represents the relative L^2-norm error as in Figure 2.24, but for the second seismic event. We observe a clear convergence of the time values, and the results seem to be robust with respect to the value of $\beta_{\min}$.

Figure 2.26 represents the relative error in time at which the slip-rate V first exceeds 1 m/s for the first and the second seismic event with respect to the tolerance $\varepsilon_{\text{solver}}$ for the explicit time-stepping method. We observe a clear convergence of the time values towards the reference solution.

Figure 2.27 represents the relative error in time at which the slip-rate V first exceeds 1 m/s for the first and the second seismic event with respect to the tolerance $\varepsilon_{\text{solver}}$ for the explicit time-stepping method, using H-BEM. We observe a clear convergence of the interface unknown values towards the refined reference.

Figure 2.28 represents the relative error in time at which the slip-rate V first exceeds 1 m/s for the first and the second seismic event with respect to the tolerance $\varepsilon_{\text{solver}}$ for different values of the tolerance $\varepsilon_{\text{Newton}}$ for the hybrid time-stepping method, using H-BEM. We observe a clear convergence of the time values towards the refined reference, and we notice the influence of $\varepsilon_{\text{Newton}}$ on $\varepsilon_{\text{solver}}$. If $\varepsilon_{\text{Newton}} > \varepsilon_{\text{solver}}$, this limits the convergence. Error values are smaller than the one obtained with the prediction-correction and the explicit time-stepping method as we also used the hybrid time-stepping method to compute the reference solution.

Figure 2.29 represents the relative L^2-norm error on each interface unknown at time at which the slip-rate V first exceeds 1 m/s for the second seismic event with respect to the

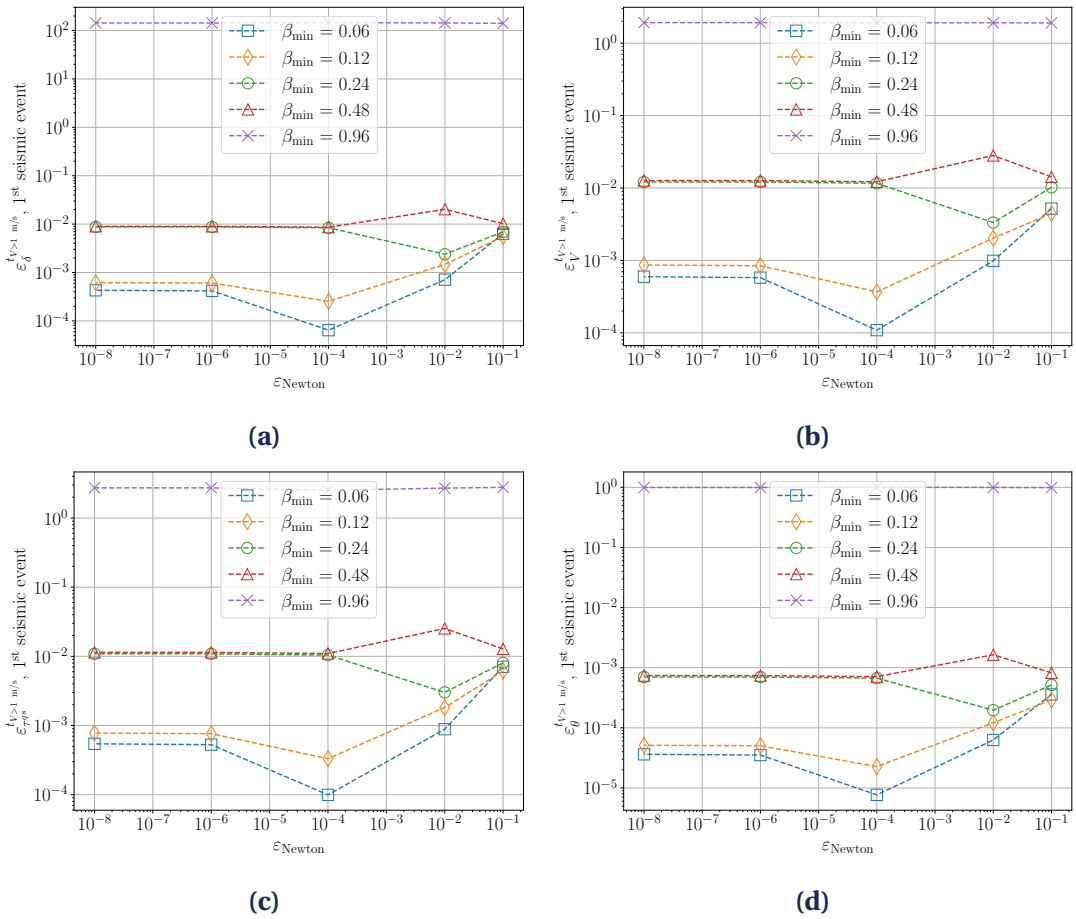

Figure 2.24 • Relative L^2-norm error on each interface unknown, for the 1st seismic event, when solved with prediction-correction method.

tolerance $\varepsilon_{\text{solver}}$ for different values of the tolerance $\varepsilon_{\text{Newton}}$ for the hybrid time-stepping method using H-BEM. We observe a clear convergence of the interface unknown values towards the refined reference, and we notice the influence of $\varepsilon_{\text{Newton}}$ on $\varepsilon_{\text{solver}}$. If $\varepsilon_{\text{Newton}} > \varepsilon_{\text{solver}}$, this limits the convergence. To sum up, for given values of $\varepsilon_{\text{solver}}$, $\varepsilon_{\text{Newton}}$ (such that $\varepsilon_{\text{solver}} \leqslant \varepsilon_{\text{Newton}}$), and $\beta_{\min}$, the error in time at which the slip rate first exceeds 1 m/s during a seismic event cumulates at each new seismic cycle.

5 Numerical test on a seismic cycle benchmark

Finally, we compared our results to results approved by the seismic cycles' community. We take as reference results the results provided by Junle Jiang for the first benchmark problem BP1 proposed in the framework of the SEAS benchmark/validation exercise project (Erickson et al., 2020a). The benchmark description is given in Erickson and Jiang (2018). We consider a planar fault embedded in a homogeneous, linear, elastic, isotropic half-space with a free surface. The fault is governed by rate-and-state friction down to the depth W_f and creeps at an imposed constant rate V_{pl} down to the infinite depth. Anti-plane motion is considered and the quasi-dynamic approximation is used. Tables 2.17 to 2.19 give parameters used for this case. 36 seismic cycles are simulated over 3 000 years. Jiang's results are obtained using a

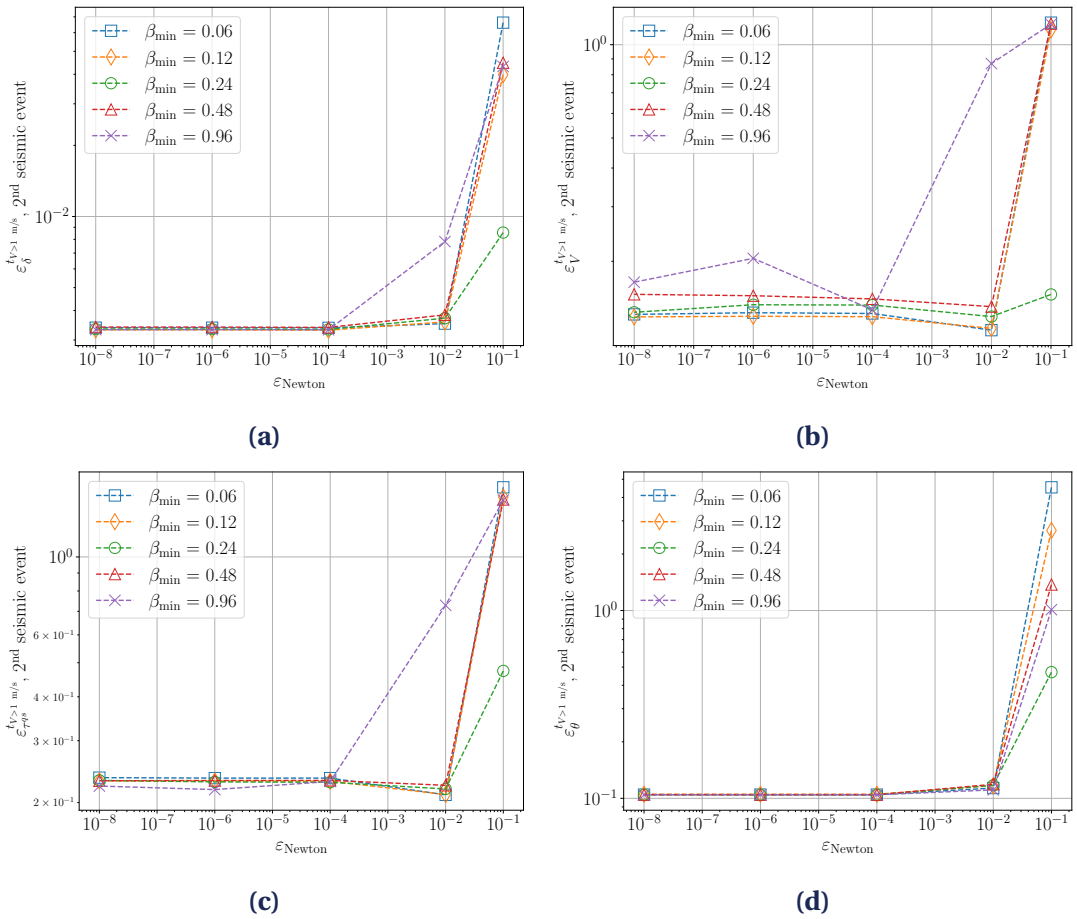

Figure 2.25 • Relative L^2-norm error on each interface unknown, for the 2nd seismic event, when solved with prediction-correction method.

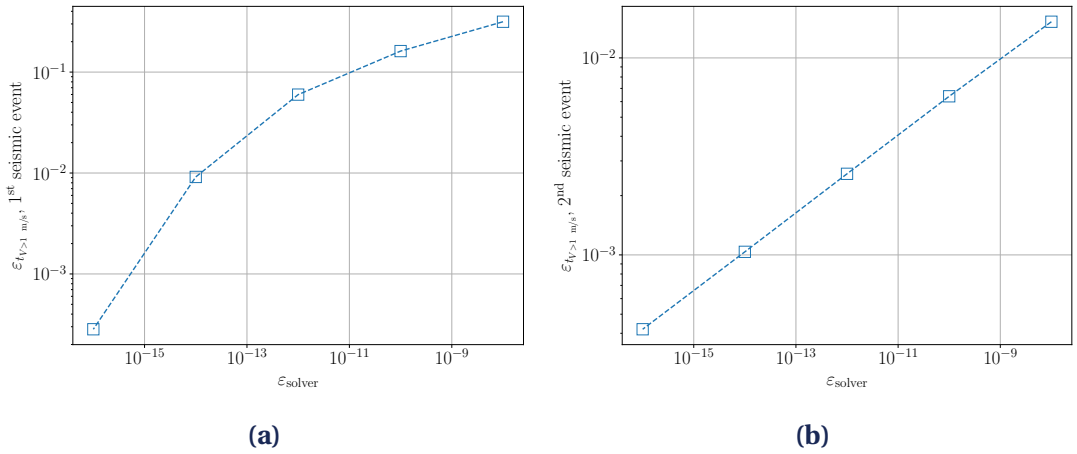

Figure 2.26 • Error in time at which $V > 1$ m/s for 1st and 2nd seismic event when solved with explicit method.

prediction-correction method using S-BEM inspired by Lapusta et al. (2000). However, apart from the space step and the size of the discretized domain $\Delta z = 25$ m, $N_{\text{rep}} = 4$, we do not have any information on the parameters used by Jiang. Figure 2.31 shows the time evolution of the interface unknowns (slip, slip rate, shear stress, state variable) at 12.5 km at depth (close

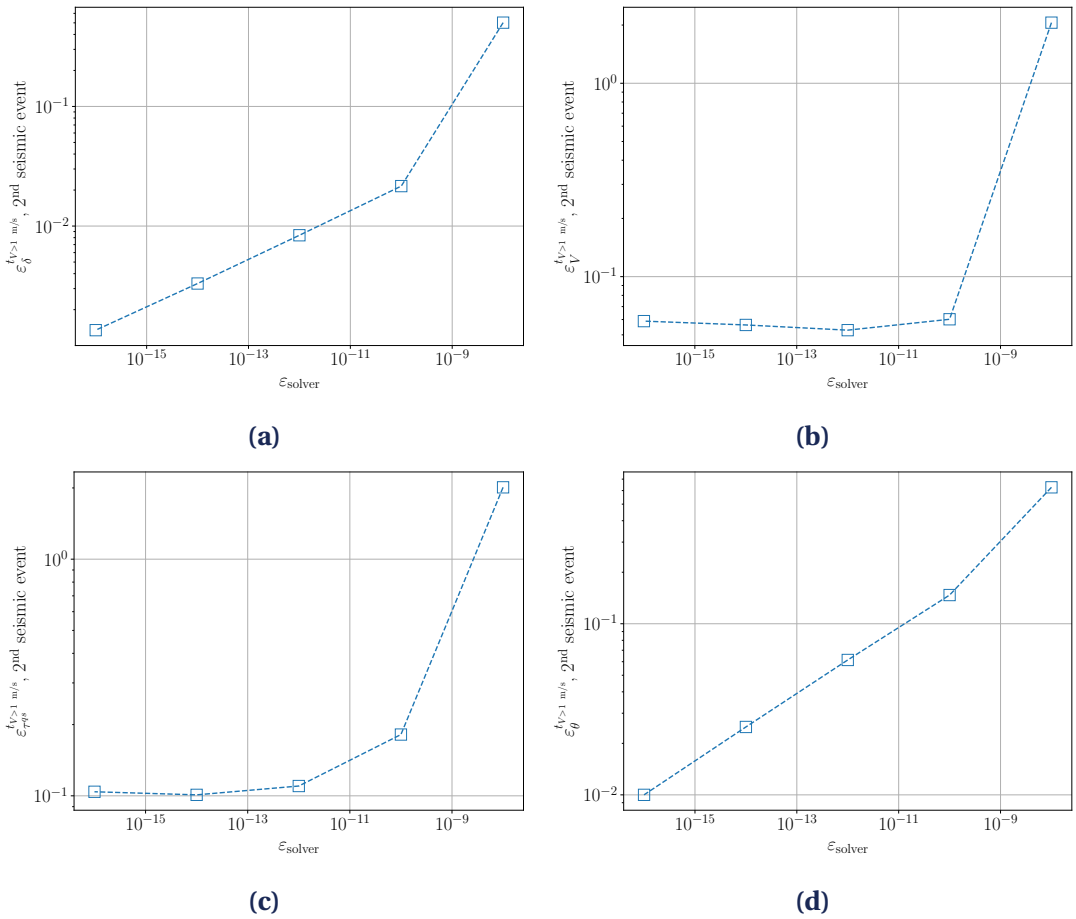

Figure 2.27 • Relative L^2-norm error on each interface unknown, for the 2nd seismic event, when solved with explicit method.

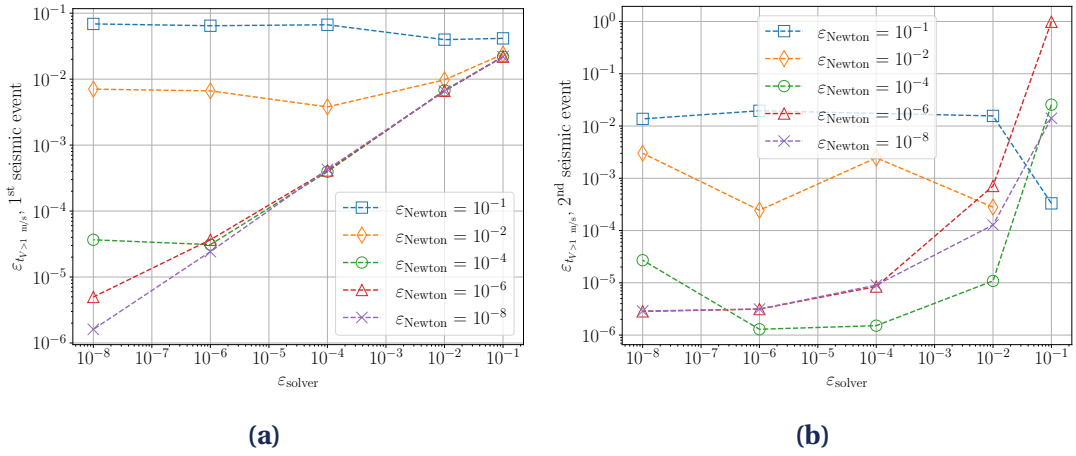

Figure 2.28 • Error in time at which $V > 1$ m/s for 1st and 2nd seismic event when solved with hybrid method.

to the nucleation zone) obtained with the three developed time integration method, and using H-BEM. Our results show good agreement with Jiang's results for the slip, the slip-rate and the state variable. We observe a small difference in the amplitude of the shear stress. It may be due to the fact that the space discretization parameters chosen by Jiang does not

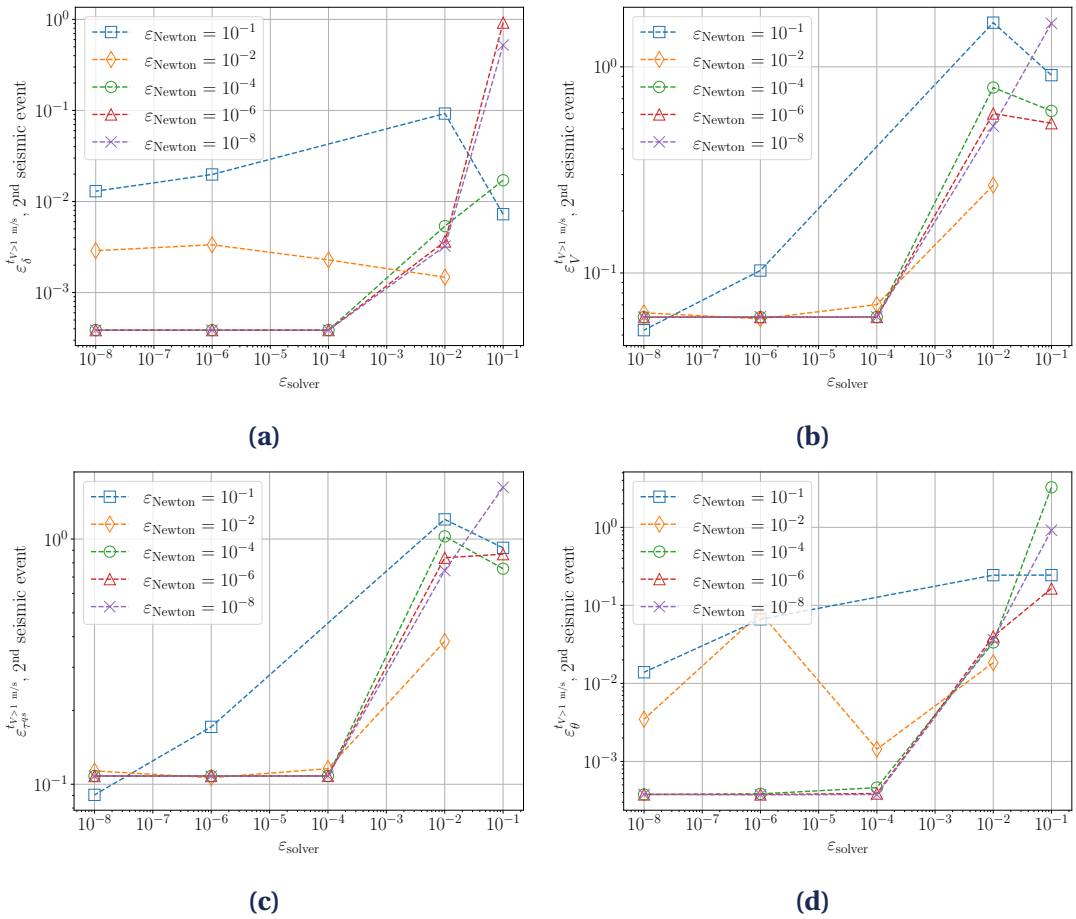

Figure 2.29 • Relative L^2-norm error on each interface unknown, for the 2nd seismic event, when solved with hybrid method.

lead to the same precision as ours for the calculation of the shear stress. In particular, we had insisted on the importance of a large enough size of the discretized domain when using S-BEM in Section 4.3. We also notice a small progressive shift in time between our results and Jiang's. Figure 2.32 quantifies the shift in time observed by giving (a) the error on the starting time of each seismic instability, (b) the duration of each interseismic period. Closer results to Jiang's are obtained using the explicit time integration method inspired by Ozawa et al. (2022), and both prediction-correction and hybrid method give really similar results. The explicit method uses a 5^{th} order time discretization scheme, whereas both prediction-correction and hybrid methods use a 2^{nd} order time discretization scheme, which can explain the differences observed. This can either be explained by:

- a coupling effects between the choice of the space discretization and of the time discretization as shown in Figure 2.20;
- the choice of different time discretization parameters in our simulation and Jiang's which can lead to a cumulating shift in time;
- a small discrepancy in the initialization which cumulates in time as explained in Section 4.4 in the case of the comparison between our seismic cycle results and results provided by Pierre Romanet.

The previous sensitivity study made us aware of all the potential causes of the small differences between our results and Jiang's.

Parameter	Definition	Value, Unit
μ	Shear modulus	$\simeq 32$ GPa
c_s	Shear wave velocity	3464 m/s
σ_n	Effective normal stress at the fault interface	50 MPa
$a(z)$	Rate and state parameter	Figure 2.30
$b(z)$	Rate and state parameter	Figure 2.30
$D_c(z)$	Characteristic slip distance	8 mm
V_{pl}	Imposed slip rate out of rate-and-state zone	10^{-9} m/s
V_0	Reference slip rate	10^{-6} m/s
f_0	Reference friction coefficient	0.6
W_f	Width of the rate-and-state zone	40 km

Table 2.17 • Parameter values used for BP1 SEAS benchmark simulation.

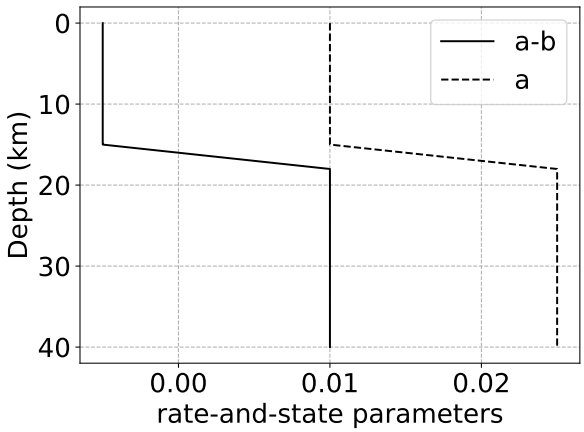

Figure 2.30 • Rate-and-state parameters with respect to depth.

Parameters	$L_b/\Delta z$	N_{rep}	N_{leaf}	η	ε_{ACA}
H-BEM	6	1	100	3	10^{-5}

Table 2.18 • Space discretization parameters for the benchmark problem 1 (BP1 SEAS).

Another cross-validation is performed on the benchmark problem BP6 from SEAS benchmark / validation exercises. This benchmark incorporates the effect of fluid injection (at constant rate, followed by along fault fluid diffusion) on fault slip in the form of a one-way coupling model. In practice, an elastodynamic equation is combined with a diffusion equation satisfied by the fluid pressure. This study is given in Appendix B.

Parameters	β_{min}	$\varepsilon_{\text{Newton}}$	$\text{maxiter}_{\text{Newton}}$	$\varepsilon_{\text{solver}}$
Prediction-correction	0.25	10^{-8}	40	/
Explicit method	0.12	/	/	10^{-12}
Hybrid method	0.12	10^{-6}	40	10^{-5}

Table 2.19 • Time discretization parameters for the benchmark problem 1 seismic cycle simulation.

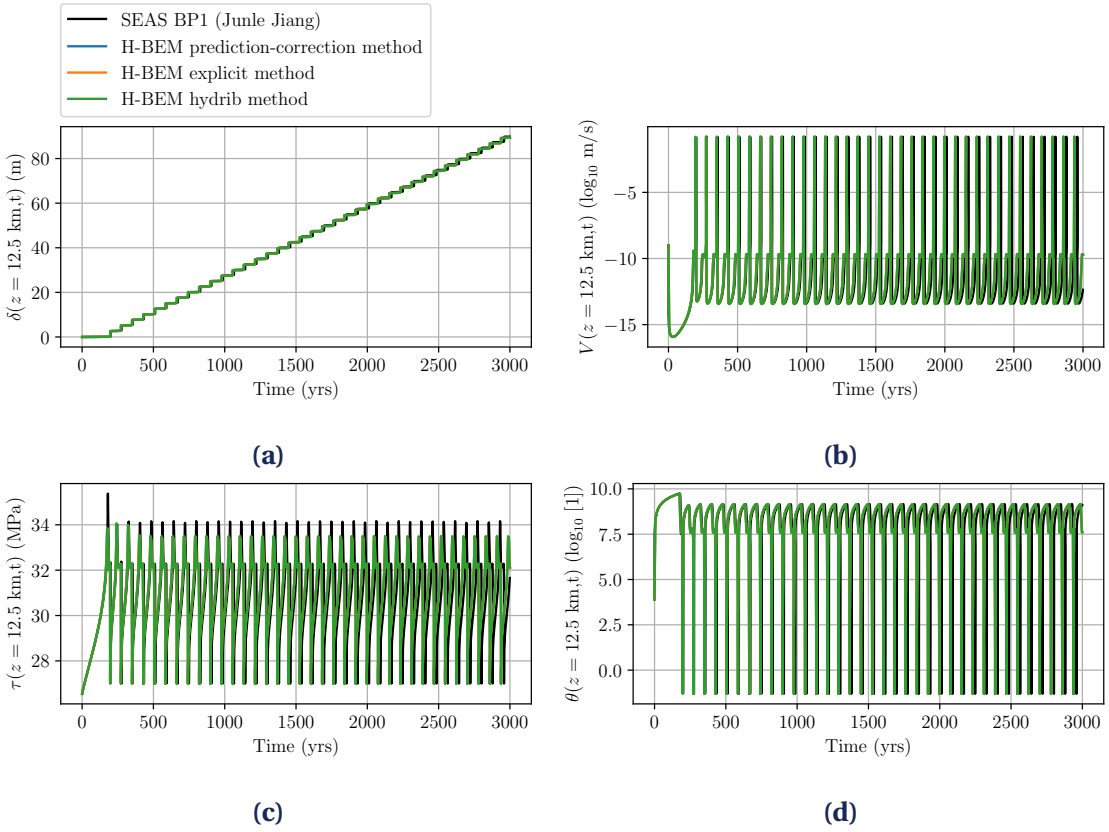

Figure 2.31 • Time evolution of (a) slip δ, (b) slip rate V, (c) shear stress τ, (d) state variable θ, at $z = 12.5$ km, close to nucleation region.

6 Summary of the qualities and drawbacks of space and time discretization/integration methods

Here we summarize and conclude on the advantages and limitations of the different space and time discretization/integration methods implemented in the present work. We choose the most appropriate methods to incorporate fluid injection effects in the vicinity of a fault at the timescale of a seismic motion, and increase the problem complexity.

Space discretization methods

In this work, we implemented three space discretization methods based on Boundary Element Methods (BEMs).

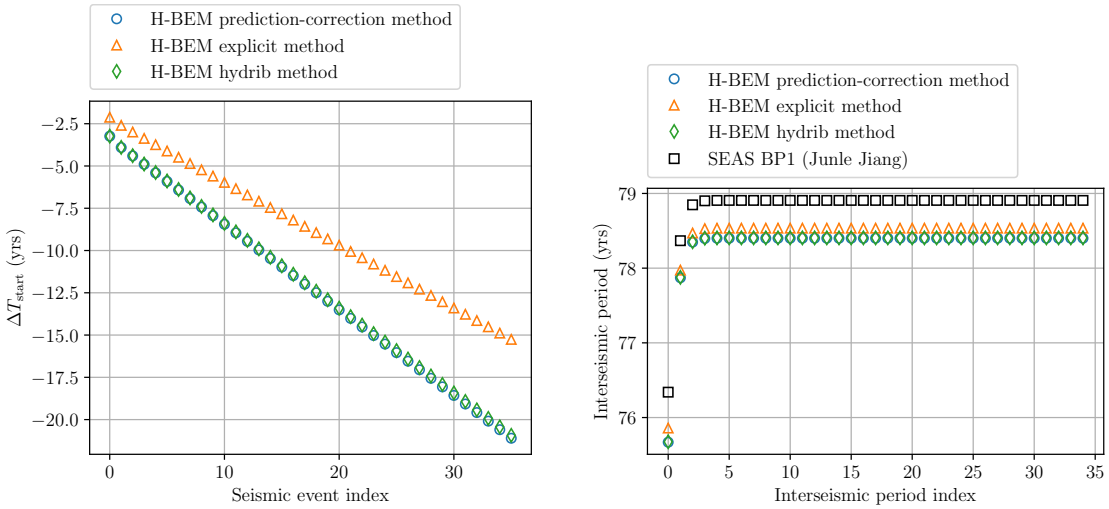

(a) **(b)**

Figure 2.32 • (a) Error on the starting time of each seismic instability, (b) Duration of each interseismic period.

Standard Boundary Element Method (Standard BEM). Standard BEM allows to consider complex fault geometries. It relies on the calculation (once if the geometry is fixed) of a fully-populated BEM matrix ($\mathcal{O}(N^2)$), and requires a matrix-vector product ($\mathcal{O}(N^2)$) to compute the shear stress induced by fault slip at each iteration. This method is expensive for large problems as shown in Figures 2.17 and 2.19. We implemented two accelerated BEM methods to tackle this drawback.

Spectral Boundary Element Method (S-BEM). S-BEM is largely used in the seismic cycle community. It is easy to implement and particularly efficient for planar faults ($\mathcal{O}(N\log(N))$). However, several limitations are inherent to the method:

- The fault has to be planar (so that the BIE can be written as a scalar equation);
- Periodic repetitions of the domain are required[1];
- A regular mesh of the fault is required.

Hierarchical matrices based Fast Boundary Element Methods (H-BEM). To efficiently consider complex fault geometries, accelerated BEM based on Hierarchical matrices can be used. This method gather the advantages of standard BEM and enables a data-sparse approximation of the dense BEM matrix:

- Adapted to non-planar fault configurations;
- No need for spatial replications of the domain;

[1] S-BEM method without spatial replications introduced by Cochard and Rice (1997) can be used and only requires a domain twice as long as the effective fault. However, it requires more elaborate calculations of the convolution kernel (once if geometry is fixed) in the Fourier domain and induces approximation of the Fourier transform of the kernel.

- Problem-independent algebraic method;
- Data-sparse approximation of the BEM matrix ($\mathcal{O}(N\log(N))$, only once if the geometry is fixed), and accelerated matrix-vector product to compute shear stress induced by slip at each iteration in time ($\mathcal{O}(N\log(N))$).

The approximation of the calculation of the shear stress induced by slip because of data-sparse approximation of the BEM matrix leads to low error on the shear stress which do not prevent from convergence for refined enough space discretization. This is shown in Figures 2.16b and 2.20a to 2.20d. As a conclusion, H-BEM is the most appropriate space discretization method to consider more complex problems.

Time discretization/integration methods

In this work, we implemented three adaptive time stepping (explicit and hybrid implicit/explicit) methods.

Prediction-correction method. Prediction-correction method is largely used in the earthquake cycles community. This method is easy to implement and can handle dynamic cases without changing the code structure. However, its main drawback relies on the non-optimal choice of the time step at each iteration. The latter is based on an heuristic, which consist in a CFL condition deduced from the combination of the LSA of a reduced order spring-block model with the discretization of its motion equation with a constant time-step. This non-optimal time step choice can induce cumulative error in time and limits convergence as shown in Table 2.10 for aseismic slip simulation and in Figures 2.23 to 2.25 for seismic cycle simulations.

Explicit RK method. Explicit RK methods are also largely considered in the earthquake cycles community. These methods are easy to implement and are available in numerous libraries. The choice of the time step at each iteration is based on a convergence criterion for the calculation of the slip and the state variable with a given solver tolerance. For sufficiently refined values of the solver tolerance, the explicit RK45 method implemented allows for accurate calculations of the interface unknowns as shown in Figure 2.21 for aseismic slip simulation, and Figures 2.26 and 2.27 for seismic cycle simulations. Explicit RK methods are particularly efficient and accurate for quasi-dynamic cases. However, such methods cannot handle dynamic cases as equations cannot be written as an ODE system in this case.

Hybrid method. The hybrid method combines the advantages of both prediction-correction and explicit RK methods. For refined enough values of the solver tolerance for the choice of the time step, and of the tolerance of the non-linear solving required at each prediction and correction steps (chosen to be smaller than the solver tolerance in order not to limit the convergence), this method allows for accurate calculations of the interface unknowns. This is shown in Figure 2.22 for aseismic slip simulations and in Figures 2.28 and 2.29 for seismic cycle simulations. As a conclusion, the hybrid method is chosen in the present work as the most appropriate time discretization/integration method to consider more complex problem and

incorporate fluid injection effects in the vicinity of a fault at the timescale of a seismic motion.

In this part, we developed numerical tools to simulate seismic cycles. We conducted an in-depth sensitivity study with respect to the simulation parameters at stake to assist in the accurate and efficient use of the methods implemented. In the following part, we are interested in studying pore fluid effects on a fault during the earthquake instability. Thus, we want to study one instability, i.e. one seismic event.

3

Modeling fluid-injection effects in the vicinity of a fault

Contents

1 Fluid-injection in simplified fault-mechanics problem 102

2 Reduction of the complete poroelastodynamic equations 104

3 Existing simplified models for fluid effects on fault slip 105

4 Scaling poroelastodynamic equations 107

4.1 Scaling 1D poroelastodynamic equations without source 107

4.2 Scaling 1D poroelastodynamic equations with a fluid source 115

4.3 Extension to 2D 117

4.4 Synthesis of the dimensional analysis of the poroelastodynamic equations 119

5 Illustration with a one-dimensional poroelastic problem 122

5.1 Problem formulation 122

5.2 Laplace domain Green's functions for both the complete and the simplified models 124

5.3 Convolution quadrature method 125

5.4 Comparison between the complete poroelastodynamic model and the simplified model at the timescale of a seismic motion 127

In this chapter, we aim at modeling fluid effects on unstable frictional slip, in the case where the fluid is injected at a given distance from the fault. Now that we have developed the numerical tools incorporating Fast BEMs for standard seismic cycles problems, we want to extend their capabilities to the simulation of fluid-injection effects on unstable frictional slip. To overcome the inherent difficulties of the numerical integration of the complete poroelastodynamic equations reformulated as boundary integral equations, we want to simplify equations rigorously. Thus, we first need to formally evaluate the predominant fluid-injection effects in the vicinity of a fault, depending on the characteristic time T_c (seismic

timescale or aseismic timescale). Then, we will discuss the validity range of the simplified model chosen as well as the simplified models used in the literature. This will enable us to implement efficiently a simplified model taking into account hydro-mechanical couplings.

1 Fluid-injection in simplified fault-mechanics problem

Figure 3.1 represents the typical fault mechanics problem with fluid-injection that we want to consider. This goal problem is very similar to the "dry" (without fluid-injection) configurations from Figure 2.1 in Section 1 of Chapter 2, the difference being that the medium containing the discontinuity is poroelastic and a fluid source is taken into account. It changes both the balance momentum equation and the interface and initial conditions. The configurations represented in Figure 3.1 consist in a planar fault (Γ) embedded in a linear, isotropic, poroelastic half-space (Ω). The fault is assumed to be infinitely long along the y-direction. The fault interface is governed by rate-and-state friction (to depth W_f) and a creep rate V_{pl} is imposed below the rate-and-state zone. Either anti-plane (Figure 3.1a, mode III) or in-plane (Figure 3.1b, mode II) motion with a no-opening condition of the fault is considered. Fluid is injected through an impermeable injection well. As a starting point, to incorporate hydro-mechanical couplings in the two-dimensional initial strike-slip configuration, we consider a fluid-injection point source in a 2D borehole (which corresponds to a fluid line source in 3D) at a given distance D (≈ 5 km for instance) from the fault. Even if the assumption for the fluid injection is unrealistic, it is a first proposition to take into account the fluid-effect. Note that a different problem is considered by Dunham and Rice (2008) and Heimisson et al. (2022): a 2D fluid injection point source at the fault plane.

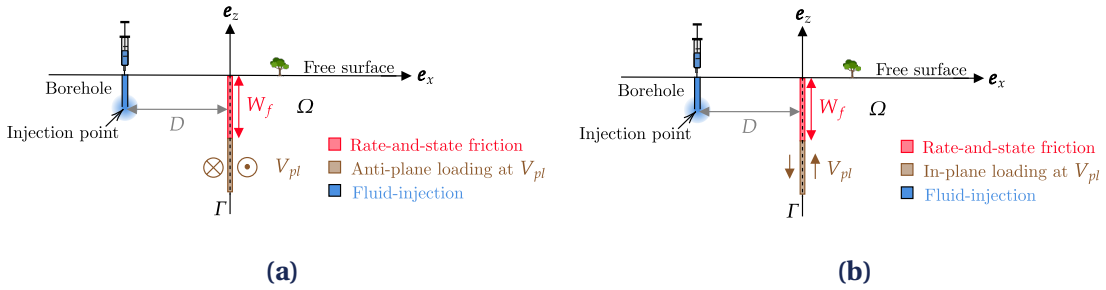

Figure 3.1 • Strike-slip fault configurations in (a) mode III or (b) mode II with a no-opening condition on the fault. Fluid is injected through an impermeable borehole at a given distance D from the fault Γ embedded in a poroelastic half-space Ω.

In the poroelastic volume $\Omega\backslash\Gamma$, the **u** - p (2D Laplace domain solid displacement-pore fluid pressure) formulation of the balance momentum equation (1.52) (see Section 4.3 of Chapter 1) is satisfied, but with a fluid source term. Modeling a fluid-injection source term consists in incorporating a rate of fluid supply per unit volume in the continuity equation for the fluid, which writes in 2D

$$\dot{\zeta} + q_{i,i} = \gamma(t)\delta_D(x_i - x_{i_0}), \tag{3.1}$$

where $\zeta = \alpha u_{i,i} + \Phi^2 p/R$ is the variation in fluid volume per unit reference volume, $q_i = \dot{w}_i$

is the fluid flux vector (time derivative of the seepage displacement w_i), and the index i corresponds to x or z coordinates.

Combining the continuity equation (mass balance) (3.1) with the Laplace transform of the "dynamic" Darcy's law recalled here.

$$\hat{w}_i = -\beta(s)/(s^2\rho_f)(\hat{p}_{,i} + s^2\rho_f\hat{u}_i - f_i^f),$$

we obtain the complete $\mathbf{u}-p$ formulation of the poroelastodynamic balance momentum equations

$$\begin{aligned} &G\hat{u}_{i,jj} + (\lambda+G)\hat{u}_{j,ij} - (\alpha-\beta(s))\hat{p}_{,i} - s^2(\rho-\beta(s)\rho_f)\hat{u}_i = \beta(s)\hat{f}_i^f - \hat{F}_i, \\ &\frac{\beta(s)}{s\rho_f}\hat{p}_{,ii} - \frac{\Phi^2 s}{R}\hat{p} - (\alpha-\beta(s))s\hat{u}_{i,i} = \frac{\beta(s)}{s\rho_f}\hat{f}_{i,i}^f - \gamma(t)\delta_D(x_i - x_{i_0}). \end{aligned} \tag{3.2}$$

u_i is the $i-th$ component of the solid displacement and p is the pore fluid pressure and the indices i, j correspond to x or z coordinates. f_i^f is the body force per unit volume in the fluid and $F_i = (1-\Phi)f_i^s + \Phi f_i^f$ denotes the bulk body forces per unit volume, with f_i^s the body force per unit volume in the solid skeleton. In the following parts we consider that from the initial values of displacement $\mathbf{u}$ and pore pressure p to their final values, the body forces in the solid skeleton f_i^s or in the fluid f_i^f do not vary. Therefore, taking the variations between the final and the initial $\mathbf{u}-p$ values as unknowns eliminates the body forces from (3.2).

Rate-and-state friction is assumed on the fault interface Γ down to depth W_f such that, the only non-vanishing shear-stress component on the fault plane $\tau(0^{\pm}, z, t)$ writes

$$\begin{aligned} &\tau(0^{\pm}, z, t) = (\sigma_n - p(0, z, t))\mu(V(z,t), \Psi(z,t)), \\ &\text{with } \mu(V(z,t), \Psi(z,t)) = a\,\mathrm{asinh}\left(\frac{V}{2V_\Psi}\right),\ V_\Psi = V_0\exp\left(-\frac{\mu_0+\Psi}{a}\right),\ \text{and } \Psi = b\ln\left(\frac{\theta}{\theta_0}\right), \end{aligned} \tag{3.3}$$

where $(\sigma_n - p(0,z,t))$ corresponds to Terzaghi's effective normal stress and $\mu(V(z,t),\Psi(z,t))$ is the regularized rate-and-state friction coefficient from Equation (1.37). The fault creeps at a given slip-rate V_{pl} below the rate-and-state zone

$$V(z,t) = V_{pl},\ \forall z \geqslant W_f \tag{3.4}$$

We consider a no-opening condition on the fault such that the normal component of the displacement discontinuity is equal to 0:

$$\boldsymbol{\delta}(z,t)\cdot\mathbf{e}_x = 0. \tag{3.5}$$

The traction components are continuous at the interface

$$\boldsymbol{\sigma}(0^+, z, t)\mathbf{e}_x = \boldsymbol{\sigma}(0^-, z, t)(-\mathbf{e}_x). \tag{3.6}$$

The momentum balance equations and the interface conditions are completed by boundary conditions. Notably, radiation conditions must be taken into account at infinity (as explained in Section 2.4 of Chapter 1) and a free surface condition is required at $z = 0$

$$\boldsymbol{\sigma}\mathbf{e}_z = \mathbf{0},\ \text{on } \partial\Omega. \tag{3.7}$$

Finally, initial conditions are required for the unknown field quantities.

2 Reduction of the complete poroelastodynamic equations

The fault dynamics can be determined by solving equations resulting from the combination of the poroelastodynamic equations (3.2) with the friction law at the fault interface (3.3) as well as boundary and initial conditions. As we use BEMs, we first need to reformulate poroelastodynamic equations as boundary integral equations at the fault interface. The boundary integral equation method solved with the displacement discontinuity method (DDM) can be used in the case of fault mechanics problems incorporating hydro-mechanical couplings. This allows to reformulate the poroelastodynamic balance momentum equation (3.2) satisfied in Ω into two boundary integral equations on the fault interface (Detournay & Cheng, 1993; Cheng & Detournay, 1998). Although the efficiency of the boundary integral equation methods for "dry" fault mechanics problems is largely agreed, the incorporation of hydro-mechanical couplings implies two main difficulties:

- Two fundamental solutions must be used, and these fundamental solutions are difficult to obtain in closed form. In the case of the complete linear poroelastodynamic equations, time-domain Green's functions for fully-dynamic poroelasticity still remain unknown. Such solutions have been derived in the frequency domain though. Manolis and Beskos (1989, 1990) derived fundamental solutions for instantaneous point forces acting on both solid and fluid phases in the Laplace domain by the potential method. Chen (1994b, 1994a) determined the fundamental solutions for a unit force and a unit fluid source (point force and source in 3D, line force and source in 2D). Zheng et al. (2013) (respectively Senjuntichai and Rajapakse (1994)) determined the 3D (respectively 2D) fundamental solutions due to a time-harmonic concentrated point force and fluid source in the frequency domain in a (semi-)infinite space. Cheng and Detournay (1998) gave time-domain fundamental solutions for quasi-static poroelasticity only. However, going back to time-domain solution cannot be done analytically.

- Time-domain boundary integral equations are required, and need to be incorporated in existing seismic cycles solving methods. The first point implies that an inverse Laplace transform (respectively inverse Fourier transform in the case of time-harmonic fundamental solutions) of the fundamental solutions must be performed numerically. This step is difficult numerically as the time-integration of seismic cycles problems is based on adaptive time stepping algorithms. Constant time step should be used for the inverse transform, but this choice would bring errors which could prevent from obtaining interpretable seismic cycles simulations results.

Hence, before considering the fault mechanic problem with fluid injection detailed in Section 1, we must concentrate on the reduction of poroelastodynamic equations in order to derive a simplified model that would be easier to integrate in our numerical tools. This will enable us to derive Green's functions adapted to our problem, and avoid the mentioned difficulties for a case incorporating hydro-mechanical couplings. The first step is to simplify rigorously poroelastodynamic equations in order to take into account predominant poroelastodynamic effects. In our case, we want to evaluate the predominant effects of injecting fluid at a given distance from a fault on the frictional behavior of this same fault on the

timescale of a seismic instability. At the timescale of a seismic instability, we suspect that fluid diffusion is negligible. To assess the latter assumption, we perform a dimensional analysis of 1D poroelastodynamic equations in Section 4.1 (for the sake of simplicity), then extend to 2D with fluid source in Section 4.3 of Section 4.

3 Existing simplified models for fluid effects on fault slip

In the literature, simplified versions of the poroelastodynamic equations (3.2) have been considered. One-way coupling models have been largely used without preliminary dimensional analysis developments to justify their use. They usually consist in an elastodynamic equation (under quasi-dynamic approximation) perturbed by the pore-fluid gradient, plus a diffusion equation which governs the evolution of the pore-fluid. This one-way coupling approximation neglects both inertial effects for the fluid and the effect of the solid dilation rate on fluid diffusion. Such simplified equations have been used to model fluid-effects on fault slip at the timescale of an aseismic motion. Also, the fluid-injection source term appears only in the interface condition as fluid-injection is considered at the fault interface. Two kinds of studies which considered this simplified model can be distinguished.

Some studies considered fluid-injection in the Earth's crust as a trigger for aseismic or seismic fault slip. They focused on consequences of fluid injection on fault slip and nucleation of earthquakes. Their objectives consisted in understanding and explaining the mechanisms behind the seismic or aseismic slip induced by fluid injection. A major part of the studies modeling fluid effects on fault slip using a one-way coupling model came after in-situ and laboratory experiments which emphasized direct and indirect effects of fluid diffusion along a strike-slip fault on fault slip. Experiments conducted at a depth of 282 m below Earth's surface in cretaceous limestone of the southeast France sedimentary basin and analyzed by Guglielmi et al. (2015a) showed that fluid injection could trigger primarily aseismic slip, and induce earthquake nucleation as a secondary effect. Fluid-injection-induced fault slip experiments conducted in the laboratory and in-situ by Cappa et al. (2019) allowed identifying three stages in fluid effects on fault slip. They first revealed that the variation in fluid pressure first induces accelerating seismic creep and fault opening. Then, a further increase in pore-fluid pressure promotes rate-strengthening friction associated with aseismic slip. Finally, induced aseismic slip is likely to induce seismic events as it loads non-pressurized fault patches (such couplings between slow slip events and large earthquakes have also recently been showed in subduction zones Maubant et al. (2022)). Corroborating these experimental results, Eyre et al. (2019), Bhattacharya and Viesca (2019), and Sáez Uribe (2023) have shown numerically that fluid diffusion was not directly responsible for the observation of repeated fault slip, but rather was a consequence of stress transfer caused by aseismic slip induced by fluid injection. Viesca (2021) provided a benchmark for numerical solving the 2D boundary value problem of fluid-injection induced fault slip with fluid diffusion along the fault interface. He identified two asymptotic regimes either emphasizing fault-slip outpacing fluid-diffusion in the case of a critically stressed fault, or predominant fluid diffusion in the case of a marginally pressurized fault. Both regimes were also identified by Dublanchet (2019).

Conversely to all these studies, we consider fluid-injection at a given distance from the

fault interface, so that a fluid source term appears in the balance momentum equations (see (3.2)). Garagash and Germanovich (2012) consider pore-fluid diffusion along fault and at a distance of it to investigate conditions leading to slip and dynamic rupture nucleation, and the rupture run-out distance before it is arrested. Here, we intend to determine a suitable model to study the effect of fluid injected at a distance from the fault at the seismic motion timescale for which the diffusion equation seem inadequate.

Other works investigated the possibility of fluid-injection in the earth's crust as an input to the dynamics of the fault system to mitigate the seismic risk and drive aseismically the system towards a lower-energy equilibrium state. Their aim is to release the energy accumulated aseismically. These strategies have been the subject of theoretical studies based on robust control theory (Stefanou (2019) for the spring-slider model, extension to the Generalized-Burridge-Knopoff model and to seismic fault models Stefanou and Tzortzopoulos (2022), Gutierrez-Oribio et al. (2023), and Gutiérrez-Oribio et al. (2024)) and experimental tests in the laboratory (Tzortzopoulos (2021), Tzortzopoulos et al. (2021), and Gutiérrez-Oribio et al. (2023)). These studies also used a one-way coupling model to test their earthquake prevention strategies numerically.

Note that some studies considered two-way coupling models, but they also focused on fluid-effects at the timescale of an aseismic motion. Segall (1989) used quasi-static poroelastodynamic equations to predict surface deformation and earthquakes locations in good agreement with measurements at Wilmington oil field near Long Beach, California (human-induced earthquakes). He explained that large pore-pressure increase had a destabilizing effect while large pore-pressure decrease were stabilizing. Heimisson et al. (2019), Heimisson et al. (2021), and Heimisson et al. (2022) studied fluid-injection induced fault slip with fluid-diffusion at the fault interface. He took into account a two-way coupling model as he incorporated the effect of the solid dilation rate on fluid diffusion. Marguin and Simpson (2023, 2024) consider a 2D plane strain configuration where fluid is injected at the base of a thrust fault. He studies the coupling between fluid injection, porous flow, thermal pressurization and strong variations in permeability at the timescale of seismic cycles.

Conversely to all the studies previously mentioned in this section, we want to study fluid effects on fault slip on the timescale of a seismic motion for which the usually used one-way coupling model is not adequate. To this aim, the most generic model would correspond to the complete poroelastodynamic equations (3.2). Nevertheless, we highlighted the difficulty to derive time domain fundamental solutions in closed form and the inherent numerical difficulties in Section 2. Thus, before solving our frictional slip problem, we need to reduce the complete poroelastodynamic equations so that their reformulation as boundary integral equations could be more easily integrated numerically. In order to rigorously reduce complete poroelastodynamic equations in agreement with our assumptions, we conduct a dimensional analysis.

> ❍ **Remark 3.1.** *Note that Segall and Rice (1995) considered a variation in the porosity related to slip-rate to model the link between dilatancy (increasing compliance of the rock) and the mitigation of the instability. Ciardo and Lecampion (2019) considered the stabilizing or at least delayed effects of dilatancy associated with fault slip on (aseismic*

to seismic) frictional slip due to fluid injection. They also modeled a variation in fault permeability and showed that it had no influence on the stabilizing value of dilatancy. In the present work, as a starting point, we neither take into account variations in the permeability nor porosity, nor dilatancy.

4 Scaling poroelastodynamic equations

4.1 Scaling 1D poroelastodynamic equations without source

In this part, we formally assess the predominant fluid effect during an earthquake and during a seismic cycle. The following developments allow to derive the appropriate simplified equations in our case. This step is key to incorporate hydro-mechanical couplings in frictional slip simulations efficiently.

For the sake of simplicity, we first consider a one-dimensional poroelastodynamic problem. Equations (3.8a) and (3.8b) give the generic $\mathbf{u}-p$ formulation of the poroelastodynamic equations (see Schanz (2009) for example). As detailed in Section 4.3 of Chapter 1, this formulation is in the Laplace domain. Einstein's convention for summation is used here. In 1D (in the in-plane z-th direction for instance), Equation (3.2) becomes:

$$M\hat{u}_{z,zz} - (\alpha - \beta(s))\hat{p}_{,z} - (\rho - \beta(s)\rho_f)s^2\hat{u}_z = 0, \tag{3.8a}$$

$$\frac{\beta(s)}{s\rho_f}\hat{p}_{,zz} - \frac{\Phi^2 s}{R}\hat{p} - (\alpha - \beta(s))s\hat{u}_{z,z} = 0, \tag{3.8b}$$

where $\hat{u}_z$ and $\hat{p}$ are respectively the Laplace transforms of the solid skeleton displacement component u_z and of the pore fluid pressure p. $\beta(s)$ corresponds to the dimensionless complex coefficient resulting from a transformation in the Laplace domain of the dynamic version of the Darcy's law (1.51). It allows to express the seepage displacement (relative fluid-solid skeleton displacement w_z) as a function of pore-fluid pressure and obtain a $\mathbf{u}-p$ formulation of poroelastodynamic equations. It is given by:

$$\beta(s) = s\rho_f\frac{k}{\eta}\left(1 + \frac{k}{\eta}\left(\frac{\rho_a}{\Phi} + \rho_f\right)\right)^{-1}. \tag{3.9}$$

It is interesting to take a look at the different terms in equations (3.8a) and (3.8b).

- $M\hat{u}_{z,zz} - \alpha\hat{p}_{,z}$ expresses the Laplace transform of the poroelastic stress variation;
- $+\beta(s)\left(\hat{p}_{,z} + \rho_f s^2\hat{u}_z\right)$ corresponds to the Laplace transform of the relative fluid-solid acceleration, it stands for relative inertial effects for the fluid;
- $\rho s^2\hat{u}_z$ is the Laplace transform of the acceleration of the solid;
- $+\beta(s)\left(\frac{1}{s\rho_f}\hat{p}_{,zz} + s\hat{u}_{z,z}\right)$ corresponds to the Laplace transform of the seepage velocity gradient. It corresponds to the relative fluid diffusion;

- $\frac{\Phi^2 s}{R}\hat{p} + \alpha s \hat{u}_{z,z}$ defines the time-derivative of the undrained pore-pressure, divided by the coupling modulus R. It couples the variation of excess pore pressure compared to the equilibrium state with the solid strain variation. Furthermore, it expresses the fluid-solid coupling in case of an impermeable solid matrix.

Now, the first step of our dimensional analysis consists in introducing scales for the dimensioned quantities $x_i, \hat{u}, \hat{p}, s$ and ρ. Non-dimensionalized quantities are written with a bar.

$$z = W_f \overline{z},\ \hat{u}_z = U\overline{\hat{u}}_z,\ \hat{p} = \Sigma\overline{\hat{p}},\ s = \frac{1}{T_c}\overline{s},\ \rho = \rho_f\overline{\rho}, \tag{3.10}$$

where:

- the length scale W_f corresponds to the fault length;
- U is a characteristic length scale for the solid phase displacement in the z-th direction;
- The characteristic scale for the pore pressure is denoted Σ and expresses as

$$\Sigma = \frac{U}{W_f}M = \epsilon_0 M, \quad \text{with } M = \lambda + 2G = K + 4/3G, \tag{3.11}$$

  where M is the longitudinal wave modulus, which can be expressed in terms of Lamé coefficients (λ, G) or using the bulk modulus K and the shear wave modulus G;
- ϵ_0 is a characteristic deformation of the solid;
- ρ and ρ_f are respectively the densities of the porous medium and of the pore fluid;
- T_c defines the characteristic timescale of forced motion. It allows to non-dimensionalize the Laplace variable s and its values may range between the characteristic timescale of a seismic motion ($\approx$ 1 s) and the characteristic timescale of an aseismic motion ($\approx$ 1 year).

The simplification of the complete poroelastodynamic equations relies on the identification of negligible timescales with respect to representative natural periods of the system. We define the different timescales considered:

- T_f expresses a characteristic diffusion timescale at the microscopic pore fluid scale.

$$T_f = \rho_f \frac{k}{\eta}, \tag{3.12}$$

  where k is the permeability of the porous medium, and η denotes the dynamic viscosity of the pore-fluid;
- T_{pw} corresponds to the characteristic longitudinal wave propagation timescale.

$$T_{pw} = \frac{W_f}{c_p}, \quad \text{with } c_p = \sqrt{M/\rho}, \tag{3.13}$$

  where c_p defines the longitudinal wave velocity. This timescale is in the same order of magnitude as the period of a seismic motion;

- T_d defines another diffusion timescale at the macroscopic scale.

$$T_d = \frac{D^2}{c_{hy}}, \quad \text{with } c_{hy} = Rk/\eta, \tag{3.14}$$

where D is the distance between the injection well and the fault, c_{hy} is the hydraulic diffusivity coefficient, and R is a coupling modulus between the fluid and the solid. T_d represents the time for the fluid to diffuse from the injection well to the fault interface, i.e. to drain through the interconnected pores in the solid matrix of the porous medium.

The different scales are gathered in Table 3.1. From the parameter values given in Table 3.2, we can deduce the values of the natural characteristic times of the system T_f, T_{pw}, and T_d.

Scale	Definition	Value / Units
$W_f = z/\overline{z}$	Characteristic fault length	≈ 5 km
$U = u_i/\overline{u}_i$	Characteristic length scale for the solid displacement in the z-direction	m
$\epsilon_0 = U/W_f$	Characteristic strain scale	$\lessapprox 10^{-3}$ $[\epsilon_0] = 1$
$\Sigma = \epsilon_0 M = p/\overline{p}$	Characteristic scale for the pore fluid pressure	$\lessapprox 18 \cdot 10^6$ Pa
T_c	Characteristic time	between 1 s and 1 year
$T_f = \rho_f k/\eta$	Characteristic diffusion timescale (at microscopic pore fluid scale)	$\approx 3.3 \cdot 10^{-4}$ s
$T_{pw} = W_f/c_p$	Characteristic longitudinal wave propagation timescale	≈ 1.7 s
$T_d = D^2/c_{hy}$	Characteristic diffusion timescale from the diffusion equation	$\approx 2.5 \cdot 10^5$ s = 70 h
$\lambda_L = D/W_f$	Characteristic length ratio	1 $[\lambda_L] = 1$

Table 3.1 • Scales introduced for the dimensional analysis of poroelastodynamic equations.

Now that we have introduced all these dimensionless quantities and their associated scales, we can rewrite (3.8) in a dimensionless form. To simplify the reading, details are omitted but given in C.2.

$$\overline{\hat{u}}_{z,zz} - \left(\alpha - \frac{T_f}{T_c}\overline{s}\left(1 + \overline{s}\frac{T_f}{T_c}\frac{\mathcal{T}}{\Phi}\right)^{-1}\right)\overline{\hat{p}}_{,z} - \left(\overline{\rho} - \frac{T_f}{T_c}\overline{s}\left(1 + \overline{s}\frac{T_f}{T_c}\frac{\mathcal{T}}{\Phi}\right)^{-1}\right)\frac{1}{\overline{\rho}}\frac{T_{pw}^2}{T_c^2}\overline{s}^2\overline{\hat{u}}_z = 0, \tag{3.15a}$$

$$\frac{T_c}{T_d}\frac{\lambda_L^2}{\Phi^2}\left(1 + \overline{s}\frac{T_f}{T_c}\frac{\mathcal{T}}{\Phi}\right)^{-1}\overline{\hat{p}}_{,zz} - \overline{s}\overline{\hat{p}} - \left(\alpha - \frac{T_f}{T_c}\overline{s}\left(1 + \overline{s}\frac{T_f}{T_c}\frac{\mathcal{T}}{\Phi}\right)^{-1}\right)\frac{R}{\Phi^2 M}\overline{s}\overline{\hat{u}}_{z,z} = 0. \tag{3.15b}$$

where $\mathcal{T}$ is the tortuosity.

In (3.15), we identify two non-dimensional timescales ratio, which are in front of potentially negligible terms. The simplifications conducted in the following developments depend on characteristic time ratios:

$$\varepsilon \hat{=} \frac{T_f}{T_c}, \text{ and } \xi \hat{=} \frac{T_{pw}}{T_c} \hat{=} \varepsilon^{\kappa/2}, \text{ with } \kappa \in \mathbb{Z}. \tag{3.16}$$

Determining the order of magnitude of these time ratios will allow us to know whether the corresponding terms in the equations are predominant or negligible. We can assume that $\varepsilon \ll 1$ to simplify our dimensionless equations. Indeed, T_c stands for the characteristic timescale of the forced motion, which ranges between the characteristic timescale of a seismic motion (≈ 1 s) and the characteristic period of an aseismic motion (≈ 1 yr). We want

to assess formally that inertial effects are predominant over diffusion effects at the timescale of an earthquake motion, whereas diffusion effects should be privileged at the timescale of an aseismic motion. In both cases $T_c \gg T_f$ as the latter corresponds to a microscopic diffusion timescale, which characterizes the motion of fluid in the pore network. As we do not know the order of magnitude of the characteristic time ratio ξ, we express it as a power of ε using the exponent κ. Determining the range of values taken by κ enables determining the order of magnitude of ξ. Assuming that $\varepsilon \to 0$, we are aware that we loose some solutions of the complete poroelastodynamic equations (in the case where the terms that are neglected were singular perturbations, Bender and Orszag (2013)). Nevertheless, this allows to simplify equations, keeping only the predominant fluid effects, which guaranties a more efficient incorporation of hydro-mechanical couplings in our numerical tools.

We write equations (3.15a) and (3.15b) in terms of ε and $\xi = \varepsilon^{\kappa/2}$ with the help of Equation (3.18):

$$\overline{\hat{u}}_{z,zz} - \left(\alpha - \varepsilon\overline{s}\left(1 + \overline{s}\varepsilon\frac{\mathcal{T}}{\Phi}\right)^{-1}\right)\overline{\hat{p}}_{,z} - \left(\overline{\rho} - \varepsilon\overline{s}\left(1 + \overline{s}\varepsilon\frac{\mathcal{T}}{\Phi}\right)^{-1}\right)\frac{1}{\overline{\rho}}\varepsilon^{\kappa}\overline{s}^2\overline{\hat{u}}_z = 0, \tag{3.17a}$$

$$\overline{\rho}\frac{R}{\Phi^2 M}\varepsilon^{1-\kappa}\left(1 + \overline{s}\varepsilon\frac{\mathcal{T}}{\Phi}\right)^{-1}\overline{\hat{p}}_{,zz} - \overline{s}\overline{\hat{p}} - \left(\alpha - \varepsilon\overline{s}\left(1 + \overline{s}\varepsilon\frac{\mathcal{T}}{\Phi}\right)^{-1}\right)\frac{R}{\Phi^2 M}\overline{s}\overline{\hat{u}}_{z,z} = 0. \tag{3.17b}$$

(3.17) corresponds to the non-dimensionalized poroelastodynamic balance momentum equations for the solid matrix and for the pore-fluid.

In order to evaluate the predominant terms in equations (3.17), we need to determine the values that can be taken by the superscript κ defined in (3.16). To this aim, the order of magnitude of the natural periods of the system, T_f, T_{pw}, T_d allow deriving inequalities which are useful to determine the range of values of κ.

$$T_d > T_{pw} > T_f \text{ and } \frac{T_f}{T_d} \ll 1, \frac{T_{pw}}{T_d} \ll 1, \frac{T_{pw}}{T_f} \gg 1, \text{ with } T_f = \frac{\lambda_L^2}{\overline{\rho}}\frac{M}{R}\frac{T_{pw}^2}{T_d}, \tag{3.18}$$

yielding

$$T_{pw} \geqslant T_f \underset{T_c>0}{\Leftrightarrow} \frac{T_{pw}}{T_c} \geqslant \frac{T_f}{T_c} \Leftrightarrow \varepsilon^{\kappa/2} \geqslant \varepsilon \underset{0<\varepsilon<1}{\Leftrightarrow} \kappa \leqslant 2,$$

which is always true.

In addition, the values reached by κ depend on the characteristic time T_c. If the characteristic time T_c is of the order of the timescale of a seismic motion, we have

$$T_{pw} \geqslant T_c \Leftrightarrow \varepsilon^{\kappa/2} \geqslant 1 = \varepsilon^0 \underset{0<\varepsilon<1}{\Leftrightarrow} \kappa \leqslant 0.$$

Finally, if the characteristic time T_c is of the order of the characteristic period of an aseismic motion or of a seismic cycle, we have

$$\text{if } T_{pw} < T_c \Leftrightarrow \varepsilon^{\kappa/2} < 1 = \varepsilon^0 \underset{0<\varepsilon<1}{\Leftrightarrow} \kappa > 0.$$

We distinguish the case where the characteristic time T_c is of the order of the characteristic timescale of a seismic motion ($\kappa \leqslant 0$, our case), from the case where the characteristic time

T_c is of the order of the characteristic period of an aseismic motion or of a seismic cycle ($0 < \kappa \leqslant 2$, cases majorly considered in the literature) in equations (3.17). This allows to give simplified models (i) at the timescale of a seismic motion or (ii) at the timescale of an aseismic motion or a seismic cycle.

We first consider that the period T_c is of the order of the timescale of a seismic motion. This corresponds to the case where $\kappa = 0$ ($T_c = T_{pw}$). Separating terms of the order of ε from the others, (3.17) becomes

$$\overline{\hat{u}}_{z,zz} - \alpha \overline{\hat{p}}_{,z} - \overline{s}^2 \overline{\hat{u}}_z = \varepsilon \left(-\overline{s} \frac{\mathcal{T}}{\Phi} \overline{\hat{u}}_{z,zz} + \left(\alpha \frac{\mathcal{T}}{\Phi} - 1 \right) \overline{s} \overline{\hat{p}}_{,z} + \left(\frac{\mathcal{T}}{\Phi} - \frac{1}{\overline{\rho}} \right) \overline{s}^3 \overline{\hat{u}}_z \right) \tag{3.19a}$$

$$-\overline{s}\overline{\hat{p}} - \alpha \frac{R}{\Phi^2 M} \overline{s} \overline{\hat{u}}_{z,z} = \varepsilon \left(-\overline{\rho} \frac{R}{\Phi^2 M} \overline{\hat{p}}_{,zz} + \frac{\mathcal{T}}{\Phi} \overline{s}^2 \overline{\hat{p}} + \left(\alpha \frac{\mathcal{T}}{\Phi} - 1 \right) \frac{R}{\Phi^2 M} \overline{s}^2 \overline{\hat{u}}_{z,z} \right) \tag{3.19b}$$

Assuming $\varepsilon \to 0$ to keep only the predominant poroelastodynamic terms, (3.19) write

$$\overline{\hat{u}}_{z,zz} - \alpha \overline{\hat{p}}_{,z} - \overline{s}^2 \overline{\hat{u}}_z = 0, \tag{3.20a}$$

$$\overline{s}\overline{\hat{p}} + \alpha \frac{R}{\Phi^2 M} \overline{s} \overline{\hat{u}}_{z,z} = 0. \tag{3.20b}$$

The characteristic time $T_c \to T_{pw}$. T_{pw} is the compression wave timescale. It is a representative characteristic timescale of the system, and it is of the order of magnitude of the characteristic period of a seismic motion (≈ 1 s). As expected, (3.20) shows that no relative movement of the fluid is permitted in this case of fast timescale. Thus, both diffusion effects and inertial effects for the fluid are neglected, whereas the inertial effects for the solid, the poroelastic stress variation, and the rate of undrained pore pressure are predominant effects. This is equivalent to $w_z \to 0$ (w_z is the seepage displacement, $w_z \to 0$ means no relative fluid movement) and $k \to 0$ (the medium behaves as impermeable) in (3.8). The corresponding dimensionalized system to (3.20) is

$$M u_{z,zz} - \alpha p_{,z} - \rho \ddot{u}_z = 0, \tag{3.21a}$$

$$\dot{p} + \alpha \frac{R}{\Phi^2} \dot{u}_{z,z} = 0. \tag{3.21b}$$

Equation (3.21a) corresponds to an elastodynamic equation perturbed with the pore pressure gradient, and Equation (3.21b) is the time derivative of the undrained pore pressure p_u

$$p_u = p + \alpha \frac{R}{\Phi^2} u_{z,z}. \tag{3.22}$$

In (3.21), the fluid mass does not vary, which leads to a simplification of the continuity equation and the pore pressure is proportional to solid strains. As a consequence, in the Laplace domain, we can reduce (3.20) to one elastodynamic equation on the unknown u_z (vertical solid displacement) alone, with undrained material properties. After an inverse Laplace transform, we obtain the corresponding equation in the dimensionalized form and in the time-domain

$$\left(M + \alpha^2 \frac{R}{\Phi^2} \right) u_{z,zz} - \rho \ddot{u}_z = 0, \text{ with } u_{z,z} = -\frac{\Phi^2}{\alpha R} p. \tag{3.23}$$

In (3.23), only the compression-wave modulus M is modified in its undrained form $M + \alpha^2 R/\Phi^2$ compared to a "dry" elastodynamic problem. Therefore, the solution of the poroelastodynamic equations at the timescale of the seismic motion can be obtained either using the $\mathbf{u} - p$ formulation given by (3.21) or with the reduced equation (3.23). Thus, we may propose to use these undrained equations to take into account the fluid effects on fault slip when the response of the system corresponds to a seismic event.

Next, we consider that the characteristic time T_c is of the order of the timescale of an aseismic motion or of a seismic cycle. This corresponds to the case where $0 < \kappa \leqslant 2$. In the particular case where $\kappa = 1$ ($T_c > T_{pw}$), separating terms of the order of ε or lower from the others, (3.17) becomes

$$\overline{\hat{u}}_{z,zz} - \alpha \overline{\hat{p}}_{,z} = \varepsilon \left(-\overline{s} \frac{\mathcal{T}}{\Phi} \overline{\hat{u}}_{z,zz} + \left(\alpha \frac{\mathcal{T}}{\Phi} - 1 \right) \overline{s} \overline{\hat{p}}_{,z} + \overline{s}^2 \overline{\hat{u}}_z \right) + \varepsilon^2 \left(\frac{\mathcal{T}}{\Phi} - \frac{1}{\overline{\rho}} \right) \overline{s}^3 \overline{\hat{u}}_z \tag{3.24a}$$

$$\overline{\rho} \frac{R}{\Phi^2 M} \overline{\hat{p}}_{,zz} - \overline{s} \overline{\hat{p}} - \alpha \frac{R}{\Phi^2 M} \overline{s} \overline{\hat{u}}_{z,z} = \varepsilon \left(\frac{\mathcal{T}}{\Phi} \overline{s}^2 \overline{\hat{p}} + \left(\alpha \frac{\mathcal{T}}{\Phi} - 1 \right) \frac{R}{\Phi^2 M} \overline{s}^2 \overline{\hat{u}}_{z,z} \right) \tag{3.24b}$$

Assuming $\varepsilon \to 0$ to keep only the predominant poroelastodynamic terms, (3.24) writes

$$\overline{\hat{u}}_{z,zz} - \alpha \overline{\hat{p}}_{,z} = 0 \tag{3.25a}$$

$$\overline{\rho} \frac{R}{\Phi^2 M} \overline{\hat{p}}_{,zz} - \overline{s} \overline{\hat{p}} - \alpha \frac{R}{\Phi^2 M} \overline{s} \overline{\hat{u}}_{z,z} = 0 \tag{3.25b}$$

The characteristic time T_c is larger than the compression wave timescale T_{pw}. We can assume that T_c takes the order of the characteristic period of an aseismic motion (≈ 1 year). Then, both acceleration terms for the solid and for the fluid can be neglected in (3.25), whereas the poroelastic stress variation, the dimensionless diffusion term $\overline{\rho} R/(\Phi^2 M) \overline{\hat{p}}_{,zz}$, and the rate of undrained pore pressure cannot. This is equivalent to a sufficiently slow motion such $\ddot{u}_z \to 0$ and $\ddot{w}_z \to 0$ in the complete poroelastodynamic equation (3.8). Thus, in the case where $\kappa = 1$ ($T_c > T_{pw}$) and $\varepsilon \to 0$, (3.8) is reduced to a quasi-static problem. The corresponding dimensionalized equations in the time domain write

$$M u_{z,zz} - \alpha p_{,z} = 0, \tag{3.26a}$$

$$\frac{c_{hy}}{\Phi^2} p_{,zz} - \dot{p} - \alpha \frac{R}{\Phi^2} \dot{u}_{z,z} = 0. \tag{3.26b}$$

(3.26) corresponds to the consolidation equations (Biot, 1941; Zienkiewicz et al., 1980) considered by Heimisson et al. (2019), Heimisson et al. (2021), and Heimisson et al. (2022). This long-term behavior approximation consists in a two-way coupling between the fluid and the solid that is modelled by a poroelastostatic equation (3.26a) and a diffusion equation perturbed by a solid deformation term (3.26b).

> **Remark 3.2.** *For a lot of practical configurations the poroelastostatic equations* (3.26) *uncouple. In the case of an irrotational displacement field, equations can uncouple using Biot's (potentials) decomposition as detailed by Detournay and Cheng (1993) and Cheng (2016). It is also the case for flow-driven deformation in a layer surrounded by*

impermeable material (Marck et al., 2015), or when the layer is much more permeable than the surrounding host rock as considered by Viesca (2021) and Sáez et al. (2022) among others. In this work we do not consider such assumptions.

In the particular case where $\kappa = 2$ we must come back to (3.17) to reevaluate the predominant poroelastodynamic terms. Hence, we separate terms of the order of ε or lower from the others in (3.17). We obtain

$$\overline{\hat{u}}_{z,zz} - \alpha \overline{\hat{p}}_{,z} = \varepsilon \left(-\overline{s} \frac{\mathcal{T}}{\Phi} \overline{\hat{u}}_{z,zz} + \left(\alpha \frac{\mathcal{T}}{\Phi} - 1 \right) \overline{s} \overline{\hat{p}}_{,z} \right) + \varepsilon^2 \overline{s}^2 \overline{\hat{u}}_z + \varepsilon^3 \left(\frac{\mathcal{T}}{\Phi} - \frac{1}{\overline{\rho}} \right) \overline{s}^3 \overline{\hat{u}}_z \tag{3.27a}$$

$$\overline{\rho} \frac{R}{\Phi^2 M} \overline{\hat{p}}_{,zz} = \varepsilon \left(\overline{s} \overline{\hat{p}} + \alpha \frac{R}{\Phi^2 M} \overline{s} \overline{\hat{u}}_{z,z} \right) + \varepsilon^2 \left(\frac{\mathcal{T}}{\Phi} \overline{s}^2 \overline{\hat{p}} + \left(\alpha \frac{\mathcal{T}}{\Phi} - 1 \right) \frac{R}{\Phi^2 M} \overline{s}^2 \overline{\hat{u}}_{z,z} \right) \tag{3.27b}$$

Assuming $\varepsilon \to 0$ to keep only the predominant poroelastodynamic terms, we obtain a further approximation of equations (3.25), and (3.27)

$$\overline{\hat{u}}_{z,zz} - \alpha \overline{\hat{p}}_{,z} = 0, \tag{3.28a}$$

$$\overline{\hat{p}}_{,zz} = 0. \tag{3.28b}$$

Since $\kappa = 2$, the characteristic time T_c is larger than the compression wave timescale T_{pw}, of the order of the characteristic timescale of an aseismic motion (≈ 1 year). Both acceleration terms for the solid and for the fluid, and the rate of undrained pore pressure have been neglected, whereas the poroelastic stress variation and the dimensionless diffusion term $\overline{\hat{p}}_{,zz}$ are predominant. It results in uncoupled equations which correspond to drained poroelastostatic equations in case of a constant fluid pore pressure (or zero excess pore pressure compared to the equilibrium state). Drained equations can also be obtained in the approximation of an infinitely permeable medium ($k \to 0$) in the quasi-static version of equations (3.8a) and (3.8b). In this case, K and G are thus identified as the bulk and the shear modulus of the drained elastic solid. The corresponding dimensionalized equations when $\kappa = 2$ ($T_c > T_{pw}$), and $\varepsilon \to 0$ write

$$M u_{z,zz} - \alpha p_{,z} = 0, \tag{3.29a}$$

$$\frac{k}{\eta} p_{,zz} = 0. \tag{3.29b}$$

(3.29a) corresponds to a poroelastostatic equation (respectively a drained elastostatic equation in case of a constant fluid pore pressure) and (3.29b) corresponds to a Laplace equation for the fluid pore pressure. They are one-way coupled equations. As a consequence, the above analysis suggests the use of the first-order approximation system of equations (3.26) to take into account fluid-effects on fault slip when the response of the system is likely to correspond to an aseismic motion as in the context of fluid-injection induced aseismic slip. (3.26) corresponds to the model used by Heimisson et al. (2019), Heimisson et al. (2021), and Heimisson et al. (2022).

In the following developments, we focus on the case where $\kappa = 0$ and $\varepsilon \to 0$, which corresponds to the case where the characteristic time T_c is of the order of the characteristic

time of a seismic motion. The results of the dimensional analysis of the poroelastodynamic equations are summarized in Table 3.3. All the parameters and variables used are defined in Table 3.2. The choices for numerical values in Table 3.2 are detailed in C.1. A reasonable choice of the orders of magnitude of the parameters allows to discuss the importance of each term in the poroelastodynamic equations considered.

Parameter	Definition	Value / Units
$M = K + 4/3G$	longitudinal wave modulus	≈ 18 GPa
K	Bulk modulus of the elastic skeleton	≈ 10 GPa
G	Shear modulus of the elastic skeleton	≈ 6 GPa
α	Biot effective stress coefficient	0.8
ρ	Density of the porous medium	2500 kg.m^{-3}
$c_p = \sqrt{M/\rho}$	longitudinal wave velocity	≈ 2683 m.s^{-1}
ρ_f	Density of the fluid phase	1000 kg.m^{-3}
ρ_a	Apparent density of the fluid phase	99 kg.m^{-3}
$\mathcal{T} = (\rho_a/\rho_f + \Phi)/\Phi$	Tortuosity	≈ 1.66
Φ	Porosity	0.15
k	Permeability of the medium	10^{-10} m^2
η	Dynamic viscosity	$3 \cdot 10^{-4}$ Pa.s
$c_{hy} = Rk/\eta$	Diffusion coefficient	$\approx 10^2$ m^2.s^{-1}
R	Coupling modulus between the fluid and the solid	≈ 0.31 GPa
D	Characteristic distance between the injection well and the fault	5 km
s	Laplace variable	s^{-1}
u_i	Solid displacement in the i-direction	m
x_i	Space variable in the i-direction	m
p	Pore fluid pressure	MPa

Table 3.2 • Parameters for the dimensional analysis of poroelastodynamic equations.

4.2 Scaling 1D poroelastodynamic equations with a fluid source

We now add a fluid-injection point source in the generic 1D poroelastodynamic equation (3.8b), and we extend the results of the dimensional analysis conducted in Section 4.1. This new one-dimensional problem is closer to the one we considered in Section 1. The objectives are to model a fluid-injection source in the initial version of the poroelastodynamic equations (3.8), and to assess formally the conditions under which the fluid-source term is considered as a predominant term in the poroelastodynamic equations.

The balance momentum equations used here are the one-dimensional version of (3.2).

$$M\hat{u}_{z,zz} - (\alpha - \beta(s))\hat{p}_{,z} - (\rho - \beta(s)\rho_f)s^2\hat{u}_z = 0, \tag{3.30a}$$

$$\frac{\beta(s)}{s\rho_f}\hat{p}_{,zz} - \frac{\Phi^2 s}{R}\hat{p} - (\alpha - \beta(s))s\hat{u}_{z,z} = -\hat{\gamma}\delta_D(z - z_0). \tag{3.30b}$$

In addition to the dimensionless quantities and the corresponding scales considered in Section 4.1, we introduce T_s to scale the rate of fluid supply per unit volume

$$\hat{\gamma} = T_s^{-1}\overline{\hat{\gamma}}, \tag{3.31}$$

where T_s corresponds to a fluid-injection characteristic time. Here, $\overline{\hat{\gamma}} = \mathcal{O}(1)$ and $\overline{s} = \mathcal{O}(1)$. The objective is to assess formally the conditions under which the fluid injection source term is part of the predominant terms in (3.30b). We perform the non-dimensionalization of (3.30) following the same stages as previously.

In the case with a fluid-injection source, equation (3.17), obtained after having performed the scaling, using the expression of $\overline{\beta}(\overline{s})$ (C.1), and introduced ε and $\varepsilon^{\kappa/2}$ becomes

$$\overline{\hat{u}}_{z,zz} - \left(\alpha - \varepsilon\overline{s}\left(1 + \overline{s}\varepsilon\frac{\mathcal{T}}{\Phi}\right)^{-1}\right)\overline{\hat{p}}_{,z} - \left(\overline{\rho} - \varepsilon\overline{s}\left(1 + \overline{s}\varepsilon\frac{\mathcal{T}}{\Phi}\right)^{-1}\right)\frac{1}{\overline{\rho}}\varepsilon^{\kappa}\overline{s}^2\overline{\hat{u}}_z = 0 \tag{3.32a}$$

$$\begin{aligned}\overline{\rho}\frac{R}{\Phi^2 M}\varepsilon^{1-\kappa}\left(1 + \overline{s}\varepsilon\frac{\mathcal{T}}{\Phi}\right)^{-1}\overline{\hat{p}}_{,zz} - \overline{s}\overline{\hat{p}} - \left(\alpha - \varepsilon\overline{s}\left(1 + \overline{s}\varepsilon\frac{\mathcal{T}}{\Phi}\right)^{-1}\right)\frac{R}{\Phi^2 M}\overline{s}\overline{\hat{u}}_{z,z} \\ = -\underbrace{\frac{R}{\Phi^2\Sigma}\frac{T_c}{T_s}}_{\Psi\equiv\varepsilon^{\Lambda}}\overline{\hat{\gamma}}\delta_D(\overline{z} - \overline{z}_0)\end{aligned} \tag{3.32b}$$

where we introduced the more compact notation $\Psi \equiv \varepsilon^{\Lambda}$. Therefore, assessing whether the fluid-injection source term must be kept in the balance momentum equations is equivalent to determining the range of values reached by Λ.

As in Section 4.1, we first need to determine the values reached by κ in order to simplify the non-dimensionalized complete poroelastodynamic equations (3.32).

$$T_{pw} \geqslant T_f \Leftrightarrow \kappa \leqslant 2, \text{ and } \kappa \leqslant 0 \text{ if } T_{pw} \geqslant T_c, \text{ otherwise } \kappa > 0 \text{ if } T_{pw} < T_c.$$

We concentrate on the case where the time T_c is of the order of the earthquake instability timescale ($\kappa \leqslant 0$, our case) in (3.32). This case allows us to focus on the simplification of

the complete poroelastodynamic equations at the timescale of a seismic motion. When the period T_c is of the order of the earthquake instability timescale, $\kappa = 0$ ($T_c = T_{pw}$). Separating terms of the order of ε from the others, (3.32) writes

$$\overline{\hat{u}}_{z,zz} - \alpha \overline{\hat{p}}_{,z} - \overline{s}^2 \overline{\hat{u}}_z = \varepsilon \left(-\overline{s} \frac{\mathcal{T}}{\Phi} \overline{\hat{u}}_{z,zz} + \left(\alpha \frac{\mathcal{T}}{\Phi} - 1 \right) \overline{s} \overline{\hat{p}}_{,z} + \left(\frac{\mathcal{T}}{\Phi} - \frac{1}{\overline{\rho}} \right) \overline{s}^3 \overline{\hat{u}}_z \right) \tag{3.33a}$$

$$-\overline{s}\overline{\hat{p}} - \alpha \frac{R}{\Phi^2 M} \overline{s} \overline{\hat{u}}_{z,z} + \varepsilon^{\Lambda} \overline{\hat{\gamma}} \delta_D(\overline{z} - \overline{z}_0) = \varepsilon \left(-\overline{\rho} \frac{R}{\Phi^2 M} \overline{\hat{p}}_{,zz} + \frac{\mathcal{T}}{\Phi} \overline{s}^2 \overline{\hat{p}} + \left(\alpha \frac{\mathcal{T}}{\Phi} - 1 \right) \frac{R}{\Phi^2 M} \overline{s}^2 \overline{\hat{u}}_{z,z} \right) \tag{3.33b}$$

We now focus on the conditions under which the fluid source term can be maintained in the simplified equations. In equation (3.33b), if we want to keep the fluid source term when $\varepsilon \to 0$, its order of magnitude must be comparable to the order of the rate of fluid pressure. As we assumed $\overline{\hat{\gamma}} = \mathcal{O}(1)$ and $\overline{s} = \mathcal{O}(1)$, this corresponds to the case where the coefficient Ψ has the same order of magnitude as the dimensionless pore-fluid pressure ($\overline{\hat{p}} = \hat{p}/\Sigma$, defined as the ratio of pressure over the characteristic stress scale). The value of Λ depends on the values of the pore-fluid pressure compared to the characteristic stress scale Σ. For instance if $\hat{p} = \Sigma$, $\Lambda = 0$. This gives a condition on the characteristic fluid injection timescale T_s.

$$\Lambda = 0 \Rightarrow \Psi(=1) \sim \overline{\hat{p}} \Rightarrow T_s \underset{\frac{R}{\Phi^2 M} \approx 1}{\approx} \left(\frac{\hat{p}}{M} \right)^{-1} T_c. \tag{3.34}$$

(3.34) highlights that maintaining the fluid source term in (3.33b), implies the characteristic fluid injection time to be of the order of $(\hat{p}/M)^{-1} T_c$. The ratio $\hat{p}/M$ quantifies the volume strain to which the solid matrix is submitted due to fluid injection. This strain level must be acceptable to prevent the solid matrix to collapse when injecting fluid underground. As expected, the fluid injection timescale T_s also depends on the characteristic time T_c. In fact, the injection time must be adapted to the period which characterizes the fault slip so that a coupling effect could be at stake. To maintain the fluid source term in (3.33b), the characteristic fluid injection time must satisfy (3.34).

Assuming (3.34) is satisfied and $\varepsilon \to 0$, (3.33) becomes

$$\overline{\hat{u}}_{z,zz} - \alpha \overline{\hat{p}}_{,z} - \overline{s}^2 \overline{\hat{u}}_z = 0, \tag{3.35a}$$

$$\overline{s}\overline{\hat{p}} + \alpha \frac{R}{\Phi^2 M} \overline{s} \overline{\hat{u}}_{z,z} = \overline{\hat{\gamma}} \delta_D(\overline{z} - \overline{z}_0). \tag{3.35b}$$

Thus, when $\kappa = 0$, no relative movement of the fluid is permitted (see Section 4.1). Both diffusion effects and inertial effects for the fluid are neglected, whereas the inertial effects for the solid, the poroelastic stress variation, the rate of undrained pore pressure and the fluid source, if (3.34) is satisfied, are predominant effects. This is equivalent to $w_z \to 0$ and $k \to 0$ in equations (3.30). The dimensioned form of (3.35) gives

$$M u_{z,zz} - \alpha p_{,z} - \rho \ddot{u}_z = 0, \tag{3.36a}$$

$$\dot{p} + \alpha \frac{R}{\Phi^2} \dot{u}_{z,z} = \frac{R}{\Phi^2} \gamma \delta_D(z - z_0). \tag{3.36b}$$

Equation (3.36a) corresponds to an elastodynamic equation perturbed with the pore pressure gradient, and Equation (3.36a) gives a relation between the time derivative of the undrained pore pressure and the fluid source. In the Laplace domain, we can reduce equations (3.35a) and (3.35b) to one elastodynamic equation with undrained material properties and a dipole source term (spatial derivative of the fluid-injection point-source term).

$$\left(M+\alpha^2\frac{R}{\Phi^2}\right)\hat{u}_{z,zz}-\rho s^2\hat{u}_z=\alpha\frac{R}{\Phi^2}\frac{\hat{\gamma}}{s}\delta_D(z-z_0)_{,z} \text{ and } \hat{u}_{z,z}=-\frac{\Phi^2}{\alpha R}\hat{p}+\frac{\hat{\gamma}}{\alpha s}\delta(z-z_0). \tag{3.37}$$

After an inverse Laplace transform, we obtain the corresponding equation in the time domain

$$\begin{aligned}&\left(M+\alpha^2\frac{R}{\Phi^2}\right)u_{z,zz}-\rho\ddot{u}_z=\alpha\frac{R}{\Phi^2}\int_0^t\gamma(t')dt'\delta_D(z-z_0)_{,z}\\ &\text{and } u_{z,z}=-\frac{\Phi^2}{\alpha R}p+\frac{1}{\alpha}\int_0^t\gamma(t')dt'\delta_D(z-z_0).\end{aligned} \tag{3.38}$$

As a result, the previous analyses suggest the use the system (3.36) or (3.38) to take into account fluid effects on fault slip when the characteristic time T_c of the system correspond to the timescale of a seismic motion.

4.3 Extension to 2D

In practice, 1D equations are not sufficient to take into account fluid effects on fault. At least, 2D equations must be considered. Here, we present the procedure to extend the dimensional analysis conducted in section 4.1 to a 2D/3D generic poroelastodynamic problem with a fluid-injection point source as introduced in Section 1. For the sake of simplicity we present the 2D case.

In 2D, the generic poroelastodynamic equations with a fluid-injection source term write as (3.2).

$$G\hat{u}^s_{i,jj}+(K+(1/3)G)\,\hat{u}^s_{j,ij}-\left(\alpha-\beta(s)\right)\hat{p}_{,i}-s^2\left(\rho-\beta(s)\rho_f\right)\hat{u}^s_i=0, \tag{3.39a}$$

$$\frac{\beta(s)}{s\rho_f}\hat{p}_{,ii}-\frac{\Phi^2 s}{R}\hat{p}-\left(\alpha-\beta(s)\right)s\hat{u}^s_{i,i}=-\hat{\gamma}\delta_D(x_i-x_{i_0}), \tag{3.39b}$$

where $\delta_D(\mathbf{x})$ is the two-dimensional Dirac distribution, with $\mathbf{x}^{\mathrm{T}}=(x_i,\,x_j)=(x,\,z)$ in Figure 3.1.

In addition to the parameters and scales defined in Tables 3.2 and 3.1, we give the shear wave velocity

$$c_s=\sqrt{G/\rho}, \tag{3.40}$$

where G is the shear wave modulus and ρ is the density of the porous medium. In the 1D case, only compression waves could occur, so that we had used the longitudinal wave modulus to define the characteristic scale Σ for the pore pressure. In the 2D case, both shear and compression waves can occur. Hence, we choose to define the characteristic stress scale Σ using the shear modulus G.

$$\Sigma=G\epsilon_0. \tag{3.41}$$

And we re-define the dimensionless displacement field and space variable to take into account each direction in space.

$$\begin{aligned} x_i &= W_f \overline{L}_{ij} \overline{x}_j, \text{ where } \overline{L}_{ij} = W_f^{-1} \text{diag}(L_1, L_2), \\ u_i &= U \overline{U}_{ij} \overline{u}_j, \text{ where } \overline{U}_{ij} = U^{-1} \text{diag}(U_1, U_2). \end{aligned} \tag{3.42}$$

We conduct the non-dimensionalization of equations (3.39) following the same stages as in C.2.

In the case of a two-dimensional configuration with a fluid-injection point source, after having performed the scaling, and introduced ε and $\varepsilon^{\kappa/2}$, the 2D poroelastodynamic equations (3.39) writes

$$\begin{aligned} &\overline{U}_{ik}\overline{L}_{jl}^{-2}\hat{\overline{u}}_{k,ll} + \frac{K+1/3G}{G}\overline{U}_{ik}\overline{L}_{il}^{-1}\overline{L}_{jm}^{-1}\hat{\overline{u}}_{k,lm} - \left(\alpha - \varepsilon\overline{s}\left(1+\overline{s}\varepsilon\frac{\mathscr{T}}{\Phi}\right)^{-1}\right)\overline{L}_{ij}^{-1}\hat{\overline{p}}_{,j} \\ &\qquad - \left(\overline{\rho} - \varepsilon\overline{s}\left(1+\overline{s}\varepsilon\frac{\mathscr{T}}{\Phi}\right)^{-1}\right)\frac{1}{\overline{\rho}}\varepsilon^{\kappa}\overline{s}^2\overline{U}_{ij}\hat{\overline{u}}_j = 0, \end{aligned} \tag{3.43a}$$

$$\begin{aligned} &\overline{\rho}\frac{R}{\Phi^2 G}\varepsilon^{1-\kappa}\left(1+\overline{s}\varepsilon\frac{\mathscr{T}}{\Phi}\right)^{-1}\overline{L}_{ij}^{-2}\hat{\overline{p}}_{,jj} - \overline{s}\hat{\overline{p}} - \left(\alpha - \varepsilon\overline{s}\left(1+\overline{s}\varepsilon\frac{\mathscr{T}}{\Phi}\right)^{-1}\right)\frac{R}{\Phi^2 G}\overline{s}\overline{U}_{ij}\overline{L}_{ik}^{-1}\hat{\overline{u}}_{j,k} \\ &\qquad = -\underbrace{\frac{R}{\Phi^2\Sigma}\frac{T_c}{T_s}}_{\Psi\equiv\varepsilon^{\Lambda}}\hat{\overline{\gamma}}\delta_D(\overline{\mathbf{x}}-\overline{\mathbf{x}}_0). \end{aligned} \tag{3.43b}$$

As previously, we first need to determine the values reached by κ in order to simplify the non-dimensionalized complete poroelastodynamic system of equations (3.43)

$$T_{pw} \geqslant T_f \Leftrightarrow \kappa \leqslant 2, \text{ and } \kappa \leqslant 0 \text{ if } T_{pw} \geqslant T_c, \kappa > 0 \text{ if } T_{pw} < T_c.$$

The condition (3.34) has again to be satisfied by the characteristic scale of the fluid-source term so that it could be maintained in the equations. Here it is given by

$$\Lambda = 0 \Rightarrow \Psi(=1) \sim \overline{\hat{p}} \Rightarrow T_s \underset{\frac{R}{\Phi^2 G}\approx 1}{\approx} \left(\frac{\hat{p}}{G}\right)^{-1} T_c. \tag{3.44}$$

Thus, in the particular case where $\kappa = 0$ (when the characteristic observation time of the fault $T_c = T_{pw}$, thus is of the order of the seismic timescale (≈ 1 s)), condition (3.44) is satisfied, and $\varepsilon \to 0$ to keep only the predominant poromechanics effects, (3.43) now writes

$$\overline{U}_{ik}\overline{L}_{jl}^{-2}\hat{\overline{u}}_{k,ll} + \frac{K+1/3G}{G}\overline{U}_{ik}\overline{L}_{il}^{-1}\overline{L}_{jm}^{-1}\hat{\overline{u}}_{k,lm} - \alpha\overline{L}_{ij}^{-1}\hat{\overline{p}}_{,j} - \overline{s}^2\overline{U}_{ij}\hat{\overline{u}}_j = 0, \tag{3.45a}$$

$$\overline{s}\hat{\overline{p}} + \alpha\frac{R}{\Phi^2 G}\overline{s}\overline{U}_{ij}\overline{L}_{ik}^{-1}\hat{\overline{u}}_{j,k} = \hat{\overline{\gamma}}\delta_D(\overline{x}_i - \overline{x}_{i_0}). \tag{3.45b}$$

The corresponding dimensionalized version of (3.45) in the time-domain is given by

$$Gu_{i,jj} + (K + 1/3G)u_{j,ij} - \alpha p_{,i} - \rho \ddot{u}_i = 0, \tag{3.46a}$$

$$\dot{p} + \alpha \frac{R}{\Phi^2}\dot{u}_{i,i} = \frac{R}{\Phi^2}\gamma \delta_D(x_i - x_{i_0}). \tag{3.46b}$$

In (3.46), both the fluid diffusion and inertial effects for the fluid have been neglected, while the inertial effects for the solid, the poroelastic stress variation, the rate of undrained pore pressure and the fluid source if (3.34) is satisfied are predominant effects. The relative movement of the fluid is neglected in this case, which is equivalent to $w_i \to 0$ and $k \to 0$ in equation (3.39). Equation (3.46a) corresponds to a 2D elastodynamic equation perturbed with the pore fluid pressure gradient, and Equation (3.46b) gives a relation between the time derivative of the undrained pore pressure and the fluid source. They can again be reduced to one elastodynamic equation with undrained material properties and a dipole source term (spatial derivative of the fluid-injection point source term). In the time domain, we obtain

$$\begin{aligned} &Gu_{i,jj} + (K + 1/3G)u_{j,ij} + \alpha^2 \frac{R}{\Phi^2}u_{i,ii} - \rho \ddot{u}_i = \alpha \frac{R}{\Phi^2}\int_0^t \gamma(t')dt'\delta_D(\mathbf{x} - \mathbf{x}_0)_{,i} \\ &\text{with } u_{i,i} = -\frac{\Phi^2}{\alpha R}p + \frac{1}{\alpha}\int_0^t \gamma(t')dt'\delta_D(\mathbf{x} - \mathbf{x}_0). \end{aligned} \tag{3.47}$$

Thus, for a 2D configuration with a fluid point source (see Figure 3.1), the above analysis suggests the use of equation (3.46) or (3.47) to take into account fluid effects on fault slip when the characteristic time T_c correspond to the timescale of a seismic motion.

4.4 Synthesis of the dimensional analysis of the poroelastodynamic equations

Table 3.3 summarizes our results for the scaling of the poroelastodynamic equations at different timescales.

In the 1D case without fluid-injection, at the timescale of an aseismic motion (Aseismic 1), we obtained simplified poroelastodynamic equations given by

$$Mu_{z,zz} - \alpha p_{,z} = 0, \tag{3.48a}$$

$$\frac{c_{hy}}{\Phi^2}p_{,zz} - \dot{p} - \alpha \frac{R}{\Phi^2}\dot{u}_{z,z} = 0. \tag{3.48b}$$

A further simplification of (3.48) at the timescale of an aseismic motion (Aseismic 2) gives

$$Mu_{z,zz} - \alpha p_{,z} = 0, \tag{3.49a}$$

$$\frac{k}{\eta}p_{,zz} = 0. \tag{3.49b}$$

At the timescale of a seismic motion, the complete model simplifies as an undrained poroelastodynamic equation

$$\left(M+\alpha^2\frac{R}{\Phi^2}\right)u_{z,zz}-\rho\ddot{u}_z=0,\ \text{with}\ u_{z,z}=-\frac{\Phi^2}{\alpha R}p. \tag{3.50}$$

In the 1D case with fluid injection, at the timescale of a seismic motion, the fluid-injection source term is maintained in the equations under the condition

$$\Lambda=0\Rightarrow\Psi(=1)\sim\overline{\hat{p}}\Rightarrow T_s\underset{\frac{R}{\Phi^2 M}\approx 1}{\approx}\left(\frac{\hat{p}}{M}\right)^{-1}T_c. \tag{3.51}$$

Hence, the complete model simplifies as the undrained poroelastodynamic equation

$$\begin{aligned}&\left(M+\alpha^2\frac{R}{\Phi^2}\right)u_{z,zz}-\rho\ddot{u}_z=\alpha\frac{R}{\Phi^2}\int_0^t\gamma(t')dt'\delta(z-z_0)_{,z}\\&\text{and}\ u_{z,z}=-\frac{\Phi^2}{\alpha R}p+\frac{1}{\alpha}\int_0^t\gamma(t')dt'\delta_D(z-z_0).\end{aligned} \tag{3.52}$$

In the 2D case with fluid injection, at the timescale of a seismic motion, the fluid-injection source term is maintained in the equations under the condition

$$\Lambda=0\Rightarrow\Psi(=1)\sim\overline{\hat{p}}\Rightarrow T_s\underset{\frac{R}{\Phi^2 G}\approx 1}{\approx}\left(\frac{\hat{p}}{G}\right)^{-1}T_c. \tag{3.53}$$

The complete model simplifies as the undrained poroelastodynamic equation

$$\begin{aligned}&Gu_{i,jj}+(K+1/3G)u_{j,ij}+\alpha^2\frac{R}{\Phi^2}u_{i,ii}-\rho\ddot{u}_i=\alpha\frac{R}{\Phi^2}\int_0^t\gamma(t')dt'\delta_D(\mathbf{x}-\mathbf{x}_0)_{,i}\\&\text{with}\ u_{i,i}=-\frac{\Phi^2}{\alpha R}p+\frac{1}{\alpha}\int_0^t\gamma(t')dt'\delta_D(\mathbf{x}-\mathbf{x}_0).\end{aligned} \tag{3.54}$$

We highlight that inertial effects are important to model fluid-injection effects on fault slip at the timescale of a seismic motion. A first step towards the incorporation of these effects into the numerical framework proposed would be to conduct fully-dynamic simulation instead of the quasi-dynamic simulations considered. The difficulty is that the calculation of a convolution product in time is required. To ensure efficient solving, in the frame of seismic cycle simulations, a constant time step is usually imposed as detailed by Lapusta and Liu (2009), which can induce cumulative errors and prevent from obtaining interpretable results.

Configuration	Timescale	Poroelastic stress variation	Inertial effects for the solid	Inertial effects for the fluid	Fluid diffusion	Rate of fluid pressure	Rate of solid dilation	Fluid source	Equations
1D without fluid source	Aseismic 1 ($T_c \approx 1$ year) $\kappa = 1$ i.e. $\frac{T_{pw}}{T_c} = \mathcal{O}(\sqrt{\varepsilon}) \ll 1$	✓	×	×	✓	✓	✓	/	(3.48)
	Aseismic 2 ($T_c \approx 1$ year) $\kappa = 2$ i.e. $\frac{T_{pw}}{T_c} = \mathcal{O}(\varepsilon) \ll 1$	✓	×	×	✓	×	×	/	(3.49)
	Seismic ($T_c \approx 1$ s) $\kappa = 0$ i.e. $\frac{T_{pw}}{T_c} = \mathcal{O}(1)$	✓	✓	×	×	✓	✓	/	(3.50)
1D with fluid source	Seismic ($T_c \approx 1$ s) $\kappa = 0$ i.e. $\frac{T_{pw}}{T_c} = \mathcal{O}(1)$	✓	✓	×	×	✓	✓	✓	(3.51) + (3.52)
2D with fluid source	Seismic ($T_c \approx 1$ s) $\kappa = 0$ i.e. $\frac{T_{pw}}{T_c} = \mathcal{O}(1)$	✓	✓	×	×	✓	✓	✓	(3.53) + (3.54)

Table 3.3 • Summary of our results for the scaling of poroelastodynamic equations at different timescales: predominant effects (✓), negligible effects (X), corresponding equations.

5 Illustration with a one-dimensional poroelastic problem

In this section, we illustrate the limitations of the simplifications of the complete poroelastodynamic equation at the timescale of a seismic motion with the help of a semi-analytical 1D example (see Schanz and Cheng (2000)). The numerical analysis first requires to determine the impulse responses of the equations considered in the Laplace domain using standard techniques for ordinary differential equations. Then, the inverse Laplace transform and the calculation of time-domain solutions using a convolution product in time with the function defining the temporal behavior of the loading are performed using the convolution quadrature method. Finally, the time domain responses of the complete poroelastodynamic model and of its simplified form at the timescale of a seismic motion are compared under and outside the assumptions of the simplified model to illustrate the conditions under which such an approximation if valid.

5.1 Problem formulation

Figure 3.2 defines the geometry and the boundary conditions of a wave-propagation problem in a one-dimensional poroelastic column (see Schanz and Cheng (2000)). We consider a

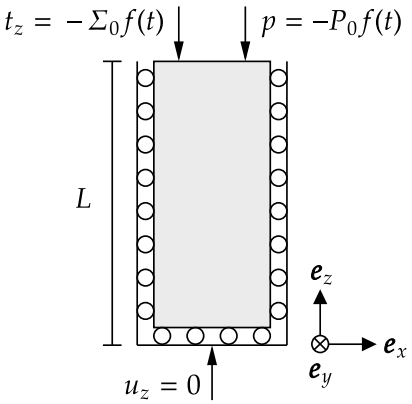

Figure 3.2 • Geometry and boundary conditions of the poroelastic column.

poroelastic column of length L along the $z-th$ direction for instance. The sidewalls and the bottom are rigid, frictionless, and impermeable so that normal displacement to the surface were blocked, and the column could only slide parallel to the wall. At the top, the traction t_z and the fluid pressure p are prescribed. At the bottom the displacement u_z is assumed to be equal to zero as well as the fluid flux q_z. This one-dimensional example can be seen as an approximation of a poroelastic half-space by setting the layer depth L large enough. The unknowns are the displacement u_z and the pore pressure p, which are governed by the poroelastodynamic balance momentum equations given in the Laplace domain by

$$M\hat{u}_{z,zz} - (\alpha - \beta(s))\hat{p}_{,z} - (\rho - \beta(s)\rho_f)s^2\hat{u}_z = 0 \tag{3.55a}$$

$$\frac{\beta(s)}{s\rho_f}\hat{p}_{,zz} - \frac{\Phi^2 s}{R}\hat{p} - (\alpha - \beta(s))s\hat{u}_{z,z} = 0 \tag{3.55b}$$

In the following parts we consider that from the initial values of displacement $\mathbf{u}$ and pore pressure p to their final values, the body forces in the solid skeleton f_i^s or in the fluid f_i^f do not vary. Therefore, taking the variations between the final and the initial $\mathbf{u} - p$ values as unknowns eliminates the body forces from (3.55). The Laplace domain boundary conditions in the case of an impulse loading $f(t) = \delta_D(t)$ are

$$\hat{u}_z(z=0) = 0,\ \hat{q}_z(z=0) = 0, \text{ and } \hat{t}_z(z=L) = -\Sigma_0,\ \hat{p}(z=L) = P_0. \tag{3.56}$$

Each of the nonzero boundary conditions in (3.56) represent a different type of loading. In the present work, the traction boundary condition stands for the steady-state far-field tectonic loading in a poroelastic half-space, and the pressure boundary condition plays the role of the fluid-injection in the medium. A more realistic way to take into account the fluid source term, would be in a second step to add a fluid-source term in (3.55b). As a starting point, we consider zero source term and the boundary conditions given in (3.56).

The aim is to demonstrate numerically that at the timescale of a seismic motion, the response of the complete poroelastodynamic model coincides with the response of the simplified model. Therefore, we also give the problem formulation in its simplified undrained form at the timescale of an earthquake instability resulting from the dimensional analysis previously conducted.

$$\left(M + \alpha^2 \frac{R}{\Phi^2}\right) \hat{u}_{z,zz} - \rho s^2 \hat{u}_z = 0 \tag{3.57a}$$

$$\text{with } \hat{p} = -\alpha \frac{R}{\Phi^2} \hat{u}_{z,z} \tag{3.57b}$$

In this case, in the Laplace domain, the boundary conditions in the case of an impulse loading are given by

$$\hat{u}_z(z=0) = 0 \text{ and } \hat{t}_z(z=L) = -\Sigma_0. \tag{3.58}$$

The one-dimensional version of the poroelastic constitutive law (1.48) is given by

$$\hat{t}_z = M \hat{u}_{z,z} - \alpha \hat{p}. \tag{3.59}$$

Hence, using the boundary conditions (3.58), and (3.57b), we deduce the imposed pressure p at the top of the poroelastic column.

$$\begin{aligned} &\hat{t}_z(z=L) \underset{(3.58)}{=} -\Sigma_0 = M \hat{u}_{z,z}(z=L) - \alpha \hat{p}(z=L) \underset{(3.57b)}{=} -\frac{M + \alpha^2 R/\Phi^2}{\alpha R/\Phi^2} \hat{p}(z=L) \\ &\Rightarrow \hat{p}(z=L) = \Sigma_0 \frac{\alpha R/\Phi^2}{M + \alpha^2 R/\Phi^2} \triangleq P_0^*. \end{aligned} \tag{3.60}$$

Using the dynamic Darcy's law (1.51) without body forces and no fluid source term, we verify

that, as expected, the fluid flux $\hat{q}_z$ is equal to zero at the bottom

$$\begin{aligned}\hat{q}_z(z=0) &= -\frac{\beta(s)}{\rho_f s}(\hat{p}_{,z}(z=0) + \rho_f s^2 \underbrace{\hat{u}_z(z=0)}_{=0}) \\ &\underset{(3.57b)}{=} \frac{\beta(s)}{\rho_f s}\alpha\frac{R}{\Phi^2}\hat{u}_{z,zz}(z=0) \\ &\underset{(3.57a)}{=} \frac{\beta(s)}{\rho_f}\frac{\alpha\rho s R/\Phi^2}{M+\alpha^2 R/\Phi^2}\underbrace{\hat{u}_z(z=0)}_{=0} = 0,\end{aligned} \tag{3.61}$$

Before comparing the response of the complete model with the one from the simplified model, we first need to solve their equations. The first step is to determine the displacement and pressure fundamental solutions of the complete and the simplified model.

5.2 Laplace domain Green's functions for both the complete and the simplified models

Both the complete and the simplified model are in the form of homogeneous ordinary differential equations with inhomogeneous boundary conditions. Such systems can be solved using the exponential ansatz

$$\hat{G}^u_z(z,s) = Ue^{\lambda sz},\ \hat{G}^p(z,s) = Pe^{\lambda sz}, \tag{3.62}$$

where $\hat{G}^u$ and $\hat{G}^p$ are the Laplace transforms of the displacement and pressure fundamental solutions. The procedure to derive these Laplace domain impulse responses is given in Schanz and Cheng (2000). It consists in injecting the exponential solutions (3.62) in equations (3.55a), (3.55b) (respectively equations (3.57a) and (3.57b)), which leads to an eigenvalue problem for λ. Once the eigenvalues (λ_i) are determined, the fundamental solutions for the displacement express as

$$\hat{G}^u_z(z,s) = \sum_i U_i e^{\lambda_i sz},\ \hat{G}^p(z,s) = \sum_i P_i e^{\lambda_i sz}. \tag{3.63}$$

The eigenvectors of the system give a relation between the unknown constants U_i and P_i, which divides the number of unknown constants by two. Finally, we find the values of U_i using the boundary conditions. The details of the calculations for both the complete and the simplified poroelastodynamic equations are omitted here but are given in C.3.

Going back to spatio-temporal solutions requires to apply an inverse Laplace transform of the fundamental solutions (3.63), convoluted in time with the function $f(t)$ defining the temporal behavior of the loading.

$$\begin{aligned}u_z(z,t) &= \int_0^t \mathscr{L}^{-1}\{\hat{G}^u\}(z,t-t')f(t')dt' \\ p(z,t) &= \int_0^t \mathscr{L}^{-1}\{\hat{G}^p\}(z,t-t')f(t')dt'\end{aligned} \tag{3.64}$$

The solid displacement $u_z(z,t)$ and of the pore fluid pressure $p(z,t)$ are evaluated numerically.

5.3 Convolution quadrature method

The most efficient method is to use the Convolution Quadrature Method (CQM) proposed by Lubich (1988a, 1988b). This method enables to approximate convolution integrals numerically using the Laplace transformed impulse response functions $\hat{G}^u(z,s)$ and $\hat{G}^p(z,s)$ of the ODE system (3.55), and a linear multistep method (see Mavaleix-Marchessoux (2020) and Schanz (2001) for details). The principle is to consider a convolution product given by

$$q(t) = \int_0^t G(t-t')f(t')dt' = \int_0^t G(t')f(t-t')dt'. \tag{3.65}$$

$G(t-t')$ can be expressed as the inverse Laplace transform of $\hat{G}(s)$: $\mathscr{L}^{-1}\{\hat{G}\}(t-t')$:

$$\mathscr{L}^{-1}\{\hat{G}\}(t-t') = \frac{1}{2\pi i}\int_{c-i\infty}^{c+i\infty} \hat{G}(s)e^{s(t-t')}ds, \tag{3.66}$$

where the real constant c is chosen so that the integral in (3.66) converged, and $\hat{G}$ is assumed to be well-defined (zero initial conditions on G and on its time derivative). Injecting (3.66) in (3.65) and assuming applicability of Fubini's theorem, we obtain

$$q(t) = \frac{1}{2\pi i}\int_{c-i\infty}^{c+i\infty} \hat{G}(s)h(t;s)ds, \text{ with } h(t;s) = \int_0^t e^{s(t-t')}f(t')dt', \tag{3.67}$$

where $(f(t_n))_{n\geqslant 0}$ is a set of discrete loading term values. The key point is to note that the inner function $h(t;s)$ satisfies the initial-value problem

$$\begin{cases} \dfrac{\mathrm{d}h}{\mathrm{d}t}(t;s) = sh(t;s) + f(t) \\ h(t\leqslant 0;s) = 0 \end{cases} \tag{3.68}$$

The solution of the first order ODE (3.68) can be approximated using a linear k-step method:

$$\begin{aligned} &\sum_{j=0}^{k}\alpha_j h_{n+j-k}(s) = \Delta t\sum_{j=0}^{k}\beta_j(sh_{n+j-k}(s) + f_{n+j-k}),\ \forall n\in\mathbb{N}, \\ &h_{-p}(s) = f_{-p} = 0,\ \forall p\in\{1\dots k\}, \end{aligned} \tag{3.69}$$

where $h(n\Delta t;s)\approx h_n(s)$ is the approximated solution $h(t;s)$ evaluated at the discrete time $n\Delta t$, and the coefficients α_j and β_j are the constants of the multistep method. We consider the Backward Differentiation Formula of order 2 for which we have $k=2$, $\alpha_0 = 1/2$, $\alpha_1 = -2$, $\alpha_2 = 3/2$, $\beta_0 = 0$, $\beta_1 = 0$, $\beta_2 = 1$. As equation (3.69) is not in a suitable form to extract the solution $h_n(s)$, we reformulate (3.69) relating $(h_n(s))$ and $\left(f_n\right)$ in terms of the $\mathscr{Z}$-transforms of those sequences. We recall that the $\mathscr{Z}$-transform $\mathscr{Z}[(x_n)](\xi)$ of a discrete-time signal (x_n) is defined by

$$\mathscr{Z}:(x_n)\mapsto \mathscr{Z}[(x_n)](\xi) = \sum_{n=0}^{\infty} x_n\xi^n \triangleq X(\xi),\ \xi\in\mathbb{C}. \tag{3.70}$$

Taking the $\mathscr{Z}$-transform of (3.69), we obtain

$$\begin{aligned} &\sum_{j=0}^{k}\alpha_j\xi^{k-j}H(\xi;s) = \Delta t\sum_{j=0}^{k}\beta_j\xi^{k-j}(sH(\xi;s)+F(\xi)) \Rightarrow H(\xi;s) = \left(\frac{\rho(\xi)}{\Delta t} - s\right)^{-1}F(\xi), \\ &\text{with } \rho(\xi) = \frac{\sum_{j=0}^{k}\alpha_j\xi^{k-j}}{\sum_{j=0}^{k}\beta_j\xi^{k-j}}. \end{aligned} \tag{3.71}$$

The function $\rho(\xi)$ is the characteristic polynomial of the linear multistep method of order k. $\rho(\xi) = 1/2\xi^2 - 2\xi + 3/2$ for the BDF2 scheme. Therefore, the $\mathcal{Z}$-transform of the convolution product (3.67) is given as

$$Q(\xi) = \frac{1}{2i\pi}\int_{c-i\infty}^{c+i\infty} \hat{G}(s)\left(\frac{\rho(\xi)}{\Delta t} - s\right)^{-1} F(\xi)ds. \tag{3.72}$$

Using Cauchy's residue theorem (valid if $\hat{G}(s)$ is bounded at infinity, which is an inherent property of the fundamental solutions we consider in place of $\hat{G}(s)$ in our developments), we find

$$Q(\xi) = \hat{G}\left(\frac{\rho(\xi)}{\Delta t}\right)F(\xi) \Leftrightarrow \sum_{n=0}^{\infty} q(n\Delta t)\xi^n = \hat{G}\left(\frac{\rho(\xi)}{\Delta t}\right)\sum_{n=0}^{\infty} f(n\Delta t)\xi^n. \tag{3.73}$$

To find an expression for $q(n\Delta t)$ in the form of a quadrature formula in which we can identify the quadrature weights. We first need to represent the right-hand side of (3.73) in a power series with coefficients independent of the $\mathcal{Z}$-transform variable ξ. It requires developing $\hat{G}\left(\rho(\xi)/\Delta t\right)$ in a power series

$$\hat{G}\left(\frac{\rho(\xi)}{\Delta t}\right) = \sum_{n=0}^{\infty} \omega_n(\Delta t)\xi^n, \tag{3.74}$$

where the coefficients $\omega_n(\Delta t)$ can be determined by Cauchy's integral formula. They are given by

$$\omega_n(\Delta t) = \frac{1}{2\pi i}\int_{\xi=\mathscr{R}} \hat{G}\left(\frac{\rho(\xi)}{\Delta t}\right)\xi^{-n-1}d\xi, \tag{3.75}$$

with $\mathscr{R}$ the radius of a circle in the domain of analyticity of $\hat{G}\left(\rho(\xi)/\Delta t\right)$. Incorporating (3.74) in (3.73) we obtain

$$\sum_{n=0}^{\infty} q(n\Delta t)\xi^n = \sum_{n=0}^{\infty}\omega_n(\Delta t)\xi^n \sum_{n=0}^{\infty} f(n\Delta t)\xi^n = \sum_{n=0}^{\infty}\sum_{k=0}^{n}\omega_{n-k}(\Delta t)f(n\Delta t)\xi^n. \tag{3.76}$$

Comparing the left-hand-side and the right-hand side of equation (3.76), we finally identify the discrete form of the convolution integral (3.68) written as the quadrature formula

$$q(n\Delta t) = \sum_{k=0}^{n}\omega_{n-k}(\Delta t)f(n\Delta t),\ n = \{0,1,\dots N\}. \tag{3.77}$$

The quadrature weights $\omega_{n-k}(\Delta t)$ are given by (3.75). In practice, after a polar coordinate change ($\xi = \mathscr{R}e^{i\phi}$) in (3.75) to get a real valued integral, the quadrature weights are approximated by the trapezoidal rule

$$\omega_n(\Delta t) = \frac{\mathscr{R}^{-n}}{J}\sum_{j=0}^{J-1}\hat{G}\left(\frac{\rho(\mathscr{R}e^{ij\frac{2\pi}{J}})}{\Delta t}\right)e^{-inj\frac{2\pi}{J}}, \tag{3.78}$$

with J equal steps $2\pi/J$. We can calculate the quadrature weights for the solid displacement and for the pore pressure, and they are given by

$$\begin{aligned}
\omega^u_{n-k}(n\Delta t) &= \frac{\mathscr{R}^{-n}}{J}\sum_{m=0}^{J-1}\hat{G}^u\left(\frac{\rho(\mathscr{R}e^{ij2\pi/J})}{\Delta t}\right)e^{-inj2\pi/J},\\
\omega^p_{n-k}(n\Delta t) &= \frac{\mathscr{R}^{-n}}{J}\sum_{m=0}^{J-1}\hat{G}^p\left(\frac{\rho(\mathscr{R}e^{ij2\pi/J})}{\Delta t}\right)e^{-inj2\pi/J}.
\end{aligned} \tag{3.79}$$

In practice, the quadrature weights can be efficiently computed using the Fast Fourier Transform. $\mathscr{R}$ is chosen such that $\mathscr{R}^n = \varepsilon$ in order to have an $\mathscr{O}(\varepsilon)$ accuracy. The J complex frequencies $s = \rho(\xi)/\Delta t$ depend on the desired accuracy ε and on the step size Δt ($J = N$ is considered here).

We first perform a validation test of the implemented CQM. We consider the function $G(t) = \cos(t)\mathscr{H}(t)$. Its Laplace transform is known analytically $\hat{G} = s/(s^2+\omega^2)$. Considering $f(t) = \mathscr{H}(t)$, we have

$$q(t) = \int_0^t \mathscr{L}^{-1}\{\hat{G}\}(t-t')f(t')dt' = \int_0^t \mathscr{L}^{-1}\{\hat{G}\}(t')f(t-t')dt' = \int_0^t \cos(t')dt' = \sin(t). \quad (3.80)$$

Figure 3.3 represents the comparison between the analytical solution $q(t)$ of the convolution product (3.80), and its numerical approximation using the CQM. The results obtained with different time steps are superposed for $t \in [0, 6\pi]$. Figure 3.3a shows, on the left, the superposition of the approximated values $q_{\text{app}}(t)$ of $q(t)$ (with $t = n\Delta t$) obtained with different time-steps with the expected solution, and on the right, the time evolution of the absolute error $\mathrm{E}_q(t)$ between the analytical values of the convolution product $q(t)$ and its numerical approximation $q_{\text{app}}(t)$ such that

$$\mathrm{E}_q(t) = |q(t) - q_{\text{app}}(t)|.$$

The maximum absolute error on the convolution product is in the order of the time step Δt chosen for the CQM. Figure 3.3b represents the relative L^2-norm error in time on $q(t)$ such that

$$\varepsilon_q^t = \left\| \frac{q(t) - q_{\text{app}}(t)}{q(t)} \right\|_{L^2([0,t_f])}.$$

In the following part we choose $\Delta t = 10^{-3}$ s as it allows an error smaller than 0.1%,and a reasonable computational cost to evaluate the convolution product.

5.4 Comparison between the complete poroelastodynamic model and the simplified model at the timescale of a seismic motion

At the timescale of the seismic motion, we showed in Section 4.1 that the complete poroelastodynamic equations (3.55) simplified as an undrained system (3.57). Under this approximation, no relative fluid motion is permitted. Inertial effects for the fluid are neglected as well as diffusion effects. It imposes a direct relation between the pore pressure and the solid deformation.

We begin by assuming that the assumptions of the simplified model are satisfied. This means adding undrained boundary conditions to the complete model. Such boundary conditions satisfy the relation (3.57b). Hence, for both models, we add the boundary conditions

$$t_z(z = L, t) = -\Sigma_0\mathscr{H}(t) \quad \text{and} \quad p(z = L, t) = P_0^*\mathscr{H}(t), \text{ with } \Sigma_0 = 1\ \mathrm{N/m^2}, \quad (3.81)$$

as in (3.60).

In addition, the choice of the final simulation time is important. First, the loading of the top of the column leads to the propagation of a compression wave in the poroelastic column

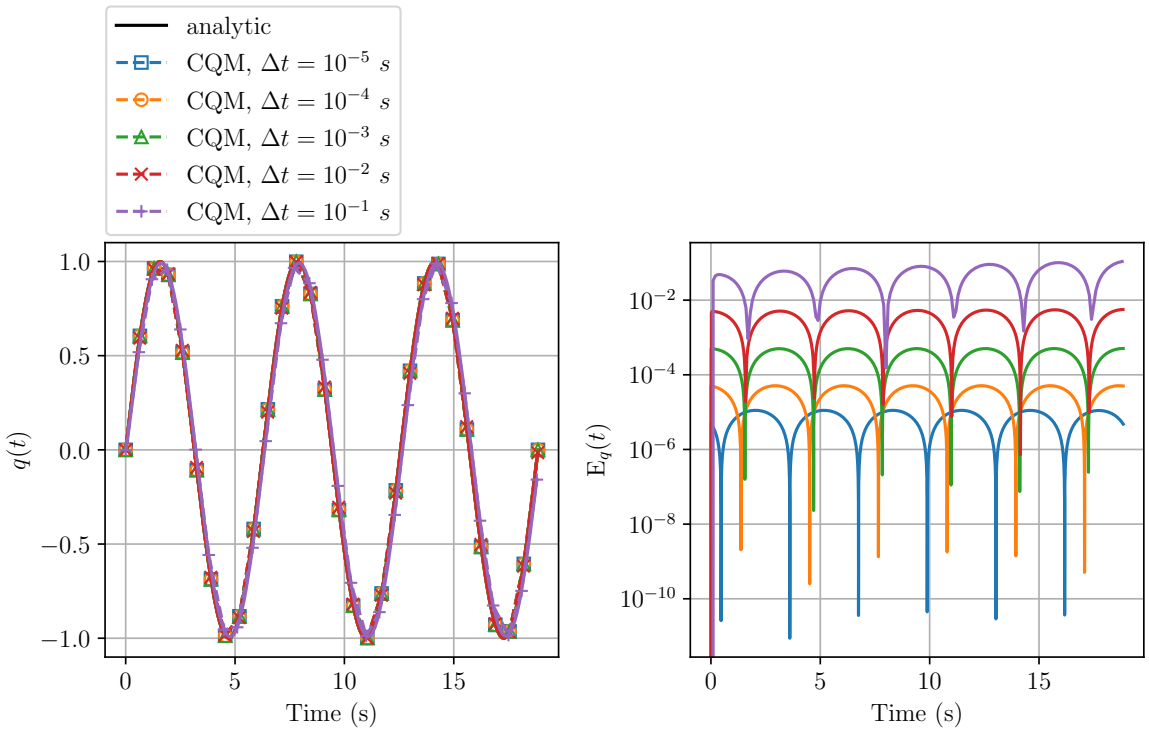

(a)

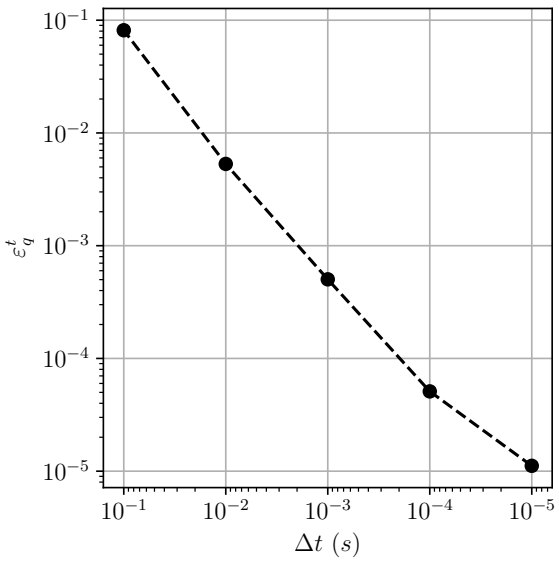

(b)

Figure 3.3 • Validation test of the CQM with $G = \cos(t)\mathscr{H}(t)$, $f(t) = \mathscr{H}(t)$ and $q(t) = \sin(t)$ for different time steps Δt, (a) (left) Superposition of the approximated convolution product $q_{\text{app}}(t)$ of $q(t)$ (with $t = n\Delta t$) obtained with different time steps and compared to the analytical solution $q(t)$, (right) Time evolution of the absolute error $\mathrm{E}_q(t)$ (b) Evolution of the relative L^2-norm error in time on $q(t)$: ε_q^t with respect to Δt.

according to complete poroelastodynamic equations. This compression wave results from a fast compression wave propagating in the elastic solid matrix and a slow compression wave propagating in the fluid. Their characteristic velocities can be determined with the help of the solid matrix properties and with the fluid properties respectively, and are denoted c^s and c^f

$$c^s = \sqrt{\frac{K_s + 4/3G_s}{\rho_s}} \approx 2683 \text{ m/s}, \quad c^f = \sqrt{\frac{K_f + 4/3G_f}{\rho_f}} \approx 1581 \text{ m/s}.$$

At the timescale of a seismic motion, the loading of the column leads to the propagation of a compression wave in the undrained poroelastic column according to simplified poroelastodynamic equations. Its characteristic velocity is denoted c^u, and is given by

$$c^u = \sqrt{\frac{M + \alpha^2 R/\Phi^2}{\rho}} \approx 3275 \text{ m/s}$$

Their values are determined with the help of Table 3.2. Knowing the length L of the column, we can deduce the time required for each wave to reach the bottom of the column

$$t^s = \frac{L}{c^s} \approx 1.86 \text{ s}, \quad t^f = \frac{L}{c^f} \approx 3.2 \text{ s},, \quad t^u = \frac{L}{c^u} \approx 1.52 \text{ s}.$$

Hence, choosing a sufficiently short final time t_{final} compared to t^u, so that none of the compression waves could reach the bottom of the column would approximate the case of an infinitely long column. Otherwise, perfect reflections would occur at the bottom of the column for longer values of t_{final}. Observing reflections of the compression waves at the bottom of the column would not be of great interest as the objective of 1D example we study here is to illustrate the validity range of the simplified poroelastodynamic equations to use them in the context of a fault mechanics problem in an unbounded domain. On the basis of these arguments, we have set

$$t_{\text{final}} = 1.50 \text{ s} \approx 0.99 t^u.$$

We also discretize the column with 100 points along the z-coordintate to compare the response of the simplified model to the response of the complete model. In the following Figures, the complete poroelastodynamic model, given by equations (3.55), is denoted "Full" in the graphs' legend, and the simplified poroelastodynamic model, given by equations (3.57), is denoted "Simplified" in the graphs' legend.

Figure 3.4 represents the comparison between the "Simplified" and "Full" model when undrained boundary conditions (see (3.81)) are applied for both models. Figures 3.4a and 3.4b and 3.4c correspond to given instants $t = \{\Delta t, t_{\text{final}}/2, t_{\text{final}}\}$. Figure (i) (respectively (ii)) represents the spatial evolution of the "Full" and the "Simplified" solid displacement u_z responses (respectively pore fluid pressure p responses).

At the first computed instant $t = \Delta t$, we observe that identical boundary conditions are applied at the first time step. At $t = t_{\text{final}}/2$ and $t = t_{\text{final}}$, we observe the propagation of a compression wave front in the poroelastic column and shows good agreement between the "Full" and the "Simplified" models at these instants too.

Figure 3.5 compares the "Full" and the "Simplified" solutions in the half height of the column. As expected, we observe that the wave front reaches the middle of the column

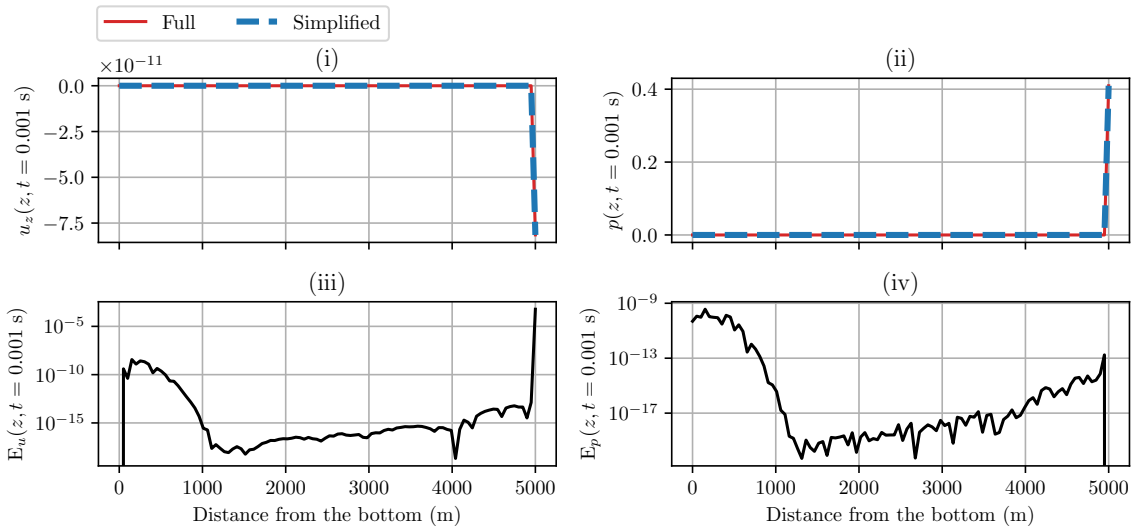

(a) Spatial evolution at $t = 10^{-3}$ s.

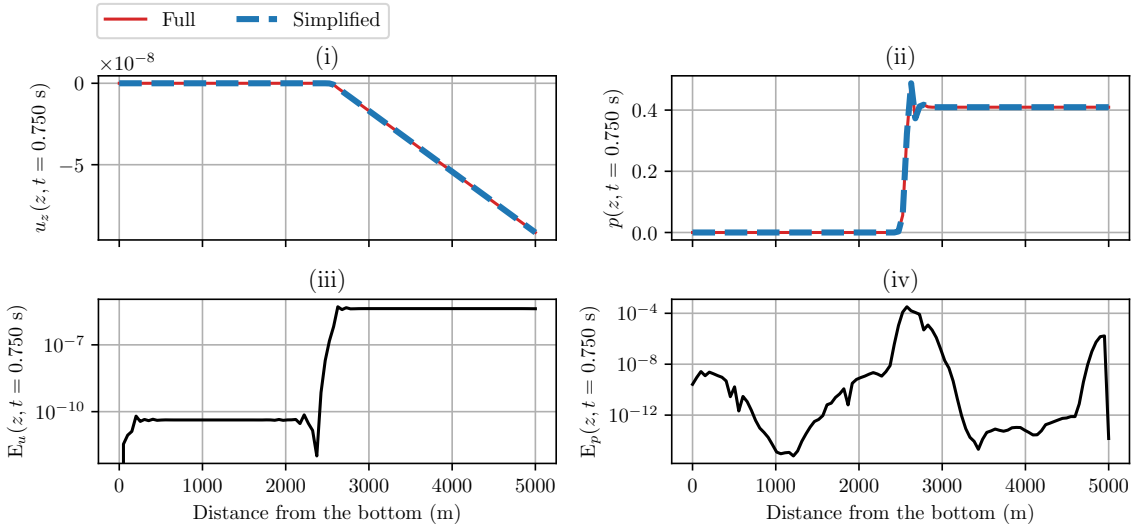

(b) Spatial evolution at $t = 0.75$ s.

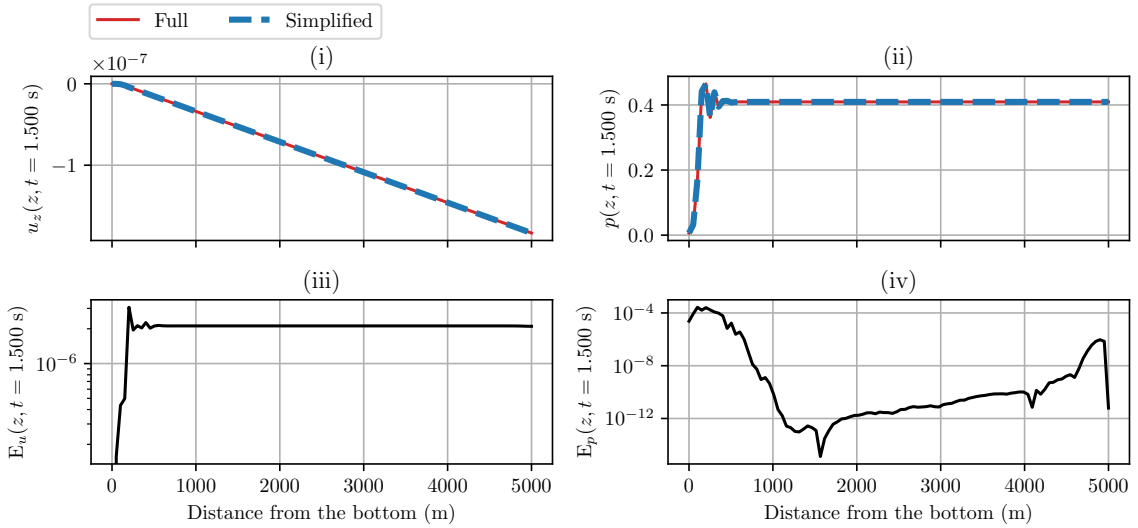

(c) Spatial evolution at $t = 1.5$ s.

Figure 3.4 • Comparison of the "Simplified" with the "Full" models with respect to the z-coordinate for undrained boundary conditions applied to both models.

at $t_{\text{final}}/2 \approx (L/2)/c^u$, and we again observe good agreement between the "Full" and the "Simplified" models.

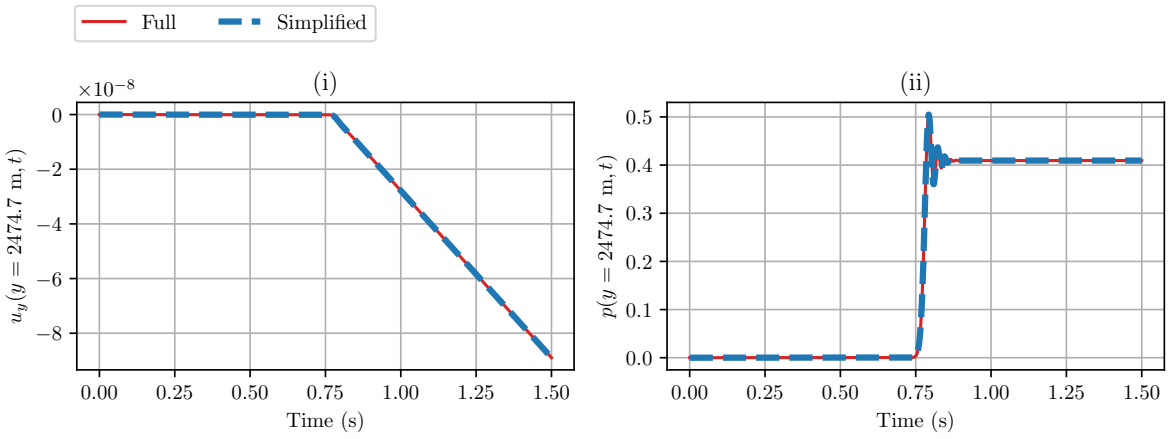

Figure 3.5 • Comparison of the "Simplified" with the "Full" models with respect to time for "undrained" boundary conditions applied to both models.

We can calculate global L^2-norm relative errors (one with respect to the displacement and the other with respect to the pore pressure) in space and time between the "Full" and the "Simplified" models. It allows us to quantify the extent to which the "Simplified model" is an accurate approximation of the "Full" model. These global errors are defined as

$$\varepsilon_u^{z,t} = \left\| \frac{u_z^{\text{Full}} - u_z^{\text{Simplified}}}{u_z^{\text{Full}}} \right\|_{L^2([0,L])\times L^2([0,t_{\text{final}}])}, \quad \varepsilon_p^{z,t} = \left\| \frac{p^{\text{Full}} - p^{\text{Simplified}}}{p^{\text{Full}}} \right\|_{L^2([0,L])\times L^2([0,t_{\text{final}}])},$$

where u_z^{Full} and p^{Full} are the displacement and pore-pressure solutions of the "Full" model and $u_z^{\text{Simplified}}$ and $p^{\text{Simplified}}$ are the displacement and pore-pressure solutions of the "Simplified" model. In the case where the "undrained loading" (3.81) is applied we obtain

$$\varepsilon_u^{z,t} = 5.1 \cdot 10^{-6}, \quad \varepsilon_p^{z,t} = 6.6 \cdot 10^{-5},$$

which confirms that the "Simplified" model is a very good approximation of the "Full" model at the timescale of a seismic motion. This is an interesting point as the "Simplified" undrained model is much easier to implement and to integrate.

We want to check when the simplified model is no longer valid. We therefore need to consider a general case outside the assumptions of the simplified model. This is what we are interested in. We approach the general case by perturbing the boundary conditions. This involves adding perturbed boundary conditions to the complete model compared with the undrained boundary conditions previously considered.

In a real case scenario, the "Full" poroelastodynamic model applies, and the undrained relation between the pore pressure and the solid deformation (3.57b) is not satisfied. At the timescale of a seismic motion, we had showed in equation (3.19b) resulting from the dimensional analysis performed in Section 4.1 that an additional term in the order of $\varepsilon =$

T_f / T_c (ratio of the natural characteristic microscopic fluid diffusion period of the system over the characteristic time T_c) was at stake. In the following, we take into account the influence of this term in the form of a small regular perturbation on the pressure boundary condition of the "Full" model. Hence, the boundary conditions for the "Simplified" remain the same as in (3.81), while the boundary conditions for the "Full" model are given by

$$t_z(z=L,t) = -\Sigma_0 \mathscr{H}(t) \quad \text{and} \quad p(z=L,t) = P_0 = P_0^* \mathscr{H}(t) + \Delta P(t)\mathscr{H}(t). \tag{3.82}$$

> **Remark 3.3.** *In addition to the perturbation of the boundary conditions, choosing a longer final simulation time would be another way to consider a case where the simplified model is no longer valid. In fact, it would allow fluid diffusion to become a preponderant effect too. We recall that the characteristic fluid diffusion time is*
>
> $$t^d = \frac{L}{c_{hy}} \approx 2.5 \cdot 10^5 \; s \gg t^f, t^s \text{ and } t^u.$$
>
> *However, imposing a longer final simulation time implies perfect reflections in the poroelastic column that we do not want to consider.*

Initially, a constant perturbation is added to approximate the general case. In a second step, we get closer to a generic case by varying the perturbation on the boundary conditions over time, acting on its frequency. The aim is to see if, in this case, other fluid effects are predominant in addition to the predominant effects in the simplified model, in which case the latter would no longer be a good approximation of the complete model. Hence, we distinguish two scenarios for the value of ΔP in (3.82) in order to assess the effect of the amplitude and of the frequency of the perturbation:

- 1st scenario: we consider a constant perturbation on the pressure boundary condition $\Delta P = \varepsilon P_0^*$ where we vary $\varepsilon \ll 1$. This perturbation only affects the displacement and the pore pressure fundamental solution of the "Full" model.

- 2nd scenario: we consider a sinusoidal perturbation on the pressure boundary condition $\Delta P(t) = \varepsilon P_0^* \cos(\omega t)$, where we vary $\varepsilon \ll 1$ and ω. This perturbation affects only the time evolution of the loading imposed. This impacts the convolution product in time, which determines the time domain displacement and pore pressure responses (3.64).

We first introduce a perturbation expressed as $\Delta P / P_0^* = (P_0 - P_0^*)/P_0^* = \varepsilon$. This perturbation has an effect on the displacement and the pore pressure fundamental solutions only,

which write in the Laplace domain

$$
\begin{aligned}
\hat{u}_y(y,s) = {} & \frac{\Sigma_0}{Ms(d_1\lambda_2 - d_2\lambda_1)}\left[\frac{d_2\left(e^{-\lambda_1 s(L-y)} - e^{-\lambda_1 s(L+y)}\right)}{1+e^{-2\lambda_1 sL}} - \frac{d_1\left(e^{-\lambda_2 s(L-y)} - e^{-\lambda_2 s(L+y)}\right)}{1+e^{-2\lambda_2 sL}}\right] \\
& + \frac{P_0^*(1+\varepsilon)}{Ms(d_1\lambda_2 - d_2\lambda_1)}\left[\frac{(M\lambda_2 - \alpha d_2)\left(e^{-\lambda_1 s(L-y)} - e^{-\lambda_1 s(L+y)}\right)}{1+e^{-2\lambda_1 sL}}\right. \\
& \qquad \left. - \frac{(M\lambda_1 - \alpha d_1)\left(e^{-\lambda_2 s(L-y)} - e^{-\lambda_2 s(L+y)}\right)}{1+e^{-2\lambda_2 sL}}\right] \\
\hat{p}(y,s) = {} & \frac{\Sigma_0 d_1 d_2}{M(d_1\lambda_2 - d_2\lambda_1)}\left[\frac{\left(e^{-\lambda_1 s(L-y)} + e^{-\lambda_1 s(L+y)}\right)}{1+e^{-2\lambda_1 sL}} - \frac{\left(e^{-\lambda_2 s(L-y)} + e^{-\lambda_2 s(L+y)}\right)}{1+e^{-2\lambda_2 sL}}\right] \\
& + \frac{P_0^*(1+\varepsilon)}{M(d_1\lambda_2 - d_2\lambda_1)}\left[\frac{d_1(M\lambda_2 - \alpha d_2)\left(e^{-\lambda_1 s(L-y)} + e^{-\lambda_1 s(L+y)}\right)}{1+e^{-2\lambda_1 sL}}\right. \\
& \qquad \left. - \frac{d_2(M\lambda_1 - \alpha d_1)\left(e^{-\lambda_2 s(L-y)} + e^{-\lambda_2 s(L+y)}\right)}{1+e^{-2\lambda_2 sL}}\right]
\end{aligned}
\tag{3.83}
$$

Figure 3.6 compares the "Simplified" and "Full" models for a constant perturbation of the boundary conditions (1st perturbation scenario). Figures 3.6a and 3.6b and 3.6c correspond to given instants $t = \{\Delta t, t_{\text{final}}/2, t_{\text{final}}\}$. Figure (i) (respectively (ii)) represents the spatial evolution of the "Full" and the "Simplified" solid displacement u_z responses (respectively, pore fluid pressure responses). Figure (iii) (respectively (iv)) gives the spatial evolution of the normalized absolute error E_u (respectively E_p) between these responses.

At the first computed instant $t = \Delta t$, as expected, we observe that the boundary conditions of the "Full" model and of the "Simplified" model diverge. The amplitude of the error on the pore-pressure at the top of the column scales as ΔP.

At $t = t_{\text{final}}/2$ and $t = t_{\text{final}}$, we observe an increase in the amplitude of the normalized errors E_u and E_p. This shows that the perturbation on the pressure boundary condition propagates as the compression wave propagates through the poroelastic column. However, the larger error value is located at the top of the column. Hence, the first perturbation scenario results in the creation of a "boundary layer" effect of the perturbation imposed on the pore-pressure boundary condition. This behavior was expected due to the regular perturbation imposed.

Figure 3.7 shows the evolution of the global L^2-norm relative errors on the displacement $\varepsilon_u^{z,t}$ and on the pore pressure $\varepsilon_p^{z,t}$ between the "Full" and the "Simplified" models with respect to the amplitude of the perturbation $\Delta P/P_0^*$. $\varepsilon_p^{z,t}$ scales as a tenth of the perturbation ($0.1\Delta P/P_0^*$), while $\varepsilon_u^{z,t}$ scales as a hundredth of the perturbation $10^{-2}\Delta P/P_0^*$.

In the 1st perturbation scenario, we showed that the "Simplified" model is not a good approximation of the "Full" model close to the top of the column where we perturbed the boundary conditions. Outside the boundary, the "Simplified" model remains a good approximation of the "Full" model. In order to get closer to a generic case, where the assumptions of the "Simplified" model are not satisfied, we now consider the 2nd perturbation scenario. The perturbation expresses as $\Delta P = \varepsilon P_0^* \cos(\omega t)$. It evolves with time. We are particularly interested in the effect of the pulsation ω with respect to the 1st perturbation scenario. ε is chosen as in the first scenario and the pulsation ω corresponds to an imposed period to the

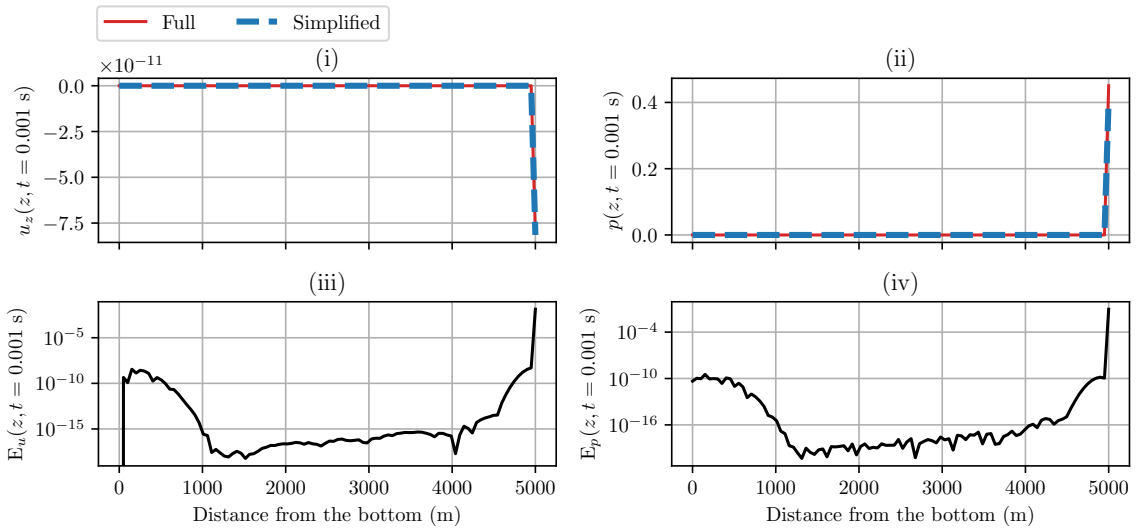

(a) $t = 10^{-3}$ *s*.

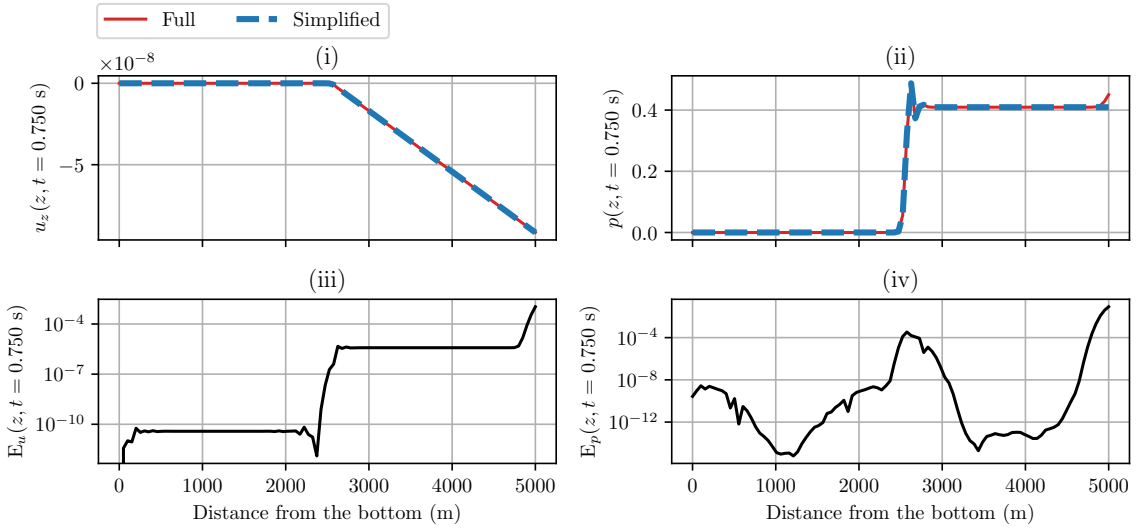

(b) $t = 0.75$ *s*.

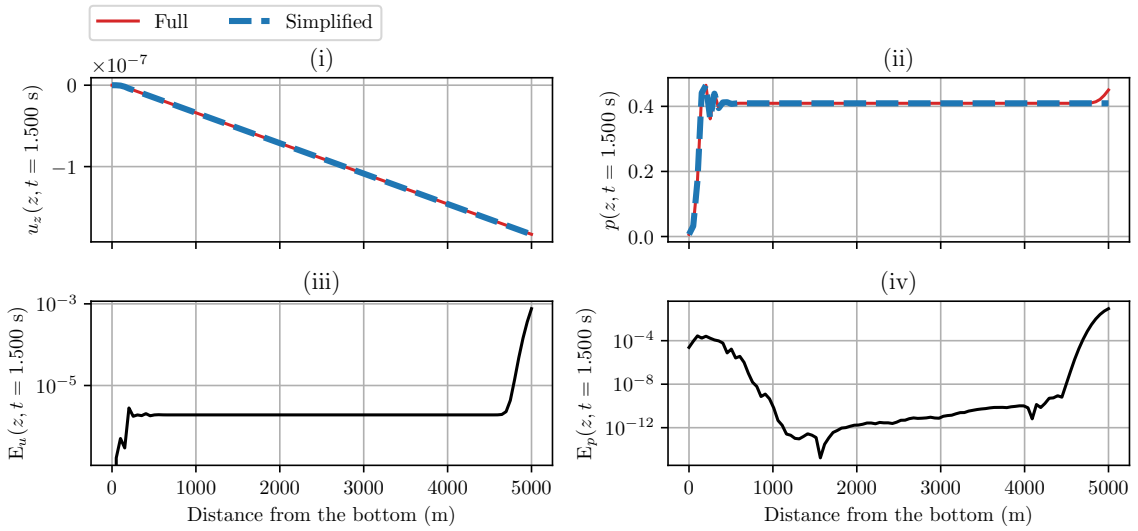

(c) $t = 1.5$ *s*.

Figure 3.6 • Comparison of the "Simplified" with the "Full" models with respect to the z-coordinate for a constant perturbation ($\Delta P / P_0^* = 10^{-1}$) on the pressure at the top of the column for the "Full" model.

system. High values of ω (i.e. high frequency regime) correspond to a fast loading of the system, whereas small values of ω (low-frequency regime) stand for a slow loading regime. In theory, the high-frequency (fast loading) regime tends to the undrained boundary conditions configuration, whereas in the low-frequency (slow loading) the "Simplified" model would not be appropriate to approximate the "Full" model as non-negligible fluid effects such as fluid diffusion should be included. It is a bit different here. In particular, we impose either a fast or a slow perturbation of the initially undrained boundary conditions. In the case where a fast perturbation is imposed, the response of the system should still tend to the response obtained in the undrained boundary conditions configuration. In the case where a slow perturbation is imposed, for a short time interval, $\omega t \ll 1$, so $\cos(\omega t) \approx 1$ and $\Delta P/P_0^* = \varepsilon \cos(\omega t) \approx \varepsilon$, which tends to the constant perturbation case (1st perturbation scenario). For larger time values, we should see a non-negligible effect of the pulsation ω on the divergence between the "Simplified" and the "Full" model.

Figures 3.8 and 3.9 and 3.10 compare the "Simplified" and "Full" model for a sinusoidal perturbation ($\Delta P/P_0^* = \varepsilon \cos(\omega t)$ with $\varepsilon = 10^{-1}$ and $\omega \in \{10^{-2}, 1, 10^3\}$) on the pressure at the top of the column for the "Full" model (2st perturbation scenario). Figures 3.8a and 3.9a and 3.10a correspond to $t = \Delta t$ for the different values of ω. At the first computed instant $t = \Delta t$, as expected, we observe that the boundary conditions of the "Full" model and of the "Simplified" model diverge. The amplitude of the error on the pore pressure at the top of the column scales as ΔP.

Figure 3.8 compares both solutions at three given instants $t = \{\Delta t, t_{\text{final}}/2, t_{\text{final}}\}$, in the case where a fast sinusoidal perturbation ($\omega = 10^3$ rad/s) is applied. At $t = t_{\text{final}}/2$ and $t = t_{\text{final}}$, we do not observe a significant influence of a fast sinusoidal perturbation imposed on the pressure boundary condition for the "Full" model on the divergence between the "Simplified" and the "Full" model. The spatial evolutions of the errors on the displacement and on the pore pressure are similar to those obtained in Figure 3.6 for the 1st perturbation scenario. The

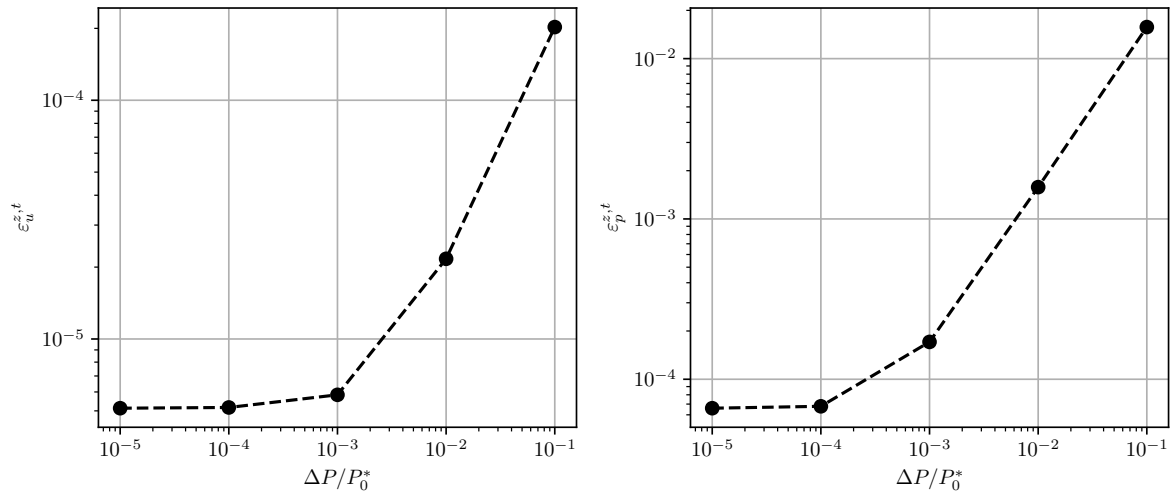

Figure 3.7 • Evolution of the L^2-norm relative errors in space and time on the solid displacement $\varepsilon_u^{z,t}$ and on the pore pressure $\varepsilon_p^{z,t}$ with respect to the amplitude of the loading perturbation $\Delta P/P_0^*$.

error on the pore pressure E_p (respectively the error on the displacement E_u) scales as $10^{-2}\varepsilon$ relatively to the amplitude of the pressure (respectively to the amplitude of the displacement).

Figure 3.9 compares both solutions at three given instants $t = \{\Delta t, t_{\text{final}}/2, t_{\text{final}}\}$, in the case where a sinusoidal perturbation ($\omega = 1$ rad/s) is applied. At $t = t_{\text{final}}/2$ and $t = t_{\text{final}}$, we observe a more significant propagation of the perturbation through the column than in the 1st perturbation scenario or in the 2nd perturbation scenario with high values of ω. Compared to the results obtained in Figure 3.8, the corresponding spatial evolution of the error values E_u and E_p scale as ε. This shows that for $\omega = 1$ the perturbation on the boundary conditions corresponds to a generic case in which the assumptions of the "Simplified" model are not satisfied, and the "Simplified" model is not a good approximation of the "Full" model anymore.

Figure 3.10 compares both solutions at three given instants $t = \{\Delta t, t_f/2, t_f\}$, in the case where a slow sinusoidal perturbation ($\omega = 10^{-2}$ rad/s) is applied to the pressure boundary condition of the "Full" model. At $t = t_f/2$ and $t = t_f$, we observe a more significant propagation of the perturbation through the column than in the 1st perturbation scenario or in the 2nd perturbation scenario with high values of ω. Compared to the results obtained in Figure 3.8, the corresponding spatial evolution of the error values E_u and E_p both errors scale as ε. In particular, the error on the pressure does not vary much with respect to space (offset error). The divergence between the "Simplified" and the "Full" is more significant as the pulsation ω decreases. Thus, when a slow perturbation of the boundary condition is imposed, the "Simplified" models is no longer a good approximation of the "Full" model.

Figure 3.11 shows the evolution of the global L^2-norm relative errors in space and time on the displacement $\varepsilon_u^{z,t}$ and on the pore pressure $\varepsilon_p^{z,t}$ between the "Full" and the "Simplified" models with respect to the pulsation ω of the perturbation. It confirms that a fast sinusoidal perturbation leads to a better agreement between the "Simplified" and the "Full" models than a slow sinusoidal perturbation.

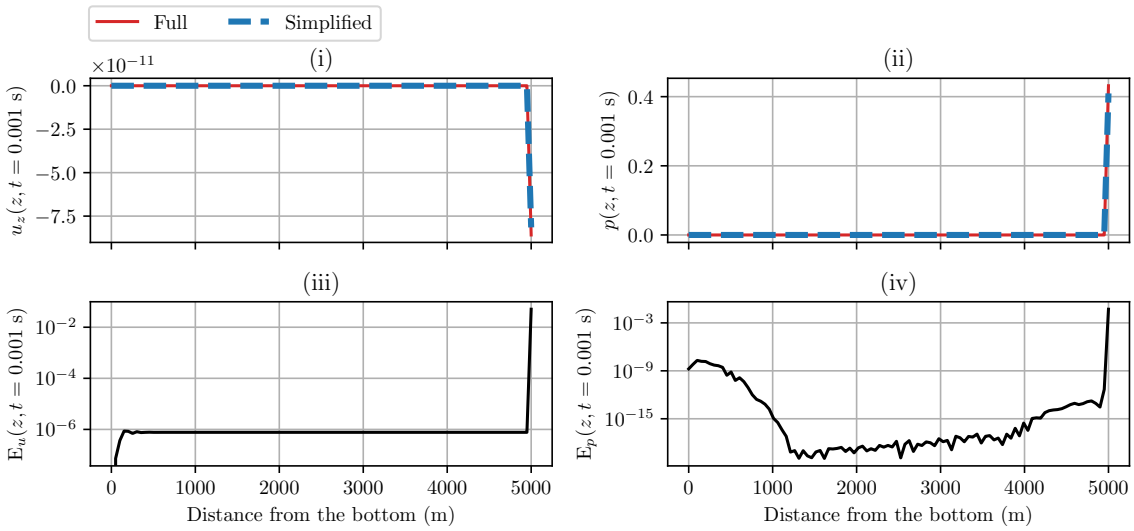

(a) $t = 10^{-3}$ s.

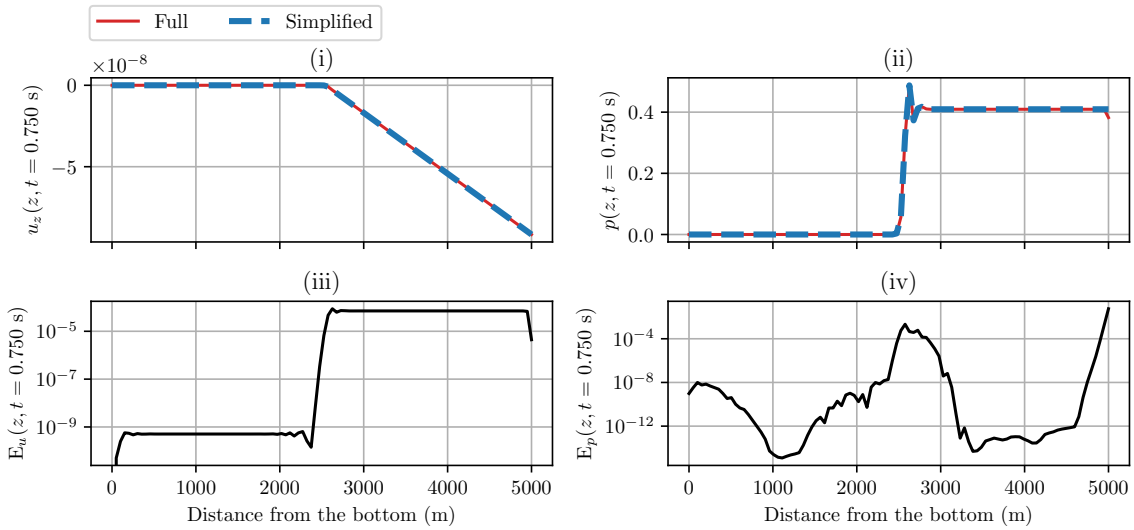

(b) $t = 0.75$ s.

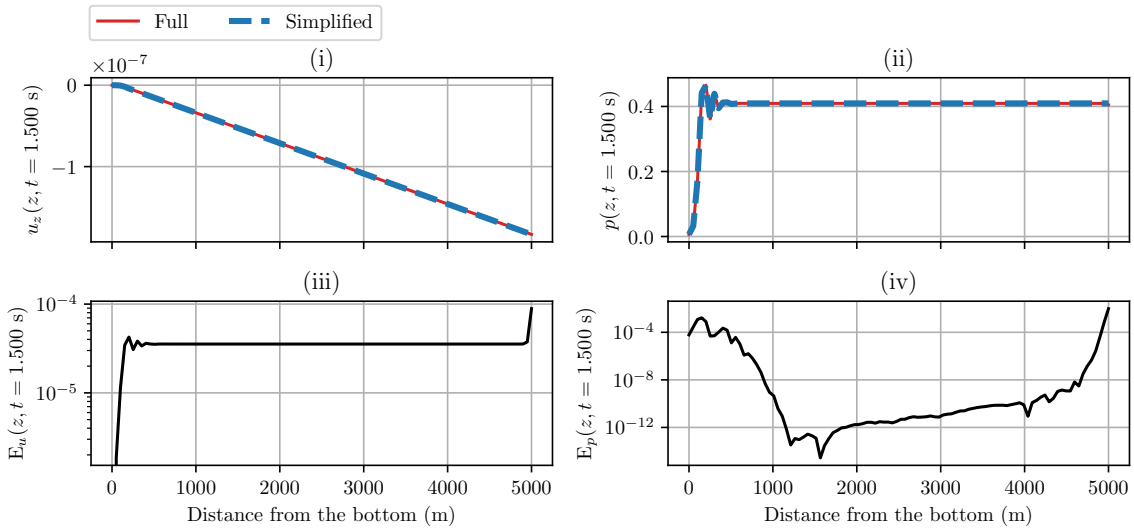

(c) $t = 1.5$ s.

Figure 3.8 • Comparison of the "Simplified" with the "Full" models with respect to the z-coordinate for a sinusoidal perturbation ($\Delta P / P_0^* = 10^{-1} \cos(10^3 t)$) on the pressure at the top of the column.

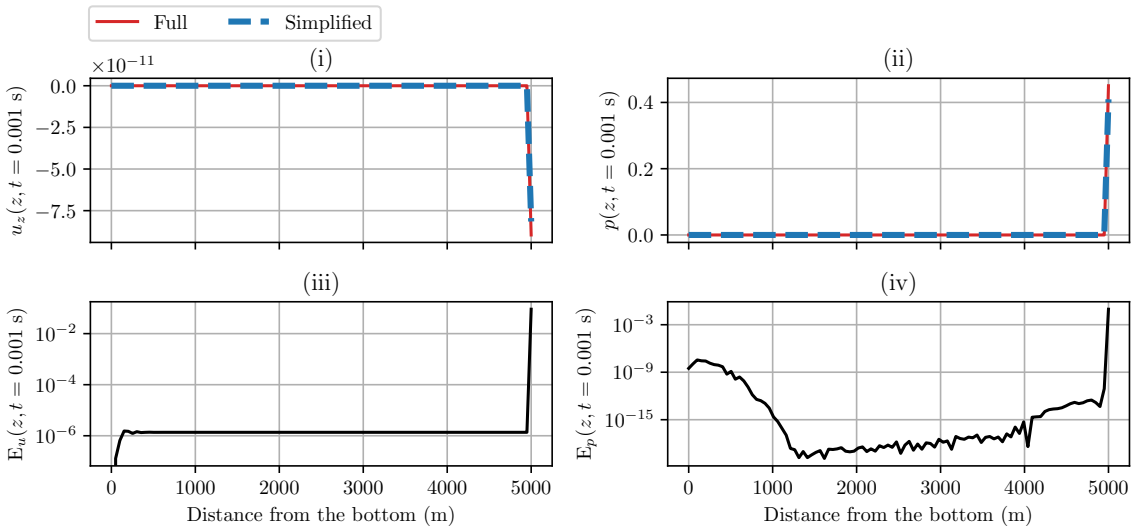

(a) $t = 10^{-3}$ s.

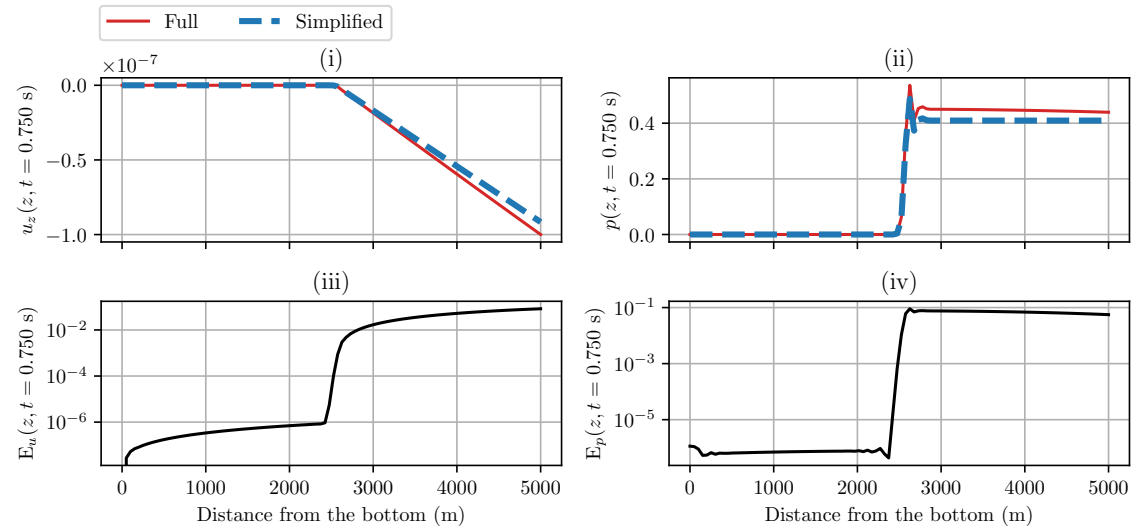

(b) $t = 0.75$ s.

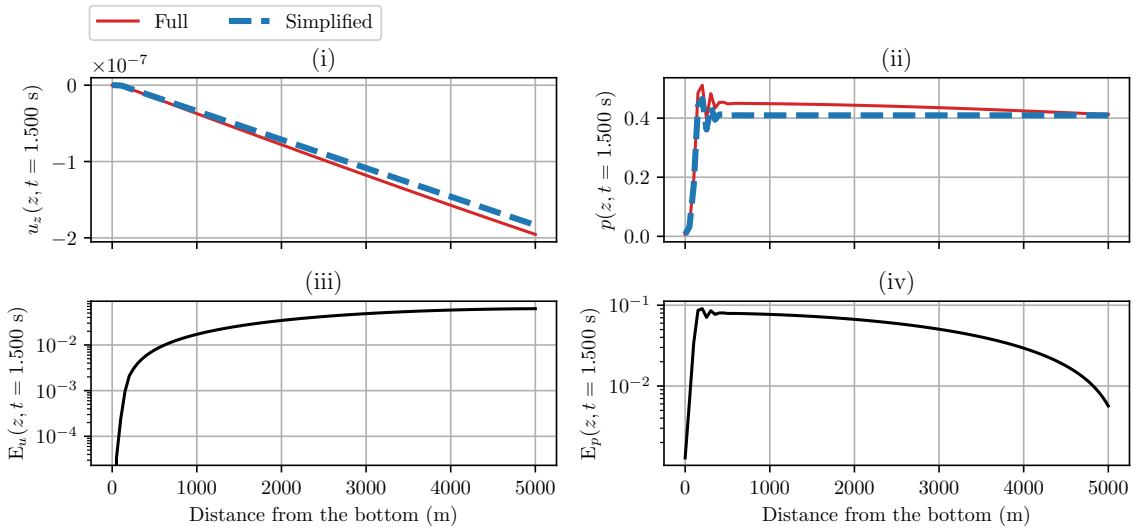

(c) $t = 1.5$ s.

Figure 3.9 • Comparison of the "Simplified" with the "Full" models with respect to the z-coordinate for a sinusoidal perturbation ($\Delta P / P_0^* = 10^{-1}\cos(t)$) on the pressure at the top of the column.

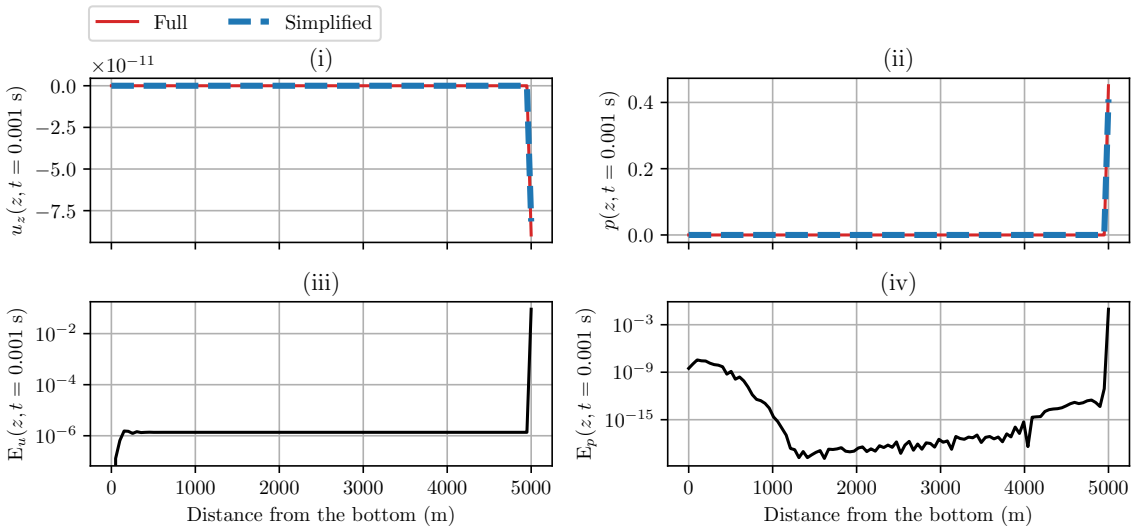

(a) $t = 10^{-3}$ s.

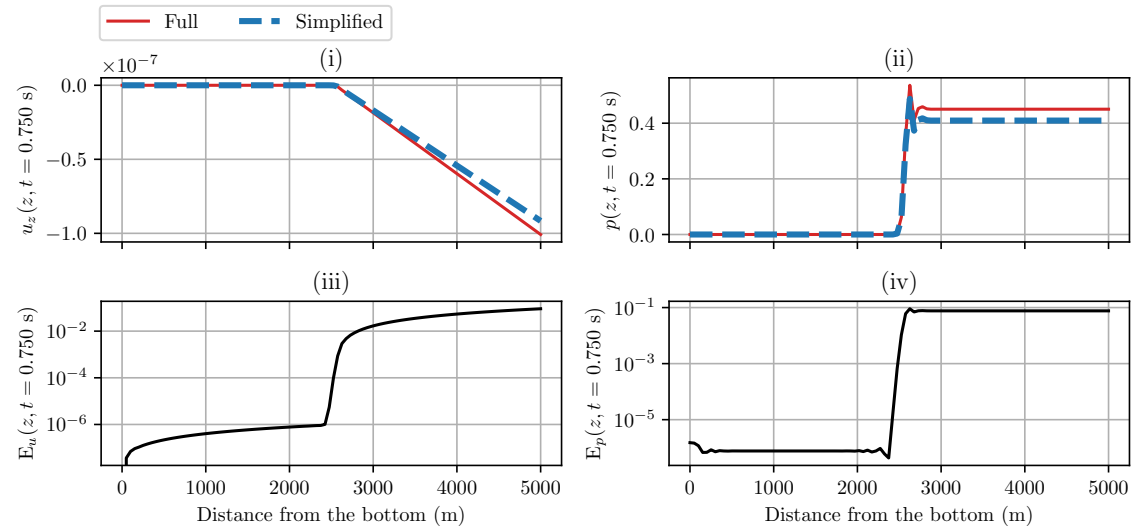

(b) $t = 0.75$ s.

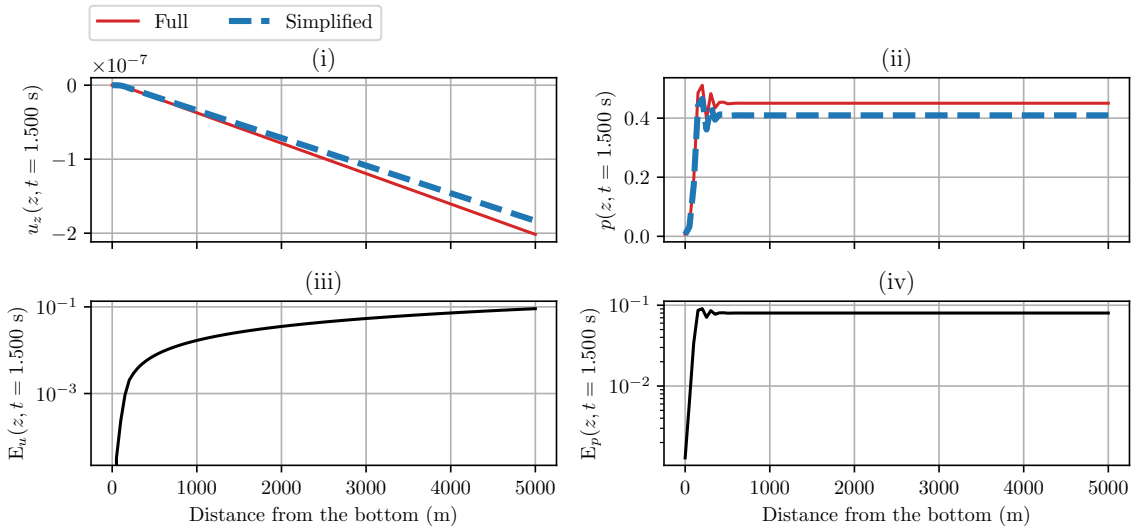

(c) $t = 1.5$ s.

Figure 3.10 • Comparison of the "Simplified" with the "Full" models with respect to the z-coordinate for a sinusoidal perturbation ($\Delta P / P_0^* = 10^{-1} \cos(10^{-2} t)$) on the pressure at the top of the column.

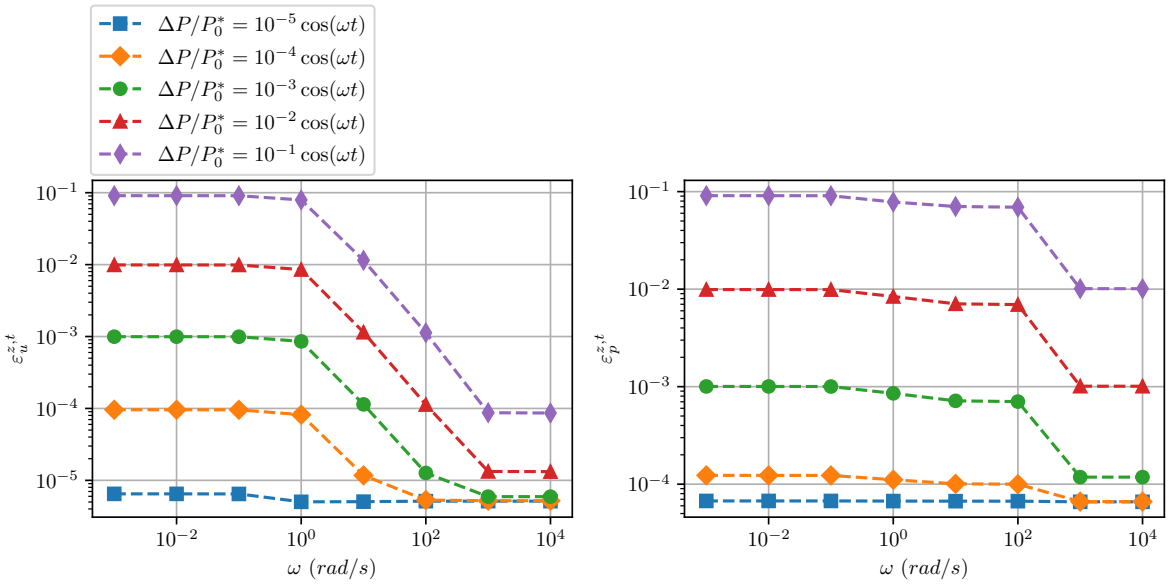

Figure 3.11 • Evolution of the L^2-norm relative errors in space and time on the solid displacement $\varepsilon_u^{z,t}$ and on the pore pressure $\varepsilon_p^{z,t}$ with respect to the pulsation of the loading perturbation.

To conclude on this 1D example, under the condition to an imposed "undrained" loading that is compatible with our simplified undrained approximation, the simplified model is a very good simplification of the complete one, which is important as the simplified model is easier to implement and integrate. However, in real case scenarios modeled as a perturbation of the "undrained" pressure loading, errors are expected, which scale with the amplitude of the perturbation ΔP and its time evolution. Assuming that the pressure loading represents a fluid source, the previous illustration confirms that the characteristic time of the fluid source term should be derived with respect to the characteristic time of the system (timescale of a seismic instability here) so that the undrained approximation of the complete model would remain valid.

Conclusions and perspectives

1 Main contributions to the modeling of fluid injection effects in dynamic fault rupture using Fast Boundary Element Methods

Chapter 1 summarizes available literature on dynamic fault rupture and gives a comprehensive approach of the concepts used in the present work. The nucleation of a dynamic fault rupture and its arrest are part of the seismic cycle process that is defined using a kinematic approach (spring-slider reduced-order-model, see Section 1.2). A linear stability analysis is performed in Section 1.3 to (re-)derive the instability condition when a rate-and-state friction law is considered without fluid injection (resp with fluid injection in Section 1.4). After having emphasized the limitations of a reduced-order-model to model seismic cycle problems in Section 1.5, Section 2 presents the ingredients required to model a generic seismic cycle problem. We pay particular attention to the incorporation of hydromechanical couplings in the problem statement in Section 4. This key point is investigated in Chapter 3. Specifically, we justify the use of poroelastodynamic equations to take into account fluid effects, and we detail their impact in the interface condition and the balance momentum equation. Section 3 provides a large literature review on existing numerical methods in space and time to simulate seismic cycles. We insist on the advantages of the Fast Boundary Element Method based on hierarchical matrices (H-BEM) to solve seismic cycle problems for planar faults as well as for faults of complex geometries. A boundary element based solver for seismic cycle problem is developed from scratch in the next chapter. Moreover, we raise attention about the challenging verification and code comparison for seismic cycle simulations, which set the context for our contribution in Chapter 2.

Chapter 2 presents a significant part of our contribution. We assert the importance of accurate and efficient numerical tools to simulate seismic cycles problems before incorporating fluid-effects on fault slip. An important part of this work is devoted to the verification of seismic cycles simulations for standard two-dimensional quasi-dynamic mode II and III rate-and-state planar faults. For this purpose, we developed a boundary element method solver for seismic cycle problems from scratch. This solver incorporates the standard boundary element method (BEM), the fast boundary element method based on hierarchical matrices (H-BEM) and the spectral boundary element method (S-BEM) to solve the problem in space. Three time integration methods are implemented: an explicit-implicit prediction-correction method inspired by Lapusta et al. (2000), an explicit fourth-fifth order Runge-Kutta (RK45)

method inspired by Ozawa et al. (2022), and a hybrid prediction-correction - RK45 method inspired by Romanet and Ozawa (2021). The problem formulation for mode II and mode III simplified configurations using the boundary integral equation method (BIEM) is detailed in Section 1. The space and time discretization methods implemented are detailed in Section 2 and Section 3 respectively. A significant part of this chapter is the study of both the convergence and the sensitivity of the seismic cycle simulation results with respect to parameters that scale the space and time discretization in Section 4.2. Such a sensitivity study has not been investigated in the literature. This in-depth review of the most widely used methods represents a promising contribution to help the seismic cycle community develop a joint code. In Section 4.3, we compare the space discretization methods implemented. We first focus on one calculation of the shear stress at the fault interface using the traction Boundary Integral Equation (BIE) previously derived in Section 1. As expected, we show that the convergence of the calculation of the on-fault shear stress depends on the choice of the space step only for both standard BEM and H-BEM, whereas it relies on both the choice of the space step and the size of the discretized domain for S-BEM. We insist on the comparison of the performances of BEM, H-BEM and S-BEM, which shows the advantages of H-BEM over standard BEM in case of large problems. In order to provide accurate results, we investigate the coupled effect of the space step and the time step to prevent numerical artifacts that could be confused with seismic instabilities, leading to non-interpretable results. Section 4.4 studies the sensitivity of the calculation of the interface unknowns δ, V, τ, θ, with respect to parameters that scale the time discretization for the different implemented time-stepping methods, using H-BEM. We distinguish aseismic phases for which we are able to provide an analytical solution from the seismic phases. For the latter, we propose a strategy to compare our results with reference results provided by Pierre Romanet (personal communication) as analytical solutions for seismic slip simulations are unknown. We first show convergence results in the case of an aseismic simulation using the analytical solution proposed as a reference. Then, we compare seismic cycle results to results provided by Pierre Romanet. In particular, we compare the time at which the slip-rate first overcomes 1 m/s for each seismic event, and show that a small perturbation of the initialization leads to errors that cumulate at each new seismic event. In fact, we do not use the same method to mesh the fault as Pierre Romanet, which implies this small discrepancy at initialization. Finally, this study allows us to assess our numerical tools on a standard mode III benchmark and compare our results those obtained by Junle Jiang (member of the SEAS project, see Erickson et al. (2020a)) in Section 5. The previous results made us aware that the accumulated time shift could be explained by a difference in the initialization and/or a difference in the parameters that scale the time discretization. Such results could enhance the strategy that is currently proposed in the SEAS project for code verification procedure, and could help develop a joint code for seismic cycle simulations.

Now that we implemented accurate numerical tools for seismic cycle simulations, Chapter 3 concentrates on the modeling of fluid-injection effects on fault slip. The originality of this work is to focus on the case where the fluid is injected at a given distance from the fault and on fluid effects at the timescale of a seismic motion. It is a key step in order to incorporate the appropriate hydro-mechanical couplings in the boundary-element-based solver. After having extended the “dry” two-dimensional mode II and mode III problem from Chapter 2 to a case with fluid injection in Section 1, we emphasize on the numerical difficulties inherent

to the use of the complete poroelastodynamic model to incorporate hydro-mechanical couplings in Section 2. Moreover, in Section 3, we assess existing works on fluid effects on fault slip which highlight the use of simplified poroelastodynamic equations. Nevertheless, such simplified models are not necessarily adapted to the configuration we consider. We propose a simplified model allowing to account for fluid effects on fault slip at the timescale of a seismic motion. Therefore, we conduct a dimensional analysis on poroelastodynamic equations in Section 4 to formally assess predominant fluid effects at the timescale of a seismic or aseismic motion. We show that at the timescale of a seismic instability, we can neglect the relative fluid-solid skeleton motion, and we obtain an undrained model. Conversely, at the timescale of an aseismic motion, both inertial effects for the solid and for the fluid can be neglected leading to consolidation equations. We also derive a condition of a fluid-injection characteristic time so that a fluid injection source term could be maintained in the simplified model at the timescale of a seismic motion. Hence, these developments enable us to deduce the simplified poroelastodynamic equations of interest at the timescale of a seismic motion as well as to assess the validity range of the models used in the literature. The results of the dimensional analysis are summarized in Section 4.4. Finally, in Section 5, we consider a simplified 1D poroelastodynamic problem to illustrate the validity range of the simplified model obtained at the timescale of a seismic motion.

2 Main numerical developments

In order to choose the most appropriate numerical tools to simulate fluid injection effects on dynamic fault rupture, I have started the seismic cycle code from scratch. It allowed me to compare different numerical methods in space and time, developed using the same techniques within a single code base. It was also a new subject in my host laboratories. For the sake of clarity, I summarize here all the numerical developments of this thesis. Important numerical developments have been done to assess the capabilities of different numerical tools incorporating Fast BEMs to solve seismic cycle problems as well as dynamic fault rupture before incorporating hydromechanical couplings. I have developed a 2D boundary element method solver for seismic cycle problems to obtain the results presented in Chapter 2. The implementation is done in Python, and solves 2D quasi-dynamic seismic cycle and dynamic fault rupture problems for planar fault:

- Mode III and mode II (with a no-opening condition on the fault) with or without a free-surface option can be considered with a fault governed by rate-and-state friction with aging law to a given depth, and an imposed creep rate outside the rate-and-state zone;
- Mode III problems, with a fault governed by rate-and-state friction with aging law or slip law, and subjected to perturbations in effective normal stress due to fluid injection and along fault pore fluid diffusion can also be considered.

More precisely, the main software development contributions are:

- The 2D BEM and H-BEM have been implemented from scratch. They also allow to efficiently compute the quasi-static shear stress τ^{qs} (respectively its time-derivative).

The BEM matrix obtained by discretizing the boundary integral equation relating τ^{qs} to the slip δ is first computed (once for all before the solving when the geometry is fixed).

- The 2D Spectral-BEM has also been implemented from scratch. It allows to efficiently compute the quasi-static shear stress τ^{qs} (respectively its time-derivative) by calculating the boundary integral equation relating τ^{qs} to the slip δ as a simple product in the Fourier domain with respect to space. I needed this method for the comparisons studies I proposed as it is mostly used in the seismic cycle community.

- Three time integration methods (the corresponding algorithms are presented in Section 3.1) have been implemented from scratch too:

  – an explicit-implicit prediction-correction method inspired by Lapusta et al. (2000);

  – an explicit fourth-fifth order Runge-Kutta (RK45) method inspired by Ozawa et al. (2022);

  – a hybrid prediction-correction - RK45 method inspired by Romanet and Ozawa (2021).

We also implemented a CQM routine in Python from scratch to obtain the results presented in Chapter 3.

Although the efficiency of the mentioned codes can be improved in many ways, we developed a full prototype code for solving 2D quasi-dynamic seismic cycle problems for planar faults. It allows comparison between commonly used numerical tools in the seismic cycle community. In particular, a new time integration or space discretization method can easily be added to the code, which is promising for future use like the development of a common code for seismic cycle simulations. A specific routine and several bash scripts have been proposed to conduct each convergence and sensitivity study efficiently, and the same structure is used to store results in order to ease the post-process step. The codes developed contains 11469 lines for source codes, and 5243 lines for post-processing codes. A public repository on Git will soon be set up to make these developments available to the community. We will also soon provide our results on SEAS benchmarks to the SCEC group to participate in the effort of the SEAS project.

3 Directions for future work

The main results of this work are promising and give path to lots of extensions.

A direct extension to this work is to incorporate hydro-mechanical couplings in the code to provide reliable simulation results for fluid injection induced earthquake as well as for the assessment of earthquake mitigation strategies using fluid injection. This could be done using the simplified models resulting from the dimensional analysis performed in Section 4 in Chapter 3. To study fluid effects on fault slip at the timescale of a seismic motion, we could use the undrained system (3.47). We could start with a quasi-dynamic version of the undrained model to ease the incorporation of hydromechanical coupling in the boundary element based solver and avoid the difficulties mentioned in Section 2 of Chapter 3 as analytical time domain Green function could be derived. Next we could consider a fully-dynamic

model. However, the difficulty is that the calculation of a convolution product in time is required. To ensure efficient solving, in the frame of seismic cycle simulations, a constant time step is usually imposed as detailed by Lapusta and Liu (2009), which can induce cumulative errors and prevent from obtaining interpretable results. If we keep a varying time step, new values of the fundamental solutions should be computed at each iteration. In both cases, a cut-off criterion can be estimated to truncate the convolution in time and accelerate its calculation. The balance between the approximation introduced and the efficiency of the method should be assessed. To study fluid effects on fault slip at the timescale of a seismic motion, we could use the 2D equivalent of the consolidation system (3.48) as done by Heimisson et al. (2022), but with a fluid source term at a given distance from the fault.

Other extensions to this work are also possible.

Short-term:. We can first distinguish short-term extensions to improve the accuracy of the developed numerical tools. Time integration methods for seismic cycle problems could be improved. We could implement more accurate methods by using higher order time discretization schemes in prediction-correction methods. Moreover, we could prevent the time step from oscillating, using control techniques for time step selection (Gustafsson (1991), Söderlind (2002), or Arévalo et al. (2021) for multistep methods). The computation efficiency could also be improved. The low-rank approximation of admissible blocks in H-BEM can be parallelized as well as the two prediction-correction steps on a full time step and on two successive half-time steps respectively in the hybrid prediction-correction - RK45 method implemented.

Mid-term:. Next, mid-term extensions could be considered. Regarding the verification of the accuracy of solving methods for seismic cycle problems, we could use the method of manufactured solutions to provide an analytical solution to assess the convergence of the solving methods during seismic phases. The principle of the method of manufactured solutions relies on adapting the initial problem so that it is satisfied by an a priori chosen solution. In practice, we choose a (manufactured) solution which is similar to the expected one. This manufactured solution must satisfy the boundary and initial conditions. Next, we add a source term to the initial balance momentum equation so that the manufactured solution is an analytical solution of this new problem. Assuming that the order of approximation of the new governing equation is the same as for the original one, the problem is solved, and the solution compared to the manufactured solution which stands for the analytical solution. In general, two manufactured solutions are introduced, which can respectively be exactly approximated in space or time with the discretization chosen in order to study independently convergence in space and time. Erickson and Dunham (2014) and Erickson et al. (2017) introduce a manufactured solution to study convergence in space only, assuming that the accumulation of error in time is negligible. This method has only been proposed to verify sufficient accuracy of some Finite Difference Codes (Erickson & Dunham, 2014; Erickson et al., 2017). This would be complementary to the use of benchmark to validate solving methods for seismic cycle problems.

Fully-dynamic seismic cycle simulations (based on elastodynamic balance momentum

equation) would improve the realism of the simulation results without and with fluid injection. The method proposed by Lapusta and Liu (2009) and largely used in the seismic cycle community (see Erickson et al. (2023)) gives a starting point to incorporate full elastodynamics in seismic cycle simulations. However, the main drawback of this method is that it introduces a constant time step to tackle the expensive computation of the time-convolution product inherent to the dynamic part. This can induce errors that can cumulate in space and time and prevent from obtaining interpretable results. As such dynamic effects are especially relevant during seismic instabilities, we could include such effects during seismic phase only in our simulations and add a safety coefficient to the minimum time step chosen such that it would be lower than the minimum optimal seismic time step given in the quasi-dynamic approximation.

Long-term:. Long-term extensions would focus on the reliability of the seismic cycle model as a faithful abstraction of reality. Now that we developed a boundary element solver for standard two-dimensional mode II and mode III seismic cycle problems, we could consider fully-dynamic three-dimensional problems, with realistic fault geometries, which is possible with H-BEM (Ando, 2016; Ozawa et al., 2022). However, such cases could lead to prohibitive computational costs due to the large problem size required so that the cell size could accurately resolve the nucleation length. In addition, the Spectral-BEM cannot be applied. To avoid these difficulties, we could consider the approach detailed by Ando (2016), who proposes a clever way to decompose the boundary integral equation so that its calculation could be further accelerate using Fast BEMs bases on Hierarchical matrices. Ozawa et al. (2022) investigates the use of Lattice Hierarchical matrices to accelerate seismic cycle simulations in the case of non-planar faults. Considering realistic fault geometries could drastically enhance the reliability of the prediction of fluid effects on fault slip.

Appendices

A

Currently used codes for seismic cycles simulations

Table A.1 is modified from Erickson et al. (2020a, 2023) and gives details (problem configuration, spatial and temporal discretization methods, ... etc.) of the currently used codes for simulations of sequences of earthquakes and aseismic slips. Numerical methods for both spatial and temporal discretization are given.

Code name	Modeler name	2D or 3D	Friction[a]	Rock structure[b]	Geometry[c]	Rock response[d]	Problem[e]	Spatial discretization	Time-stepping method
Garnet[1]	Li M. Allison K. L. Rivet M.	2D and 3D	RSF	Homog.	Planar fault in SIS	QD and FD elastic	EC	FDM	Adams-Moulton or BDF
SCYCLE[2]	Yang Y. Dunham E. Zhu W. Erickson B. A. Duru K.	2D	RSF	Homog.	Planar fault in SIS	QD and FD elastic / viscoelastic / thermoelastic	EC and Icesteam	SBP-FDM	Prediction-correction with RK23 or RK45
FDCYCLE[3]	Erickson B.	2D	RSF	Homog.	Planar fault in SIS	QD elastic / plastic	EC	SBP-FDM	RK45
sbplib[4]	Almquist M.	2D and 3D	RSF	Homog.	(Dipping) planar fault in SIS	QD elastic / viscoelastic	EC	SBP-FDM	RK23
Thrase[5]	Harvey T. W.	2D	RSF	Homog.	Planar fault in SIS	QD and FD elastic	EC	SBP-FDM	Adaptive time-stepping method in Julia
EQSimu[6]	Liu D. Duan B.	2D and 3D	RSF	Homog.	Planar fault in SIS	QD and FD elastic	EC	FEM	Prediction-correction with Euler scheme
QDESDG[7]	Kozdon J. E.	2D	RSF	Homog.	Planar fault in SIS	QD elastic	EC	DG	RK45
tandem[8]	Uphoff C.	2D and 3D	RSF	Homog.	(Dipping) planar fault in SIS	QD elastic	EC	DG	RK23 or RK45
Sem2pack[9]	Liang C.	2D	RSF	Homog. and Heterog.	Planar fault in SIS	QD and FD elastic / inelastic	EC and DR	SEM	Prediction-correction with Newmark scheme
SPEAR[10]	Thakur P.	2D	RSF	Homog.	Planar fault in SIS	QD and FD elastic	EC	SEM	Prediction-correction with Euler scheme
FEBE[11]	Abdelmeguid M.	2D	RSF	Homog.	Planar fault in SIS	QD and FD elastic	EC	Hybrid FEM/S-BEM	Prediction-correction with Euler scheme
BICYCLE[12]	Jiang J. Lambert V. Ma X.	2D	RSF	Homog.	Planar fault in SIS	QD and FD elastic	EC	S-BEM	Prediction-correction with Euler scheme
Motorcycle[13]	Barbot S.	2D and 3D	RSF	Homog.	(Multi-) planar fault(s) in SIS	QD elastic	EC	S-BEM	RK45
Unicycle[14]	Barbot S.	2D and 3D	RSF	Homog.	(Dipping) planar fault in SIS	QD elastic / viscoelastic	EC	S-BEM	RK45
MDSBI[15]	Dunham E.	2D and 3D	TP-FH-RSF	Homog. and Bimaterial	Planar fault in SIS	QD and FD elastic	EC and DR	MDSBI	Prediction-correction with RK45
ESAM[16]	Liu Y.	2D and 3D	RSF	Homog.	Planar fault in SIS	QD elastic	EC	S-BEM	RK45
QDYN[17]	Luo Y. Idini B. Van den Ende M. Ampuero J. P.	2D and 3D	RSF and CNS friction and heterog. friction properties	Homog.	(Non-) planar fault in SIS and fault surrounded by damaged zone	QD elastic	EC	S-BEM	Bulirsch-Stoer and RK45
Fastcycles[18]	Romanet P.	2D and 3D	RSF	Homog.	(Non-) planar fault in SIS	QD and FD elastic	EC	S-BEM	Hybrid prediction-correction + RK45
HBI[19]	Ozawa S.	2D and 3D	RSF	Homog.	(Non-) planar fault in SIS	QD elastic	EC	Lattice-H-BEM	RK45
TriBIE[20]	Li D.	2D and 3D	RSF	Homog.	(Dipping/Non-) planar fault in SIS	QD elastic	EC	S-BEM	Not given
FDRA[21]	Cattania C.	2D and 3D	RSF	Homog.	(Dipping/Non-) planar fault in SIS	QD elastic	EC	H-BEM	Not given

Table A.1 • Details of currently active codes for seismic cycles simulations and configurations considered.

Several abreviations are used in Table A.1: [a] RSF is Rate-and-State Friction, TP-FH-RSF is Rate-and-State Friction with Thermal Pressurization and Flash Heating, CNS is Chen-Niemeijer-Spiers friction model; [b] Homog. is Homogeneous et Heterog. is Heterogeneous; [c] SIS is Semi-Infinite Space; [d] QD is quasi-dynamic and FD is fully-dynamic; [e] EC is earthquake cycles and DR is dynamic rupture.

Below are the corresponding useful references for code development and url if code is available online.

[1] Pranger (2020)

[2] Erickson and Dunham (2014), Allison and Dunham (2018), https://github.com/kali-allison/SCycle

[3] Erickson and Dunham (2014), Erickson et al. (2017), https://github.com/brittany-erickson/FDCycle

[4] Almquist and Dunham (2021)

[5] https://github.com/Thrase/Thrase

[6] Liu et al. (2020), Lapusta et al. (2000)

[7] https://github.com/jkozdon/QDESDG

[8] Uphoff et al. (2022), Abhyankar et al. (2018), https://github.com/TEAR-ERC/tandem

[9] https://github.com/jpampuero/sem2dpack

[10] Thakur et al. (2020), https://github.com/thehalfspace/Spear

[11] Hajarolasvadi and Elbanna (2017), Abdelmeguid et al. (2019), Lapusta et al. (2000)

[12] Lapusta and Liu (2009), Lapusta et al. (2000)

[13] Barbot (2021)

[14] Barbot (2019), http://bitbucket.org/sbarbot

[15] https://pangea.stanford.edu/$\sim$edunham/codes/codes.html

[16] Liu and Rice (2007)

[17] Luo et al. (2017), https://github.com/ydluo/qdyn

[18] Romanet and Ozawa (2021)

[19] Ozawa et al. (2022), https://github.com/sozawa94/hbi

[20] Li and Liu (2016), Li and Liu (2017)

[21] Segall and Bradley (2012), Bradley (2014)

B

Numerical test on fluid-injection induced slow slip Benchmark

Here, we present a supplementary cross-validation of the numerical tools developed on the benchmark problem BP6 from SEAS benchmark / validation exercises. This benchmark incorporates the effect of fluid injection (at constant rate, followed by along fault fluid diffusion) on fault slip in the form of a one-way coupling model. In practice, an elastodynamic equation is combined with a diffusion equation satisfied by the fluid pressure. Quasi-dynamic approximation is assumed for this problem.

We consider the case of a 2D problem in whole-space containing a 1D fault subjected to rate-and-state friction with perturbation of the effective normal stress due to fluid-injection and along-fault pore fluid diffusion Figure B.1. Anti-plane motion is considered The problem

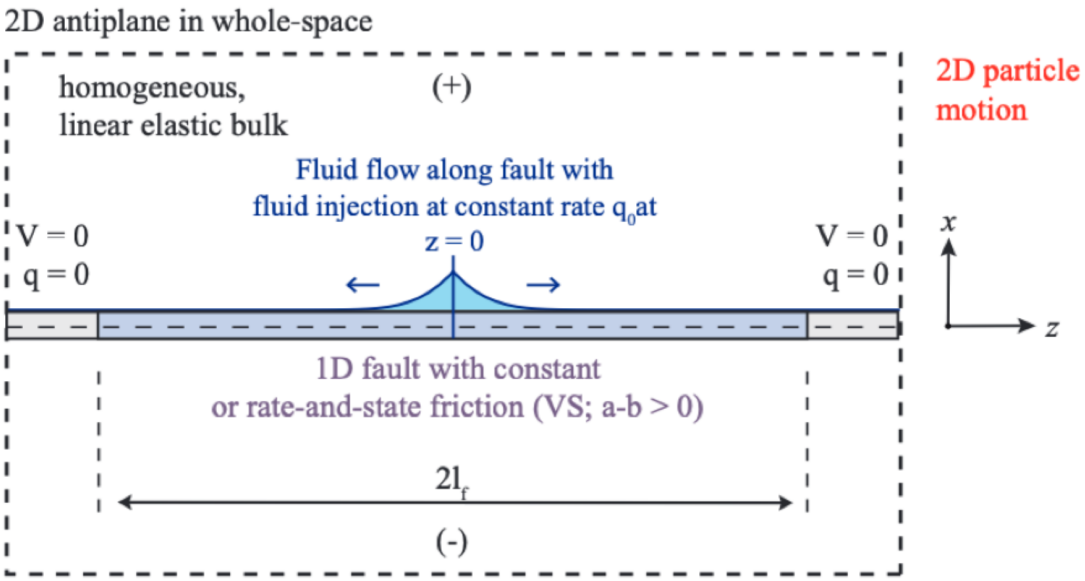

Figure B.1 • 2D illustration of benchmark problem 6 (BP6 SEAS) from https://strike.scec.org/cvws/seas/download/SEAS_BP6_Nov18.pdf.

statement is similar to the one of BP1 SEAS. The only change consists in a perturbation of the

effective normal stress due to the pore fluid pressure.

$$\sigma_n(z,t) = \overline{\sigma}_0 - p(z,t) \tag{B.1}$$

The pore-fluid pressure satisfies a 1D diffusion equation (B.2).

$$\frac{\partial p}{\partial t} - \frac{k}{\Phi\beta\eta}\frac{\partial^2 p}{\partial z^2} = \frac{q_{\text{inj}}(t)}{\beta\Phi}\delta(z) \tag{B.2}$$

where the parameters are given in table B.1 and the solution of Equation (B.2) is known analytically (see Equation (B.3))

$$p(z,t) = \frac{q_0}{\beta\Phi\sqrt{\alpha}}[G(z,t,\alpha)\mathscr{H}(t) - G(z,t-t_{\text{off}},\alpha)\mathscr{H}(t-t_{\text{off}})] \tag{B.3}$$

where,

$$G(z,t,\alpha) = \sqrt{t}\left[\frac{\exp\left(\frac{-z^2}{4\alpha t}\right)}{\sqrt{\pi}} - \frac{|z|}{\sqrt{4\alpha t}}\text{erfc}\left(\frac{|z|}{\sqrt{4\alpha t}}\right)\right],$$

and $\mathscr{H}(t)$ is the Heaviside function.

Parameter	Definition	Value, Unit
μ	Shear modulus	$\simeq 32$ GPa
c_s	Shear wave speed	3464 m/s
σ_n	Initial effective normal stress at the fault interface	50 MPa
$a(z)$	Rate and state parameter	0.007
$b(z)$	Rate and state parameter	0.005
$D_c(z)$	Characteristic slip distance	4 mm
V_{pl}	Imposed slip rate out of rate-and-state zone	0 m/s
V_{init}	Initial slip rate	10^{-12} m/s
V_0	Reference slip rate	10^{-6} m/s
f_0	Reference friction coefficient	0.6
W_f	Width of the rate-and-state zone	40 km
q_0	fluid injection rate	$1.25\ 10^{-6}$ m/s
β	pore and fluid compressibility	10^{-8} Pa^{-1}
Φ	Porosity	0.1
k	permeability	10^{-13} m^2
η	fluid viscosity	10^{-3} Pa.s
α	hydraulic diffusivity	0.1 m^2/s
t_{off}	injection turn-of time	100 days

Table B.1 • Parameter values used for BP1 SEAS.

Here, we consider a weak coupling between the fluid and the solid. We used the hybrid prediction-correction - RK45 method (inspired by Romanet and Ozawa (2021)) with hierarchical matrices based fast boundary element methods to obtain the results presented here.

Parameters	$\beta_{\min}$	$\varepsilon_{\text{Newton}}$	$\text{maxiter}_{\text{Newton}}$	$\varepsilon_{\text{solver}}$
Hybrid method	0.12	10^{-6}	40	10^{-5}

Table B.2 • Time discretization parameters for the benchmark problem 6 (BP6) seismic cycle simulation.

Parameters	$L_b/\Delta z$	N_{rep}	N_{leaf}	η	ε_{ACA}
H-BEM	6	1	100	3	10^{-5}

Table B.3 • Space discretization parameters for the benchmark problem 6 (BP6) seismic cycle simulation.

The parameters used for the time-stepping method are given in Table B.2. The parameters used for the H-BEM are given in Table B.3

Figure B.2 shows the time evolution of each interface unknown: the slip δ, the slip-rate V, the shear stress τ, the state-variable θ, and the fluid pressure p. We observe that a slow slip is induced by fluid diffusion along the fault. Our results are in good agreement with results from So Ozawa, approved by seismic cycles' community (See Figure B.2).

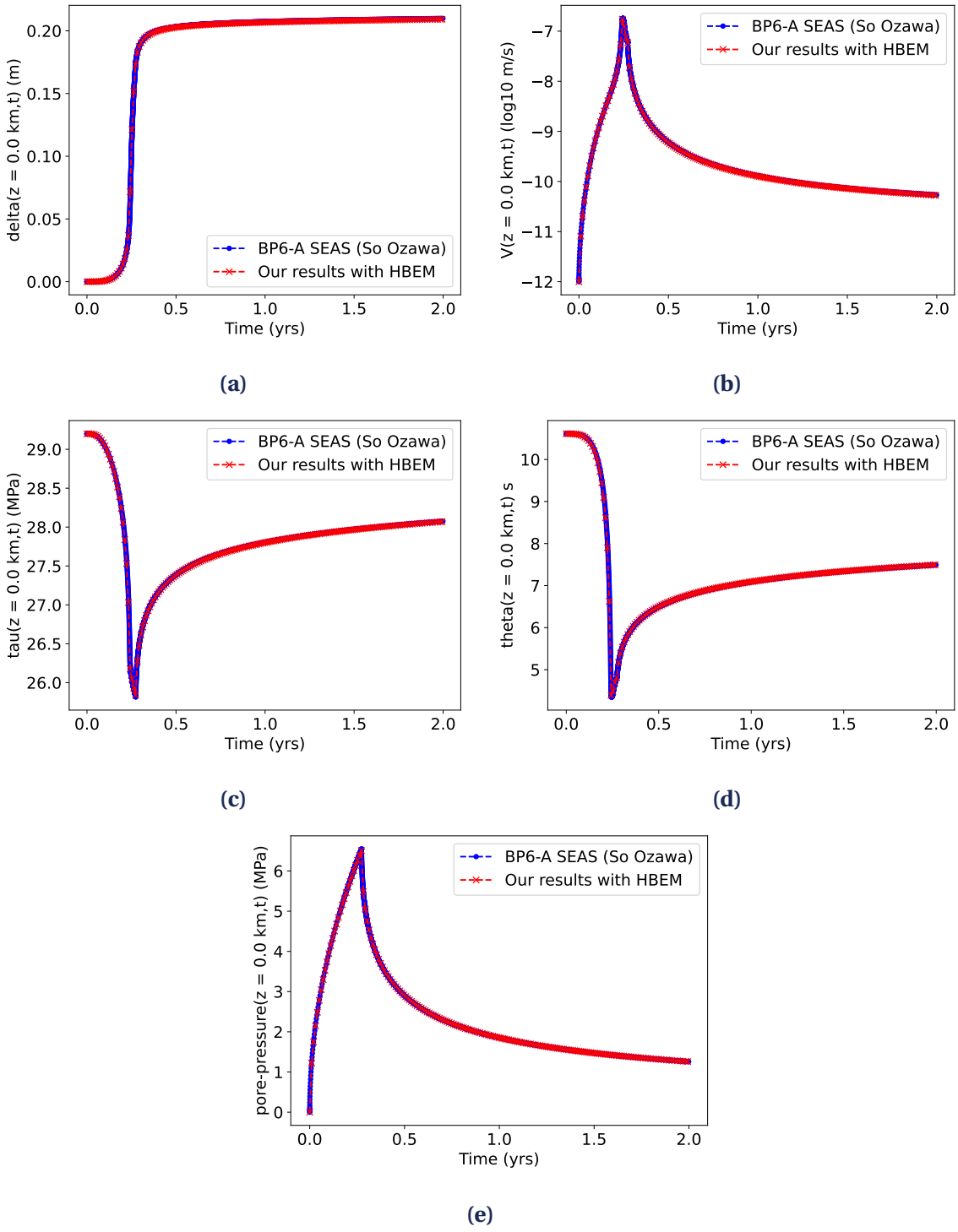

Figure B.2 • Time evolution of the slip rate at $z = 0$ km, close to the fluid injection point and to the nucleation region of the slow slip event (SSE).

C

Dimensional analysis of poroelastodynamic equations

1 Assessing the governing parameters

Here we describe the methodology to choose orders of magnitude for the governing parameters in Table 3.2

These developments are conducted under Biot's poroelastic assumptions. To determine the longitudinal wave modulus M, we calculate the bulk modulus of the skeleton K and the shear modulus of the skeleton G. From equation (6) in Schanz (2009) which defines the Biot's effective stress coefficient, we have:

$$K = K^s(1-\alpha)$$

where K^s is the bulk modulus of the solid grains.

We then use the relation between the bulk modulus and the shear modulus of the solid grains (K_s and G_s respectively).

$$K^s = \frac{2G^s(1+\nu)}{3(1-2\nu)}$$

We impose the shear modulus of the solid grains $G^s = 30\cdot 10^9$ Pa, the Poisson ratio $\nu = 0.25$ and Biot's coefficient $\alpha = 0.8$. Consequently, $K \approx 10^{10}$ Pa. Then we reuse the previous relation (1) to deduce G from K.

$$G = \frac{3K(1-2\nu)}{2(1+\nu)}$$

We obtain $G \approx 6\cdot 10^9$ Pa and $M \approx 18\cdot 10^9$ Pa.

We choose the following values for bulk density ρ, the fluid density ρ_f and apparent mass density ρ_a.

$$\rho = 2500\ \text{kg.m}^{-3},\ \rho_f = 1000\ \text{kg.m}^{-3},\ \rho_a = 0.66\Phi\rho_f \approx 99\ \text{kg.m}^{-3}$$

ρ_a is linked to the tortuosity and is defined in Schanz (2009).

We choose the following values for porosity, permeability and dynamic viscosity.

$$\Phi = 0.15,\ k = 10^{-10}\ \mathrm{m}^2,\ \eta \approx 3 \cdot 10^{-4}\ \mathrm{Pa.s}$$

To calculate R, we use the expression from Equation (4) in Schanz (2009).

$$R = \frac{\Phi^2 K^s}{(1 - K/K^s) + \Phi(K^s/K^f - 1)}$$

We take K^f as the inverse of the fluid compressibility $\beta \approx 4 \cdot 10^{-10}\ \mathrm{Pa}^{-1}$. We obtain $R \approx 3.1 \cdot 10^8$ Pa.

2 Scaling poroelastodynamic equations

Here, we describe the methodology for the non-dimensionalization of the poroelastodynamic equations (3.8a) and (3.8b) using the scales introduced in Table 3.1. We give the developments for the one-dimensional version of the poroelastodynamic equations for the sake of simplicity. The method used the one-dimensional poroelastodynamic equations with fluid source, and for the two-dimensional and three-dimensional version of the poroelastodynamic equations follows the same steps. Only the scales for the non-dimensionalization of the space coordinate and for the displacement field are different. They are given in (3.42).

We first rewrite the quantity $\beta(s)$ from Equation (3.9) in terms of the timescales introduced in Table 3.1.

$$\beta(s) = \frac{T_f}{T_c}\overline{s}\left(1 + \overline{s}\frac{T_f}{T_c}\frac{\mathcal{T}}{\Phi}\right)^{-1} = \frac{T_f}{T_c}\overline{\beta}(\overline{s}),\ \text{with}\ \overline{\beta}(\overline{s}) = \overline{s}\left(1 + \overline{s}\frac{T_f}{T_c}\frac{\mathcal{T}}{\Phi}\right)^{-1},\ \text{and}\ \mathcal{T} = \frac{\rho_a/\rho_f + \Phi}{\Phi}, \quad \text{(C.1)}$$

where $\mathcal{T}$ is the tortuosity.

Then, we perform the non-dimensionalization of the poroelastodynamic equations (3.8a) and (3.8b) using the scales introduced in Table 3.1, and using the expression of $\beta(s)$ from (C.1)

$$\frac{M\epsilon_0}{W_f}\underline{\hat{u}}_{z,zz} - \left(\alpha - \frac{T_f}{T_c}\overline{\beta}(\overline{s})\right)\frac{\Sigma}{W_f}\underline{\hat{p}}_{,z} - \left(\overline{\rho} - \frac{T_f}{T_c}\overline{\beta}(\overline{s})\right)\frac{\rho_f U}{T_c^2}\overline{s}^2\underline{\hat{u}}_z = 0, \quad \text{(C.2a)}$$

$$\frac{T_f\Sigma}{\rho_f W_f^2}\frac{\overline{\beta}(\overline{s})}{\overline{s}}\underline{\hat{p}}_{,zz} - \frac{\Phi^2\Sigma}{RT_c}\overline{s}\underline{\hat{p}} - \left(\alpha - \frac{T_f}{T_c}\overline{\beta}(\overline{s})\right)\frac{\epsilon_0}{T_c}\overline{s}\underline{\hat{u}}_{z,z} = 0. \quad \text{(C.2b)}$$

Then, we divide (C.2a) by $\frac{M\epsilon_0}{W_f}$ and (C.2b) by $\frac{\Phi^2\Sigma}{RT_c}$, and we can notice that

$$\begin{aligned}
\frac{\Sigma}{W_f}\times\left(\frac{M\epsilon_0}{W_f}\right)^{-1} &= 1\\
\frac{\rho_f U}{T_c^2}\times\left(\frac{M\epsilon_0}{W_f^2}\right)^{-1} &= \frac{1}{\overline{\rho}}\frac{W_f^2}{c_p^2}\frac{1}{T_c^2} = \frac{1}{\overline{\rho}}\frac{T_{pw}^2}{T_c^2}\\
\frac{T_f\Sigma}{\rho_f W_f^2}\times\left(\frac{\Phi^2\Sigma}{RT_c}\right)^{-1} &= \frac{Rk}{\eta D^2}\frac{T_c\lambda_L^2}{\Phi^2} = \frac{T_c}{T_d}\frac{\lambda_L^2}{\Phi^2}\\
\frac{\epsilon_0}{T_c}\times\left(\frac{\Phi^2\Sigma}{RT_c}\right)^{-1} &= \frac{R}{\Phi^2 M}
\end{aligned}$$

Thus, (C.2a) and (C.2b) write

$$\overline{\hat{u}}_{z,zz} - \left(\alpha - \frac{T_f}{T_c}\overline{\beta}(\overline{s})\right)\overline{\hat{p}}_{,z} - \left(\overline{\rho} - \frac{T_f}{T_c}\overline{\beta}(\overline{s})\right)\frac{1}{\overline{\rho}}\frac{T_{pw}^2}{T_c^2}\overline{s}^2\overline{\hat{u}}_z = 0, \tag{C.3a}$$

$$\frac{T_c}{T_d}\frac{\lambda_L^2}{\Phi^2}\frac{\overline{\beta}(\overline{s})}{\overline{s}}\overline{\hat{p}}_{,zz} - \overline{s}\overline{\hat{p}} - \left(\alpha - \frac{T_f}{T_c}\overline{\beta}(\overline{s})\right)\frac{R}{\Phi^2 M}\overline{s}\overline{\hat{u}}_{z,z} = 0. \tag{C.3b}$$

We develop the expression of $\overline{\beta}(\overline{s})$ in Equations (C.3a) and (C.3b)

$$\overline{\hat{u}}_{z,zz} - \left(\alpha - \frac{T_f}{T_c}\overline{s}\left(1+\overline{s}\frac{T_f}{T_c}\frac{\mathcal{T}}{\Phi}\right)^{-1}\right)\overline{\hat{p}}_{,z} - \left(\overline{\rho} - \frac{T_f}{T_c}\overline{s}\left(1+\overline{s}\frac{T_f}{T_c}\frac{\mathcal{T}}{\Phi}\right)^{-1}\right)\frac{1}{\overline{\rho}}\frac{T_{pw}^2}{T_c^2}\overline{s}^2\overline{\hat{u}}_z = 0, \tag{C.4a}$$

$$\frac{T_c}{T_d}\frac{\lambda_L^2}{\Phi^2}\left(1+\overline{s}\frac{T_f}{T_c}\frac{\mathcal{T}}{\Phi}\right)^{-1}\overline{\hat{p}}_{,zz} - \overline{s}\overline{\hat{p}} - \left(\alpha - \frac{T_f}{T_c}\overline{s}\left(1+\overline{s}\frac{T_f}{T_c}\frac{\mathcal{T}}{\Phi}\right)^{-1}\right)\frac{R}{\Phi^2 M}\overline{s}\overline{\hat{u}}_{z,z} = 0. \tag{C.4b}$$

3 Determining 1D poroelastodynamic fundamental solutions

Here, we detail the calculation of the displacement fundamental solutions of the homogeneous complete poroelastodynamic equations (3.55a) and (3.55b) with non-homogeneous boundary conditions (3.56). Such an ordinary differential equation system can be solved using the exponential ansatz

$$\hat{G}_y^u(z,s) = Ue^{\lambda sz},\ \hat{G}^p(z,s) = Pe^{\lambda sz}, \tag{C.5}$$

where $\hat{G}^u$ and $\hat{G}^p$ are the Laplace transforms of the displacement and pressure fundamental solutions. Injecting the exponential solution forms in equations (3.55a) and (3.55b), we obtain

$$\begin{bmatrix} M\lambda^2 - (\rho - \beta(s)\rho_f) & -(\alpha - \beta(s))\lambda/s \\ -s(\alpha-\beta(s))\lambda & \lambda^2\dfrac{\beta(s)}{\rho_f} - \dfrac{\phi^2}{R} \end{bmatrix}\begin{bmatrix} U \\ P \end{bmatrix} = \begin{bmatrix} 0 \\ 0 \end{bmatrix} \tag{C.6}$$

To obtain a non-trivial solution of equation (C.6), we have to satisfy the equation

$$\underbrace{\frac{M\beta(s)}{\rho_f}}_{A}\lambda^4 - \underbrace{\left(\frac{M\phi^2}{R}+\left(\rho-\beta(s)\rho_f\right)\frac{\beta(s)}{\rho_f}+\left(\alpha-\beta(s)\right)^2\right)}_{B}\lambda^2 + \underbrace{\frac{\phi^2\left(\rho-\beta(s)\rho_f\right)}{R}}_{C}=0 \tag{C.7}$$

which leads to the following eigenvalues:

$$\lambda_1=-\lambda_3=\sqrt{\frac{B+\sqrt{B^2-4AC}}{2A}},\ \lambda_2=-\lambda_4=\sqrt{\frac{B-\sqrt{B^2-4AC}}{2A}}$$

Moreover, the eigenvectors of the system (C.6) satisfy the relation

$$P_i=\frac{M\lambda_i^2-(\rho-\beta(s)\rho_f)}{(\alpha-\beta(s))\lambda_i}sU_i \hat{=} d_i sU_i,\ \Rightarrow d_1=-d_3,\ d_2=-d_4$$

Hence, the complete solution of the homogeneous problem can write as

$$\begin{aligned}
\hat{G}_z^u(z,s)&=\sum_{i=1}^{4}U_i e^{\lambda_i sz}\\
\hat{G}^p(z,s)&=\sum_{i=1}^{4}P_i e^{\lambda_i sz}\\
\hat{T}_z(z,s)&=M\hat{G}^u_{z,z}(z,s)-\alpha\hat{G}^p(z,s)\\
\hat{Q}_z(z,s)&=-\frac{\beta(s)}{s\rho_f}\left(\hat{G}^p_{,z}(z,s)+s^2\rho_f\hat{G}^u_z(z,s)\right)\\
&=-\frac{\beta(s)Ms}{\rho_f(\alpha-\beta(s))}\sum_{i=1}^{4}\lambda_i^2U_i e^{\lambda_i sz}+\beta(s)s\frac{\rho-\alpha\rho_f}{\rho_f(\alpha-\beta(s))}\hat{G}^u_z(z,s)
\end{aligned}$$

where $\hat{T}_z$ and $\hat{Q}_z$ are the Laplace transform of the traction and the fluid flux fundamental solutions of the complete poroelastodynamic equations.

Finally, we find the values of U_i using the boundary conditions. As we are dealing with a linear problem, the superposition principle is valid. Therefore, the calculation of the solutions can be divided into different loading cases

- first loading case: $\hat{u}_z(z=0)=0, \hat{q}_z(z=0)=0,\ \hat{t}_z(z=L)=-\Sigma_0,\ \hat{p}(z=L)=0$
- second loading case: $\hat{u}_z(z=0)=0, \hat{q}_z(z=0)=0,\ \hat{t}_z(z=L)=0,\ \hat{p}(z=L)=P_0$

We apply boundary conditions for the first load case:

$$\hat{u}_y(y=0,s) = 0 = U_1 + U_2 + U_3 + U_4 \tag{C.8}$$

$$\begin{aligned}\hat{q}(y=0,s) = 0 = &-\frac{\beta(s)Ms}{\rho_f(\alpha-\beta(s))}\left(\lambda_1^2(U_1+U_3)+\lambda_2^2(U_2+U_4)\right)\\ &+\beta(s)s\frac{\rho-\alpha\rho_f}{\rho_f(\alpha-\beta(s))}(U_1+U_2+U_3+U_4)\end{aligned} \tag{C.9}$$

$$\begin{aligned}\hat{\sigma}_y(y=L,s) = -\Sigma_0 &= M\left(\lambda_1 sU_1e^{\lambda_1 sL}+\lambda_2 sU_2e^{\lambda_2 sL}-\lambda_1 sU_3e^{-\lambda_1 sL}-\lambda_2 sU_4e^{-\lambda_2 sL}\right)\\ &-\alpha\left(d_1 sU_1e^{\lambda_1 sL}+d_2 sU_2e^{\lambda_2 sL}-d_1 sU_3e^{-\lambda_1 sL}-d_2 sU_4e^{-\lambda_2 sL}\right)\\ &=(M\lambda_1-\alpha d_1)s\left(U_1e^{\lambda_1 sL}-U_3e^{-\lambda_1 sL}\right)\\ &+(M\lambda_2-\alpha d_2)s\left(U_2e^{\lambda_2 sL}-U_4e^{-\lambda_2 sL}\right)\end{aligned} \tag{C.10}$$

$$\hat{p}(y=L,s) = 0 = d_1 s\left(U_1e^{\lambda_1 sL}-U_3e^{-\lambda_1 sL}\right)+d_2 s\left(U_2e^{\lambda_2 sL}-U_4e^{-\lambda_2 sL}\right) \tag{C.11}$$

(C.8) $\Leftrightarrow$ $U_1 + U_3 = -(U_2 + U_4)$

(C.8) injected in (C.9) gives $(-\lambda_1^2+\lambda_2^2)(U_2+U_4)=0 \Rightarrow U_4 = -U_2$ and $U_3 = -U_1$

(C.11) $\Leftrightarrow$ $U_2 = -\dfrac{d_1}{d_2}U_1\dfrac{e^{\lambda_1 sL}}{e^{\lambda_2 sL}}\dfrac{1+e^{-2\lambda_1 sL}}{1+e^{-2\lambda_2 sL}}$

(C.10) $\Leftrightarrow$ $U_1 = \Sigma_0\dfrac{d_2}{Ms(d_1\lambda_2-d_2\lambda_1)}\dfrac{e^{-\lambda_1 sL}}{1+e^{-2\lambda_1 sL}} \Rightarrow U_2 = -\Sigma_0\dfrac{d_1e^{-\lambda_2 sL}}{Ms(d_1\lambda_2-d_2\lambda_1)(1+e^{-2\lambda_2 sL})}$

Finally, we obtain

$$\begin{aligned}\hat{u}_y(y,s) &= \frac{\Sigma_0}{Ms(d_1\lambda_2-d_2\lambda_1)}\left[\frac{d_2\left(e^{-\lambda_1 s(L-y)}-e^{-\lambda_1 s(L+y)}\right)}{1+e^{-2\lambda_1 sL}}-\frac{d_1\left(e^{-\lambda_2 s(L-y)}-e^{-\lambda_2 s(L+y)}\right)}{1+e^{-2\lambda_2 sL}}\right]\\ \hat{p}(y,s) &= \frac{\Sigma_0 d_1 d_2}{M(d_1\lambda_2-d_2\lambda_1)}\left[\frac{\left(e^{-\lambda_1 s(L-y)}+e^{-\lambda_1 s(L+y)}\right)}{1+e^{-2\lambda_1 sL}}-\frac{\left(e^{-\lambda_2 s(L-y)}+e^{-\lambda_2 s(L+y)}\right)}{1+e^{-2\lambda_2 sL}}\right]\end{aligned} \tag{C.12}$$

We apply boundary conditions for the second load case:

$$\hat{u}_y(y=0,s) = 0 = U_1 + U_2 + U_3 + U_4 \tag{C.13}$$

$$\begin{aligned}\hat{q}(y=0,s) = 0 = &-\frac{\beta(s)Ms}{\rho_f(\alpha-\beta(s))}\left(\lambda_1^2(U_1+U_3)+\lambda_2^2(U_2+U_4)\right)\\ &+\beta(s)s\frac{\rho-\alpha\rho_f}{\rho_f(\alpha-\beta(s))}(U_1+U_2+U_3+U_4)\end{aligned} \tag{C.14}$$

$$\begin{aligned}\hat{\sigma}_y(y=L,s) = 0 &= M\left(\lambda_1 sU_1e^{\lambda_1 sL}+\lambda_2 sU_2e^{\lambda_2 sL}-\lambda_1 sU_3e^{-\lambda_1 sL}-\lambda_2 sU_4e^{-\lambda_2 sL}\right)\\ &-\alpha\left(d_1 sU_1e^{\lambda_1 sL}+d_2 sU_2e^{\lambda_2 sL}-d_1 sU_3e^{-\lambda_1 sL}-d_2 sU_4e^{-\lambda_2 sL}\right)\\ &=(M\lambda_1-\alpha d_1)s\left(\lambda_1 sU_1e^{\lambda_1 sL}-\lambda_1 sU_3e^{-\lambda_1 sL}\right)\\ &+(M\lambda_2-\alpha d_2)s\left(\lambda_2 sU_2e^{\lambda_2 sL}-\lambda_2 sU_4e^{-\lambda_2 sL}\right)\end{aligned} \tag{C.15}$$

$$\hat{p}(y=L,s) = P_0 = d_1 s\left(\lambda_1 sU_1e^{\lambda_1 sL}-\lambda_1 sU_3e^{-\lambda_1 sL}\right)+d_2 s\left(\lambda_2 sU_2e^{\lambda_2 sL}-\lambda_2 sU_4e^{-\lambda_2 sL}\right) \tag{C.16}$$

(C.13) $\Leftrightarrow U_1 + U_3 = -(U_2 + U_4)$

(C.13) injected in (C.14) gives $(-\lambda_1^2 + \lambda_2^2)(U_2 + U_4) = 0 \Rightarrow U_4 = -U_2$ and $U_3 = -U_1$

$$(C.15) \Leftrightarrow U_2 = -\frac{(M\lambda_1 - \alpha d_1)}{(M\lambda_2 - \alpha d_2)} U_1 \frac{e^{\lambda_1 sL}}{e^{\lambda_2 sL}} \frac{1 + e^{-2\lambda_1 sL}}{1 + e^{-2\lambda_2 sL}}$$

$$(C.16) \Leftrightarrow U_1 = P_0 \frac{(M\lambda_2 - \alpha d_2)}{Ms(d_1\lambda_2 - d_2\lambda_1)} \frac{e^{-\lambda_1 sL}}{1 + e^{-2\lambda_1 sL}} \Rightarrow U_2 = -P_0 \frac{(M\lambda_1 - \alpha d_1) e^{-\lambda_2 sL}}{Ms(d_1\lambda_2 - d_2\lambda_1)(1 + e^{-2\lambda_2 sL})}$$

Finally, we obtain

$$\begin{aligned}
\hat{u}_y(y,s) &= \frac{P_0}{Ms(d_1\lambda_2 - d_2\lambda_1)} \left[\frac{(M\lambda_2 - \alpha d_2)\left(e^{-\lambda_1 s(L-y)} - e^{-\lambda_1 s(L+y)}\right)}{1 + e^{-2\lambda_1 sL}} \right. \\
&\qquad \left. - \frac{(M\lambda_1 - \alpha d_1)\left(e^{-\lambda_2 s(L-y)} - e^{-\lambda_2 s(L+y)}\right)}{1 + e^{-2\lambda_2 sL}} \right] \\
\hat{p}(y,s) &= \frac{P_0}{M(d_1\lambda_2 - d_2\lambda_1)} \left[\frac{d_1(M\lambda_2 - \alpha d_2)\left(e^{-\lambda_1 s(L-y)} + e^{-\lambda_1 s(L+y)}\right)}{1 + e^{-2\lambda_1 sL}} \right. \\
&\qquad \left. - \frac{d_2(M\lambda_1 - \alpha d_1)\left(e^{-\lambda_2 s(L-y)} + e^{-\lambda_2 s(L+y)}\right)}{1 + e^{-2\lambda_2 sL}} \right]
\end{aligned} \tag{C.17}$$

Hence, for the boundary conditions considered in (3.56), the displacement and pore-pressure fundamental solutions express as

$$\begin{aligned}
\hat{u}_y(y,s) &= \frac{\Sigma_0}{Ms(d_1\lambda_2 - d_2\lambda_1)} \left[\frac{d_2\left(e^{-\lambda_1 s(L-y)} - e^{-\lambda_1 s(L+y)}\right)}{1 + e^{-2\lambda_1 sL}} - \frac{d_1\left(e^{-\lambda_2 s(L-y)} - e^{-\lambda_2 s(L+y)}\right)}{1 + e^{-2\lambda_2 sL}} \right] \\
&\quad + \frac{P_0}{Ms(d_1\lambda_2 - d_2\lambda_1)} \left[\frac{(M\lambda_2 - \alpha d_2)\left(e^{-\lambda_1 s(L-y)} - e^{-\lambda_1 s(L+y)}\right)}{1 + e^{-2\lambda_1 sL}} \right. \\
&\qquad \left. - \frac{(M\lambda_1 - \alpha d_1)\left(e^{-\lambda_2 s(L-y)} - e^{-\lambda_2 s(L+y)}\right)}{1 + e^{-2\lambda_2 sL}} \right] \\
\hat{p}(y,s) &= \frac{\Sigma_0 d_1 d_2}{M(d_1\lambda_2 - d_2\lambda_1)} \left[\frac{\left(e^{-\lambda_1 s(L-y)} + e^{-\lambda_1 s(L+y)}\right)}{1 + e^{-2\lambda_1 sL}} - \frac{\left(e^{-\lambda_2 s(L-y)} + e^{-\lambda_2 s(L+y)}\right)}{1 + e^{-2\lambda_2 sL}} \right] \\
&\quad + \frac{P_0}{M(d_1\lambda_2 - d_2\lambda_1)} \left[\frac{d_1(M\lambda_2 - \alpha d_2)\left(e^{-\lambda_1 s(L-y)} + e^{-\lambda_1 s(L+y)}\right)}{1 + e^{-2\lambda_1 sL}} \right. \\
&\qquad \left. - \frac{d_2(M\lambda_1 - \alpha d_1)\left(e^{-\lambda_2 s(L-y)} + e^{-\lambda_2 s(L+y)}\right)}{1 + e^{-2\lambda_2 sL}} \right]
\end{aligned} \tag{C.18}$$

Now, we detail the calculation of the displacement fundamental solutions of the homogeneous simplified poroelastodynamic equations (3.57a) and (3.57b) with non-homogeneous boundary conditions (3.58), from which we can deduce the pore-pressure at the top of the column (see Equation (3.60)) and verify that there is no fluid flux at the bottom of the column (see Equation (3.61)). (3.57a) is a second order ordinary differential equation on $\hat{u}_z$, its characteristic equation is given by

$$\left(M + \alpha^2 \frac{R}{\phi^2}\right) \lambda^2 - \rho = 0 \tag{C.19}$$

yielding

$$\lambda_1 = -\lambda_2 = \sqrt{\frac{\rho}{M + \alpha^2 R/\phi^2}}$$

this leads to the complete solution of the homogeneous problem

$$\hat{G}_z^u(z,s) = \sum_{i=1}^{2} U_i e^{\lambda_i s z}$$

We apply the boundary conditions:

$$\hat{u}_y(y=0,s) = 0 = U_1 + U_2 \;\Rightarrow\; U_1 = -U_2 \tag{C.20}$$

$$\begin{aligned}\hat{\sigma}_y(y=L,s) &= -\Sigma_0 = M\hat{u}_{y,y}(y=L,s) - \alpha\hat{p}(y=L,s) = (M + \alpha^2 R/\phi^2)\hat{u}_{y,y}(y=L,s) \\ &= \left(M + \alpha^2 \frac{R}{\phi^2}\right)\lambda_1 s U_1 \left(e^{\lambda_1 s L} + e^{-\lambda_1 s L}\right) \\ \Rightarrow U_1 &= -\frac{\Sigma_0}{s\lambda_1\left(M + \alpha^2 R/\Phi^2\right)}\frac{e^{-\lambda_1 s L}}{1 + e^{-2\lambda_1 s L}} = -U_2\end{aligned} \tag{C.21}$$

Finally we obtain the solutions

$$\begin{aligned}\hat{u}_y(y,s) &= \frac{-\Sigma_0}{s\lambda_1\left(M + \alpha^2 R/\Phi^2\right)}\frac{e^{-\lambda_1 s(L-y)} - e^{-\lambda_1 s(L+y)}}{1 + e^{-2\lambda_1 s L}} \\ \hat{p}(y,s) &= -\alpha\frac{R}{\Phi^2}\hat{u}_{y,y}(y,s) = \frac{\alpha\Sigma_0 R/\Phi^2}{\left(M + \alpha^2 R/\Phi^2\right)}\frac{e^{-\lambda_1 s(L-y)} + e^{-\lambda_1 s(L+y)}}{1 + e^{-2\lambda_1 s L}} \\ &= P_0^* \frac{e^{-\lambda_1 s(L-y)} + e^{-\lambda_1 s(L+y)}}{1 + e^{-2\lambda_1 s L}}\end{aligned} \tag{C.22}$$

D

Extended abstract in French

1 Motivations

Le 11 mars 2011, un séisme sous-marin d'une magnitude de 9.1 s'est produit dans l'océan Pacifique, à 72 km à l'est de la péninsule d'Oshika, dans la région de Tohoku. La fosse du Japon s'est déplacée de 60 m à la suite du séisme, la Terre a été déplacée sur son axe de sorte que le jour a été raccourci de 1.8 microseconde, et le tremblement de terre a déclenché un tsunami qui a provoqué la catastrophe nucléaire de Fukushima Daiichi. Le 6 février 2023, un tremblement de Terre de magnitude 7.8 a frappé le sud et le centre de la Turquie, ainsi que le nord et l'ouest de la Syrie. Il a rompu environ 370 km de la faille anatolienne orientale, produisant un glissement maximal de 9 m dans la croûte terrestre. Ce qui est intéressant, c'est que les ondes sismiques détectées dans le monde entier et responsables de graves dégâts humains et infrastructurels ne représentent qu'une petite partie de l'énergie libérée lors d'un événement sismique. En fait, la majeure partie de l'énergie est dissipée par la friction (Kanamori & Brodsky, 2004; Kanamori & Rivera, 2006). Par conséquent, les mécanismes à l'origine de la friction sont toujours étudiés pour comprendre la nucléation, l'évolution et l'arrêt des événements sismiques. Une attention particulière est accordée au comportement de friction cyclique apparent des failles (Bakun & Lindh, 1985).

Les tremblements de Terre sont généralement considérés comme des catastrophes naturelles, mais ils peuvent également être induits par l'activité humaine. Le 12 septembre 2016 et le 15 novembre 2017, deux tremblements de Terre de magnitude 5.5 ont frappé la Corée du Sud (respectivement à Gyeongju et à Pohang) sur une importante faille latérale droite, la faille de Yangsan, et à proximité d'un site de géothermie (Enhanced Geothermal Systems, EGS). Sur ce site EGS, entre début 2016 et septembre 2017, plusieurs milliers de mètres cubes d'eau ont été injectés sous pression dans des puits atteignant environ 4 km de profondeur, ce qui suggère que l'activité EGS a induit les deux tremblements de Terre. Le 12 novembre 2019, l'entreprise de géothermie Georhin est susceptible d'avoir provoqué un séisme de magnitude 3,1 au nord de Strasbourg. Les activités industrielles respectueuses de l'environnement, telles que les projets de géothermie profonde et la séquestration du CO2, nécessitent l'injection de grandes quantités de fluides dans la croûte terrestre. Les expériences actuelles montrent que des tremblements de Terre de magnitude modérée à importante peuvent être induits/déclenchés, ce qui met en péril la viabilité de ces projets

prometteurs pour l'environnement.

Nous ne sommes toujours pas en mesure de prédire les tremblements de Terre naturels et induits par l'activité humaine. Cependant, sur la base du concept établi selon lequel le glissement des failles peut être stimulé par l'injection de fluide dans la croûte terrestre, une nouvelle question d'actualité dans la communauté est de montrer que l'instabilité des tremblements de Terre pourrait être atténuée par un contrôle actif de la pression du fluide. Une telle étude est menée dans le cadre du projet CoQuake (Controlling earthQuakes, www.coquake.eu) du Conseil européen de la recherche. Ce projet propose d'éviter les instabilités sismiques en les provoquant à un niveau énergétique inférieur, réduisant ainsi le risque sismique et son coût humain et économique. Ces points et le fait que la nucléation des tremblements de Terre naturels et induits reposent sur des principes physiques similaires justifient le développement d'outils numériques efficaces à grande échelle pour simuler l'instabilité sismique.

Dans ce travail, nous nous concentrons sur le développement de simulations efficaces et précises des effets du fluide dans la rupture dynamique des failles, lorsque le fluide est injecté à une distance donnée de la faille. Cet objectif peut être décomposé en deux tâches principales :

- Une étude comparative approfondie des outils numériques existants pour les cycles sismiques afin de déterminer l'approche la plus prometteuse pour une description précise de la rupture dynamique des failles ;
- Proposition de modèles simplifiés destinés à l'étude des effets de l'injection de fluide dans la rupture de faille dynamique.

Les outils numériques développés constituent des éléments de base pour aider la communauté à développer des simulations de plus en plus réalistes (incorporant des géométries de faille réalistes en 3D et des couplages multi-physiques), afin de comprendre et d'atténuer les instabilités des tremblements de Terre.

2 Approche scientifique

Ce travail vise à modéliser les effets de l'injection de fluide sur la rupture dynamique de faille, c'est-à-dire le glissement sismique à l'interface. Pour atteindre cet objectif, la première étape consiste à modéliser l'instabilité sismique. Une rupture dynamique de faille est l'une des trois étapes principales d'un cycle sismique, qui prend en compte la lente accumulation de la contrainte de cisaillement au niveau de la faille jusqu'à la nucléation d'un glissement sismique, et son arrêt suivi par l'accommodation de la croûte terrestre à un nouvel état d'équilibre. Par conséquent, nous proposons tout d'abord de modéliser et de simuler un problème de cycle sismique afin de décrire avec précision le mouvement sismique depuis son initiation jusqu'à son arrêt.

Une partie importante de cette thèse est consacrée au développement d'outils numériques efficaces, issus de l'état de l'art, afin de simuler des cycles sismiques, avant d'incorporer les effets de l'injection de fluide sur le glissement des failles. Nous utilisons la méthode des éléments de frontière (BEM), connue pour son efficacité dans la résolution de problèmes

élastodynamiques dans des domaines non bornés à grande échelle (Chaillat et al., 2017; Kpadonou et al., 2020), et de problèmes de cycles sismiques (Ando (2016), Luo et al. (2017), Barbot (2021), and Ozawa et al. (2022) parmi d'autres). Pour cette classe de problèmes, la BEM présente de nombreux avantages par rapport aux méthodes volumiques telles que la méthode des Différences Finies (FD) ou la Méthode des Éléments Finis (FEM) : réduction d'une dimension du domaine de calcul, très bonne précision et pas de troncature artificielle du domaine de calcul grâce à une formulation exacte de la condition de rayonnement à l'infini. De plus, le développement récent des BEM rapides, tels que les BEM accélérés par multipôles rapides ou les BEM basés sur des matrices hiérarchiques, permet de réaliser des simulations compétitives avec un coût de calcul très faible. La méthode est maintenant suffisamment mature pour traiter des géométries complexes et des configurations réalistes Chaillat et al. (2012), mais pour une physique unique. Une approche progressive est adoptée dans ce travail, en considérant des problèmes simplifiés avant qu'un cas plus complexe à grande échelle puisse être considéré avec les outils numériques développés. Étant donné que les tremblements de Terre naturels et induits par l'injection de fluide suivent des principes physiques similaires en ce qui concerne leur nucléation, un point de départ est de se concentrer d'abord sur un cas "sec" sans injection de fluide.

Cette thèse se concentre sur la vérification et la comparaison de différentes méthodes d'intégration temporelle incorporant des BEMs rapides, qui sont couramment utilisées dans la communauté des cycles sismiques, et sur leur sensibilité par rapport à leurs paramètres. Les exercices de vérification de codes sont encore largement discutés, comme le détaillent Erickson et al. (2020a, 2023). Dans le but de proposer une méthode de vérification applicable quelque soit le solveur employé, la simulation d'un mouvement asismique est distinguée de la simulation d'un cycle sismique. Une solution analytique est proposée pour vérifier la simulation d'un glissement asismique, et une procédure pour comparer les résultats des cycles sismiques aux résultats de référence est détaillée.

Un autre défi consiste à étendre les capacités des outils numériques développés pour intégrer les effets de l'injection de fluide dans le glissement de faille. Dans cette thèse, on s'intéresse principalement aux effets d'injection de fluide à l'échelle de temps spécifique d'un mouvement sismique, ce qui n'a pas été pris en compte dans la littérature. Nous supposons également que le fluide est injecté dans la croûte terrestre à une distance donnée de la faille. Le cadre poroélastodynamique est choisi pour intégrer les couplages hydromécaniques. Cependant, un modèle poroélastodynamique complet nécessiterait des coûts de calcul ou des approximations non négligeables. Ainsi, une réduction du modèle complet est nécessaire pour fournir un modèle efficace qui serait plus facile à intégrer dans le cadre numérique proposé, et qui prendrait en compte avec précision les effets du fluide prédominants à l'échelle de temps d'un mouvement sismique ou asismique. Une analyse dimensionnelle permet des simplifications rigoureuses du modèle complet. Une illustration numérique des résultats obtenus est cruciale avant d'effectuer un test multi-physique utilisant les BEM rapides pour résoudre un problème de rupture de faille dynamique avec injection de fluide à l'échelle de temps d'un glissement sismique.

3 Organisation de la thèse

Cette thèse est organisée en trois chapitres. Le chapitre 1 introduit les notions d'instabilité sismique et de cycle sismique, en abordant à la fois le glissement sec et le glissement induit par le fluide dans les systèmes de failles frictionnelles. Ce chapitre permet de situer ce travail dans le contexte de la littérature existante, justifie la méthodologie de recherche et propose une revue des notions et des outils (existants) utilisés dans la suite. Les chapitres 2 et 3 sont consacrés aux principales contributions de ce travail :

- la proposition d'une méthode de comparaison des méthodes de simulation des cycles sismiques et le développement d'un solveur 2D incluant les différentes méthodes d'intégration temporelle et spatiale comparées.
- la determination des outils numériques les plus performants pour incorporer les effets de l'injection de fluide à l'échelle de temps d'un mouvement sismique dans les simulations.
- la justification rigoureuse de la modélisation des effets de l'injection de fluide à distance d'une faille sur son comportement en frottement.

4 Principaux résultats et conclusions

Le chapitre 1 résume la littérature disponible sur les ruptures dynamique de faille et donne une approche pédagogique des concepts utilisés dans cette thèse. La nucléation d'une rupture dynamique de faille et son arrêt font partie du processus de cycle sismique qui est défini à l'aide d'une approche cinématique (modèle d'ordre réduit de type patin-ressort, voir section 1.2). Une analyse de stabilité linéaire est effectuée à la section 1.3 pour (re)dériver la condition d'instabilité lorsqu'une loi de frottement dépendante en vitesse et en variable d'état est considérée sans injection de fluide (respectivement avec injection de fluide à la section 1.4). Après avoir souligné les limites d'un modèle d'ordre réduit pour modéliser les problèmes de cycles sismiques dans la section 1.5, la section 2 présente les ingrédients nécessaires pour modéliser un problème générique de cycle sismique. Nous accordons une attention particulière à l'incorporation des couplages hydromécaniques dans l'énoncé du problème à la section 4. Ce point clé est étudié au chapitre 3. En particulier, nous justifions l'utilisation des équations poroélastodynamiques pour prendre en compte les effets du fluide, et nous détaillons leur impact dans la condition d'interface et l'équation de mouvement. La section 3 fournit une large revue de la littérature sur les méthodes numériques existantes dans l'espace et le temps pour simuler les cycles sismiques. Nous insistons sur les avantages de la méthode des éléments de frontière rapide basée sur les matrices hiérarchiques (H-BEM) pour résoudre les problèmes de cycles sismiques pour les failles planes ainsi que pour les failles de géométries complexes. Un solveur basé sur les éléments de frontière pour les problèmes de cycles sismiques est développé à partir de zéro dans le chapitre suivant. En outre, nous attirons l'attention sur la difficulté de la vérification et de la comparaison des codes pour les simulations de cycles sismiques, ce qui définit le contexte de notre contribution au chapitre 2.

Le chapitre 2 présente une partie importante de notre contribution. Disposer d'outils numériques précis et efficaces est essentiel pour simuler les problèmes de cycles sismiques avant d'incorporer les effets du fluide sur le glissement des failles. Une partie importante de ce travail est consacrée à la vérification des simulations de cycles sismiques pour des cas standard de failles planes bidimensionnelles en quasi-dynamiques et chargées en mode II et III. Pour ce faire, nous avons développé à partir de zéro un solveur 2D basé sur la méthode des éléments de frontière pour les problèmes de cycles sismiques. Ce solveur intègre la méthode des éléments de frontière standard (BEM), la méthode des éléments de frontière rapide basée sur des matrices hiérarchiques (H-BEM) et la méthode des éléments de frontière spectrale (S-BEM) pour résoudre le problème dans l'espace. Trois méthodes d'intégration temporelle sont mises en œuvre : une méthode de prédiction-correction explicite-implicite inspirée de Lapusta et al. (2000), une méthode explicite de Runge-Kutta (RK45) à l'ordre quatre et cinq inspirée de Ozawa et al. (2022), et une méthode hybride prédiction-correction - RK45 inspirée de Romanet and Ozawa (2021). La formulation du problème pour les configurations simplifiées en modes II et III utilisant la méthode des équations intégrales de frntière (BIEM) est détaillée dans la section 1. Les méthodes de discrétisation spatiale et temporelle mises en œuvre sont détaillées dans les sections 2 et Section 3 respectivement. Une partie importante de ce chapitre concerne l'étude de la convergence et de la sensibilité des résultats de simulation de cycles sismiques par rapport aux paramètres de discrétisation spatiale et temporelle dans la section Section 4.2. Une telle étude de sensibilité n'a pas été proposée dans la littérature. Cet examen approfondi des méthodes les plus utilisées représente une contribution prometteuse pour aider la communauté des cycles sismiques à développer un code commun. Dans la section 4.3, nous comparons les méthodes de discrétisation spatiale mises en œuvre. Nous nous concentrons d'abord sur un calcul de la contrainte de cisaillement à l'interface de la faille en utilisant l'équation intégrale de frontière en traction (BIE) dérivée précédemment dans la section 1. Comme attendu, nous montrons que la convergence du calcul de la contrainte de cisaillement sur la faille ne dépend que du choix du pas d'espace pour la BEM standard et la H-BEM, alors qu'elle dépend à la fois du choix du pas d'espace et de la taille du domaine discrétisé pour la S-BEM. Nous insistons sur la comparaison des performances de BEM, H-BEM et S-BEM, qui montre les avantages de la H-BEM par rapport à la BEM standard dans le cas de problèmes de grande taille. Afin de fournir des résultats précis, nous étudions l'effet couplé du pas d'espace et du pas de temps pour éviter les artefacts numériques qui pourraient être confondus avec des instabilités sismiques, conduisant à des résultats non interprétables. La section 4.4 étudie la sensibilité du calcul des inconnues d'interface δ, V, τ, et θ par rapport aux paramètres de discrétisation temporelle pour les différentes méthodes d'intégration temporelle implémentées, en utilisant la H-BEM. Nous distinguons les phases asismiques pour lesquelles nous sommes en mesure de fournir une solution analytique des phases sismiques. Pour ces dernières, nous proposons une stratégie de comparaison de nos résultats avec des résultats de référence fournis par Pierre Romanet (communication personnelle) car les solutions analytiques pour les simulations de glissement sismique sont inconnues. Nous montrons d'abord les résultats de convergence dans le cas d'une simulation asismique en utilisant la solution analytique proposée comme référence. Ensuite, nous comparons les résultats des cycles sismiques aux résultats fournis par Pierre Romanet. En particulier, nous comparons le temps auquel le taux de glissement

dépasse pour la première fois 1 m/s pour chaque événement sismique, et nous montrons qu'une petite perturbation de l'initialisation conduit à des erreurs qui se cumulent à chaque nouvel événement sismique. En effet, nous n'utilisons pas la même méthode de maillage de la faille que Pierre Romanet, ce qui implique ce petit écart à l'initialisation. Enfin, cette étude nous permet d'évaluer nos outils numériques sur un benchmark standard en mode III et de comparer nos résultats à ceux obtenus par Junle Jiang (membre du projet SEAS, voir Erickson et al. (2020a)) dans la section 5. Les résultats précédents nous ont fait prendre conscience que le décalage temporel accumulé pouvait s'expliquer par une différence dans l'initialisation et/ou une différence dans les paramètres qui échelonnent la discrétisation temporelle. De tels résultats pourraient améliorer la stratégie actuellement proposée dans le projet SEAS pour la procédure de vérification du code, et pourraient aider à développer un code commun pour les simulations de cycles sismiques.

A présent que nous avons mis en œuvre des outils numériques précis pour les simulations de cycles sismiques, le chapitre 3 se concentre sur la modélisation des effets de l'injection de fluide sur le glissement des failles. L'originalité de ce travail est de se concentrer sur le cas où le fluide est injecté à une distance donnée de la faille et sur les effets du fluide à l'échelle de temps d'un mouvement sismique. Il s'agit d'une étape essentielle pour intégrer les couplages hydromécaniques appropriés dans le solveur basé sur les éléments de frontière. Après avoir étendu le problème bidimensionnel "sec" en modes II et III du chapitre 2 à un cas avec injection de fluide dans la section 1, nous mettons l'accent sur les difficultés numériques inhérentes à l'utilisation du modèle poroélastodynamique complet pour incorporer les couplages hydromécaniques dans la section 2. En outre, dans la section 3, nous évaluons les travaux existants sur les effets du fluide sur le glissement des failles qui mettent en évidence l'utilisation d'équations poroélastodynamiques simplifiées. Néanmoins, ces modèles simplifiés ne sont pas nécessairement adaptés à la configuration que nous considérons. Nous proposons un modèle simplifié permettant de prendre en compte les effets du fluide sur le glissement des failles à l'échelle de temps d'un mouvement sismique. Par conséquent, nous effectuons une analyse dimensionnelle des équations poroélastodynamiques dans la section 4 afin d'évaluer formellement les effets prédominants du fluide à l'échelle de temps d'un mouvement sismique ou asismique. Nous montrons qu'à l'échelle de temps d'une instabilité sismique, nous pouvons négliger le mouvement relatif du fluide par rapport à la matrice solide, et nous obtenons un modèle non drainé. Inversement, à l'échelle de temps d'un mouvement asismique, les effets d'inertie pour le solide et pour le fluide peuvent être négligés, ce qui conduit à des équations de consolidation. Nous déduisons également une condition sur le temps caractéristique d'injection du fluide afin qu'un terme source d'injection de fluide puisse être maintenu dans le modèle simplifié à l'échelle de temps d'un mouvement sismique. Ces développements nous permettent donc de déduire les équations poroélastodynamiques simplifiées d'intérêt à l'échelle de temps d'un mouvement sismique et d'évaluer le domaine de validité des modèles utilisés dans la littérature. Les résultats de l'analyse dimensionnelle sont résumés à la section 4.4. Enfin, dans la section 5, nous considérons un problème poroélastodynamique 1D simplifié pour illustrer le domaine de validité du modèle simplifié obtenu à l'échelle de temps d'un mouvement sismique.

5 Principaux développements numériques

Afin de choisir les outils numériques les plus appropriés pour simuler les effets de l'injection de fluide sur la rupture dynamique des failles, j'ai implementé un code pour la simulation de cycles sismiques à partir de zéro. Cela m'a permis d'implémenter et de comparer différentes méthodes numériques en espace et en temps au sein d'un seul et même code. Il s'agissait également d'un nouveau sujet dans mes laboratoires d'accueil. Par souci de clarté, je résume ici tous les développements numériques de cette thèse. Des développements numériques importants ont été réalisés pour évaluer les capacités de différents outils numériques incorporant les BEM rapides pour résoudre des problèmes de cycles sismiques ainsi que de rupture dynamique de faille avant d'incorporer des couplages hydromécaniques. J'ai développé un solveur 2D basé sur la méthode des éléments de frontière pour les problèmes de cycles sismiques afin d'obtenir les résultats présentés dans le chapitre 2. L'implémentation est faite sous Python et Matlab, et résout des problèmes 2D en quasi-dynamique de cycles sismiques et de rupture dynamique de faille pour une faille plane :

- Des configurations en mode III et en mode II (avec une condition de non-ouverture sur la faille) avec ou sans surface libre peuvent être considérés dans le cas d'une faille régie par une loi de frottement dépendante en vitesse et en variable d'état complétée par une loi d'évolution jusqu'à une profondeur donnée. En dehors de cette zone, une vitesse de glissement est imposée ;

- Des problèmes en mode III, dans le cas d'une faille régie par une loi de frottement dépendante en vitesse et en variable d'état complétée par différentes lois d'évolution, et soumise à des perturbations de la contrainte normale effective dues à l'injection de fluide et à la diffusion de fluide interstitiel le long de la faille, peuvent également être pris en compte.

Plus précisément, les principales contributions au développement du solveur sont les suivantes :

- Les BEM et H-BEM en 2D ont été implémentés à partir de zéro sur Matlab. La matrice BEM est obtenue en discrétisant l'équation intégrale de frontière reliant la contrainte de cisaillement quasi-statique τ^{qs} au glissement δ est d'abord calculée (une fois pour toutes avant la résolution lorsque la géométrie est fixe).

- La BEM spectrale en 2D a également été implémenté à partir de zéro sur Python. Elle permet de calculer efficacement la contrainte de cisaillement quasi-statique τ^{qs} (respectivement sa dérivée temporelle) en calculant l'équation intégrale de frontière reliant τ^{qs} au glissement δ comme un simple produit dans le domaine de Fourier en espace. Cette méthode s'est révelée être très utile pour les études comparatives que j'ai menées, car elle est largement utilisée dans la communauté des cycles sismiques.

- Trois méthodes d'intégration temporelle (les algorithmes correspondants sont présentés à la section 3.1) ont également été implémentées à partir de zéro :

- une méthode de prédiction-correction explicite-implicite inspirée de Lapusta et al. (2000)
- une méthode explicite de Runge-Kutta (RK45) à l'ordre quatre et cinq inspirée de Ozawa et al. (2022)
- une méthode hybride prédiction-correction - RK45 inspirée de Romanet and Ozawa (2021)

Nous avons également mis en œuvre une routine CQM en Python à partir de zéro pour obtenir les résultats présentés au chapitre 3. Bien que l'efficacité des codes mentionnés puisse être améliorée de nombreuses façons, nous avons développé un code prototype complet pour résoudre les problèmes 2D de cycles sismiques en quasi-dynamique pour les failles planes. Il permet de comparer les outils numériques couramment utilisés dans la communauté des cycles sismiques. En particulier, une nouvelle méthode d'intégration temporelle ou de discrétisation spatiale peut facilement être ajoutée au code, ce qui est prometteur pour une utilisation future comme le développement d'un code commun pour les simulations de cycles sismiques. Une routine spécifique et plusieurs scripts bash ont été proposés pour mener efficacement chaque étude de convergence et de sensibilité, et la même structure est utilisée pour stocker les résultats afin de faciliter l'étape de post-traitement. Les codes développés contiennent 11469 lignes pour les codes sources, et 5243 lignes pour les codes de post-traitement. Un dépôt public sur Git sera bientôt mis en place pour mettre ces développements à la disposition de la communauté scientifique. Nous allons également bientôt fournir nos résultats sur les benchmarks SEAS au groupe SCEC afin de participer à l'effort du projet SEAS.

Bibliography

Abdelmeguid, M., Ma, X., & Elbanna, A. (2019). A novel hybrid finite element-spectral boundary integral scheme for modeling earthquake cycles: Application to rate and state faults with low-velocity zones. *Journal of Geophysical Research: Solid Earth*, *124*(12), 12854–12881. https://doi.org/10.1029/2019JB018036 (cit. on pp. 31, 32, 155)

Abhyankar, S., Brown, J., Constantinescu, E. M., Ghosh, D., Smith, B. F., & Zhang, H. (2018). PETSc/TS: A modern scalable ODE/DAE solver library. https://doi.org/10.48550/arXiv.1806.01437. (Cit. on pp. 29, 155)

Aki, K., & Richards, P. G. (2002). *Quantitative seismology* (Vol. 1). (Cit. on p. 46).

Aldam, M., Weikamp, M., Spatschek, R., Brener, E. A., & Bouchbinder, E. (2017). Critical nucleation length for accelerating frictional slip. *Geophysical Research Letters*, *44*(22), 11, 390–11, 398. https://doi.org/10.1002/2017GL074939 (cit. on p. 18)

Allison, K. L., & Dunham, E. M. (2018). Earthquake cycle simulations with rate-and-state friction and power-law viscoelasticity. *Tectonophysics*, *733*, 232–256. https://doi.org/10.1016/j.tecto.2017.10.021 (cit. on pp. 20, 29, 32, 155)

Almquist, M., & Dunham, E. M. (2021). Elastic wave propagation in anisotropic solids using energy-stable finite differences with weakly enforced boundary and interface conditions. *Journal of Computational Physics*, *424*, 109842. https://doi.org/10.1016/j.jcp.2020.109842 (cit. on pp. 28, 29, 155)

Ampuero, J. P., Vilotte, J.-P., & Sánchez-Sesma, F. (2002). Nucleation of rupture under slip dependent friction law: Simple models of fault zone. *Journal of Geophysical Research: Solid Earth, 107*, 2324. https://doi.org/10.1029/2001JB000452 (cit. on p. 27)

Ando, R. (2016). Fast domain partitioning method for dynamic boundary integral equations applicable to non-planar faults dipping in 3-d elastic half-space. *Geophysical Journal International*, *207*(2), 833–847. https://doi.org/10.1093/gji/ggw299 (cit. on pp. 2, 148, 171)

Andrews, D. J. (1976). Rupture velocity of plane strain shear cracks. *Journal of Geophysical Research (1896-1977)*, *81*(32), 5679–5687. https://doi.org/10.1029/JB081i032p05679 (cit. on pp. 24, 44)

Andrews, D. J. (1999). Test of two methods for faulting in finite-difference calculations. *Bulletin of the Seismological Society of America*, *89*(4), 931–937. https://doi.org/10.1785/BSSA0890040931 (cit. on p. 30)

Andrews, D. J. (2005). Rupture dynamics with energy loss outside the slip zone. *Journal of Geophysical Research: Solid Earth, 110*. https://doi.org/10.1029/2004JB003191 (cit. on p. 21)

Aochi, H., Fukuyama, E., & Matsu'ura, M. (2000). Spontaneous rupture propagation on a non-planar fault in 3-d elastic medium. *pure and applied geophysics, 157*(11), 2003–2027. https://doi.org/10.1007/PL00001072 (cit. on p. 19)

Aochi, H., & Fukuyama, E. (2002). Three-dimensional nonplanar simulation of the 1992 landers earthquake. *Journal of Geophysical Research: Solid Earth, 107*, ESE 4–1–ESE 4–12. https://doi.org/10.1029/2000JB000061 (cit. on p. 19)

Arévalo, C., Söderlind, G., Hadjimichael, Y., & Fekete, I. (2021). Local error estimation and step size control in adaptive linear multistep methods. *Numerical Algorithms, 86*(2), 537–563. https://doi.org/10.1007/s11075-020-00900-1 (cit. on p. 147)

Bagur, L., Chaillat, S., & Ciarlet, P. (2022). Improvement of hierarchical matrices for 3d elastodynamic problems with a complex wavenumber. *Advances in Computational Mathematics, 48*(2), 9. https://doi.org/10.1007/s10444-021-09921-3 (cit. on p. 63)

Bakun, W. H., & Lindh, A. G. (1985). The parkfield, california, earthquake prediction experiment. *Science, 229*(4714), 619–624. https://doi.org/10.1126/science.229.4714.619 (cit. on pp. 1, 8, 169)

Barall, M., & Harris, R. A. (2014). Metrics for comparing dynamic earthquake rupture simulations. *Seismological Research Letters, 86*(1), 223–235. https://doi.org/10.1785/0220140122 (cit. on p. 34)

Barbot, S. (2019). Slow-slip, slow earthquakes, period-two cycles, full and partial ruptures, and deterministic chaos in a single asperity fault. *Tectonophysics, 768*, 228171. https://doi.org/10.1016/j.tecto.2019.228171 (cit. on pp. 19, 31, 32, 57, 58, 62, 155)

Barbot, S. (2021). A spectral boundary-integral method for quasi-dynamic ruptures of multiple parallel faults. *Bulletin of the Seismological Society of America, 111*(3), 1614–1630. https://doi.org/10.1785/0120210004 (cit. on pp. 2, 19, 31, 32, 62, 155, 171)

Barras, F., Aldam, M., Roch, T., Brener, E. A., Bouchbinder, E., & Molinari, J.-F. (2019). Emergence of cracklike behavior of frictional rupture: The origin of stress drops. *Physical Review X, 9*(4), 041043. https://doi.org/10.1103/PhysRevX.9.041043 (cit. on p. 13)

Bebendorf, M. (Ed.)**. (2008)**. Hierarchical matrices. In *Hierarchical matrices: A means to efficiently solve elliptic boundary value problems* (Springer, pp. 49–98). Springer. https://doi.org/10.1007/978-3-540-77147-0_3. (Cit. on p. 63)

Beguin, P., & Yastrebov, V. A. (2023). Electrical and thermal conductivity of complex-shaped contact spots. https://doi.org/10.48550/arXiv.2311.14854. (Cit. on p. 63)

Bender, C. M., & Orszag, S. A. (2013). *Advanced mathematical methods for scientists and engineers i: Asymptotic methods and perturbation theory*. Springer Science & Business Media. (Cit. on p. 110).

Bhat, H., Almakari, M., Kheirdast, N., Villafuerte, C., & Thomas, M. (2023). *Fault zone complexity naturally produces the full slip spectrum: Insights from numerical models* (EGU23-16290). Copernicus Meetings. https://doi.org/10.5194/egusphere-egu23-16290. (Cit. on p. 18)

Bhat, H. S., Dmowska, R., Rice, J. R., & Kame, N. (2004). Dynamic slip transfer from the denali to totschunda faults, alaska: Testing theory for fault branching. *Bulletin of the Seismological Society of America, 94*(6), S202–S213. https://doi.org/10.1785/0120040601 (cit. on p. 19)

Bhat, H. S., Olives, M., Dmowska, R., & Rice, J. R. (2007). Role of fault branches in earthquake rupture dynamics. *Journal of Geophysical Research: Solid Earth, 112*. https://doi.org/10.1029/2007JB005027 (cit. on p. 19)

Bhattacharya, P., & Viesca, R. C. (2019). Fluid-induced aseismic fault slip outpaces pore-fluid migration. *Science, 364*(6439), 464–468. https://doi.org/10.1126/science.aaw7354 (cit. on pp. 40, 105)

Biot, M. A. (1956a). Theory of deformation of a porous viscoelastic anisotropic solid. *Journal of Applied Physics, 27*(5), 459–467. https://doi.org/10.1063/1.1722402 (cit. on p. 37)

Biot, M. A. (1956b). Theory of propagation of elastic waves in a fluid-saturated porous solid. II. higher frequency range. *The Journal of the Acoustical Society of America, 28*(2), 179–191. https://doi.org/10.1121/1.1908241 (cit. on p. 37)

Biot, M. A. (1941). General theory of three-dimensional consolidation. *Journal of Applied Physics, 12*(2), 155–164. https://doi.org/10.1063/1.1712886 (cit. on pp. 37, 112)

Bizzarri, A., & Bhat, H. S. (2012). *The mechanics of faulting: From laboratory to earthquakes*. Researhc Signpost. (Cit. on pp. 8, 30).

Blanc, E. (2013). *Time-domain numerical modeling of poroelastic waves: The biot-JKD model with fractional derivatives* (Doctoral dissertation). Aix-Marseille Université. (Cit. on p. 37).

Bonnet, M. (1999). *Boundary integral equations methods in solids and fluids*. John Wiley; sons. (Cit. on pp. 30, 46, 48–50, 53, 59).

Booker, J. R. (1974). Time dependent strain following faulting of a porous medium. *Journal of Geophysical Research (1896-1977), 79*(14), 2037–2044. https://doi.org/10.1029/JB079i014p02037 (cit. on p. 34)

Bouchon, M., & Streiff, D. (1997). Propagation of a shear crack on a nonplanar fault: A method of calculation. *Bulletin of the Seismological Society of America, 87*(1), 61–66. https://doi.org/10.1785/BSSA0870010061 (cit. on p. 19)

Bradley, A. M. (2014). Software for efficient static dislocation-traction calculations in fault simulators. *Seismological Research Letters, 85*(6), 1358–1365. https://doi.org/10.1785/0220140092 (cit. on pp. 63, 67, 155)

Burridge, R., & Knopoff, L. (1967). Model and theoretical seismicity. *Bulletin of the Seismological Society of America, 57*(3), 341–371. https://doi.org/10.1785/BSSA0570030341 (cit. on pp. 17, 24)

Cambonie, T., Klinger, Y., & Lazarus, V. (2018). Similarities between mode III crack growth patterns and strike-slip faults. *Philosophical Transactions of the Royal Society A: Mathematical, Physical and Engineering Sciences, 377*(2136), 20170392. https://doi.org/10.1098/rsta.2017.0392 (cit. on p. 44)

Cappa, F., Scuderi, M. M., Collettini, C., Guglielmi, Y., & Avouac, J.-P. (2019). Stabilization of fault slip by fluid injection in the laboratory and in situ. *Science Advances, 5*(3), eaau4065. https://doi.org/10.1126/sciadv.aau4065 (cit. on pp. 36, 105)

Carcione, J. M. (2007). *Wave fields in real media: Wave propagation in anisotropic, anelastic, porous and electromagnetic media*. Elsevier. (Cit. on p. 37).

Carlson, J. M., & Langer, J. S. (1989). Mechanical model of an earthquake fault. *Physical Review A, 40*(11), 6470–6484. https://doi.org/10.1103/PhysRevA.40.6470 (cit. on p. 17)

Chaillat, S., Semblat, J. F., & Bonnet, M. (2012). A preconditioned 3-d multi-region fast multipole solver for seismic wave propagation in complex geometries. *Communications in Computational Physics, 11*(2), 594–609. https://doi.org/10.4208/cicp.231209.030111s (cit. on pp. 2, 171)

Chaillat, S., & Bonnet, M. (2013). Recent advances on the fast multipole accelerated boundary element method for 3d time-harmonic elastodynamics. *Wave Motion, 50*(7), 1090–1104 (cit. on p. 31).

Chaillat, S., Bonnet, M., & Semblat, J.-F. (2008). A multi-level fast multipole BEM for 3-d elastodynamics in the frequency domain. *Computer Methods in Applied Mechanics and Engineering, 197*(49), 4233–4249. https://doi.org/10.1016/j.cma.2008.04.024 (cit. on p. 31)

Chaillat, S., Desiderio, L., & Ciarlet, P. (2017). Theory and implementation of h-matrix based iterative and direct solvers for helmholtz and elastodynamic oscillatory kernels. *Journal of Computational Physics, 351*, 165–186. https://doi.org/10.1016/j.jcp.2017.09.013 (cit. on pp. 2, 31, 63, 66, 171)

Chen, J. (1994a). Time domain fundamental solution to biot's complete equations of dynamic poroelasticity part II: Three-dimensional solution. *International Journal of Solids and Structures, 31*(2), 169–202. https://doi.org/10.1016/0020-7683(94)90049-3 (cit. on pp. 39, 104)

Chen, J. (1994b). Time domain fundamental solution to biot's complete equations of dynamic poroelasticity. part i: Two-dimensional solution. *International Journal of Solids and*

Structures, 31(10), 1447–1490. https://doi.org/10.1016/0020-7683(94)90186-4 (cit. on pp. 39, 104)

Cheng, A.-D., & Detournay, E. (1998). On singular integral equations and fundamental solutions of poroelasticity. *International Journal of Solids and Structures, 35*(34), 4521–4555. https://doi.org/10.1016/S0020-7683(98)00082-1 (cit. on p. 104)

Cheng, A. (2016). *Poroelasticity* (Vol. 27). https://doi.org/10.1007/978-3-319-25202-5. (Cit. on pp. 38, 112)

Cheng, J., Almakari, M., Peruzzo, C., Lecampion, B., & Bhat, H. (2023). *3d quasidynamic cycles accelerated using hierarchical matrices: Role of complex fault geometry* (EGU23-7807). Copernicus Meetings. https://doi.org/10.5194/egusphere-egu23-7807. (Cit. on pp. 18, 31)

Ciardo, F., & Lecampion, B. (2019). Effect of dilatancy on the transition from aseismic to seismic slip due to fluid injection in a fault. *Journal of Geophysical Research: Solid Earth, 124*(4), 3724–3743. https://doi.org/10.1029/2018JB016636 (cit. on p. 106)

Cochard, A., & Madariaga, R. (1994). Dynamic faulting under rate-dependent friction. *pure and applied geophysics, 142*(3), 419–445. https://doi.org/10.1007/BF00876049 (cit. on pp. 53, 60)

Cochard, A., & Rice, J. R. (1997). A spectral method for numerical elastodynamic fracture analysis without spatial replication of the rupture event. *Journal of the Mechanics and Physics of Solids, 45*(8), 1393–1418. https://doi.org/10.1016/S0022-5096(97)00004-5 (cit. on pp. 63, 97)

Coltice, N., Gérault, M., & Ulvrová, M. (2017). A mantle convection perspective on global tectonics. *Earth-Science Reviews, 165*, 120–150. https://doi.org/10.1016/j.earscirev.2016.11.006 (cit. on p. 9)

Comninou, M., & Dundurs, J. (1975). The angular dislocation in a half space. *Journal of Elasticity, 5*(3), 203–216. https://doi.org/10.1007/BF00126985 (cit. on p. 63)

Cooley, J. W. (1987). The re-discovery of the fast fourier transform algorithm. *Microchimica Acta, 93*(1), 33–45. https://doi.org/10.1007/BF01201681 (cit. on p. 62)

Crouch, S. L., & Starfield, A. M. (1983). *Boundary element methods in solid mechanics* (Vol. 5). (Cit. on p. 59).

Day, S. M. (1982). Three-dimensional simulation of spontaneous rupture: The effect of nonuniform prestress. *Bulletin of the Seismological Society of America, 72*(6), 1881–1902. https://doi.org/10.1785/BSSA07206A1881 (cit. on p. 24)

Day, S. M., Dalguer, L. A., Lapusta, N., & Liu, Y. (2005). Comparison of finite difference and boundary integral solutions to three-dimensional spontaneous rupture. *Journal of Geophysical Research: Solid Earth, 110*. https://doi.org/10.1029/2005JB003813 (cit. on pp. 34, 72)

Detournay, E., & Cheng, A. H.-D. (1993). 5 - fundamentals of poroelasticity. In C. Fairhurst (Ed.), *Analysis and design methods* (pp. 113–171). Pergamon. https://doi.org/10.1016/B978-0-08-040615-2.50011-3. (Cit. on pp. 39, 40, 104, 112)

Dieterich, J. H. (1979). Modeling of rock friction: 1. experimental results and constitutive equations. *Journal of Geophysical Research: Solid Earth, 84*, 2161–2168. https://doi.org/10.1029/JB084iB05p02161 (cit. on pp. 13, 24)

Dieterich, J. H. (1992). Earthquake nucleation on faults with rate-and state-dependent strength. *Tectonophysics, 211*(1), 115–134. https://doi.org/10.1016/0040-1951(92)90055-B (cit. on p. 23)

Duan, B., & Oglesby, D. D. (2005). Multicycle dynamics of nonplanar strike-slip faults. *Journal of Geophysical Research: Solid Earth, 110*. https://doi.org/10.1029/2004JB003298 (cit. on p. 19)

Dublanchet, P. (2019). Fluid driven shear cracks on a strengthening rate-and-state frictional fault. *Journal of the Mechanics and Physics of Solids, 132*, 103672. https://doi.org/10.1016/j.jmps.2019.07.015 (cit. on pp. 40, 105)

Dunham, E. M., Belanger, D., Cong, L., & Kozdon, J. E. (2011a). Earthquake ruptures with strongly rate-weakening friction and off-fault plasticity, part 1: Planar faults. *Bulletin of the Seismological Society of America, 101*(5), 2296–2307. https://doi.org/10.1785/0120100075 (cit. on p. 20)

Dunham, E. M., Belanger, D., Cong, L., & Kozdon, J. E. (2011b). Earthquake ruptures with strongly rate-weakening friction and off-fault plasticity, part 2: Nonplanar faults. *Bulletin of the Seismological Society of America, 101*(5), 2308–2322. https://doi.org/10.1785/0120100076 (cit. on p. 20)

Dunham, E. M., & Rice, J. R. (2008). Earthquake slip between dissimilar poroelastic materials. *Journal of Geophysical Research: Solid Earth, 113*. https://doi.org/10.1029/2007JB005405 (cit. on pp. 37, 102)

Ellsworth, W. L. (2013). Injection-induced earthquakes. *Science, 341*(6142), 1225942. https://doi.org/10.1126/science.1225942 (cit. on p. 35)

Erickson, B., Birnir, B., & Lavallée, D. (2008). A model for aperiodicity in earthquakes. *Nonlinear Processes in Geophysics, 15*(1), 1–12. https://doi.org/10.5194/npg-15-1-2008 (cit. on p. 17)

Erickson, B., & Jiang, J. (2018). *SEAS benchmark problem BP1-QD*. https://strike.scec.org/cvws/seas/download/SEAS_BP1_QD.pdf. (Cit. on pp. 59, 91)

Erickson, B., Jiang, J., & Dunham, E. (2021). *SEAS benchmark problems BP3-QD and BP3-FD*. https://strike.scec.org/cvws/seas/download/SEAS_BP3.pdf. (Cit. on p. 59)

Erickson, B. A., Birnir, B., & Lavallée, D. (2011). Periodicity, chaos and localization in a burridge-knopoff model of an earthquake with rate-and-state friction: Burridge-

knopoff model of an earthquake. *Geophysical Journal International*, *187*(1), 178–198. https://doi.org/10.1111/j.1365-246X.2011.05123.x (cit. on p. 17)

Erickson, B. A., & Dunham, E. M. (2014). An efficient numerical method for earthquake cycles in heterogeneous media: Alternating subbasin and surface-rupturing events on faults crossing a sedimentary basin. *Journal of Geophysical Research: Solid Earth*, *119*(4), 3290–3316. https://doi.org/10.1002/2013JB010614 (cit. on pp. 21, 28–30, 32, 147, 155)

Erickson, B. A., Dunham, E. M., & Khosravifar, A. (2017). A finite difference method for off-fault plasticity throughout the earthquake cycle. *Journal of the Mechanics and Physics of Solids, 109*, 50–77. https://doi.org/10.1016/j.jmps.2017.08.002 (cit. on pp. 21, 29, 32, 147, 155)

Erickson, B. A., Jiang, J., Barall, M., Lapusta, N., Dunham, E. M., Harris, R., Abrahams, L. S., Allison, K. L., Ampuero, J.-P., Barbot, S., Cattania, C., Elbanna, A., Fialko, Y., Idini, B., Kozdon, J. E., Lambert, V., Liu, Y., Luo, Y., Ma, X., . . . Wei, M. (2020a). Community code verification exercise for simulating sequences of earthquakes and aseismic slip (SEAS). *Seismological Research Letters*, *91*(2), 874–890. https://doi.org/10.1785/0220190248 (cit. on pp. 3, 19, 34, 59, 62, 72, 91, 144, 153, 171, 174)

Erickson, B. A., Jiang, J., Lambert, V., Barbot, S. D., Abdelmeguid, M., Almquist, M., Ampuero, J.-P., Ando, R., Cattania, C., Chen, A., Dal Zilio, L., Deng, S., Dunham, E. M., Elbanna, A. E., Gabriel, A.-A., Harvey, T. W., Huang, Y., Kaneko, Y., Kozdon, J. E., . . . Yang, Y. (2023). Incorporating full elastodynamic effects and dipping fault geometries in community code verification exercises for simulations of earthquake sequences and aseismic slip (SEAS). *Bulletin of the Seismological Society of America*, *113*(2), 499–523. https://doi.org/10.1785/0120220066 (cit. on pp. 3, 72, 148, 153, 171)

Erickson, B. A., Kozdon, J. E., & Harvey, T. W. (2020b). A non-stiff summation-by-parts finite difference method for the scalar wave equation in second order form: Characteristic boundary conditions and nonlinear interfaces. *Journal of Computational Physics, 408*, 109294. https://doi.org/10.1016/j.jcp.2020.109294 (cit. on pp. 28, 29)

Eyre, T. S., Eaton, D. W., Garagash, D. I., Zecevic, M., Venieri, M., Weir, R., & Lawton, D. C. (2019). The role of aseismic slip in hydraulic fracturing–induced seismicity. *Science Advances*, *5*(8), eaav7172. https://doi.org/10.1126/sciadv.aav7172 (cit. on p. 105)

Fedotov, S. (1968). The seismic cycle, quantitative seismic zoning, and longterm seismic forecasting. *Seismic Zoning in the USSR* (cit. on p. 9).

Ferrand, T. P., Eberhard, L., Gilio, M., & Parameswaran, R. (2023). *Transdisciplinary connections help understand natural mechanisms behind major seismic ruptures* (EGU23-10076). Copernicus Meetings. https://doi.org/10.5194/egusphere-egu23-10076. (Cit. on p. 8)

Fialko, Y., Sandwell, D., Simons, M., & Rosen, P. (2005). Three-dimensional deformation caused by the bam, iran, earthquake and the origin of shallow slip deficit. *Nature, 435*(7040), 295–299. https://doi.org/10.1038/nature03425 (cit. on p. 21)

Fineberg, J., & Bouchbinder, E. (2015). Recent developments in dynamic fracture: Some perspectives. *International Journal of Fracture, 196*(1), 33–57. https://doi.org/10.1007/s10704-015-0038-x (cit. on p. 44)

Fliss, S., Bhat, H. S., Dmowska, R., & Rice, J. R. (2005). Fault branching and rupture directivity. *Journal of Geophysical Research: Solid Earth, 110*. https://doi.org/10.1029/2004JB003368 (cit. on p. 19)

Francfort, G. A., & Marigo, J. .-. (1998). Revisiting brittle fracture as an energy minimization problem. *Journal of the Mechanics and Physics of Solids, 46*(8), 1319–1342. https://doi.org/10.1016/S0022-5096(98)00034-9 (cit. on p. 30)

Frérot, L. H. G. (2020). *Bridging scales in wear modeling with volume integral methods for elastic-plastic contact* (Doctoral dissertation). EPFL. Lausanne. https://doi.org/10.5075/epfl-thesis-7640. (Cit. on p. 23)

Garagash, D. I., & Germanovich, L. N. (2012). Nucleation and arrest of dynamic slip on a pressurized fault. *Journal of Geophysical Research: Solid Earth, 117*. https://doi.org/10.1029/2012JB009209 (cit. on p. 106)

Geubelle, P. H., & Rice, J. R. (1995). A spectral method for three-dimensional elastodynamic fracture problems. *Journal of the Mechanics and Physics of Solids, 43*(11), 1791–1824. https://doi.org/10.1016/0022-5096(95)00043-I (cit. on pp. 31, 54, 56, 62)

Gilbert, G. K. (1884). A theory of the earthquakes of the great basin, with a practical application. *American Journal of Science, s3-27*(157), 49–53. https://doi.org/10.2475/ajs.s3-27.157.49 (cit. on p. 17)

Grasedyck, L. (2005). Adaptive recompression of -matrices for BEM. *Computing, 74*(3), 205–223. https://doi.org/10.1007/s00607-004-0103-1 (cit. on p. 63)

Grasedyck, L., & Hackbusch, W. (2003). Construction and arithmetics of h-matrices. *Computing, 70*(4), 295–334. https://doi.org/10.1007/s00607-003-0019-1 (cit. on p. 63)

Grasso, E., Chaillat, S., Bonnet, M., & Semblat, J.-F. (2012). Application of the multi-level time-harmonic fast multipole BEM to 3-d visco-elastodynamics. *Engineering Analysis with Boundary Elements, 36*(5), 744–758. https://doi.org/10.1016/j.enganabound.2011.11.015 (cit. on p. 31)

Greengard, L., & Rokhlin, V. (1987). A fast algorithm for particle simulations. *Journal of Computational Physics, 73*(2), 325–348. https://doi.org/10.1016/0021-9991(87)90140-9 (cit. on pp. 31, 61)

Gu, J.-C., Rice, J. R., Ruina, A. L., & Tse, S. T. (1984). Slip motion and stability of a single degree of freedom elastic system with rate and state dependent friction. *Journal of*

the Mechanics and Physics of Solids, *32*(3), 167–196. https://doi.org/10.1016/0022-5096(84)90007-3 (cit. on p. 17)

Guglielmi, Y., Cappa, F., Avouac, J.-P., Henry, P., & Elsworth, D. (2015a). Seismicity triggered by fluid injection–induced aseismic slip. *Science*, *348*(6240), 1224–1226. https://doi.org/10.1126/science.aab0476 (cit. on p. 105)

Guglielmi, Y., Elsworth, D., Cappa, F., Henry, P., Gout, C., Dick, P., & Durand, J. (2015b). In situ observations on the coupling between hydraulic diffusivity and displacements during fault reactivation in shales. *Journal of Geophysical Research: Solid Earth*, *120*(11), 7729–7748. https://doi.org/10.1002/2015JB012158 (cit. on p. 36)

Gustafsson, K. (1991). Control theoretic techniques for stepsize selection in explicit runge-kutta methods. *ACM Transactions on Mathematical Software*, *17*(4), 533–554. https://doi.org/10.1145/210232.210242 (cit. on p. 147)

Gutierrez-Oribio, D., Stefanou, I., & Plestan, F. (2023). Passivity-based control of underactuated mechanical systems with coulomb friction: Application to earthquake prevention. https://doi.org/10.48550/arXiv.2207.07181. (Cit. on p. 106)

Gutiérrez-Oribio, D., Stefanou, I., & Plestan, F. (2024). Passivity-based control of underactuated mechanical systems with coulomb friction: Application to earthquake prevention. *Automatica*, *165*, 111661. https://doi.org/10.1016/j.automatica.2024.111661 (cit. on p. 106)

Gutiérrez-Oribio, D., Tzortzopoulos, G., Stefanou, I., & Plestan, F. (2023). Earthquake control: An emerging application for robust control. theory and experimental tests. *IEEE Transactions on Control Systems Technology*, *31*(4), 1747–1761. https://doi.org/10.1109/TCST.2023.3242431 (cit. on p. 106)

Hackbusch, W. (1999). A sparse matrix arithmetic based on $\cal h$-matrices. part i: Introduction to ${\cal h}$-matrices. *Computing*, *62*(2), 89–108. https://doi.org/10.1007/s006070050015 (cit. on pp. 31, 63)

Hackbusch, W. (2015). *Hierarchical matrices: Algorithms and analysis* (Vol. 49). Springer. https://doi.org/10.1007/978-3-662-47324-5. (Cit. on pp. 31, 63, 65)

Hajarolasvadi, S., & Elbanna, A. E. (2017). A new hybrid numerical scheme for modelling elastodynamics in unbounded media with near-source heterogeneities. *Geophysical Journal International*, *211*(2), 851–864. https://doi.org/10.1093/gji/ggx337 (cit. on pp. 31, 32, 155)

Hale, J. K. (1977). *Theory of functional differential equations*. Springer-Verlag. (Cit. on p. 14).

Harris, R. A., Barall, M., Archuleta, R., Dunham, E., Aagaard, B., Ampuero, J. P., Bhat, H., Cruz-Atienza, V., Dalguer, L., Dawson, P., Day, S., Duan, B., Ely, G., Kaneko, Y., Kase, Y., Lapusta, N., Liu, Y., Ma, S., Oglesby, D., . . . Templeton, E. (2009). The SCEC/USGS dynamic earthquake rupture code verification exercise. *Seismological Research Letters*, *80*(1), 119–126. https://doi.org/10.1785/gssrl.80.1.119 (cit. on pp. 19, 34, 72)

Harris, R. A., Archuleta, R. J., & Day, S. M. (1991). Fault steps and the dynamic rupture process: 2-d numerical simulations of a spontaneously propagating shear fracture. *Geophysical Research Letters, 18*(5), 893–896. https://doi.org/10.1029/91GL01061 (cit. on p. 19)

Harris, R. A., Barall, M., Aagaard, B., Ma, S., Roten, D., Olsen, K., Duan, B., Liu, D., Luo, B., Bai, K., Ampuero, J.-P., Kaneko, Y., Gabriel, A.-A., Duru, K., Ulrich, T., Wollherr, S., Shi, Z., Dunham, E., Bydlon, S., . . . Dalguer, L. (2018). A suite of exercises for verifying dynamic earthquake rupture codes. *Seismological Research Letters, 89*(3), 1146–1162. https://doi.org/10.1785/0220170222 (cit. on p. 34)

Harris, R. A., & Day, S. M. (1993). Dynamics of fault interaction: Parallel strike-slip faults. *Journal of Geophysical Research: Solid Earth, 98*, 4461–4472. https://doi.org/10.1029/92JB02272 (cit. on p. 19)

Heimisson, E. R., Dunham, E. M., & Almquist, M. (2019). Poroelastic effects destabilize mildly rate-strengthening friction to generate stable slow slip pulses. *Journal of the Mechanics and Physics of Solids, 130*, 262–279. https://doi.org/10.1016/j.jmps.2019.06.007 (cit. on pp. 40, 106, 112, 113)

Heimisson, E. R., Liu, S., Lapusta, N., & Rudnicki, J. (2022). A spectral boundary-integral method for faults and fractures in a poroelastic solid: Simulations of a rate-and-state fault with dilatancy, compaction, and fluid injection (cit. on pp. 40, 102, 106, 112, 113, 147).

Heimisson, E. R., Rudnicki, J., & Lapusta, N. (2021). Dilatancy and compaction of a rate-and-state fault in a poroelastic medium: Linearized stability analysis. *Journal of Geophysical Research: Solid Earth, 126*(8), e2021JB022071. https://doi.org/10.1029/2021JB022071 (cit. on pp. 40, 106, 112, 113)

Hillers, G., Ben-Zion, Y., & Mai, P. M. (2006). Seismicity on a fault controlled by rate- and state-dependent friction with spatial variations of the critical slip distance. *Journal of Geophysical Research: Solid Earth, 111*. https://doi.org/10.1029/2005JB003859 (cit. on p. 62)

Hodapp, M., Anciaux, G., & Curtin, W. A. (2019). Lattice green function methods for atomistic/continuum coupling: Theory and data-sparse implementation. *Computer Methods in Applied Mechanics and Engineering, 348*, 1039–1075. https://doi.org/10.1016/j.cma.2019.02.006 (cit. on p. 63)

Huang, J., & Turcotte, D. L. (1992). Chaotic seismic faulting with a mass-spring model and velocity-weakening friction. *pure and applied geophysics, 138*(4), 569–589. https://doi.org/10.1007/BF00876339 (cit. on pp. 17, 24)

Huang, J., & Turcotte, D. L. (1990). Are earthquakes an example of deterministic chaos? *Geophysical Research Letters, 17*(3), 223–226. https://doi.org/10.1029/GL017i003p00223 (cit. on p. 17)

Ida, Y. (1972). Cohesive force across the tip of a longitudinal-shear crack and griffith's specific surface energy. *Journal of Geophysical Research (1896-1977), 77*(20), 3796–3805. https://doi.org/10.1029/JB077i020p03796 (cit. on p. 24)

Johnson, K. M., & Segall, P. (2004). Viscoelastic earthquake cycle models with deep stress-driven creep along the san andreas fault system: STRESS-DRIVEN CREEP. *Journal of Geophysical Research: Solid Earth, 109*. https://doi.org/10.1029/2004JB003096 (cit. on p. 20)

Kame, N., Rice, J. R., & Dmowska, R. (2003). Effects of prestress state and rupture velocity on dynamic fault branching. *Journal of Geophysical Research: Solid Earth, 108*. https://doi.org/10.1029/2002JB002189 (cit. on p. 19)

Kanamori, H., & Brodsky, E. E. (2004). The physics of earthquakes. *Reports on Progress in Physics, 67*(8), 1429. https://doi.org/10.1088/0034-4885/67/8/R03 (cit. on pp. 1, 15, 35, 36, 169)

Kanamori, H., & Rivera, L. (2006). Energy partitioning during an earthquake. *Geophysical Monograph Series, 170*, 3–13. https://doi.org/10.1029/170GM03 (cit. on pp. 1, 169)

Kaneko, Y., Ampuero, J.-P., & Lapusta, N. (2011). Spectral-element simulations of long-term fault slip: Effect of low-rigidity layers on earthquake-cycle dynamics. *Journal of Geophysical Research: Solid Earth, 116*. https://doi.org/10.1029/2011JB008395 (cit. on pp. 20, 29, 32)

Kaneko, Y., & Fialko, Y. (2011). Shallow slip deficit due to large strike-slip earthquakes in dynamic rupture simulations with elasto-plastic off-fault response. *Geophysical Journal International, 186*(3), 1389–1403. https://doi.org/10.1111/j.1365-246X.2011.05117.x (cit. on p. 20)

Kato, N. (2002). Seismic cycle on a strike-slip fault with rate- and state-dependent strength in an elastic layer overlying a viscoelastic half-space. *Earth, Planets and Space, 54*(11), 1077–1083. https://doi.org/10.1186/BF03353305 (cit. on p. 20)

Kozdon, J. E., Erickson, B. A., & Wilcox, L. C. (2021). Hybridized summation-by-parts finite difference methods. *Journal of Scientific Computing, 87*(3), 85. https://doi.org/10.1007/s10915-021-01448-5 (cit. on pp. 28, 29)

Kpadonou, F., Chaillat, S., & Ciarlet, P. (2020). On the efficiency of nested GMRES preconditioners for 3d acoustic and elastodynamic h-matrix accelerated boundary element methods. *Computers & Mathematics with Applications, 80*(3), 471–489. https://doi.org/10.1016/j.camwa.2020.03.021 (cit. on pp. 2, 171)

Lambert, V., & Barbot, S. (2016). Contribution of viscoelastic flow in earthquake cycles within the lithosphere-asthenosphere system. *Geophysical Research Letters, 43*(19), 10, 142–10, 154. https://doi.org/10.1002/2016GL070345 (cit. on p. 20)

Lapusta, N., & Liu, Y. (2009). Three-dimensional boundary integral modeling of spontaneous earthquake sequences and aseismic slip. *Journal of Geophysical Research: Solid Earth,*

114. https://doi.org/10.1029/2008JB005934 (cit. on pp. 31, 32, 54, 58, 62, 120, 147, 148, 155)

Lapusta, N., Rice, J. R., Ben-Zion, Y., & Zheng, G. (2000). Elastodynamic analysis for slow tectonic loading with spontaneous rupture episodes on faults with rate- and state-dependent friction. *Journal of Geophysical Research: Solid Earth, 105*, 23765–23789. https://doi.org/10.1029/2000JB900250 (cit. on pp. 11, 17, 19, 20, 31, 32, 44, 58, 62, 67, 68, 72, 83, 90, 92, 143, 146, 155, 173, 176)

Larochelle, S., Lapusta, N., Ampuero, J.-P., & Cappa, F. (2021). Constraining fault friction and stability with fluid-injection field experiments. *Geophysical Research Letters, 48*(10). https://doi.org/10.1029/2020GL091188 (cit. on p. 40)

LaSalle, J. (1960). Some extensions of liapunov's second method. *IRE Transactions on Circuit Theory, 7*(4), 520–527. https://doi.org/10.1109/TCT.1960.1086720 (cit. on p. 14)

Li, D., & Liu, Y. (2016). Spatiotemporal evolution of slow slip events in a nonplanar fault model for northern cascadia subduction zone. *Journal of Geophysical Research: Solid Earth, 121*(9), 6828–6845. https://doi.org/10.1002/2016JB012857 (cit. on p. 155)

Li, D., & Liu, Y. (2017). Modeling slow-slip segmentation in cascadia subduction zone constrained by tremor locations and gravity anomalies. *Journal of Geophysical Research: Solid Earth, 122*(4), 3138–3157. https://doi.org/10.1002/2016JB013778 (cit. on p. 155)

Liu, D., Duan, B., & Luo, B. (2020). EQsimu: A 3-d finite element dynamic earthquake simulator for multicycle dynamics of geometrically complex faults governed by rate- and state-dependent friction. *Geophysical Journal International, 220*(1), 598–609. https://doi.org/10.1093/gji/ggz475 (cit. on pp. 28–30, 155)

Liu, Y., & Rice, J. R. (2007). Spontaneous and triggered aseismic deformation transients in a subduction fault model. *Journal of Geophysical Research: Solid Earth, 112*. https://doi.org/10.1029/2007JB004930 (cit. on pp. 32, 155)

Lizé, B. (2014). *Résolution directe rapide pour les éléments finis de frontière en électromagnétisme et acoustique : $\mathcal{H}$-Matrices. Parallélisme et applications industrielles* (Doctoral dissertation). Université Paris-Nord - Paris XIII. (Cit. on p. 65).

Lubich, C. (1988a). Convolution quadrature and discretized operational calculus. i. *Numerische Mathematik, 52*(2), 129–145. https://doi.org/10.1007/BF01398686 (cit. on p. 125)

Lubich, C. (1988b). Convolution quadrature and discretized operational calculus. II. *Numerische Mathematik, 52*(4), 413–425. https://doi.org/10.1007/BF01462237 (cit. on p. 125)

Luo, Y., Ampuero, J. P., Galvez, P., Ende, M. v. d., & Idini, B. (2017). *QDYN: A quasi-DYNamic earthquake simulator (v1.1)*. Zenodo. https://doi.org/10.5281/zenodo.322459. (Cit. on pp. 2, 31, 32, 62, 155, 171)

Ma, S., & Andrews, D. J. (2010). Inelastic off-fault response and three-dimensional dynamics of earthquake rupture on a strike-slip fault. *Journal of Geophysical Research: Solid Earth, 115*. https://doi.org/10.1029/2009JB006382 (cit. on p. 20)

Maerten, F. (2010). Adaptive cross-approximation applied to the solution of system of equations and post-processing for 3d elastostatic problems using the boundary element method. *Engineering Analysis with Boundary Elements, 34*(5), 483–491. https://doi.org/10.1016/j.enganabound.2009.10.016 (cit. on pp. 59, 63)

Maier, G., Novati, G., & Cen, Z. (1993). Symmetric galerkin boundary element method for quasi-brittle-fracture and frictional contact problems. *Computational Mechanics, 13*(1), 74–89. https://doi.org/10.1007/BF00350704 (cit. on p. 59)

Manolis, G. D., & Beskos, D. E. (1989). Integral formulation and fundamental solutions of dynamic poroelasticity and thermoelasticity. *Acta Mechanica, 76*(1), 89–104. https://doi.org/10.1007/BF01175798 (cit. on pp. 39, 104)

Manolis, G. D., & Beskos, D. E. (1990). Errata in "integral formulation and fundamental solutions of dynamic poroelasticity and thermoelasticity". *Acta Mechanica, 83*(3), 223–226. https://doi.org/10.1007/BF01172983 (cit. on pp. 39, 104)

Marck, J., Savitski, A. A., & Detournay, E. (2015). Line source in a poroelastic layer bounded by an elastic space. *International Journal for Numerical and Analytical Methods in Geomechanics, 39*(14), 1484–1505. https://doi.org/10.1002/nag.2405 (cit. on p. 113)

Marguin, V., & Simpson, G. (2023). Influence of fluids on earthquakes based on numerical modeling. *Journal of Geophysical Research: Solid Earth, 128*(2), e2022JB025132. https://doi.org/10.1029/2022JB025132 (cit. on p. 106)

Marguin, V., & Simpson, G. (2024). Numerical modelling of earthquake sequences involving valving and pumping of fluids. *Geophysical Journal International, 238*(1), 334–345. https://doi.org/10.1093/gji/ggae161 (cit. on p. 106)

Marone, C. (1998). LABORATORY-DERIVED FRICTION LAWS AND THEIR APPLICATION TO SEISMIC FAULTING. https://doi.org/10.1146/ANNUREV.EARTH.26.1.643 (cit. on p. 25)

Maubant, L., Radiguet, M., Pathier, E., Doin, M.-P., Cotte, N., Kazachkina, E., & Kostoglodov, V. (2022). Interseismic coupling along the mexican subduction zone seen by InSAR and GNSS. *Earth and Planetary Science Letters, 586*, 117534. https://doi.org/10.1016/j.epsl.2022.117534 (cit. on p. 105)

Mavaleix-Marchessoux, D. (2020). *Modelling the fluid-structure coupling caused by a far-field underwater explosion* (Doctoral dissertation). Institut Polytechnique de Paris. (Cit. on p. 125).

Morrissey, J. W., & Geubelle, P. H. (1997). A numerical scheme for mode iii dynamic fracture problems. *International Journal for Numerical Methods in Engineering, 40*(7), 1181–

1196. https://doi.org/10.1002/(SICI)1097-0207(19970415)40:7<1181::AID-NME108>3.0.CO;2-X (cit. on pp. 40, 54, 62)

Myers, R., & Aydin, A. (2004). The evolution of faults formed by shearing across joint zones in sandstone. *Journal of Structural Geology*, *26*(5), 947–966. https://doi.org/10.1016/j.jsg.2003.07.008 (cit. on p. 25)

Noda, H. (2021). Dynamic earthquake sequence simulation with a SBIEM without periodic boundaries. *Earth, Planets and Space*. https://doi.org/10.1186/s40623-021-01465-6 (cit. on p. 63)

Nur, A., & Booker, J. R. (1972). Aftershocks caused by pore fluid flow? *Science*, *175*(4024), 885–887. https://doi.org/10.1126/science.175.4024.885 (cit. on p. 34)

Nussbaum, J., & Ruina, A. (1987). A two degree-of-freedom earthquake model with static/-dynamic friction. *pure and applied geophysics*, *125*(4), 629–656. https://doi.org/10.1007/BF00879576 (cit. on p. 17)

Oglesby, D. D., & Archuleta, R. J. (2003). The three-dimensional dynamics of a nonplanar thrust fault. *Bulletin of the Seismological Society of America*, *93*(5), 2222–2235. https://doi.org/10.1785/0120020204 (cit. on p. 19)

Ohtani, M., Hirahara, K., Takahashi, Y., Hori, T., Hyodo, M., Nakashima, H., & Iwashita, T. (2011). Fast computation of quasi-dynamic earthquake cycle simulation with hierarchical matrices. *Procedia Computer Science*, *4*, 1456–1465. https://doi.org/10.1016/j.procs.2011.04.158 (cit. on pp. 31, 63)

Ortiz, M., & Pandolfi, A. (1999). Finite-deformation irreversible cohesive elements for three-dimensional crack-propagation analysis. *International Journal for Numerical Methods in Engineering*, *44*(9), 1267–1282. https://doi.org/10.1002/(SICI)1097-0207(19990330)44:9<1267::AID-NME486>3.0.CO;2-7 (cit. on p. 30)

Ozawa, S., Ida, A., Hoshino, T., & Ando, R. (2022). Large-scale earthquake sequence simulations on 3d nonplanar faults using the boundary element method accelerated by lattice h-matrices. *Geophysical Journal International*, *232*(3), 1471–1481. https://doi.org/10.1093/gji/ggac386 (cit. on pp. 2, 31, 32, 44, 63, 67, 69, 72, 82, 83, 94, 144, 146, 148, 155, 171, 173, 176)

Palmer, A. C., Rice, J. R., & Hill, R. (1997). The growth of slip surfaces in the progressive failure of over-consolidated clay. *Proceedings of the Royal Society of London. A. Mathematical and Physical Sciences*, *332*(1591), 527–548. https://doi.org/10.1098/rspa.1973.0040 (cit. on p. 36)

Perrin, G., Rice, J. R., & Zheng, G. (1995). Self-healing slip pulse on a frictional surface. *Journal of the Mechanics and Physics of Solids*, *43*(9), 1461–1495. https://doi.org/10.1016/0022-5096(95)00036-I (cit. on pp. 25, 62)

Pipping, E. (2019). Existence of long-time solutions to dynamic problems of viscoelasticity with rate-and-state friction. *ZAMM - Journal of Applied Mathematics and Mechanics*

/ *Zeitschrift für Angewandte Mathematik und Mechanik*, *99*(11), e201800263. https://doi.org/10.1002/zamm.201800263 (cit. on p. 25)

Pranger, C. C. (2020). *Unstable physical processes operating on self-governing fault systems, improved modeling methodology* (Doctoral Thesis). ETH Zurich. https://doi.org/10.3929/ethz-b-000475293. (Cit. on pp. 29, 32, 155)

Press, W. H., & Teukolsky, S. A. (1992). Adaptive stepsize runge-kutta integration. *Computers in Physics*, *6*(2), 188–191. https://doi.org/10.1063/1.4823060 (cit. on p. 69)

Raleigh, C. B., Healy, J. H., & Bredehoeft, J. D. (1976). An experiment in earthquake control at rangely, colorado. *Science*, *191*(4233), 1230–1237. https://doi.org/10.1126/science.191.4233.1230 (cit. on p. 36)

Ranjith, K., & Rice, J. R. (2001). Slip dynamics at an interface between dissimilar materials. *Journal of the Mechanics and Physics of Solids*, *49*(2), 341–361. https://doi.org/10.1016/S0022-5096(00)00029-6 (cit. on p. 21)

Rattez, H., Stefanou, I., & Sulem, J. (2018a). The importance of thermo-hydro-mechanical couplings and microstructure to strain localization in 3d continua with application to seismic faults. part i: Theory and linear stability analysis. *Journal of the Mechanics and Physics of Solids*, *115*, 54–76. https://doi.org/10.1016/j.jmps.2018.03.004 (cit. on pp. 17, 21)

Rattez, H., Stefanou, I., Sulem, J., Veveakis, M., & Poulet, T. (2018b). The importance of thermo-hydro-mechanical couplings and microstructure to strain localization in 3d continua with application to seismic faults. part II: Numerical implementation and post-bifurcation analysis. *Journal of the Mechanics and Physics of Solids*, *115*, 1–29. https://doi.org/10.1016/j.jmps.2018.03.003 (cit. on pp. 17, 21)

Reid, H. (1910). The mechanics of the earthquake, the california earthquake of april 18, 1906. *Report of the state earthquake investigation commission*, *2*, 16–18 (cit. on p. 9).

Rice, J. R., & Ruina, A. L. (1983). Stability of steady frictional slipping. *Journal of Applied Mechanics*, *50*(2), 343–349. https://doi.org/10.1115/1.3167042 (cit. on pp. 14, 18, 24)

Rice, J. (1973). "the initiation and growth of shear bands,". *Plasticity and Soil Mechanics* (cit. on p. 36).

Rice, J. R. (1993). Spatio-temporal complexity of slip on a fault. *Journal of Geophysical Research: Solid Earth*, *98*, 9885–9907. https://doi.org/10.1029/93JB00191 (cit. on pp. 18–20, 54, 60)

Rice, J. R., & Cleary, M. P. (1976). Some basic stress diffusion solutions for fluid-saturated elastic porous media with compressible constituents. *Reviews of Geophysics*, *14*(2), 227–241. https://doi.org/10.1029/RG014i002p00227 (cit. on p. 37)

Richart, N., & Molinari, J. F. (2015). Implementation of a parallel finite-element library: Test case on a non-local continuum damage model. *Finite Elements in Analysis and Design*, *100*, 41–46. https://doi.org/10.1016/j.finel.2015.02.003 (cit. on p. 29)

Ringoot, E., Roch, T., Molinari, J.-F., Massart, T. J., & Cohen, T. (2021). Stick–slip phenomena and schallamach waves captured using reversible cohesive elements. *Journal of the Mechanics and Physics of Solids, 155,* 104528. https://doi.org/10.1016/j.jmps.2021.104528 (cit. on p. 30)

Roch, T., Barras, F., Geubelle, P. H., & Molinari, J.-F. (2022a). cRacklet: A spectral boundary integral method library for interfacial rupture simulation. *Journal of Open Source Software, 7*(69), 3724. https://doi.org/10.21105/joss.03724 (cit. on p. 31)

Roch, T., Brener, E. A., Molinari, J.-F., & Bouchbinder, E. (2022b). Velocity-driven frictional sliding: Coarsening and steady-state pulses. *Journal of the Mechanics and Physics of Solids, 158*, 104607. https://doi.org/10.1016/j.jmps.2021.104607 (cit. on p. 44)

Roch, T. D. (2023). *Friction and fracture: Richness and complexity in dynamic rupture* (Doctoral dissertation). EPFL. Lausanne. https://doi.org/10.5075/epfl-thesis-9737. (Cit. on pp. 29–31)

Rolandone, F. (2022). *The seismic cycle: From observation to modeling*. John Wiley & Sons. (Cit. on pp. 8–10, 18, 23).

Romanet, P. (2017). *Thèse de pierre romanet | INSTITUT DE PHYSIQUE DU GLOBE DE PARIS* (Doctoral dissertation). INSTITUT DE PHYSIQUE DU GLOBE DE PARIS (IPGP) - Equipe de Tectonique et Mécanique de la Lithosphère. (Cit. on pp. 8, 18, 19, 31, 32, 52, 60, 61, 63, 73).

Romanet, P., & Ozawa, S. (2021). Fully dynamic earthquake cycle simulations on a nonplanar fault using the spectral boundary integral element method (sBIEM). *Bulletin of the Seismological Society of America*. https://doi.org/10.1785/0120210178 (cit. on pp. 32, 44, 53, 54, 56, 57, 60, 62, 67, 69, 72, 82, 83, 89, 144, 146, 155, 158, 173, 176)

Romanet, P., Sato, D. S., & Ando, R. (2020). Curvature, a mechanical link between the geometrical complexities of a fault: Application to bends, kinks and rough faults. *Geophysical Journal International, 223*(1), 211–232. https://doi.org/10.1093/gji/ggaa308 (cit. on pp. 18, 19, 31)

Rubin, A. M., & Ampuero, J.-P. (2005). Earthquake nucleation on (aging) rate and state faults. *Journal of Geophysical Research: Solid Earth, 110*. https://doi.org/10.1029/2005JB003686 (cit. on pp. 23, 73)

Ruina, A. (1983). Slip instability and state variable friction laws. *Journal of Geophysical Research: Solid Earth, 88,* 10359–10370. https://doi.org/https://doi.org/10.1029/JB088iB12p10359 (cit. on pp. 11, 17, 24)

Sáez, A., Lecampion, B., Bhattacharya, P., & Viesca, R. C. (2022). Three-dimensional fluid-driven stable frictional ruptures. *Journal of the Mechanics and Physics of Solids, 160*, 104754. https://doi.org/10.1016/j.jmps.2021.104754 (cit. on pp. 40, 113)

Sáez Uribe, A. A. (2023). *Three-dimensional fluid-driven frictional ruptures: Theory and applications* (Doctoral dissertation). EPFL. Lausanne. https://doi.org/10.5075/epfl-thesis-10303. (Cit. on pp. 35, 37, 105)

Schanz, M., & Cheng, A. H. .-. (2000). Transient wave propagation in a one-dimensional poroelastic column. *Acta Mechanica, 145*(1), 1–18. https://doi.org/10.1007/BF01453641 (cit. on pp. 122, 124)

Schanz, M. (2001). *Wave propagation in viscoelastic and poroelastic continua: A boundary element approach*. Springer-Verlag. https://doi.org/10.1007/978-3-540-44575-3. (Cit. on p. 125)

Schanz, M. (2009). Poroelastodynamics: Linear models, analytical solutions, and numerical methods. *Applied Mechanics Reviews, 62*(3). https://doi.org/10.1115/1.3090831 (cit. on pp. 37–39, 107, 161, 162)

Scholz, C. H. (2002). *The mechanics of earthquakes and faulting* (2nd ed.). Cambridge University Press. https://doi.org/10.1017/CBO9780511818516. (Cit. on p. 24)

Segall, P. (1989). Earthquakes triggered by fluid extraction. *Geology, 17*(10), 942–946. https://doi.org/10.1130/0091-7613(1989)017<0942:ETBFE>2.3.CO;2 (cit. on p. 106)

Segall, P., & Lu, S. (2015). Injection-induced seismicity: Poroelastic and earthquake nucleation effects. *Journal of Geophysical Research: Solid Earth, 120*(7), 5082–5103. https://doi.org/10.1002/2015JB012060 (cit. on p. 40)

Segall, P. (2010). *Earthquake and volcano deformation*. Princeton University Press. (Cit. on pp. 9, 62, 72, 73).

Segall, P., & Bradley, A. M. (2012). The role of thermal pressurization and dilatancy in controlling the rate of fault slip. *Journal of Applied Mechanics, 79*(3), 031013. https://doi.org/10.1115/1.4005896 (cit. on p. 155)

Segall, P., & Rice, J. R. (1995). Dilatancy, compaction, and slip instability of a fluid-infiltrated fault. *Journal of Geophysical Research: Solid Earth, 100*, 22155–22171. https://doi.org/10.1029/95JB02403 (cit. on pp. 40, 106)

Senjuntichai, T., & Rajapakse, R. K. N. D. (1994). Dynamic green's functions of homogeneous poroelastic half-plane. *Journal of Engineering Mechanics, 120*(11), 2381–2404. https://doi.org/10.1061/(ASCE)0733-9399(1994)120:11(2381) (cit. on pp. 39, 104)

Snyder, M. D., & Cruse, T. A. (1975). Boundary-integral equation analysis of cracked anisotropic plates. *International Journal of Fracture, 11*(2), 315–328. https://doi.org/10.1007/BF00038898 (cit. on p. 48)

Söderlind, G. (2002). Automatic control and adaptive time-stepping. *Numerical Algorithms, 31*(1), 281–310. https://doi.org/10.1023/A:1021160023092 (cit. on p. 147)

Stathas, A., & Stefanou, I. (2023). Fault friction under thermal pressurization during large seismic-slip: Numerical analyses and extension of the model of frictional slip. *Interna-*

tional Journal of Mechanical Sciences, 248, 108184. https://doi.org/10.1016/j.ijmecsci.2023.108184 (cit. on pp. 17, 21, 25)

Stefanou, I. (2019). Controlling anthropogenic and natural seismicity: Insights from active stabilization of the spring-slider model. *Journal of Geophysical Research: Solid Earth, 124*(8), 8786–8802. https://doi.org/10.1029/2019JB017847 (cit. on pp. 14, 16, 17, 35, 36, 106)

Stefanou, I., & Tzortzopoulos, G. (2022). Preventing instabilities and inducing controlled, slow-slip in frictionally unstable systems. *Journal of Geophysical Research: Solid Earth, 127*(7), e2021JB023410. https://doi.org/10.1029/2021JB023410 (cit. on p. 106)

Tada, T., & Yamashita, T. (1996). The paradox of smooth and abrupt bends in two-dimensional in-plane shear-crack mechanics. *Geophysical Journal International, 127*(3), 795–800. https://doi.org/10.1111/j.1365-246X.1996.tb04058.x (cit. on p. 49)

Tada, T., & Yamashita, T. (1997). Non-hypersingular boundary integral equations for two-dimensional non-planar crack analysis. *Geophysical Journal International, 130*(2), 269–282. https://doi.org/10.1111/j.1365-246X.1997.tb05647.x (cit. on pp. 49, 52, 53)

Templeton, E. L., Baudet, A., Bhat, H. S., Dmowska, R., Rice, J. R., Rosakis, A. J., & Rousseau, C.-E. (2009). Finite element simulations of dynamic shear rupture experiments and dynamic path selection along kinked and branched faults. *Journal of Geophysical Research: Solid Earth, 114*. https://doi.org/10.1029/2008JB006174 (cit. on p. 19)

Templeton, E. L., Bhat, H. S., Dmowska, R., & Rice, J. R. (2010). Dynamic rupture through a branched fault configuration at yucca mountain, and resulting ground motions. *Bulletin of the Seismological Society of America, 100*(4), 1485–1497. https://doi.org/10.1785/0120090121 (cit. on p. 19)

Terzaghi, K. (1923). Die berechnug der durchlassigkeit des tones aus dem verlauf der hydromechanischen spannungserscheinungen. *Sitzungsber. Akad. Wiss. (Wien). Math.-Naturwiss. Kl., Abt. Iia, 132*, 125–138 (cit. on p. 16).

Thakur, P., Huang, Y., & Kaneko, Y. (2020). Effects of low-velocity fault damage zones on long-term earthquake behaviors on mature strike-slip faults. *Journal of Geophysical Research: Solid Earth, 125*(8), e2020JB019587. https://doi.org/10.1029/2020JB019587 (cit. on pp. 29, 32, 155)

Tse, S. T., & Rice, J. R. (1986). Crustal earthquake instability in relation to the depth variation of frictional slip properties. *Journal of Geophysical Research: Solid Earth, 91*, 9452–9472. https://doi.org/10.1029/JB091iB09p09452 (cit. on p. 20)

Tzortzopoulos, G., Braun, P., & Stefanou, I. (2021). Absorbent porous paper reveals how earthquakes could be mitigated. *Geophysical Research Letters, 48*(3), e2020GL090792. https://doi.org/10.1029/2020GL090792 (cit. on p. 106)

Tzortzopoulos, G. (2021). *Controlling earthQuakes (CoQuake) in the laboratory using pertinent fault stimulating techniques* (Doctoral dissertation). École centrale de Nantes. (Cit. on pp. 14, 15, 17, 25, 36, 106).

Udías, A., Madariaga, R., & Buforn, E. (2014). *Source mechanisms of earthquakes: Theory and practice*. Cambridge University Press. (Cit. on p. 46).

Uphoff, C., May, D. A., & Gabriel, A.-A. (2022). A discontinuous galerkin method for sequences of earthquakes and aseismic slip on multiple faults using unstructured curvilinear grids (cit. on pp. 29, 32, 155).

Van den Ende, M. P. A., Chen, J., Ampuero, J. .-., & Niemeijer, A. R. (2018). A comparison between rate-and-state friction and microphysical models, based on numerical simulations of fault slip. *Tectonophysics, 733*, 273–295. https://doi.org/10.1016/j.tecto.2017.11.040 (cit. on p. 25)

Viesca, R. C. (2016a). Self-similar slip instability on interfaces with rate- and state-dependent friction. *Proceedings of the Royal Society A: Mathematical, Physical and Engineering Sciences, 472*(2192), 20160254. https://doi.org/10.1098/rspa.2016.0254 (cit. on p. 15)

Viesca, R. C. (2016b). Stable and unstable development of an interfacial sliding instability. *Physical Review E, 93*(6), 060202. https://doi.org/10.1103/PhysRevE.93.060202 (cit. on p. 15)

Viesca, R. C. (2021). Self-similar fault slip in response to fluid injection. *Journal of Fluid Mechanics, 928*. https://doi.org/10.1017/jfm.2021.825 (cit. on pp. 105, 113)

Xu, S., Ben-Zion, Y., & Ampuero, J.-P. (2012). Properties of inelastic yielding zones generated by in-plane dynamic ruptures—i. model description and basic results. *Geophysical Journal International, 191*(3), 1325–1342. https://doi.org/10.1111/j.1365-246X.2012.05679.x (cit. on p. 21)

Ying, L., Biros, G., & Zorin, D. (2004). A kernel-independent adaptive fast multipole algorithm in two and three dimensions. *Journal of Computational Physics, 196*(2), 591–626. https://doi.org/10.1016/j.jcp.2003.11.021 (cit. on p. 61)

Zheng, P., Zhao, S.-X., & Ding, D. (2013). Dynamic green's functions for a poroelastic half-space. *Acta Mechanica, 224*(1), 17–39. https://doi.org/10.1007/s00707-012-0720-2 (cit. on pp. 39, 104)

Zienkiewicz, O. C., Chang, C. T., & Bettess, P. (1980). Drained, undrained, consolidating and dynamic behaviour assumptions in soils. *Géotechnique, 30*(4), 385–395. https://doi.org/10.1680/geot.1980.30.4.385 (cit. on p. 112)

Titre : Modélisation des effets de l'injection de fluide sur une instabilité sismique en utilisant les méthodes d'éléments de frontière rapides

Mots clés : Instabilité sismique, Cycles sismiques, BEMs rapides, Poroelastodynamique, Effets fluides

Résumé : Les tremblements de terre d'origine naturelle ou anthropique provoquent d'importants dégâts humains et matériels. Dans les deux cas, la présence de fluides interstitiels influe sur le déclenchement des instabilités sismiques. Une nouvelle question d'actualité dans la communauté est de montrer que l'instabilité sismique peut être atténuée par un contrôle actif de la pression des fluides. Dans ce travail, nous étudions la capacité des méthodes d'éléments de frontière rapides (Fast BEMs) à fournir un solveur robuste multi-physique à grande échelle nécessaire à la modélisation des processus sismiques, de la sismicité induite et de leur atténuation.
Dans une première partie, un solveur BEM rapide avec différents algorithmes d'intégration temporelle est utilisé. Nous évaluons les performances de diverses méthodes à pas de temps adaptatif sur la base de problèmes de cycles sismiques 2D usuels pour les failles planes. Nous proposons une solution asismique analytique pour effectuer des études de convergence et fournir une comparaison rigoureuse des capacités des différentes méthodes en plus des problèmes de cycles sismiques de référence testés. Dans le cas d'un problème de cycles sismiques, une stratégie de comparaison par rapport à des résultats de référence est proposée. Une étude de convergence et de sensibilité approfondie des différentes méthodes utilisée par rapport aux paramètres de discrétisation en espace et en temps est effectuée. Nous montrons qu'une méthode hybride prédiction-correction / Runge-Kutta à pas de temps adaptatif permet non seulement une résolution précise, mais aussi d'incorporer à la fois les effets inertiels et les couplages hydro-mécaniques dans les simulations de rupture dynamique de faille.
Dans une deuxième partie, une fois les outils numériques développés pour des configurations standards, notre objectif est de prendre en compte les effets de l'injection de fluide sur le glissement sismique. Nous choisissons le cadre poroélastodynamique pour incorporer les effets de l'injection sur l'instabilité sismique. Un modèle poroélastodynamique complet nécessiterait des coûts de calcul ou des approximations non négligeables. Les modèles faiblement couplés sont les plus largement pris en compte dans la littérature. Nous justifions rigoureusement quels effets fluides prédominants sont en jeu lors d'un tremblement de Terre ou d'un cycle sismique. Pour cela, nous effectuons une analyse dimensionnelle des équations. Plus précisément, nous montrons qu'à l'échelle de temps de l'instabilité sismique, les effets inertiels sont prédominants alors qu'une combinaison de la diffusion du fluide et de la déformation élastique de la matrice solide due à la variation de la pression interstitielle devrait être privilégiée à l'échelle de temps du cycle sismique, au lieu du modèle de diffusion principalement utilisé dans la littérature. Enfin, nous considérons un problème de poroelastodynamique 1D simplifié pour illustrer les conditions sous lesquelles le modèle de poroélastodynamique complet peut être simplifié à l'échelle de temps d'un mouvement sismique.

Title : Modeling fluid injection effects in dynamic fault rupture using Fast Boundary Element Methods

Keywords : Seismic instability, Seismic cycles, Fast BEMs, Poroelastodynamics, Fluid effects

Abstract : Earthquakes due to either natural or anthropogenic sources cause important human and material damage. In both cases, the presence of pore fluids influences the triggering of seismic instabilities. A new and timely question in the community is to show that the earthquake instability could be mitigated by active control of the fluid pressure. In this work, we study the ability of Fast Boundary Element Methods (Fast BEMs) to provide a multi-physic large-scale robust solver required for modeling earthquake processes, human induced seismicity and their mitigation.
In a first part, a Fast BEM solver with different temporal integration algorithms is used. We assess the performances of various possible adaptive time-step methods on the basis of 2D seismic cycle benchmarks available for planar faults. We design an analytical aseismic solution to perform convergence studies and provide a rigorous comparison of the capacities of the different solving methods in addition to the seismic cycles benchmarks tested. In the case where a seismic cycle problem is considered, a methodology for the comparison between the results obtained and reference results is given. We conduct an in-depth convergence and sensitivity study of the different methods with respect to the parameters that scale both space and time discretizations. We show that a hybrid prediction-correction / adaptive time-step Runge-Kutta method allows not only for an accurate solving but also to incorporate both inertial effects and hydro-mechanical couplings in dynamic fault rupture simulations.
In a second part, once the numerical tools are developed for standard fault configurations, our objective is to take into account fluid injection effects on the seismic slip. We choose the poroelastodynamic framework to incorporate injection effects on the earthquake instability. A complete poroelastodynamic model would require non-negligible computational costs or approximations. One-way coupling models are most largely considered in the literature. We justify rigorously which predominant fluid effects are at stake during an earthquake or a seismic cycle. To this aim, we perform a dimensional analysis of the equations, and illustrate the results using a simplified 1D poroelastodynamic problem. We formally show that at the timescale of the earthquake instability, inertial effects are predominant whereas a combination of diffusion and elastic deformation due to pore pressure change should be privileged at the timescale of the seismic cycle, instead of the diffusion model mainly used in the literature. Finally, we consider a simplified 1D poroelastodynamic problem to illustrate the validity range of the simplified model obtained at the timescale of a seismic motion.

Institut Polytechnique de Paris
91120 Palaiseau, France